Lithium oxygen termination as a negative electron affinity surface on diamond: a computational and photoemission study

Tomas Liam Martin
H.H. Wills Physics Laboratory
University of Bristol

29 July 2011

A thesis submitted to the University of Bristol in accordance with the requirements for the degree of Doctor of Philosophy in the Faculty of Science, School of Physics

main text word count ≈ 80 000

Acknowledgements

Doing a PhD has been a challenging and fascinating process that has pushed me to my limits (and beyond, every now and then). Like all great adventures, I wouldn't have got through it without the help of a great number of people.

Firstly I'd like to thank Neil Fox for offering this PhD to me and for supervision on this project, and to Dave Cherns for his valuable advice. Thanks also go to Paul May, James Smith, Gareth Fuge, Suzanne Furkert, Susanna Stephens, Judy Hart, James Richley, Ben Truscott and all the Diamond Lab crew in Chemistry for taking a physicist into your kingdom, and to the crowd in Microstructures who still welcomed me back on my occasional reappearances in 2.38. Special thanks to Neil, Paul, Doug, Judy and Susanna for reading (and improving) my thesis and helping to track down those typos.

To the coffee crew, who sustained sanity through many caffeinated beverages home and abroad. To Tim Schuller, Jamie Grieve, Kian Montahan, Jim Sadler and Dave Lowndes, I offer my salute and wish luck for those of you yet to escape your own PhD travails.

To the various students who have found themselves under my guidance during the course of this project, I offer my thanks for your assistance. John Readman, Adam Fraser, Ben Rawlings, Claire Walsh, Victoria Goldsack, Fred Swadling and Luke Jones were all valiant squires to the knight of electron emission from diamond.

This thesis could not have been completed without the work collaborated with Kane O'Donnell, who was a huge support and a guru on many things computational and theoretical. Thanks also go to my collaborators at the University of Surrey, Vlad Stolojan, Cristina Giusca and Hidetsuga Shiozawa, and to S. Ravi P. Silva for allowing us access to their EELS, XPS and UPS kit. Similarly, thanks go to Chris Jones and Tom Scott at the IAC for their help on that XPS system.

To the people I've lived with during my PhD - Josh and Greeny at the beginning, Nat through the majority, Laura and Tom at the end where I was locked in my room writing most of the time. Your patience is worth its weight in gold.

Thanks ultimately to my friends and my family who supported me through a bumpy three years - especially to Nat, who put up with me through those early dark days - we both did it, even if we're now going our separate ways. To my parents, Business Dog and Phoebe for the many hours of support and for taking me in during my writing up period and feeding me so well.

To the people I've forgotten.

Declaration and Copyright

Declaration

Unless otherwise acknowledged, the content of this thesis is the original and sole work of the author. No portion of the work in this thesis has been submitted by the author in support of an application for any other degree or qualification, at this or any other university or institute of learning. The views expressed in this thesis are those of the author, and not necessarily those of the University of Bristol.

Tomas Liam Martin

Copyright ©

Abstract

This thesis presents the investigation of the interaction between lithium and the diamond surface using a number of computational and experimental techniques, with the goal of producing a low workfunction material for electron emission. Because of its theoretically shallow donor state in the diamond bulk and its potential as an alkali metal to induce a negative electron affinity (NEA) effect on the diamond surface, lithium is an interesting candidate for doping diamond.

The reaction of diamond HPHT nanoparticle powders with lithium salts at temperature in an ambient gas have been investigated. Thermionic and field emission performance was substantially improved following lithiation and further improved after washing in acqua regia, but the cause of this improvement was unclear. Characterisation of the doped powders with electron microscopy, secondary ion mass spectroscopy and electron energy loss spectroscopy was inconclusive, but indicated that any changes were likely to be due to a surface effect rather than bulk doping, so the remainder of the investigation focused on the interaction between lithium and the diamond surface.

Using *ab initio* density functional theory calculations, the stability of lithium with the C(100) and C(111) surfaces was investigated. Although lithium on the bare C(100) surface gave a predicted NEA surface of between -1.07 and 2.7 eV, the surface was fairly weakly bonded. When the adsorption of lithium on the oxygenated C(100) surface was calculated, the surface complex was much more stable, with adsorption energies as high as 4.7 eV for both the 0.5 and 1 ML coverages of Li. In addition, the electron affinity of the surface was even lower, with the LiO surface with two oxygen and two lithum atoms per unit cell having an electron affinity as negative as -4.5 eV, with a workfunction shift of -3.9 eV.

A similar behaviour was calculated on the C(111) surface, albeit with a slightly different configuration due to the one fewer dangling bonds per unit cell available on this surface. The adsorption of lithium on the bare C(111) surface was even less stable, but the 0.5 ML adsorption of Li on the fully oxygenated surface had a similar NEA to the C(100) surface of -3.97 eV, with an adsorption energy of 4.37 eV. These predictions for the two most prevalent surfaces on diamond indicate that lithium on the oxygenated diamond surface could present a stronger NEA surface than hydrogenated diamond but with a much greater stability than the equivalent CsO surface construction previously reported in the literature.

The viability of the LiO surface termination was explored experimentally using X-ray and ultraviolet photoemission (XPS and UPS), as well as low energy electron diffraction (LEED) and secondary electron emission using a scanning electron microscope. After lithium evaporation on the ozone-treated oxygenated surface and washing of the sample in deionised water, lithium was still observable using XPS, whereas on the hydrogenated sample with a similar treatment no such signal remained. Likewise, LEED patterns showed a significant change after Li coating and washing, consistent with the predicted structure from the computational results.

The LiO coated surface had a high secondary electron emission yield when observed in a scanning electron microscope, comparable to the hydrogen terminated surface and indicative of an NEA. UPS measurements of the boron-doped C(100) surface showed a clear characteristic sharp NEA peak around 5.2 eV in kinetic energy, with a calculated workfunction of 2.8 ± 0.1 eV and an NEA of -2.1 ± 0.1 eV. After annealing to a series of temperatures, it was found that the

UPS spectra remained fairly consistent until annealing to above 925°C, when the spectra began to change, with XPS and UPS showing a graphitisation of the surface and a removal of surface oxygens after annealing to 1218°C. This indicates that LiO on diamond is a strongly-bound, highly negative electron affinity surface. Experiments on the phosphorus doped C(111) surface were difficult to interpret due to large degrees of charging on the resistive surface, but an NEA peak did appear to be present.

The LiO surface termination was found to enhance the turnon and current density of field and thermionic emission, with as much as a forty-fold increase in thermionic emission current compared to a similar hydrogen-terminated sample. The conductivity of the surface treatment was also investigated, but on the macroscopic level the samples remained resistive after Li evaporation. Nonetheless this study has confirmed the predictions of a strongly bound highly negative electron affinity surface using LiO on diamond and this offers the potential for a number of applications.

Contents

List of Figures

List of Tables

A diamond is a chunk of coal that
is made good under pressure.

Henry Kissinger (b. 1923)

1 Introduction

1.1 Diamond - the 21st century material?

1.1.1 Properties of Diamond

The fourth most common element in the galaxy and solar system due to its ease of production in nuclear fusion in stars, carbon is a common element in the Earth's crust, although due to its ease in forming covalent bonds with other materials it is often found in compounds with other materials. The ability for carbon to form single, double and triple bonds with other elements is key to life on this planet, with organic compounds involving carbon forming many of the key ingredients of life, including around 18 % of the mass of the human body.

The sixth element in the periodic table, carbon has six electrons in ground-state configuration of $1s^2 2s^2 2p^2$, with two core electrons and four valence electrons split equally between s and p orbitals. When not bonded to other elements, carbon typically forms either three-fold (graphite, graphene) or four-fold (diamond) coordinated structures. In the three-fold coordinated structure, the valence electrons of carbon are hybridised into three sp^2 orbitals lying on a single plane, and one p orbital perpendicular to this plane, the electron within which is responsible for the conduction of electricity along the plane of graphite and graphene due to delocalisation into a π-bonded system.

Diamond is the four-fold coordinated structure of pure carbon, with four sp^3 hybrid orbitals in a tetrahedral configuration. Carbon atoms in the diamond structure form σ covalent bonds with four neighbouring carbon atoms, as pictured in figure 1.1. The diamond structure is also observed in crystalline silicon and various compound semiconductors. When the structure contains equal amounts of two different elements rather than one element alone it is called the zincblende structure. The stability of the structure yields excellent structural, thermal and electronic behaviour.

The crystal structure of diamond is a face-centred cubic (FCC) lattice with a basis of two atoms per lattice point located at (0,0,0) and $(\frac{1}{4}, \frac{1}{4}, \frac{1}{4})$ along the unit cell. The conventional unit cell of diamond has a unit cell length of 3.57 Å at room temperature.[2] As illustrated on figure 1.1 this leads to a C-C σ bond length of 1.54 Å and a unit cell containing eight atoms. The atomic number density of diamond is 1.76×10^{23} cm^{-3} and its mass density is 3516 kg m^{-3}. Table 1.1 lists some of the more notable physical and electronic properties of diamond. The small size of the carbon atom leads to its short bond lengths and results in low compressibility, resulting in diamond being

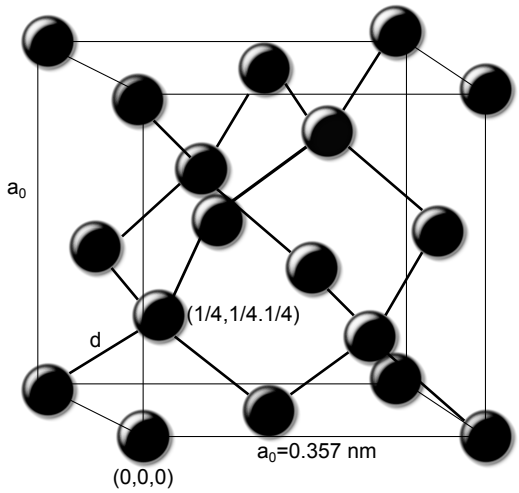

Figure 1.1: The unit cell of diamond, showing the bond lengths and tetrahedral structure. After [1].

one of the hardest known materials. On the Mohs hardness scale, diamond is the reference 'hard' material, with a maximum possible value of 10.

Property	Value	Units
Hardness	10,000	kg/mm^2
Tensile Strength	> 1.2	GPa
Compressive Strength	> 110	GPa
Sound Velocity	18,000	m/s
Density	3.52	g/cm^3
Young's Modulus	1.22	GPa
Poisson's ratio	0.2	Dimensionless
Thermal expansion coefficient	0.0000011	/K
Thermal conductivity	20	W/cm-K
Thermal shock parameter	30,000,000	W/m
Debye temperature	2,200	K
Optical refractive index at 591nm	2.41	Dimensionless
Optical transmissivity (nm to far IR)	225	Dimensionless
Loss tangent at 40 Hz	0.0006	Dimensionless
Dielectric constant	5.7	Dimensionless
Dielectric strength	10,000,000	V/cm
Electron mobility	2,200	cm^2/V-s
Hole mobility	1,600	cm^2/V-s
Electron saturated velocity	27,000,000	cm/s
Hole saturated velocity	10,000,000	cm/s
Bandgap	5.45	eV
Resistivity	10^{13}-10^{16}	Ω-cm

Table 1.1: Key physical and electronic properties of diamond. [3]

Diamond has a number of other exceptional properties. Phonons are conducted very efficiently through its covalent lattice structure, resulting in diamond possessing the highest room temperature thermal conductivity of any conventional solid, with a thermal conductivity at 300 K of 900 - 2300 W $m^{-1}K^{-1}$. Copper by comparison has a thermal conductivity of 400 W m^{-1} K^{-1}.

The shortness of the carbon bond also leads to a large overlap of the electron orbitals of adjacent carbon atoms and a large separation between the energy of the occupied sp^3 bonding orbitals that form the valence band compared to the unoccupied states in the conduction band formed by antibonding orbitals. The result is carbon's very large indirect band gap of 5.47 eV at 300 K, compared to just 1.12 eV for silicon. This allows the doping of a number of different elements within the diamond lattice in order to change the electronic properties of the material.

Another key property of diamond is its transparency to optical radiation, due to the optical transition between free electrons and holes being forbidden. Diamond is transparent from the near-ultraviolet to the far-infrared.[4] In addition to the properties listed in Table 1.1, diamond is chemically and biologically inert and very resistant to radiation damage, which makes it useful for a number of electrochemical devices and also as walls and coatings in fusion systems and high energy particle physics.

1.2 Preparation of Diamond

1.2.1 Natural Diamond

Diamond has long been considered one of the most precious stones found in the natural world, both for its hardness but also for its colour and brilliance. When cut appropriately, diamond refracts light in a more brilliant fashion than many similar stones. Diamond has been mined across the world for use in both jewellery and industrial applications, with many drilling and machining tools using diamond tipped cutting devices. Likewise, many royal crowns have included diamonds within their settings. Diamond is typically formed from silicate magma solution at pressures of 4 - 7 GPa and temperatures of 900 - 1350°C, as found in the upper mantle some 120 to 200 km below the Earth's surface.

The properties of diamond are extremely attractive for a large variety of applications, but the scarcity of large natural diamonds has made it prohibitively expensive for many applications outside jewel

1.2.2 High Temperature High Pressure Diamond

The enthalpies of formation of diamond and graphite differ only by 2.9 kJ mol^{-1}.[7] However the activation energy barrier between these two phases is large, as much as 728 kJ mol^{-1} for graphitisation at the (110) diamond surface.[8] Transition between the two phases is therefore difficult without high temperatures and pressures. While graphite is the stable allotrope of carbon at room temperature and pressure, the large energy barrier prevents the spontaneous conversion of diamond to graphite, so after formation diamond remains metastable.

It was not until the mid fifties that diamond was successfully formed artificially by General Electric using the high pressure, high temperature (HPHT) method,[9;10] in which graphite is compressed by hydraulic pressure to tens of thousands of atmospheres at temperatures above 2000 K.

In the presence of a metal catalyst, monocrystalline diamond stones are formed with dimensions between nanometres and millimetres, at a much lower cost than obtaining similar sized natural diamond. These HPHT crystals are widely used in cutting and machining blades, as well as grit powders for polishing and grinding. These stones can also be cut by laser or other methods to create substrates such as those used in this experiment.

Although the HPHT method produces diamonds cheaply and in vast quantities, with more than 300 tonnes of HPHT diamond produced each year, its major drawback is the shape of the stones produced, which are useful for some applications but limiting for others such as heat sinks and coatings. In addition, the HPHT process typically introduces large quantities of nitrogen into the diamond, giving it a yellow-brown colour and limiting its purity for use in electronic and electrochemical applications. Further HPHT treatment can remove this colour in HPHT or natural diamond, but it is difficult to control the quantity of impurities with any great precision using HPHT growth.

1.2.3 Chemical Vapour Deposition

An alternative method to HPHT is the formation of diamond as a thin film in a layer-by-layer technique. Early experiments showed that diamond could be grown onto natural diamond crystals when they were heated to 900°C in reduced pressures of carbon-containing gases, albeit with very low growth rates and a mix of diamond and graphite being formed by the thermal decomposition of the gases.[11;12] In the late 1960s it was shown by Angus *et al* that having hydrogen gas present in this gas mix etched away the graphite but not the diamond, allowing preferential growth of diamond.[13;14] Angus's group also incorporated boron into diamond during growth, producing a diamond with p-type semiconductor properties.[15] Later work by Deryagin *et al* showed that this vapour phase growth technique also worked on substrates other than diamond such as silicon or tungsten.[16;17]

This early work on chemical vapour deposition of diamond led in the early 1980s to two forms of diamond reactor, both first developed by the Japanese National Institute for Research in Inorganic Materials (NIRIM). The principle of the reactors were similar, but with very different methods of heating the gas above the substrate, as pictured in Figure 1.2. The first method uses a hot filament of metal with a high current running through it,[19;20] whilst the second method uses microwaves to ignite a plasma ball from the gases above the substrate.[21;22] In addition to these methods there have also been successful diamond growth using microwave plasma jets,[23;24] electron cyclotron resonance microwave plasma[25–28] radio frequency (RF) plasma[29;30] and d.c plasma[31–33] and plasma jets.[34–36]

The gas mix typically contains around 1-2 % of a carbon based molecule, typically acetylene or methane, although it has been shown that the growth rate of the diamond depends little on the species used.[37;38] The dissociation of the hydrogen gas into atomic hydrogen either by heat or in an ignited plasma is the key to the CVD reaction, due to the preferential etching of graphitic regions. The plasma approach typically has higher growth rates as the amount of atomic hydrogen in the hot filament approach is limited by the area of the filament exposed to the hydrogen gas.

By changing the seed layer between nanoparticle diamond and single crystal diamond, and by changing the gas mix concentrations, it is possible to grow diamond with different orientations and

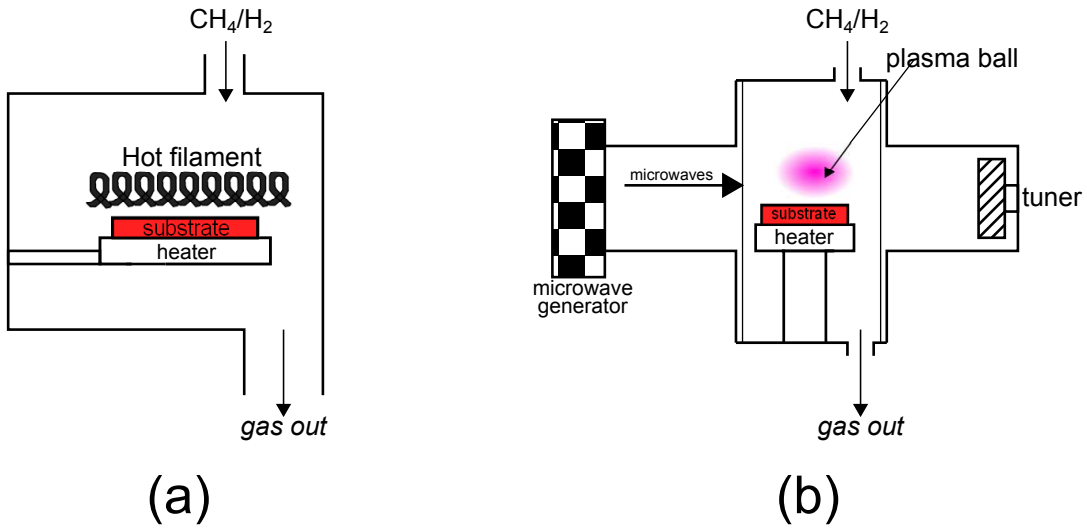

Figure 1.2: Figure showing the reactors used for (a) hot filament chemical vapour deposition and (b) microwave plasma-enhanced chemical vapour deposition. After [18].

crystallinities, from ultrananocrystalline diamond where individual grains are of the order of a few nanometres, up to single crystal materials grown epitaxially onto natural or HPHT diamond seed crystals. In addition, by changing the chemical composition of the seed layer or gas phase, it is possible to add dopants into the diamond lattice.

1.2.4 Doping Diamond

Synthetic and natural diamonds are classified into types according to the amount of certain impurities present within their structure. These can include vacancies and impurity atoms, either interstitial or substitutional. Vacancies occur where a position within the carbon lattice is empty, generally introduced by radiation damage expelling carbon atoms from the structure. Substitutional impurities occur when a carbon atom is replaced by an atom of an element other than carbon, sitting in the same position in the lattice as the atom it replaced. An interstitial impurity, on the other hand, is a foreign atom sitting inside the diamond structure but not sitting at a host lattice site.

With such a wide band gap, diamond is a semiconductor with a large number of potential dopants. Its excellent physical properties for electronic applications have led to a concerted effort to model and grow dopants into the diamond lattice in an attempt to create both n-type and p-type diamond for use in a wide variety of devices, especially high power applications not possible using traditional silicon semiconductors due to the higher thermal conductivity of diamond.

Finding a suitable dopant for p-type semiconductor behaviour in diamond has proved simpler than for its n-type counterpart due to the ease of boron-doping. Boron is a substitutional impu-

rity, and due to having one less electron than carbon, it acts as an acceptor and readily accepts electrons thermally excited from the valence band or from donor impurities. Only a very low energy is required for electrons to leave the valence band and substitutional boron induces red light absorption, and so holes are formed in boron doped diamond at room temperature, giving p-type semiconductivity. The activation energy of the boron acceptor is 0.37 eV.[39;40] Although this is quite a shallow acceptor, the activation energy is still quite large compared to k_BT at room temperature and due to this fairly low activation of acceptor sites, high concentrations of boron are required to get good electrical conductivity.[41]ity.[41]

Boron is a fairly rare impurity found in type IIb natural diamond with 1-5 ppm of boron, and a blue colour. Experimentally boron doping of CVD diamond using diborane[41] or trimethylboron[42] in the growth plasma has proved very successful, with metal-like conductivities possible with boron incorporations as high as 10^{21} atoms/cm^3.[43] Typically 500-10000 ppm (10^{19}-10^{21} atoms/cm^3) give resistivities between 5 and 100 mΩ.[44;45] Boron uptake is substantially higher in (111) growth sectors compared with (100) growth sectors.[46] Superconductivity has been investigated on super heavily boron doped diamond films.[47;48]

There are many potential n-type dopants in diamond but successful doping to semiconductor device standards has not been as successful as boron has been for p-type material.[49] Nitrogen is the most easily incorporated and is found in most natural diamonds in some quantity, as well as in HPHT and CVD films where nitrogen is present in the gas phase. The next element in the periodic table to carbon, nitrogen incorporates substitutionally into diamond.[49] Although the extra electron in the nitrogen atom compared to carbon forms some n-type behaviour, the donor level of nitrogen is deep in the band gap, at around 1.7 eV, due to the distortion of the nitrogen atom in the $(\bar{1}\bar{1}\bar{1})$ direction and the preferential formation of the nitrogen's lone pair and dangling bond on one of its four carbon neighbours. This distortion means the unpaired electron is localised closer to the carbon atom in the (111) direction than the nitrogen donor and so is not free to easily conduct.[50] This is sufficient for some interesting luminescence properties and the nitrogen vacancy centre is of interest for quantum computing. For electronic applications however the deep donor level provides only low mobilities and for many electronic properties a donor level closer to the conduction band minimum is desired.

Other theoretical n-type dopants include phosphorus, sodium, sulphur, potassium and lithium. Kajihara *et al* originally calculated that phosphorus preferred the substitutional site, whilst lithium and sodium were more stable in interstitial states.[50] All three were found to be shallow donors in the Kajihara study, with donor levels below the conduction band minimum of 0.3 eV for Na, 0.2 eV for P and just 0.1 eV for Li. The formation energies of these three dopants were calculated to be large and positive, leading to low equilibrium solubilities and making doping via indiffusion unlikely. Phosphorus was predicted to be immobile even under high temperature conditions due to the migration energy of the vacancy within, but the low activation energy for diffusion of Li along the interstitial channel meant it was likely to be mobile at moderate temperatures.

Further computational studies of sodium more recently found that the substitutional acceptor site was more stable than the interstitial donor site, so Na is unlikely to provide n-type semiconductivity. Lithium is an n-type donor in such calculations, but the predicted bonding energy was low enough that diffusion to inactive sites was expected at elevated temperatures.[51;52] These elements are all substantially more promising in theory than nitrogen, and a number of attempts

at incorporating them into the diamond lattice have been reported, with mixed results.

Sodium has been introduced into diamond through ion-implantation with measured activation energies between 0.13 eV and 0.415 eV, but conductivity was poor and conduction due to hopping between implant sites, not thermal activation.[53;54] Sulphur doped diamond has been obtained using hydrogen sulfide inclusion in the gas phase of microwave assisted plasma chemical vapour deposition, with evidence of n-type conductivity using Hall measurements in the region of 250-500 K.[55]

Substitutional phosphorus doping of CVD diamond has been reported by a number of groups, with concentrations reported up to $1 \times 10^{16} - 5 \times 10^{19}$ atoms/cm^3 after the inclusion of phosphene gas in the gas mixture of the growth plasma.[56] The breakthrough that made phosphorus doping possible was using epitaxial growth from a (111) oriented HPHT diamond substrate, rather than growing from a (100) oriented substrate. This is due to the stresses caused by the phosphorus inclusion having less of an effect on the higher quality (111) layer.[57]

Hall effect studies[58] on phosphorus doped diamond layers show that there is n-type semiconductivity with carrier mobilities above 600 cm^{2}V^{-1}s^{-1} but the activation energy of the P donor of around 0.6 eV[59] is too high for many electrons to occupy states in the conduction band at room temperature, and the resistivity of such films remain high. Mobilities in polycrystalline material is lower than that of epitaxial grown (111) layers.

Sulphur has also been introduced in the presence of boron, and with low boron concentrations can form an n-type semiconductor.[60;61] Without boron present in the gas phase, little sulphur was found to be incorporated after film growth by hot filament CVD, but as much as 0.2 % sulphur could be incorporated using microwave plasma assisted CVD, with resisitivities as much as three times lower than undoped diamond.[62] The difference between the two methods was attributed to the presence of CS radicals during microwave assisted growth but not present during hot filament growth being the key radical for sulphur inclusion. Crystal quality of S-doped (111) homoepitaxial diamond was poorer than similar homoepitaxial growth on the C(100) surface[63] and resistivity of the (111) surface was much higher than the (100) surface and indeed higher than the undoped (111) surface. Activation energy of sulphur-doped CVD diamond is estimated by Hall-effect measurements to be $0.5 - 0.75$ eV above 600 K but Hall mobilities decrease below this temperature.[64]

Lithium is in theory the shallowest donor in diamond, and is a smaller atom than the other candidate dopants, so should be incorporated more easily with less strain on the diamond structure. However, attempts to dope lithium into diamond have found that although lithium can be incorporated interstitially in the tetrahedral position of the lattice, it remains mobile at even moderate temperatures, and any substitutionally or defect-incorporated lithium is either electronically inactive or has a compensating p-type behaviour. The diffusion energy of Lithium has been estimated to be 0.26 eV,[65] (0.9 ± 0.3) eV[66] and above 1.25 eV,[67] all low enough that interstitial lithium should be mobile at even moderate temperatures and any lithium that is trapped at a vacancy or grain boundary becomes electrically inactive.

Studies that used lithium ion implantation have found some evidence of n-type behaviour but annealing to $500 - 800$°C reduced the conductivity achieved after the implantation process,[68] and some interpretations of the hopping-scheme conduction observed are that the cause is implantation damage rather than lithium donors,[53] or that if lithium donors are present, they are passified by thermal diffusion during annealing to form electrically neutral complexes with other

defects[69]. Samples with lithium added through both indiffusion[65;66;70–72] and during growth[73–75] have been found to be insulating - although the incorporation process was less damaging than ion implantation, the samples studied remained inactive, with indications that the lithium donors were compensated by high densities of acceptor states.[70] Inclusion of lithium fluoride within the growth gas phase of CVD films showed lithium concentrations of as much as 10^{21} cm^{-3} using SIMS analysis, but the p-type conductivity observed in that experiment was determined to be due to boron contamination of the growth chamber.[76]

It would be a huge advantage to the goal of diamond electronics to find improved methods to produce n-type diamond of a similar quality to the p-type doping achievable through boron-doping. For the purpose of electron emission reducing the workfunction through bulk doping is an attractive proposition, but the negative electron affinity properties of certain surface terminations of diamond mean that there are alternative ways to lower the threshold for emission.

1.3 Negative Electron Affinity

Changes to the surface of a material have a large effect on its electronic properties. Because of the large changes in electron density between the bulk of a material and vacuum, the electronic states at the surface or the interface with another material can be very different to states in the bulk. Semiconductors often have lower energy when the surface is atomically reconstructed to reduce the number of dangling bonds, and chemical bonds with adsorbate atoms or overlayers can reduce this surface energy further. As a result, there are a number of interesting stable surface configurations on many semiconductors that can have widely varying electronic properties.

A significant effect often found at the surface or interface of a semiconductor is band bending, where the electron energy level changes from the bulk to the surface due to a change in the electronic charge at the surface. In a bulk semiconductor, the Fermi level E_F is determined by the amount of doping in the bulk. The electronic states at the surface however, are fixed due to the positions of the reconstructed surface atoms, and the surface Fermi energy E_F^{sur} is pinned at a position above the valence band maximum in a way that is little affected by changes in the doping of the bulk material. As a result, the Fermi levels can differ between the surface and bulk, and so there can be a transfer of charge carriers between the bulk and surface states.

The charge carrier moved depends on the doping of the bulk but both induce an electric field within the material that bends the energy bands near the surface either upwards or downwards depending on the doping type. An n-type material will favour the transfer of electrons from the bulk into unoccupied surface states, producing an electric field between the positively charged ionised donor state and the now negatively charged surface state, bending the energy bands upwards towards the surface until the surface and bulk Fermi levels are aligned. For a p-type material the opposite occurs, with electrons in the neutral surface states being transferred to acceptor levels within the bulk, causing an electric field between positively charged unoccupied surface states and negatively charged acceptor states, bending the energy bands down from the surface until the Fermi levels align.

On diamond, this band bending effect can lead to an interesting effect where the conduction band sits above the vacuum level, lowering the electron affinity even to the point where it is negative. The termination of the surface is important in defining the behaviour of electrons near

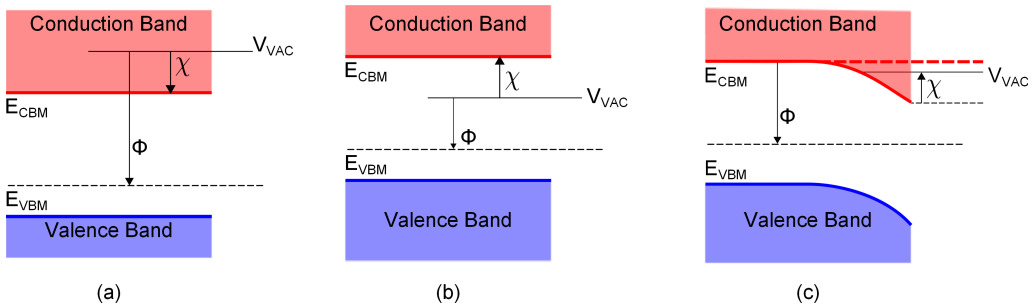

Figure 1.3: Energy band diagrams showing (a) a positive electron affinity, (b) a 'true' negative electron affinity and (c) an 'effective' negative electron affinity. After [83;84]

.

that surface. Most surfaces have a conduction band sitting below the vacuum level, known as a positive electron affinity, observed on the bare unterminated diamond surface as well as on oxygen-terminated diamond.

If however the surface termination has a positive charge relative to the carbon lattice, there will be a net attraction to the surface to an electron in the bulk, and the threshold for emission of an electron will be reduced. In certain cases the conduction-band states are shifted by this surface to a higher energy than the vacuum level, so that any conduction band electrons can be preferentially ejected from the surface into vacuum. This is known as a negative electron affinity (NEA) and is found on hydrogen terminated diamond as well as when numerous alkali metals are adsorbed onto both the bare and oxygenated diamond surfaces.

The hydrogen terminated surface is a 'true' NEA [77–82] caused by the polarised bonds between the carbon and hydrogen atoms, where the lower electronegativity ($\chi_H = 2.20$) of the hydrogen atom compared to the carbon atom ($\chi_C = 2.55$) means that the hydrogen atom gains a positive charge relative to the carbon atom, and a dipole forms along the C-H bond. This dipole has the effect of pulling the vacuum level below the conduction band minimum. [77;81] An NEA effect is also observed when thin (several nanometres) overlayers of alkali metals such as caesium are deposited on the surface. The effect of these thin metal overlayer however, is not a 'true' NEA, but to induce an 'effective' NEA by pinning the Fermi level at the interface between the diamond and metal, causing a band bending effect.

The electron affinity χ is defined as χ = E(-) - E(0) where E(0) is the energy of a substance in a neutrally charged state added to the energy of a single electron held in vacuum at infinite distance to the substance, and E(-) is the energy of the system when the electron is brought into the substance. In a material with a band structure, this translates as the difference between the lowest unoccupied electronic level E_{LOS} and the electrostatic potential in the vacuum E_{VAC}, i.e. $\chi = -(E_{LOS} - E_{VAC})$.

Fig 1.3 shows the motive diagrams of both types of negative electron affinity, in addition to an example of positive electron affinity. In the energy band description of the phenomenon, the positive electron affinity sees the electron bands at the surface shifted down relative to the vacuum level, making it harder for an electron to be removed. The 'true' negative electron affinity case, by comparison shows a upward shift in the electron bands at the surface, bringing the occupied

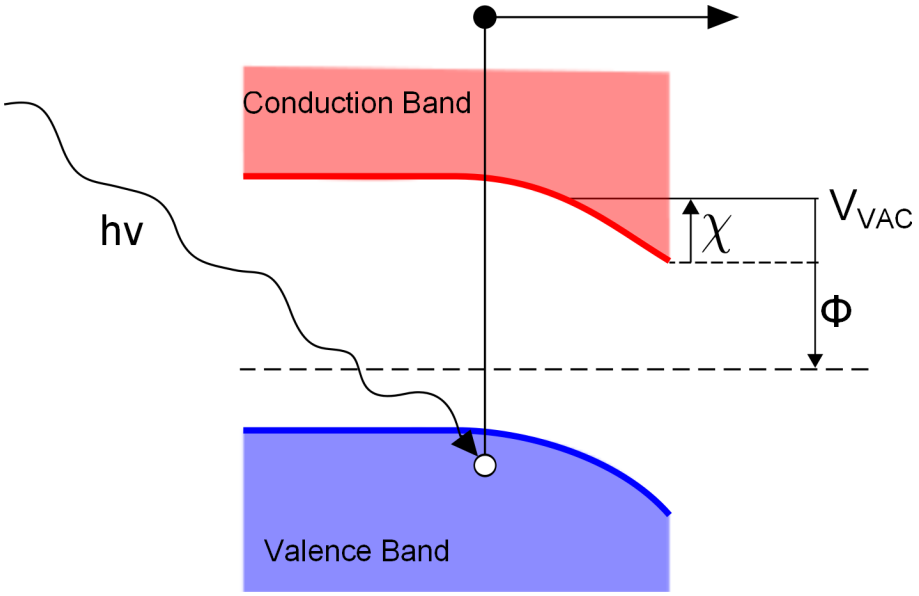

Figure 1.4: Diagram showing photoemission from a negative electron affinity material, where the electron is emitted in a two-step process.

bands closer to the vacuum level (and the conduction band above it) making it preferential for conduction electrons to escape into the vacuum and reducing the barrier for valence electrons to be excited. The 'effective' NEA case has a similar effect due to a band bending at the surface.

Electrons that are thermally excited from the bulk into the conduction band will thermalise to the bottom of the conduction band as they move towards the surface and be ejected into vacuum with a characteristic energy detectable as a sharp narrow peak in photoemission spectra. NEA surfaces also have a very high secondary electron emission yield. The photoemission process is pictured in Figure 1.4, showing the excitement by a photon of a valence band electron into the conduction band and its subsequent ejection into the vacuum.

A sharp high intensity peak around 5 eV with a narrow linewidth in a ultraviolet photoemission spectra is characteristic of an NEA causing electrons to be ejected directly from the conduction band minimum of diamond,[78;79;83–85] although it can also be observed from surfaces with a very low positive electron affinity.[86]

1.4 Potential Device Applications

Diamond has a huge range of current and potential applications across a wide range of industries. The hardness, strength and wear resistance of diamond make it an excellent cutting tool in drills, knives, saws and other cutting applications, whilst its good lubricating properties and chemical inertness are useful in bearings, dies and abrasive seals in pumps and valves. The temperature resistance and chemical inertness of CVD diamond film makes it an ideal coating for heat and corrosion protection on crucibles and reaction vessels, and the large transparency window from UV to IR and radiation resistance offers potential for fibre-optics and windows. The high thermal conductivity and low electrical conductivity of undoped diamond makes it an ideal heat-sink.

Of particular interest to this project are the electronic properties of diamond. The large band gap allows for a number of dopants that allow semiconductor behaviour and use in photonic devices, but when added to the high thermal conductivity, temperature and radiation resistance, the applications for semiconductor devices are very attractive. In addition the negative electron affinity of the hydrogen terminated surface, as well as with certain alkali metal surface coatings means diamond is an excellent potential electron emitter for use in cold cathodes, field-effect transistors and thermionic diodes. Figure 1.5 shows the combined electron-hole mobility, band gap and thermal conductivity (relative size of circles) for a number of materials, showing the clear advantages that diamond provides.

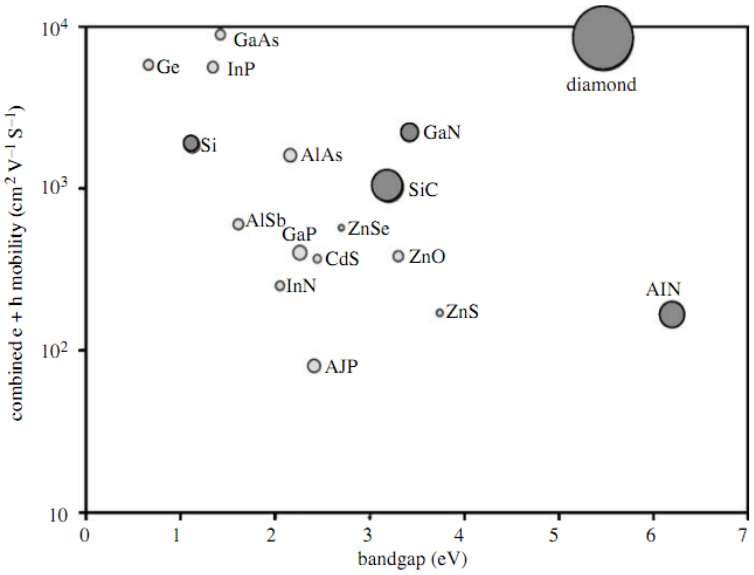

Figure 1.5: A graphic comparison of a number of electronic materials by the size of their band gap and electron-hole mobility. The area of each material's circle corresponds to its relative thermal conductivity.[87]

The central goal of this project is to optimise a diamond electron emitter, for both thermionic and field emission. There are two key parameters requiring optimisation for this purpose: the bulk workfunction and the electron affinity. Lithium, as both a potential shallow n-type donor in diamond and an alkali metal, is potentially a candidate element to improve both these aspects, and the role of lithium in diamond will be studied within this thesis.

1.5 Thermionic Emission

Thermionic emission is the ejection of electrons from a heated material. Already commonly found in electron sources for electron microscopes and X-ray sources, thermionic emission is also a process that over the years since its discovery has been studied as a method for energy conversion with no moving parts.

The simplest model of a thermionic converter consists of two electrodes separated by a gap that is either evacuated or filled with a small quantity of suitable gas. One electrode, the emitter

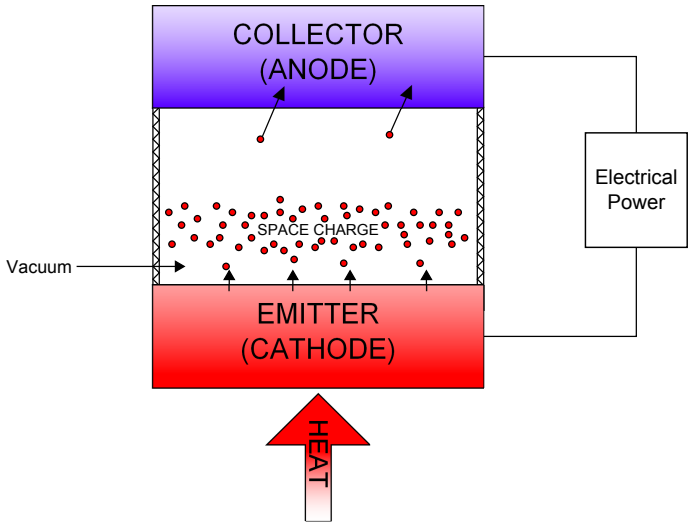

Figure 1.6: Diagram showing the simplest form of a thermionic diode converter, where electrons are emitted from the hot cathode and transferred to the cold anode, with the potential difference between the two electrodes due to the temperature gradient being available for electrical power conversion. Space charge electrons will build up in the interelectrode gap without careful device design.

or cathode, is connected to a heat source, whilst the other, the collector or anode, is connected to a heat sink, as shown in Figure 1.6. When heat is applied to the emitter sufficient to overcome the workfunction of the material, electrons are emitted across the interelectrode gap, where they can be collected by the collector. An external circuit connects the emitter and collector, allowing the emitted electrons to return to the emitter. The flux of electrons j passing through this circuit multiplied by the potential difference between the two electrodes that is overcome by the heat energy gives the total power of the system.

Figure 1.7 shows an energy motive diagram for a typical thermionic diode. An electron in the heated emitter requires an energy of $V_e = \phi_e + \phi_k$ to be emitted into the vacuum, where ϕ_e is the workfunction of the emitter and ϕ_k is the energy required to overcome the space charge within the vacuum gap - the potential barrier due to low kinetic energy electrons which have been ejected from the emitter but have insufficient energy to transfer to the collector. Once electrons have escaped the space charge, they can be absorbed by the cooler collector with workfunction ϕ_C, with the difference $V_0 = V_e - V_c$ where V_e is the energy given to the electron to liberate it from the emitter and V_c the energy used when the the electron is absorbed by the collector. If the thermionic diode is connected to a circuit, the power output depends on the output voltage V_0 and the current of electrons flowing through the circuit j. Electrons must overcome the collector workfunction (ϕ_c) to be absorbed. In addition, the collector will also emit electrons if heated, known as back emission(J_c), which can neutralize the desired emission current (J_e). To prevent back emission, a large temperature difference between the two electrodes is ideal. Too high an emitter workfunction will reduce the current, so a balance must be reached between output voltage (V_0), and current, to achieve the optimum compromise between maximum efficiency and maximum power density.

Thermionic devices in the past have been based on metal emitters operating at high temper-

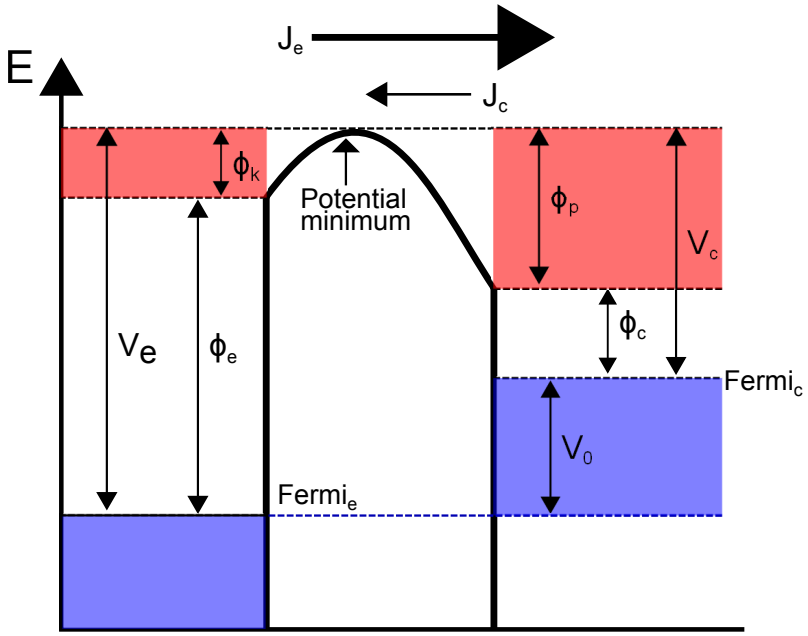

Figure 1.7: Energy diagram for a thermionic device. V_e is the energy needed to free an electron, k and p relate to the space charge, and V_0 is the output voltage. After[88;89].

atures above 1000 or even 2000°C, often using caesium vapour to overcome the problem of space charge, where a cloud of low kinetic energy electrons sits above the emitter surface, preventing most emitted electrons from transferring useful energy to the anode.[90]

1.5.1 Thermionic emission from diamond

Although field-assisted thermionic emission has been reported from nitrogen-doped microcrystalline diamond with the assistance of a hydrogen terminated NEA and nanocrystalline grain sizes with turn-ons of $260 - 500$ °C and an effective workfunction as low as 1.27 eV[91] and most reported measurements between 1.5-2 eV,[92;93] the emission currents are only a few microamps. Workfunctions of 2.4 eV have also been reported for homoepitaxial single crystal nitrogen doped diamond.[94]

Thermionic emission from phosphorus films has also been reported, from P-doped polycrystalline diamond films grown on a metallic substrate with doping concentrations of 5×10^{18} cm^{-3}. Emission from these samples showed a low turn-on of 375 °C and a very low effective workfunction of 0.9 eV[95;96] from fitting the data to the Richardson equation but, as with the nitrogen doped samples, emission currents remain low with a maximum of 200 μA at 950 K. This resulted in a low Richardson constant of 10 μA/cm^2 K^2, attributed to the low mobility of the donors and a high resistivity of the films.

Thermionic emission energy distribution measurements of nanocrystalline diamond (NCD) films without field-enhancement found a work function of around 3.3 eV at temperatures of $700 - 900$ °C, attributed to mid-band-gap states due to structural defects near the grain boundaries.[97] The advantage of using nanocrystalline diamond film is that it provides some conductivity to the film

through the large numbers of grain boundaries, helping electron transport to emission sites. Ultrananocrystalline diamond (UNCD) coated silicon tip arrays showed enhanced thermionic emission properties in the $600 - 800$ °C region due to the field enhancing geometry and the emission properties of the nitrogen doped film, but above this temperature the hydrogen termination was removed and the emission degraded. Boron-doped nanocrystalline diamond with hydrogen- and nitrophenyl-termination have shown thermionic emission at temperatures of 700-1100°C, with respective workfunctions of 3.95 and 3.88 eV.[98]

Emission has also been observed from sulphur doped nanocrystalline diamond films[93;95] with an estimated workfunction of 2.5 eV. Due to the high resistivity of sulphur doped samples, nanocrystalline diamond was used to give sufficient conductivity for field emission due to the high sp^2 content. The emission was localised to certain regions on the surface despite the uniform morphology, with emission site density estimated using field electron-emission microscopy (FEEM) to be approximately $10^4/\text{cm}^2$ with a turn-on that improved at higher temperatures. Due to the relatively poor conductivity of the various n-type doped diamond films, it seems for an effective emitter a combination of n-type doping, negative electron affinity (typically from hydrogen termination) and nanocrystalline grain sizes are required.

1.6 Field Emission from diamond

Field emission is widely used in electron microscopes and other cathodes and exploits the quantum tunnelling of electrons through a barrier under the influence of a high electric field into vacuum, as pictured in fig 1.8. The presence of the electric field lowers and thins the barrier at the surface experienced by electrons within the material. When the barrier is thin enough, a significant number of electrons are able to tunnel through into vacuum. Unlike other electron emission processes such as thermionic emission, the electrons require no energy to be excited.

The field emission from a metal in Fowler-Nordheim theory assumes that the metal follows Sommerfeld's free electron model, with Fermi-Dirac statistics, and that the potential experienced inside the metal is constant such that the electron states in the metal are not affected by the applied field. The calculation is made for a temperature of $T = 0$ K and the surface is assumed to be planar - as we will explore later, in practice the three dimensional geometry of many emitters has a non-trivial influence on the emission.

Field emission from diamond has been widely reported. Field emission occurs when the electrons in an emitting material are subject to a large electric field. Unlike in the thermionic case, the electrons are not directly emitted and instead tunnel quantum-mechanically through the barrier at the surface. Field emission devices are used in imaging tools such as scanning electron microscopes already but if the cost and resolution of the emitters can be improved, they offer interesting applications for high resolution displays.

In the absence of surface states, the strength of the field determines the energy band bending, but when surface states are present, the band bending is related to the Fermi level pinning.[100] Most early reports on field emission found that even with negative electron affinity surfaces, high field strengths of $10\text{V}/\mu\text{m}$ or more were required to initiate field emission.[101–103] Boron-doped diamond has a high threshold field due to the deep acceptor states, although some structural defects from the doping process may enhance the emission properties by the formation of gap states,[104] with a

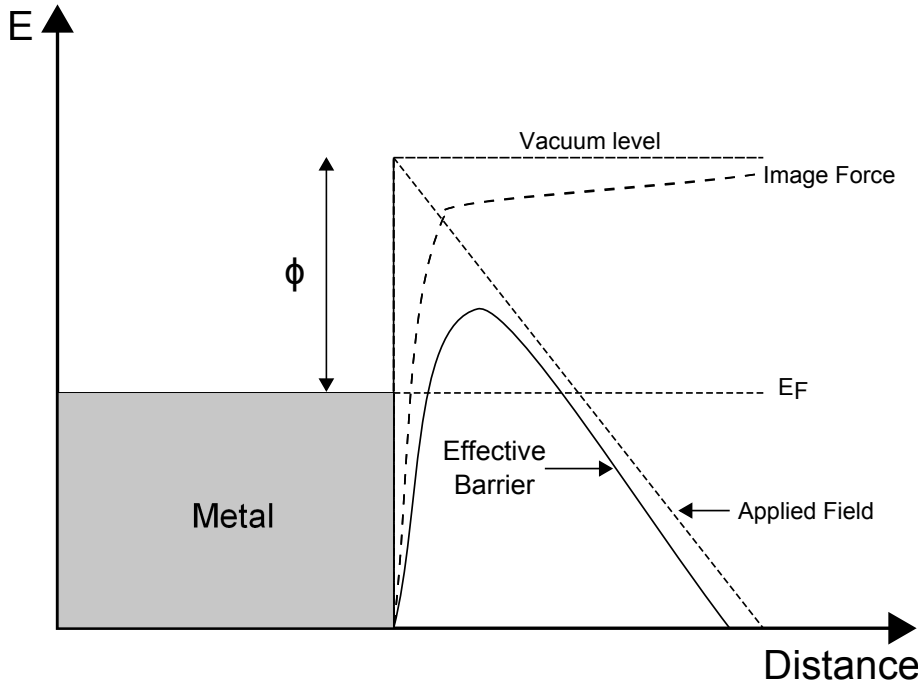

Figure 1.8: The potential experienced by an electron in a metal that must be overcome for field emission. After[99].

strong correlation between the emission threshold and the Raman FWHM of the diamond peak, indicating an increase in emission with a decrease in the diamond film quality. Emission from boron-doped diamond requires high field thresholds of 20-50 V/μm^{-1},[105] although lower field thresholds of around 3 V/μm have been reported via substantial geometric enhancement using silicon substrate micropatterning.[106] In general, lower turn-on fields and higher emission currents are observed for diamond films with higher defect density due to ion implantation or through CVD growth using a higher methane concentration, but these lower quality films have issues with reliability.[107] The enhanced emission for decreasing grain size has been theorised to be due to significant local band bending effects between negative and positive electron affinity grains on the nanocrystalline diamond surface.[108]

The best diamond field emitter is nitrogen-doped diamond with its relatively deep donor level at 1.7 eV, with threshold fields reported of as little as 0.2-0.3 V/μm,[109] although other studies have found much higher thresholds of $100 - 300$ V/μm, explained as being due to compensation of the nitrogen donors by defects[110], with large amounts of arcing due to resistive heating on the surface releasing trapped gases. It has been suggested that atomic hydrogen in hydrogen-rich CVD growth plasmas can abstract nitrogen during growth, preventing large quantities of nitrogen doping in the film, and better results have been observed using a nitrogen plasma.[111] As nitrogen doped diamond is insulating, the enhanced emission has been explained by a potential of $1-10$ kV appearing within the diamond material, with a strong dependence on the interface between the back contact metal and the diamond,[105] with rough interfaces showing a substantial increase in emission performance and the nitrogen doping producing a band bending effect that narrows the barrier between the diamond and metal sufficiently to allow electron injection across the interface.[108] The injection

of electrons from this metal backplate into the NEA diamond and then into vacuum has been proposed as a triple-junction effect,[112] but exact determination of the mechanism of emission in diamond remains a topic of debate.

Cold cathodes have also been reported from phosphorus doped diamond.[113;114] C(111) oriented single crystal diamonds with phosphorus content of 7×10^{19} cm^{-3} according to secondary ion mass spectroscopy showed lower threshold voltages for annealed, reconstructed surfaces rather than either hydrogen- or oxygen- terminated surfaces, with the hydrogen-terminated surface performing the worst due to the formation of a depletion layer preventing electrons from tunnelling into vacuum, because the vacuum level is below the phosphorus doping level. The electron affinities of the other two surfaces are both positive so this depletion layer effect does not occur and the lower electron affinity of the reconstructed surface makes it a better emitter than the oxidised surface.

No thermionic results have been reported for either bulk or surface lithium treated diamond. Field emission has been reported for lithium bulk-doped diamond with a caesium coating, after the inclusion of evaporated LiCl in the gas phase of CVD growth, with better field emission performance than phosphorus doped diamond but higher thresholds than nitrogen doped diamond or carbonised polymer.[112] One of the key outcomes of this thesis is to investigate the potential of lithium for enhancing electron emission further.

1.7 Field Effect Transistors

As well as lowering the barrier to electron emission, hydrogen termination on diamond has been shown to favour the transfer-doping effect. Due to the relative ease of electron removal compared to the oxygenated and bare diamond surfaces, chemical molecules on the surface of diamond can extract electrons from the bulk of hydrogen terminated diamond. When a molecule, for instance water, removes an electron from the diamond, it is transferred to an unoccupied state of the molecule, leaving a hole behind in the diamond valence band close to the surface. As this hole is bound to the now negatively charged adsorbate molecule, after repeated electron extractions a layer of holes can accumulate near the surface, leading to a p-type surface conductivity.[115–117]

This surface transfer effect has been explained by the interaction between the hydrogen-termination and a wetting layer from exposure to the air[115;117;118] but removal of either this wetting layer or the hydrogen termination NEA removes the p-type surface conductivity. Finding a similar surface treatment that is more stable would be of interest for a number of applications. This surface conductivity can be used for field effect transistors.[119]

Negative Electron Affinity (NEA) surfaces on diamond are also of interest for use in field-effect transistors (FETs). The transistor is the building block of modern electronics, chiefly for its use in amplifying and switching electronic signals. A transistor consists of three terminals. Controlling the voltage or current between one set of the terminals determines the current flowing between the other pair. Figure 1.9 shows the two principle types of transistor, the bipolar transistor and the field-effect transistor. Transistors rapidly replaced thermionic valves as the main component in electronic circuits due to their smaller size and ease of manufacture.[120]

The bipolar transistor consists of an emitter, collector and base terminals. It is made by sandwiching a p-type layer of semiconductor between two n-type layers, or a thin n-type semiconductor layer between two p-type semiconductor layers. The two thicker layers act as the emitter and col-

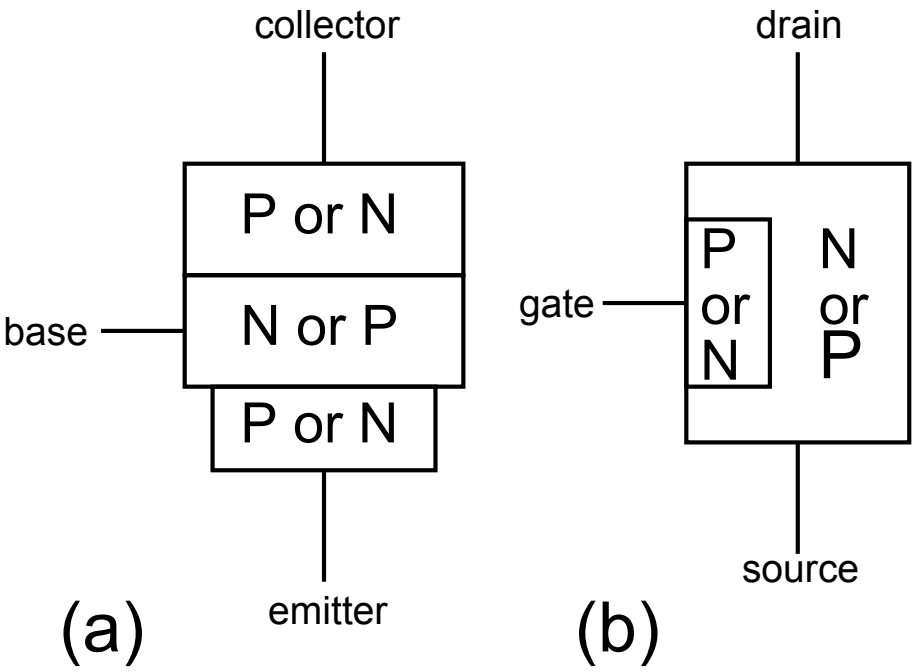

Figure 1.9: A diagram showing a typical setup for (a) a bipolar transistor and (b) a field effect transistor

lector pair, with the sandwich layer acting as the controlling base terminal. The minority carrier in the NPN circuit is the electron, whereas the PNP junction has current carried from the emitter to collector by a minority carrier of holes. As semiconductors have higher electron mobility compared to hole mobility, most bipolar transistors are of the NPN type as this allows them to carry higher currents.

Applying a small current flow between the base and emitter terminals allows a much larger current flow between the emitter and collector terminals. The bipolar transistor is often used for amplifiers due to the low current required at the gate even for large emitter-collector currents. Since the 1980s it has been widely superseded for many electronic applications by the metal-oxide field effect transistor or MOSFET.

In a field-effect transistor, the terminals are known as the source, drain and gate, and the voltage applied at the gate controls the current flowing between the source and drain. The gate is capacitively connected to the active device region, so that a voltage on the gate creates an electric field in the conductive channel, but no current flows to the gate. There are two principle types of field effect transistor - the junction field-effect transistor (JFET) and the insulated-gate field-effect transistor, more commonly known as the metal-oxide-semiconductor field-effect transistor due to the original use of a metal-oxide layer in the gate, although typically most modern MOSFETS use polycrystalline silicon for the 'metal' gate material. JFETs use a n-type channel with Ohmic contacts at the source and drain. The metal gate forms a Schottky contact with the active region, creating a depletion region within the conductive channel. Negative gate voltages increases the depletion region, shrinks the channel and reduces current to zero at a certain 'pinch-off' voltage, whereas positive gate voltages reduces the depletion region, widening the channel and allowing

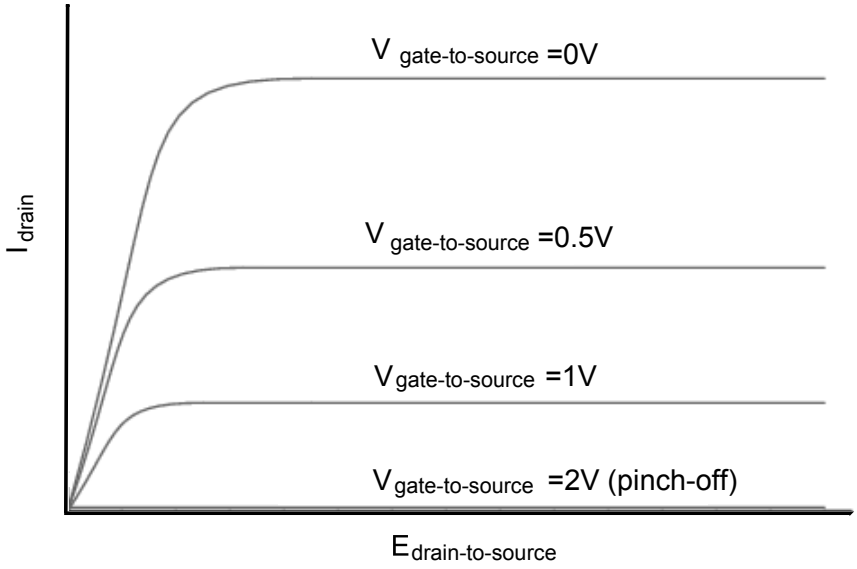

Figure 1.10: The typical drain current versus drain voltage behaviour of a JFET with changing gate voltages. Above a certain drain voltage ϕ_{Dsat} the current is saturated, and at high voltages the relationship breaks down. After[121].

higher currents, as pictured in figure 1.10.

In a typical MOSFET, the gate is separated from the semiconductor substrate by a thin layer of insulator, typically silicon dioxide or silicon oxynitride. The dielectric nature of this insulator is important, as it prevents current flow between the source/drain contacts and the gate. By changing the gate voltage, the effective electrical diameter of the conductive channel between the source and drain can be controlled, correspondingly increasing or decreasing the current flow between source and drain. As a result, a small change in gate voltage can have a large amplifying effect on a signal. Again, an n-type material is typically used for the source and drain regions of silicon FETs as the carrier mobility is higher, with a p-type silicon layer as the substrate. The typical drain-current versus drain voltage characteristic behaviour for different gate voltages is displayed in figure 1.10

Silicon based FETs are useful for weak signals such as wireless communications, and for high-impedance circuits due to the dielectric insulator. Most semiconductor computer chips consist of n-type and p-type MOSFETs arranged in logic gates. They are often unsuitable for high-power applications as the oxide layer can be destroyed, and due to the breakdown of silicon's electronic properties at high temperature are beginning to reach the limit to which they can be miniaturised. It is for these higher power, higher frequency and higher temperature devices that other semiconductors such as diamond are being studied.

1.7.1 Surface conductive diamond

The large diamond band gap of 5.5 eV allows for high voltage operation, and diamond has high intrinsic electron and hole mobility of $3800 - 4500$ cm^2/V s[122], allowing for large currents. In

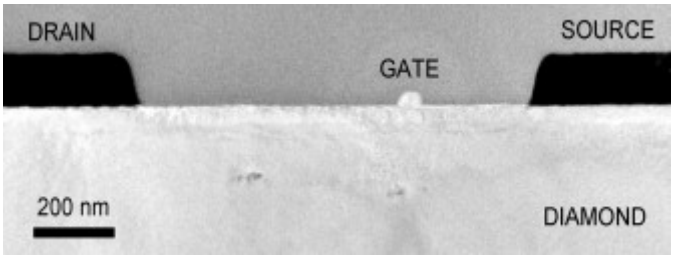

Figure 1.11: Transmission electron microscope image showing a side-on schematic of a 50 nm gate length diamond field effect transistor produced by the University of Glasgow, using gold Ohmic contacts and an aluminium gate. [129]

addition to this potential for high power densities, diamond's high thermal conductivity (22 W/K cm) and chemical stability make it an attractive substrate for FETs for high power/high frequency devices such as amplifiers in the microwave region. These are currently catered for by vacuum tubes, which have a low power efficiency, but other semiconductor alternatives such as silicon carbide are limited to frequencies of 1 GHz by low carrier mobilities. [123] Diamond FETs are also predicted to have high breakdown voltages and saturation voltages. [124] By changing the termination to that sensitive to chemical changes, the current can be monitored as a sensor, [125] such as to sense the hybridisation of DNA chains bonded to the diamond surface. [126;127]

However, as n-type doping of diamond remains a unfulfilled challenge, most diamond based FET devices use the NEA properties of surface termination rather than the typical FET structure. Gold (or gold-titanium) contacts are used for the source and drain terminals, with an aluminium gate contact, as shown in Figure 1.11. Hydrogen termination is used to create a hole channel in the surface diamond layer between the contacts. As the hole channel layer is essentially a two-dimensional hole gas, the effectiveness of the FET is determined by the width or circumference of the gate, rather than the area as in a traditional MOSFET. The p-type conductivity has been measured to have as many as 10^{19} holes cm^{-3}, with mobilities as high as 70 cm^2Vs^{-1}. [128] Prolonged heating at 300 °C removes this conductivity.

Intercontact distances of less than approximately 10 microns are required for successful devices, with effectiveness greatly improved by reduction of this length further, with typical device of 100 nm gate length showing promise. Recent results have reported gate lengths of as little as 50 nm [129] using direct etching of the gold source and drain contacts.

As well as inducing an NEA on diamond, hydrogen termination can also enable a transfer-doping effect on the diamond surface in the presence of foreign molecules such as water close to the surface. Because of the lower barrier to electron removal, it is easier for electrons to be removed from the diamond and transferred into an unoccupied state in the molecule sitting on the diamond surface, leaving behind a hole in the diamond and a negative charge on the molecule. The attraction between the two confines the hole to the near-surface region of the diamond. If enough molecules extract electrons in this manner, the near surface of the diamond gains p-type surface conductivity.

A diamond crystal with a thin layer of p-type surface conductivity can be used for a field-effect transistor, as the NEA creates a band-bending effect on the surface introducing a hole layer below

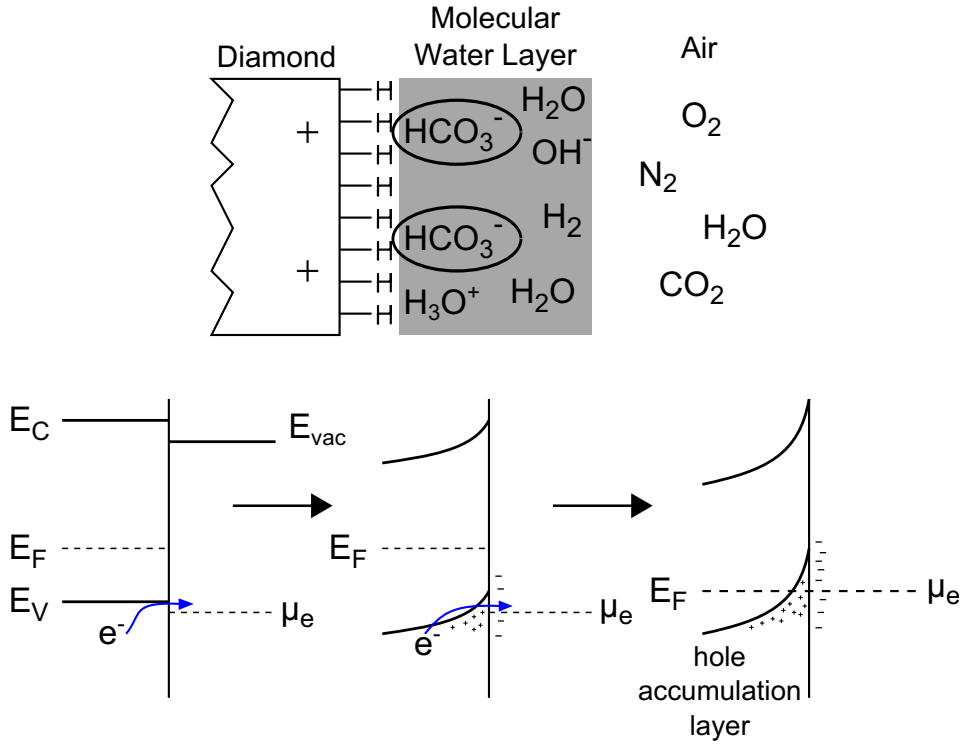

Figure 1.12: Band bending effect by hydrogen termination on the diamond surface, causing a hole layer 5-10 nm below the surface of the gate, allowing a FET-like charge carrying channel. After [130].

the surface that acts as a charge-carrying channel, as illustrated in fig 1.12.

Currently this effect is only observed on hydrogen-terminated diamond in the presence of adsorbates such as water, typically formed by exposure to air. In vacuum this layer is removed, and loss of the hydrogen termination due to oxidation also stops this effect. There is also an issue with trapped charge on the surface that limits performance. If a more solid-state example of this interaction that didn't degrade so easily could be found, the device applications could prove invaluable. In addition, the only currently reported FETs using diamond are p-type, and a system using electrons as the majority carrier for an n-type transistor device would add more options to the field of diamond electronics. Following the study of lithium-oxide as a theoretical and experimental NEA on diamond, this study will investigate the potential of using Li-O terminated diamond in a field-effect transistor.

1.8 Thesis outline

The experiments presented within this thesis aim to investigate the potential of lithium as a surface and bulk dopant in diamond, with the aim of producing an enhanced material for electron emission in either field or thermionic emission devices.

In **Chapter 2**, the theoretical background behind the methods used in this thesis will be presented, most importantly that of the density functional theory computational method used to calculate potential stable interactions between lithium and diamond.

Chapter 3 will detail the experimental tools and apparatus used in the studies presented.

Chapter 4, the first experimental chapter, will discuss early attempts at creating emission devices with diamond nanoparticles lithiated using lithium salts, as well as the characterisation of these nanodiamonds.

Chapter 5 reports the computational studies of lithium on both the bare and oxygenated C(100) and C(111) diamond surfaces, and the prediction of a stable negative electron affinity complex.

Chapter 6 reports on the investigation using X-ray and ultraviolet photoemission into the behaviour of lithium on single crystal diamond substrates and the confirmation of an NEA surface using Li-O on the diamond C(100) surface.

Chapter 7 reports on the device applications of the lithium-oxygen surface layer found in the previous chapter for surface conductivity, thermionic emission and field emission.

Chapter 8 summarises the results presented in this thesis and explores potential avenues for future work.

REFERENCES

[1] Edmonds, A. *Magnetic resonance studies of point defects in single crystal diamond.* PhD thesis, (2008).

[2] Singh, J. *Physics of semiconductors and their heterostructures.* McGraw-Hill, New York, (1993).

[3] Spear, K. and Dismukes, J. *Synthetic Diamond: Emerging CVD Sicence and Technology.* Wiley, Chichester, UK, (1994).

[4] Robertson, R., Fox, J., and Martin, A. *philosophical Transactions fo the Roay Society of London Series a-Mathematical Physical and Engineering Sciences* **232** (1934).

[5] Tennant, S. *Phil. Rans. R. Soc.* **87**, 123 (1797).

[6] Lavoisier, A. *Memoire Academie des Sciences* , 564 (1772).

[7] Bundy, F. *Science* **29**, 974 (1980).

[8] Ashfold, M., May, P., Rego, C., and Everitt, N. *Chemical Society Reviews* , 21 (1994).

[9] Field, J. *The Properties of Natural and Synthetic Diamond.* Academic Press, London, (1992).

[10] May, P. *Philosophical Transactions of the Royal Society A: Mathematical, Physical and Engineering Sciences* **358**(1766), 473–495 January (2000).

[11] Eversole, W. *Patent Nos. 3030187, 3030188* (1958).

[12] Deryagin, B., Fedoseev, D., Lukyanovich, V., Spitsyn, B., Ryanov, A., and Lavrentyev, A. *J. Cryst. Growth* **2**, 380 (1968).

[13] Angus, J., Will, H., and Stanko, W. *J. Appl. Phys.* **39**, 2915 (1968).

[14] Poferl, D., Gardner, N., and Angus, J. *J. Appl. Phys.* **44**, 1418 (1973).

[15] Angus, J., Gardner, N., Poferl, D., Chauhan, S., Dyble, T., and Sung, P. *Sin Almazy* **3**, 38 (1971).

[16] Deryagin, B., Spitsyn, B., Builov, L., Klochov, A., Gorodetskii, A., and Smol'yanimov, A. *Dokl. Akad. Nauk SSR* **231**, 333 (1976).

[17] Spitsyn, B., Builov, L., and Deryagin, B. *J. Cryst. Growth* **52**, 219 (1981).

[18] May, P. *Endeavour Magazine* **19**, 101 (1995).

[19] Matsumoto, S., Sato, Y., Kamo, M., and Setaka, N. *Jpn. J. Appl. Phys. Part 2* **21**, 183 (1982).

[20] Matsumoto, S., Sato, Y., Tsutsumi, M., and Setaka, N. *J. Mater. Sci.* **17**, 3106 (1982).

[21] Kamo, M., Sato, U., Matsumoto, S., and Setaka, N. *J. Cryst. Growth* **62**, 642 (1983).

[22] Saito, Y., Matsuda, S., and Nogita, S. *J. Mater. Sci. Lett.* **5**, 565 (1986).

[23] Mitsuda, Y., Yoshida, T., and Akashi, K. *Rev. Sci. Instrum.* **60**, 249 (1989).

[24] Smith, D., Servillano, E., Besen, M., Berkman, V., and Bourget, L. *Diamond Relat. Mater.* **3**, 325 (1992).

[25] Suzuki, J., Kawarada, H., Mar, K., Wei, K., Yokota, Y., and Hiraki, A. *Jpn. J. Appl. Phys.* **28**, L281 (1989).

[26] Kawarada, H., Mar, K., and Hiraki, A. *Jpn. J. Appl. Phys.* **26**, L1032 (1987).

[27] Tsai, W., Reynolds, O., Hikido, S., and Cooper III, C. *Appl. Phys. Lett.* **60**, 1444 (1992).

[28] Wei, W., Kawarada, H., Suzuki, J., and Hiraki, A. *J. Cryst. Growth* **99**, 1201 (1990).

[29] Matsumoto, S. *J. Mater. Sci. Lett.* **4**, 600 (1985).

[30] Beckman, J., Jackman, R., and Foord, J. *Diamond Relat. Mater.* **3**, 602 (1994).

[31] Akatsuka, F., Hirose, Y., and Komaki, K. *Jpn. J. Appl. Phys.* **27**, L160 (1988).

[32] Suzuki, K., Sawabe, A., Yasudo, H., and Inuzuka, T. *Appl. Phys. Lett.* **50**, 728 (1987).

[33] Suzuki, K., Sawabe, A., Yasuda, H., and Inuzuka, T. *Jpn. J. Appl. Phys.* **29**, 153 (1990).

[34] Kurihara, K., Sasaki, K., Kawarada, M., and Koshima, N. *Appl. Phys. Lett.* **52**, 437 (1988).

[35] Lugscheider, E., Schlump, W., Deuerler, F., and Remer, P. *Diamond Relat. Mater.* **3**, 325 (1994).

[36] Boudina, A., Fitzer, E., and Wahl, G. *Diamond Relat. Mater.* **1**, 380 (1992).

[37] Wu, C., Tamor, M., Potter, T., and Kaiser, E. *J. Appl. Phys.* **68**, 4825 (1990).

[38] Mitomo, T., Ohta, T., Kondoh, E., and Ohtsuka, K. *J. Appl. Phys* **70**, 4532 (1991).

[39] Collins, A. and Lightowlers, E. *Physical Review* **171** (1968).

[40] Collins, A. and Williams, A. *J. Phys. Part C Solid State Phys.* **4**, 1789 (1971).

[41] Scarsbrook, G., Martineau, P., Twitchen, D., Whitehead, A., Cooper, M. A., and Dorn, B. *Patent WO 03052174A2* (2003).

[42] Samlenski, R., Haug, C., Brenn, R., Wild, C., Locher, R., and Koidl, P. *Diamond and Related Materials* **5**(9), 947 – 951 (1996).

[43] Janetzko, F., Bredow, T., Geudtner, G., and Koster, A. *J. Comput. Chem.* **29**, 2295 (2008).

[44] Haenni, W., Rychen, P., Fryda, M., and Comninellis, C. *Thin-Film Diamond Part B.* Academic Press, Semiconductors and Semimetals series, Elsevier, (2004).

[45] Fryda, M., Matthee, T., Mulcahy, S., Hamel, A., Schafer, L., and Troster, I. *Diamond Rel. Mater.* **12**, 1950 (2003).

[46] Ushizawa, K., Watanabe, K., Ando, T., Sakaguchi, I., Nishitani-Gamo, M., Sato, Y., and Kanda, H. *Diamond and Related Materials* **7**(11-12), 1719 – 1722 (1998).

[47] Bustarret, E., Kačmarčik, J., Marcenat, C., Gheeraert, E., Cytermann, C., Marcus, J., and Klein, T. *Phys. Rev. Lett.* **93**(23), 237005 Dec (2004).

[48] Ekimov, E., Sidorov, V., Bauer, E., Mel'nik, N., Curro, N., Thompson, J., and Stishov, S. *Nature* **428**, 542 (2004).

[49] Popovici, G. and Prelas, M. *Diamond Relat. Mater.* **4**, 1305 (1995).

[50] Kajihara, S., Antonelli, A., Bernholc, J., and Car, R. *Physical Rev. Lett.* **66**(15), 20102013 (1991).

[51] Briddon, P. and Goss, J. *Physical review. B, Condensed Matter And Materials Physics* **75**(7), 1–9 (2007).

[52] Lombardi, E. and Mainwood, A. *Physica B: Physics of Condensed Matter* **401**, 5761 (2007).

[53] Prawer, S., Uzan-Saguy, C., Braunstein, G., and Kalish, R. *Applied Physics Letters* **63**(18), 2502 (1993).

[54] Hunn, J., Parikh, N., Swanson, M., and Zuhr, R. *Diamond and Related Materials* **2**(5-7), 847 – 851 (1993). Diamond 1992.

[55] Sakaguchi, I., N.-Gamo, M., Kikuchi, Y., Yasu, E., Haneda, H., Suzuki, T., and Ando, T. *Phys. Rev. B* **60**(4), R2139–R2141 Jul (1999).

[56] Nesladaek, M. *Semicond. Sci. Technol.* **20**(2), R19 (2005).

[57] Koizumi, S., Watanabe, K., Hasegawa, M., and Kanda, H. *Science* **292**, 1899 (2001).

[58] Katagiri, M., Isoya, J., S., K., and Kanda, H. *Appl. Phys. Lett.* **85**, 6365 (2004).

[59] Koizumi, S., Kamo, M., Y., S., Ozaki, H., and Inuzuka, T. *Appl. Phys. Lett.* **71**, 1065 (1997).

[60] Eaton, S., Anderson, A., Angus, J., Corrigan, T., Evstefeeva, Y., and Pleskov, Y. *Electrochem. Solid State Lett.* **5**, G65 (2002).

[61] Vaddiraju, S., Eaton-Magana, S., Chaney, J., and Sunkara, M. *Electrochem. Solid State Lett.* **7**, G331 (2004).

[62] Petherbridge, J., May, P., Fuge, G., Robertson, G., Rosser, K., and Ashfold, M. *Journal of Applied Physics* **91**(6), 3605 –3613 (2002).

[63] Nishitani-Gamo, M., Xiao, C., Zhang, Y., Yasu, E., Kikuchi, Y., Sakaguchi, I., Suzuki, T., Sato, Y., and Ando, T. *Thin Solid Films* **382**(1-2), 113 – 123 (2001).

[64] Nakazawa, K., Tachiki, M., Kawarada, H., Kawamura, A., Horiuchi, K., and Ishikura, T. *Applied Physics Letters* **82**(13), 2074 –2076 mar (2003).

[65] Uzan-Saguy, C., Cytermann, C., Fizgeer, B., Richter, V., Brener, R., and Kalish, R. *Phy. Status Solidi A* **193**, 508 (2002).

[66] te Nijenhuis, J., Cao, G. Z., Smits, P., vanEnckevort, W., Giling, L., Alkemade, P., Nesladek, M., and Remes, Z. *Diamond Relat. Mater.* **6**, 1726 (1997).

[67] Restle, M., Bharuth-Ram, K., Quintel, H., Ronning, C., Hofsäss, H., Jahn, S., and Wahl, U. *Applied Physics Letters* **66**(May), 2733 (1995).

[68] Chernyshev, V., Meijer, J., Grambole, D., Herrmann, F., Dagkaldiran, U., and Wieck, A. *Diamond and Related Materials* **17**(11), 19331935 (2008).

[69] Job, R., Werner, M., Denisenko, A., Zaitsev, A., and Fahrner, W. *Diamond and Related Materials* **5**, 757–760 (1996).

[70] Okumura, K., Mort, J., and Machonkin, M. *Applied Physics Letters* **57**, 1907 (1990).

[71] Popovici, G., Prelas, M., Sung, T., Khasawinah, S., Melnikov, A., Varichenko, V., Zaitsev, A., Denisenko, A., and Fahrner, W. *Diamond Relat. Mater.* **4**, 877 (1995).

[72] Popovici, G., Wilson, R., Sung, T., Prelas, M., and Khasawinah, S. *J. Appl. Phys.* **77**, 5103 (1995).

[73] Borst, T. and Weis, O. *Diamond Relat. Mater.* **4**, 948 (1995).

[74] Sachdev, H., Haubner, R., and Lux, B. *Diamond Relat. Mater.* **6**, 494 (1997).

[75] Sternschulte, H., Schreck, M., Stritzker, B., Bergmaier, A., and Dollinger, G. *Diamond Relat. Mater.* **9**, 1046 (2000).

[76] Fountain, G., Rudder, R., Malta, D., Hattangady, S., Alley, R. G., Hudson, G., Posthill, J., Markunas, R., Humphreys, T., Nemanich, R., and Venkatesan. In *Proc. 2nd Symp. Electrochem Soc.,* Purdes, A., Angus, J., Davis, R., Meyerson, B., Spear, K., and Yoder, M., editors, 523, (1991).

[77] Maier, F., Ristein, J., and Ley, L. *Phys. Rev. B* **64**(16), 165411 Oct (2001).

[78] Himpsel, F., Knapp, J., VanVechten, J., and Eastman, D. *Phys. Rev. B* **20**(2), 624–627 Jul (1979).

[79] van der Weide, J., Zhang, Z., Baumann, P., Wensell, M., Bernholc, J., and Nemanich, R. *Phys. Rev. B* **50**, 5803 (1994).

[80] Diederich, L., Küttel, O., Aebi, P., and Schlapback, L. *Surface Science* **418**(1), 219–239 November (1998).

[81] Cui, J., Ristein, J., and Ley, L. *Phys. Rev. Lett.* **81**(2), 429–432 Jul (1998).

[82] Takeuchi, D., Kato, H., Ri, G., Yamada, T., Vinod, P., Hwang, D., Nebel, C., Okushi, H., and Yamasaki, S. *Applied Physics Letters* **86**(15), 152103 (2005).

[83] Bandis, C. and Pate, B. *Phys. Rev. B* **52**, 12056 (1995).

[84] Krainsky, I., Asnin, V., Mearini, G., and Dayton Jr, J. *Phys. Rev. B.* **53**, 7650 (1996).

[85] Wang, G., Bent, S., Russell, J., Butler, J., and D'Evelyn, M. *J. Am. Chem. Soc.* **122**, 744 (2000).

[86] Yater, J., Shih, A., and Abrams, R. *Phys. Rev. B* **56**, 4410 (1997).

[87] Balmer, R., Friel, I., Woollard, S., Wort, C., Scarsbrook, G., Coe, S., El-Hajj, H., Kaiser, A., Denisenko, A., Kohn, E., and Isberg, J. *Phil. Trans. A Math. Phys. Eng. Sci.* **366**, 251 (2008).

[88] Furkert, S. and Martin, T. *Proceedings, Renewable Energy 2010* (2010).

[89] Webster, H. *J. Appl. Phys.* **30**(4) (1959).

[90] Tanner, P., Fraser, D., and Irving, A. *Sci., Meas. Tech., IEE Proc.* **152**(1), 1–6 (2005).

[91] Koeck, F. and Nemanich, R. *Diamond Relat. Mater.* **18**, 232 (2008).

[92] Suzuki, M., Ono, T., Sakuma, N., and Sakai, T. *Diamond and Related Materials* **18**, 1274–1277 (2009).

[93] Koeck, F. A. and Nemanich, R. J. *Diamond and Related Materials* **15**(2-3), 217 – 220 (2006). Proceedings of the Applied Diamond Conference/NanoCarbon 2005 - ADC/NanoCarbon 2005.

[94] Katoaka, M., Zhu, C., Koeck, F., and Nemanich, R. *Diamond Relat. Mater* **19**, 110 (2009).

[95] Koeck, F. and Nemanich, R. *Diamond and Related Materials* **14**(11-12), 2051 – 2054 (2005). Proceedings of the 10th International Conference on New Diamond Science and Technology (ICNDST-10) - ICNDST-10 Special Issue.

[96] Koeck, F., Nemanich, R., Lazea, A., and Haenen, K. *Diamond and Related Materials* **18**(5-8), 789 – 791 (2009). Proceedings of Diamond 2008, the 19th European Conference on Diamond, Diamond-Like Materials, Carbon Nanotubes, Nitrides and Silicon Carbide.

[97] Uppireddi, K., Westover, T., Fisher, T., Weiner, B., and Morell, G. *J. Appl. Phys.* **106**, 043716 (2009).

[98] Robinson, V., Show, Y., Swain, G., Reifenberger, R., and Fisher, T. *Diamond \& Related Materials* **15**(10), 16011608 (2006).

[99] Sun, Y. *Design of a Carbon Nanotube Based Field Emission Facility.* PhD thesis, University of Waterloo, (2008).

[100] Huang, Z., Cutler, P., Miskovsky, N., and Sullivan, T. *Appl. Phys. Lett.* **65**, 2562 (1994).

[101] Wang, C., Garcia, A., Ingram, D., Lake, M., and Kordesch, M. *Electron. Lett.* **2**, 1459 (1991).

[102] Xu, N., Latham, R., and Tzeng, Y. *Electron. Lett.* **29**, 1596 (1993).

[103] Okano, K. and Gleason, K. *Electron. Lett.* **29**, 74 (1995).

[104] Zhu, W., Kochanski, G., Jin, S., and Seibles, L. *J. Appl. Phys.* **78**, 2707 (1995).

[105] Geis, M., Twichell, J., Efremow, N., Krohn, K., and Lyszczarz, T. *Symposium A Quarterly Journal In Modern Foreign Literatures* **68**(April), 2294–2296 (1996).

[106] Kang, W., Davidson, J., Wisitora-at, A., Wong, Y., Takalkar, R., Holmes, K., and Kerns, D. *Diamond Relat. Mater.* **13**, 1944 (2004).

[107] Fox, N., Wang, W., Davis, T., Steeds, J., and May, P. *Applied Physics Letters* **71**(16), 2337 (1997).

[108] Robertson, J. *J. Vac. Sci. Technol. B* **17**, 659 (1999).

[109] Okano, K., Yamada, T., Ishihara, H., Koizumi, S., and Itoh, J. *Apppl. Phys. Lett.* **70**, 2201 (1997).

[110] Sowers, A., Ward, B., English, S., and Nemanich, R. *J. Appl. Phys.* **86**(7), 3973 (1999).

[111] Zhou, D., Krauss, A., Qin, L., McCauley, T., Gruen, D., Corrigan, T., Chang, R., and Gnaser, H. *J. Appl. Phys.* **82**, 4546 (1997).

[112] Geis, M., Twichell, J., Macaulay, J., and Okano, K. *Applied Physics Letters* **67**(9), 1328 (1995).

[113] Yamada, T., Kato, H., Shikata, S., Nebel, C., Yamaguchi, H., Kudo, Y., and Okano, K. *Journal of Vacuum Science & Technology B: Microelectronics and Nanometer Structures* **24**(2), 967 (2006).

[114] Yamada, T., Nebel, C., Somu, K., Uetsuka, H., Yamaguchi, H., Kudo, Y., Okano, K., and Shikata, S. *Physica Status Solidi (a)* **204**, 2957 (2007).

[115] Maier, F., Riedel, M., Mantel, B., Ristein, J., and Ley, L. *Physical Review Letters* , 14–17 (2000).

[116] Nebel, C., Ertle, F., Sauerer, C., Stutzmann, M., Graeff, C., Bergonzo, P., Williams, O., and Jackman, R. *Diamond Relat. Mater.* **11**, 351 (2002).

[117] Ristein, J., Maier, F., Riedel, M., Stammer, M., and Ley, L. *Diamond Relat. Mater* **10**, 416 (2001).

[118] Foord, J., Lau, C., Hiramatsu, M., Jackman, R., Nebel, C., and Bergonzo, P. *Diamond Relat. Mater.* **11**, 856 (2002).

[119] Garrido, J., Nebel, C., Todt, R., Rösel, G., Amann, M., Stutzmann, M., Snidero, E., and Bergonzo, P. *Applied Physics Letters* **82**(6), 988 (2003).

[120] Mitin, V., Kochelap, V., and Stroscio, M. *Introduction to Nanoelectronics: Science, Nanotechnology, Engineering and Applications.* Cambridge Press, Cambridge, England, (2007).

[121] Kuphalt, T. *Lessons In Electric Circuits Vol. III: Semiconductors.* Faqs.org, (2002).

[122] Isberg, J., Hammersberg, J., Johansson, E., Wikstrom, T., Twitchen, D., Whitehead, A., Coe, S., and Scarsbrook, G. *Science* **297**(5587), 1670 (2002).

[123] Kasu, M. *NTT Technical Review* **8**(8) (2010).

[124] Shin, M. W., Trew, R. J., Bilbro, G. L., Dreifus, D. L., and Tessmer, A. J. *Journal of Materials Science: Materials in Electronics* **6**, 111–114 (1995).

[125] Garrido, J. A. *Biofunctionalization of Diamond Surfaces: Fundamentals and Applications*, 399–437. John Wiley and Sons, Ltd (2009).

[126] Nebel, C., Shin, D., Yamamoto, T., and Nakamura, T. *MRS Proceedings* , 956 (2006).

[127] Nebel, C., Uetsuka, H., Yang, N., Yamada, T., and Watanabe, H. *MRS Proceedings* , 1039 (2007).

[128] Looi, H. J., Pang, L. Y. S., Molloy, A. B., Jones, F., Foord, J. S., and Jackman, R. B. *Diamond and Related Materials* **7**(2-5), 550 – 555 (1998).

[129] Moran, D., MacLaren, D., Porro, S., McLelland, H., John, P., and Wilson, J. *Microelectronic Engineering* **88**(8), 2691 – 2693 (2011). Proceedings of the 36th International Conference on Micro- and Nano-Engineering (MNE), 36th International Conference on Micro- and Nano-Engineering (MNE).

[130] Smith, J. *Laser Diagnostics of a Diamond depositing Chemical Vapour Deposition gas-phase environment*. PhD thesis, University of Bristol, (2002).

I think I can safely say that nobody understands quantum mechanics.

Richard Feynman (1918-1988)

2

Computational theory and techniques

As a part of this project, computational simulations of lithium on the surface of diamond were calculated using the density functional theory (DFT) program CASTEP on the bluecrystal supercomputing cluster at the University of Bristol. As the theoretical background behind the operation of DFT is important for the interpretation of the results presented herein, the theoretical assumptions and techniques used during the computational work of this thesis are discussed in this chapter.

2.1 Crystal Notation

A material can be represented in three-dimensional space by a unit cell, a volume of the material's crystal lattice that can be repeated to reproduce the crystal as a whole. A primitive cell is the smallest unit cell that can be repeated to represent the full lattice, although for many materials it is preferable to pick a unit cell larger than this for more convenient lattice transformations. The structure of an ideal crystal without defects can be described by an infinitely repeating unit cell, and this periodicity allows a simplified description of the structure by defining a base repeatable unit cell. There are fourteen basic 3D lattices with unique symmetries, known as the Bravais lattices, which can be broken down into seven crystal systems (Cubic, Tetragonal, Orthorhombic, Hexagonal, Trigonal, Monoclinic and Triclinic). There are numerous arrangements of atoms within each Bravais lattice that define the structure of a wide variety of materials. Diamond, for instance, has a face-centred cubic unit cell, where each lattice point contains a basis of two atoms at $(0, 0, 0)$ and $(\frac{1}{4}, \frac{1}{4}, \frac{1}{4})$.

The unit cell can be described by three unit vectors, $\mathbf{a}$, $\mathbf{b}$ and $\mathbf{c}$, and thus any lattice point in the crystal can be described by the vector

$$\mathbf{r} = n_1\mathbf{a} + n_2\mathbf{b} + n_3\mathbf{c} \tag{2.1}$$

where n_1, n_2 and n_3 are integers. As surfaces are important for many properties of a material, it is useful to have a system to describe the planes that intersect the $\mathbf{x}$, $\mathbf{y}$ and $\mathbf{z}$ axes of the lattice. In the case of the plane shown in Figure 2.1, the intercepts of the $\mathbf{y}$ and $\mathbf{z}$ lattices are infinite as the plane is parallel to those axes. Thus, using the real-space intercepts creates problems for a mathematical description of the plane.

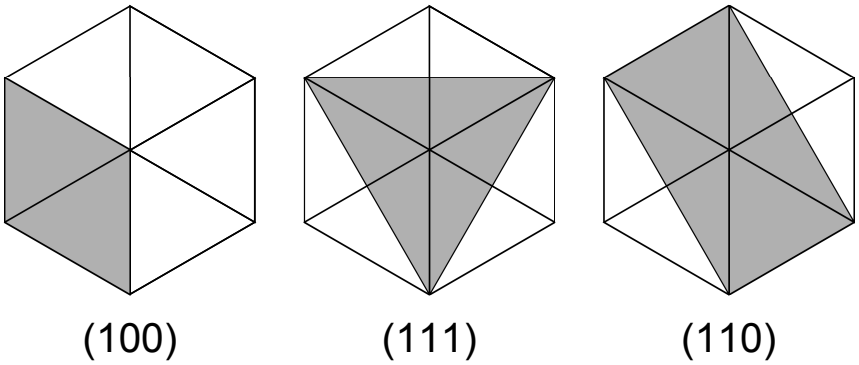

Figure 2.1: The 100, 111 and 110 planes of an arbitrary unit cell. [1]

Instead the reciprocals of the intercepts of the three axes are used, multiplied by their lowest common denominator to obtain integers. So a plane intersecting the **x**, **y** and **z** axes at 3, 4 and 1 would have reciprocal intercepts of $\frac{1}{3}$, $\frac{1}{4}$ and 1, which when multiplied by the lowest common denominator would give $(4, 3, 12)$. These integers are known as the Miller indices of the plane (hkl) and are a useful tool for describing a crystal. Fig 2.1 shows the (100), (111) and (110) planes, for example. Any atom intersecting the (110) plane would be significant for interactions and properties of the (110) surface. Any plane parallel to the one shown will have the same Miller indices and are equivalent. A reciprocal lattice vector $\mathbf{g}_{(hkl)}$ is defined as:

$$\mathbf{g}_{hkl} = h\mathbf{a}^* + k\mathbf{b}^* + l\mathbf{c}^* \tag{2.2}$$

where $\mathbf{a}^*$, $\mathbf{b}^*$ and $\mathbf{c}^*$ are the reciprocal lattice vectors. Just as the unit cell allows the lattice structure of a crystal in real space to be simplified to a small repeatable unit, a similar approach to the reciprocal lattice yields the Brillouin zone. The first Brillouin zone is defined as the volume enclosed by the Wigner-Seitz cell within reciprocal space. The Wigner-Seitz cell is a primitive unit cell that contains all the symmetry of the entire lattice.

2.2 Quantum Mechanics of electrons in crystals

2.2.1 Quantum Mechanics

The key tenets of quantum mechanics are wave particle duality and the uncertainty principle, along with the principle of energy quanta, as shown by the photoelectric effect. When monochromatic light hits a clean material surface, electrons can be emitted. However the electron flux from the surface is not solely proportional to the intensity of light incident on the surface, as might be expected from classical physics. Instead it is observed that the kinetic energy of the emitted photoelectron scales directly with the frequency of the incoming light.

Below a certain threshold frequency, no electrons are emitted no matter the intensity of the light. Similarly, at a given frequency of light, higher intensity of light causes an increase in flux but no increase in kinetic energy. This implies a certain minimum of energy is required to liberate the electron but that it must come from one interaction with the light rather than a gradual build-up

of energy. The observation of the photoelectric effect vindicated Planck and Einstein's postulate that thermal radiation which is emitted in discrete packets or quanta of energy also applies for photoelectric radiation, with the energy of the quanta given by $E = hv$, where h is Planck's constant with a value $h = 6.625 \times 10^{-34} Js$.

2.2.2 Wave-Particle Duality

In the case of the photoelectric effect, light radiation is behaving as a particle rather than as a wave as observed in other light phenomena such as diffraction and polarisation. Matter particles also have been shown to exhibit wave behaviour, with the de Broglie wavelength

$$\lambda = \frac{h}{p} \tag{2.3}$$

where h is Planck's constant and p is the momentum of the particle. De Broglie's hypothesis in 1924[2] that matter as well as light could behave as both a wave and a particle was confirmed soon after by two experiments showing the diffraction of electrons - George Thomson's observations of interference patterns from an electron beam passing through a thin metal foil,[3] and the scattering of a beam of slow moving electrons by a nickel crystal observed by Davisson and Germer[4] showing an angle-dependent diffraction pattern similar to that observed using X-rays.

2.2.3 The Uncertainty Principle

Another key tenet of quantum mechanics is the uncertainty principle first posited by Heisenberg in 1927[5] as a result of his investigation into matrix mechanics as a foundation of a new description of quantum mechanics. A key part of his work was the principle that observing motion at the quantum level did not exhibit the same predictable behaviour as classical large-scale particles, and that the behaviour of subatomic particles had at its core an amount of uncertainty. The uncertainty principle itself describes this uncertainty in terms of conjugate variables, chiefly position and momentum, or alternatively energy and time. The uncertainty principle states that the more accurately the absolute position of a particle is measured, the less well we can measure that particle's momentum. With the uncertainty in position being denoted as Δx and the uncertainty in momentum as Δp, the uncertainty principle can be written as

$$\Delta x \Delta p \geq \hbar \tag{2.4}$$

where $\hbar = \frac{h}{2\pi}$, the modified Planck's constant, with a value of 1.054×10^{-34} Js. An analogous statement is true of energy and time, in that the more accurately we measure a particle's energy, the less accurately we can measure the precise time that the particle had this energy.

$$\Delta E \Delta t \geq \hbar \tag{2.5}$$

As the modified Planck's constant is very small, these uncertainty effects are observable only for very small particles. As the uncertainty principle tells us that we cannot measure the exact momentum of a particle at a given position, or its energy at a given time, we must use probability and statistics to describe it. We use the Schrödinger wave equation to describe the behaviour of a

particle. The Schrödinger wave equation incorporates both the idea of quanta and of wave-particle duality and in its one-dimensional, nonrelativistic form is written as

$$-\frac{\hbar^2}{2m}\frac{\delta^2\Psi(x,t)}{\delta x^2}+V(x)\Psi(x,t)=j\hbar\frac{\delta\Psi(x,t)}{\delta t} \tag{2.6}$$

where $\Psi(x,t)$ is the wavefunction, V is the potential and m is the mass of the particle. The wave function is used to describe the behaviour of the system and can be a complex quantity. The wavefunction can be split into the time-dependent and time-independent parts, such that

$$\Psi(x,t)=\psi(x)\phi(t)=\psi(x)e^{\frac{-jEt}{\hbar}} \tag{2.7}$$

Because we can isolate the time-dependent part of the wavefunction, we can get physically relevant information from the square of the wavefunction, $|\Psi(x,t)|^2$. As the square of a complex quantity is the quantity multiplied by its complex conjugate, the time-dependent part of the wavefunction cancels out, so that the square of the wavefunction is purely position-related, giving us a probability density of where the particle is to be found, independent of time.

2.2.4 An electron in free space

The simplest solution of the Schrödinger wave equation is that of an electron in free space with no force or potential acting on it i.e. $V(x)=0$ for all x. The time-independent Schrödinger equation is then

$$\frac{\delta^2\psi(x)}{\delta x^2}+\frac{2mE}{\hbar^2}\psi(x)=0 \tag{2.8}$$

and the solutions are $\psi(x)=A\ exp[\frac{jx\sqrt{2mE}}{\hbar}]=B\ exp[\frac{-jx\sqrt{2mE}}{\hbar}]$

The time-dependent part of the solution is $\psi(t)=e^{\left[-j\frac{E}{\hbar}t\right]}$ meaning that the total wave function can be written as

$$\Psi(x,t)=Aexp[\frac{j}{\hbar}(x\sqrt{2mE}-Et)]+Bexp[-\frac{j}{\hbar}(x\sqrt{2mE}+Et)] \tag{2.9}$$

This solution describes a travelling wave with the first term representing the portion of the wave travelling in the positive x direction and the second representing the wave travelling in the negative x direction, with the values of the coefficients A and B dependent on the boundary conditions. Obviously this is the simplest case and as more constraints are added, such as multiple electrons and nonzero potentials we can bring this picture closer to that experienced by the electrons in a crystal.

2.2.5 An Electron in a potential well

The first constraint we can add to the picture shown above for the electron in free space is to add a non-zero potential to part of the considered domain. In Figure 2.2, a one-dimensional potential as a function of position is shown, with an infinite potential well in which the potential in region II is zero, whilst in Regions I and III the potential is infinite. If we assume the particle is in region II, the particle cannot escape across these infinite potential barriers with finite energy and as long

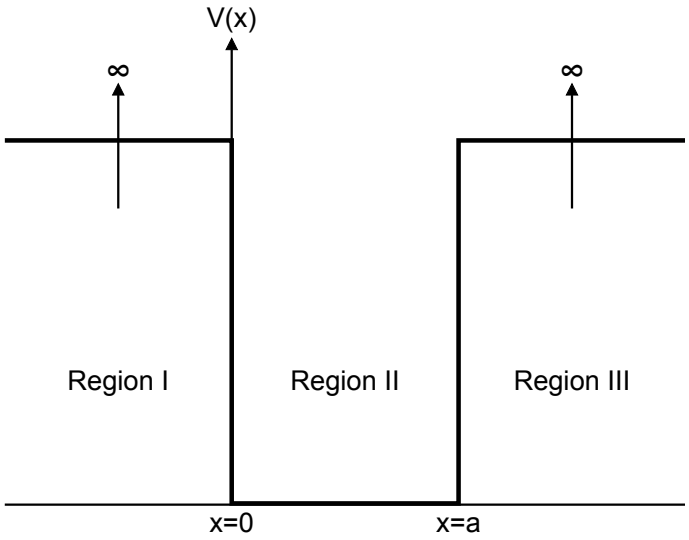

Figure 2.2: The potential function with position of an infinite potential well.

as E is finite both the wavefunction and probability of finding an electron in regions I and II is zero.

In region II, $V = 0$ and the time-independent Schrödinger wave equation is

$$\frac{\delta^2\psi(x)}{\delta x^2} + \frac{2mE}{\hbar^2}\psi(x) = 0 \tag{2.10}$$

with a solution of

$$\psi(x) = A\, cosKx + B\, sinKx \tag{2.11}$$

where $K = \sqrt{2mE/\hbar^2}$.

As the wavefunction is continuous, it must be zero at both $x = 0$ and $x = a$, so by applying these boundary conditions we can obtain values of $A = 0$ and $\psi(x = a) = 0 = BsinKa$.

Then $K = \frac{n\pi}{a}$.

$\psi(x)^*\psi(x)$ is the normalised probability density and its integral over all x must be 1, so $B = \sqrt{\frac{2}{a}}$.

The time-independent wave solution is

$$\psi(x) = \sqrt{2/a}sin(n\pi\frac{x}{a}) \tag{2.12}$$

where n is a positive integer. This is then the solution for the Schrödinger equation for an electron in an infinite potential well. Unlike the unbound free electron which had a travelling wave solution, the bound electron is represented by a standing wave. Since $K = \sqrt{\frac{2mE}{\hbar^2}}$, the energy of the electron is

$$E = E_n = \frac{\hbar^2 n^2 \pi^2}{2ma^2} \tag{2.13}$$

This is important as because n can only take integer values, it implies that both the wave vector K and the total energy of the particle are not continuous and can only have discrete values - the energy of the particle is quantised with only certain allowed energy levels.

2.2.6 An Electron at a barrier

A similar derivation to that above can be done for a barrier that is not infinite in potential energy or width. The outcome is that although the probability of an electron tunnelling through a barrier may be small compared to the probability of it remaining in the bound state, it is non-zero. For large numbers of electrons, a non-trivial number of electrons may be able to pass through the barrier. This outcome is very important for field emission of electrons, where the presence of an electric field shrinks the barrier width enough for significant quantities of electrons to tunnel from the emitter surface into the surrounding vacuum.

2.2.7 A simple one-electron atom

We can extend the case of an electron in a bound state to the conditions experienced by an electron in a one-electron atom, namely the hydrogen atom. The electron orbits, in classical Bohr theory, a positively charged nucleus that in the case of hydrogen contains a sole proton. The potential experienced by the electron due to coulombic attraction to the proton is $V(r) = \frac{-e^2}{(4\pi\epsilon_0 r^2)}$ where e is the charge on the electron and ϵ_0 the permittivity of free space. The potential is three-dimensional and spherically symmetric. Expanding the Schrödinger wave equation gives:

$$\nabla^2\psi(r,\theta,\phi) + \frac{2m_0}{\hbar^2}(E - V(r))\psi(r,\theta,\phi) = 0 \tag{2.14}$$

where ∇^2 is the Laplacian operator, which when written in spherical coordinates converts the Schrödinger equation to

$$\frac{1}{r^2}.\frac{\delta}{\delta r}(r^2\frac{\delta\psi}{\delta r}) + \frac{1}{r^2 sin^2\theta}.\frac{\delta^2\psi}{\delta\phi^2} + \frac{1}{r^2 sin\theta}.\frac{\delta}{\delta\theta}(sin\theta.\frac{\delta\psi}{\delta\theta}) + \frac{2m_0}{\hbar^2}(E - V(r))\psi = 0 \tag{2.15}$$

Using separation of variables $\psi(r,\theta,\phi) = R(r)\Theta(\theta)\Phi(\phi)$, we can write the time-independent wave equation so that R, Θ and Φ are functions only of r, θ and ϕ respectively:

$$\frac{sin^2\theta}{R}.\frac{\delta}{\delta r}(r^2\frac{dR}{dr}) + \frac{1}{\Phi}\frac{\delta^2\Phi}{\delta\phi^2} + \frac{sin\theta}{\Theta}.\frac{\delta}{\delta\theta}(sin\theta.\frac{\delta\Theta}{\delta\theta}) + r^2 sin^2\theta.\frac{2m_0}{\hbar^2}(E - V) = 0 \tag{2.16}$$

As the second term depends only on ϕ, we can separate it so that

$$\frac{1}{\Phi}.\frac{\delta^2\Phi}{\delta\Phi^2} = -m^2 \tag{2.17}$$

With the solution $\Phi = e^{(jm\phi)}$. We then obtain multiple wavefunction solutions to the Schrödinger equation, each corresponding to a different energy levels, defined by the quantum number m. m is an integer, both positive or negative $m = 0 \pm 1, 2, 3, 4, 5...$

By similar techniques the remaining two variables r and θ can be separated into two additional isolated equations depending on two more separation of variable constants, l and n, which together with m and the electron spin s are the quantum numbers corresponding to the quantum states an electron may occupy within an atom.

$$n = 1, 2, 3... \tag{2.18}$$

$$l = n - 1, n - 2, n - 3, ...0 \tag{2.19}$$

$$|m| = l, l - 1, ...0 \tag{2.20}$$

The electron energy E_n can then be written as

$$E_n = \frac{-m_0 e^2}{(4\pi\epsilon_0)^2 2\hbar^2 n^2} \tag{2.21}$$

Again, the energy of the electron is quantised and can only have discrete energy levels. The energy here is negative to indicate the fact that the electron is bound to the atomic nucleus - if the electron had a positive energy it would be free of the coulombic attraction of the nucleus and would no longer be bound to it.

2.2.8 The multi-electron atom

Although electron spin was not important in the single atom case, as atomic number increases and there are multiple electrons per atom, the electron spin becomes important. As with the energy of the electron, the spin or angular momentum of each electron is quantised and can only possess two values, $\pm\frac{1}{2}$.

This is important for atoms with more than one electron due to the Pauli Exclusion Principle, which states that no two electrons may occupy the same quantum state within a given system - in this case, that two atoms cannot share all the same quantum numbers. Due to the addition of spin, two electrons may occupy the same n, m and l quantum numbers with opposite spins, but no more electrons may fill this state. This is important in determining the electronic structure and properties of atoms as their atomic number increases. The helium atom, for instance, has two electrons with the same n, m and l numbers ($n = 1$ and l and $m = 0$ in this case) and opposing spins. This fills all possible quantum states for $n = 1$, so the lowest energy shell of helium is full. The last energy shell or valence shell in a given atom contains the electrons that interact with other atoms to form chemical bonds and define the electronic behaviour of the atom. As helium has a full valence shell it is difficult to remove or gain an electron and so helium is an inert and unreactive element. In chemical notation, the initial $l = 0, m = 0$ state is known as the s shell and the electronic structure of helium is written as $1s^2$.

By adding the Pauli exclusion principle and the spin of the electron to the solution for Schrödinger equation for the single electron atom, the general behaviour of all the atoms in the periodic table can be determined, although due to electron-electron interactions, atoms with large numbers of electrons can be slightly more complicated.

Lithium, oxygen and carbon, which are particular relevant to this project, can have electronic structure defined in this way. Lithium has three electrons, two in the filled $n = 1$ shell as in the

helium case, with an third electron that must be placed in the $n = 2$ shell as there are no states in the $n = 1$ shell remaining. There are eight possible quantum states for the $n = 2$ shell, as l can be 0 or 1, m can be $-1, 0$ or $+1$ and the electron spin can be $\pm\frac{1}{2}$ in each case. In lithium's case the remaining electron fills one of the two spin states in the $l = 0$, $m = 0$, $n = 2$ state, known as the $2s$ state. Thus, the electronic configuration for lithium is written $1s^2 2s^1$. Similarly, carbon has 6 electrons which completely fill the $n = 1$ and $n = 2$ $l = 0$ $1s$ and $2s$ states, with two additional electrons in the $l = 1$, $n = 2$ or $2p$ states. Oxygen has two more electrons than carbon which also occupy the 2p states, which can hold 6 electrons, so these electrons have spin $\pm\frac{1}{2}$ and $m = 1, 0$ or -1. The electronic notation for carbon and oxygen are $1s^2 2s^2 2p^2$ and $1s^2 2s^2 2p^4$ respectively.

2.3 Band Structure of crystals

2.3.1 Multi-atom systems

In the previous section the effects of the uncertainty principle, wave-particle duality and the Pauli exclusion principle led to an expression for the wavefunction for the electrons in single atom systems. For the purposes of this thesis we need to expand this further to cover the behaviour of an electron in a crystal of many atoms, such as the crystal lattice of diamond and other semiconductors. To do this we need to consider the effect on the electronic behaviour, particularly that of the valence electrons, when an atom is in close proximity to other atoms.

When two atoms are close together, the probability density functions $|\psi(x)|^2$ overlap, as shown in figure 2.3. This means that some identical states could be possible in both atoms, which the Pauli exclusion principle states cannot happen. When two overlapping states possess the same quantum numbers, the energy levels in each atom split to slightly different energies so that the electrons are in unique states.

As the number of atoms with overlapping states increases, this behaviour continues, such that what would be a single quantised energy level in the case of an electron in a single atom is split or 'perturbed' many times into a band of states all with slightly different energies. The Pauli exclusion principle demanding that no states should have the same quantum numbers extends across the entire electronic system independent of the system's size, with the result that as the system grows larger the band continues to extend into a large number of discrete energy levels with infinitesimally different but still distinct energies. For large systems with 10^{20} electrons or more, the gaps between each state become so small as to make the band essentially continuous for many purposes, but it is important to remember that no matter how small the difference between the levels the states of each electron remain discrete.

An important effect of this splitting of energy levels into bands is observable for the valence electron shell. For the core electrons, the individual states split across a small energy range, but do not overlap significantly with neighbouring shells, since the electrons are tightly bound to the ionic core. For the valence electrons, especially those in the part-filled valence shell which are only weakly bound to the ionic core, it is possible that when they split into bands several overlapping shells can contribute, as shown in Figure 2.4 which shows the electronic shells of a single carbon atom and the result after the orbitals split into bands. The four valence electrons in carbon lie in the $2s$ and $2p$ states corresponding to $n = 2$, $l = 0$ and $n = 2$, $l = 1$ respectively. In a single

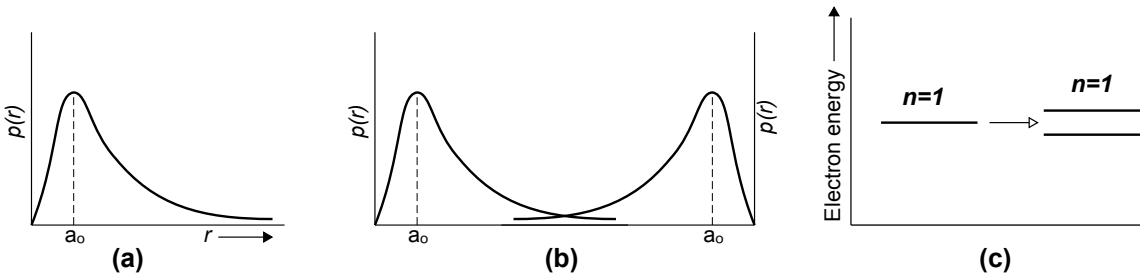

Figure 2.3: (a) shows the probability density for an electron within one atom, (b) shows the overlap of two probability densities when two atoms draw close to each other, and (c) shows the splitting caused by this overlap that splits the energy levels into two discrete and separate levels. After [6].

atom of carbon, the $2s$ state holds two electrons and the $2p$ state holds two electrons of the total of six it could hold. As carbon atoms come closer together, the $2s$ and $2p$ states overlap and split, but with a degree of mixing between the two states. As a result, instead of two bands of two and six electronic states, the two states overlap such that they form two separate bands, one at lower energy with four states and the other higher with the other four electronic states.

This splitting and overlapping is important, as it introduces an energy gap into the bands of the material. At low temperatures, only the bottom (or valence) band of four states is filled, whilst the top (or conduction) band remains empty, with a so-called 'band gap' between the two bands. It is this band gap that produces much of the interesting behaviour of semiconductors like diamond and silicon.

2.4 Density Functional Theory

2.4.1 First Principles of Computational Modelling

In order to calculate the electronic and physical structure of materials, a computationally accurate method of determining the wavefunction of the electrons in a material is needed. The ground-state behaviour can be described in a more refined way with a first-principles approach than the more empirical models shown in the previous section. The most important advantage of a first-principles approach is the inclusion of electron-electron interactions.

A number of different computational methods for solving the Scrödinger equation for systems with many atoms have been developed. Fundamental to this project is Density Functional Theory (DFT), although several other methods will be briefly discussed as part of the derivation of the DFT equations used in this project.

2.4.2 Born-Oppenheimer Approximation

One of the main approximations used to simplify the many-body wavefunction, first proposed by Born and Oppenheimer,[7] is that the wavefunctions of the electrons and nuclei can be decoupled. The mass of the electron is approximately two thousand times less than that of the nucleus so the electron responds much more quickly to forces than the nucleus that the change in the electron wavefunction in response to changes in the atomic nuclei can be assumed to be instantaneous and

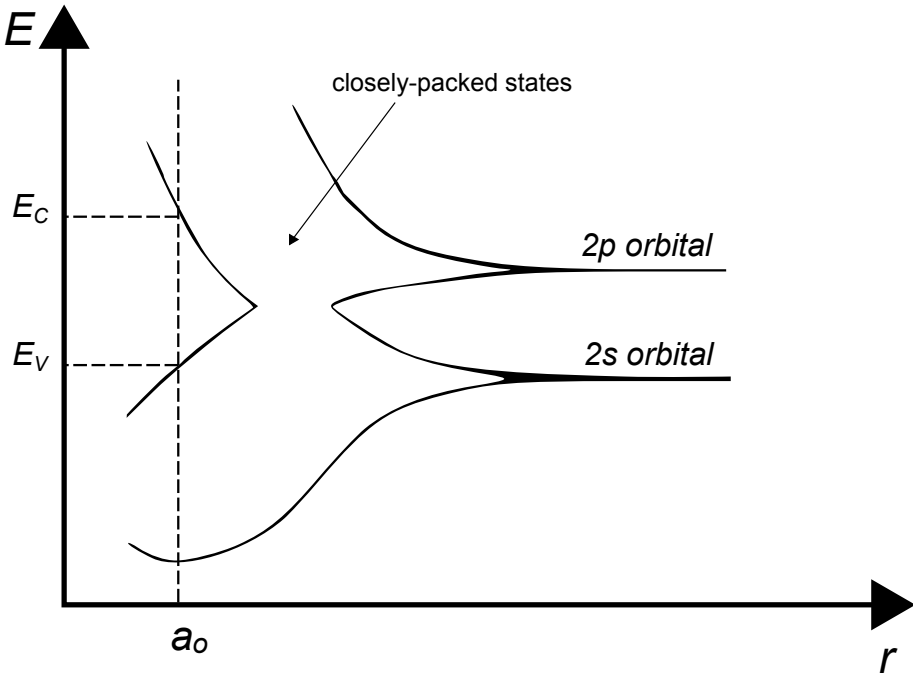

Figure 2.4: The behaviour of the valence electrons in carbon as a carbon atom is in free space and as multiple carbon atoms are brought close together so that overlapping of the $2s$ and $2p$ states occurs. After[1].

adiabatic. This means the wavefunction $\Psi(r;R)$ for the degrees of freedom for nuclei and electrons can be be rewritten as the multiple of two independent wavefunctions, one for the nuclei $\chi(R)$ and one for the electrons $\psi_R(r)$:

$$\Psi(r;R) = \chi(R)\psi_R(r) \tag{2.22}$$

The separation of the nuclear and electronic charge is very useful as it means that the two systems can be decoupled such that:

$$\left[\widehat{T}_n + \widehat{V}_{n-n}\right]\chi(R) = E_n\chi(R) \tag{2.23}$$

$$\left[\widehat{T}_e + \widehat{V}_{e-e} + \widehat{V}_{e-n}\right]\psi(R) = E_e\psi(R) \tag{2.24}$$

where the subscript e refers to electronic terms and the subscript n to the nuclear terms, with $\widehat{T}$ and $\widehat{V}$ referring to the kinetic and potential energy respectively. Using the energy eigenvalues E_n and E_e and the Born-Oppenheimer approximation in Equation 2.22 we can rewrite the Schrödinger equation for the complete system:

$$\widehat{H}\chi(R)\psi_R(r) = (E_n + E_e)\chi(R)\psi_R(r) - \sum_{\alpha}^{N_n}\frac{1}{2M_\alpha}\left[\chi(R)\nabla_\alpha^2\psi_R(r) + 2\nabla_\alpha\psi_R(r)\nabla_\alpha\chi(R)\right] \tag{2.25}$$

where α refers to the α^{th} atomic nucleus. If the electron-nuclear coupling is weak, then the

second term on the right of Equation 2.25 may be negligible due to the large mass of the nucleus, and the electronic and nuclear terms can be considered completely independent of each other, so that if the atomic positions of the nuclei remain fixed, the system's properties can be calculated using only the electronic wavefunction ψ.

2.4.3 Bloch's Theorem

Bloch's theorem states that an electron's wavefunction $\psi_{(j,k)}$ in a periodic potential can be written as the multiple of two parts - one contributed by the periodic lattice $u_j(r)$ and the other representing the wavelike part of the wavefunction $e^{ik.r}$:

$$\psi_{(j,k)}(r) = u_j(r)e^{ik.r} \tag{2.26}$$

where k is a wave vector within the first Brillouin zone of the reciprocal lattice and the band index is indicated by the subscript j. The periodicity of $u_j(r)$ is identical to the direct lattice, allowing it to be rewritten into a discrete plane-wave basis set where its wave vectors G are reciprocal lattice vectors within the crystal structure with lattice vectors r and plane wave coefficients $c_{j,G}$:

$$U_j(r) = \sum_G c_{j,G}e^{iG.r} \tag{2.27}$$

Where $G.R = 2\pi m$ and m is an integer, when R are the crystal lattice vectors. By substituting this into Equation 2.26 the electron wavefunction can be expanded to

$$\psi_{(j,k)}(r) = \sum_G c_{(j,k+G)}e^{i(k+G).r} \tag{2.28}$$

Written in this way, the wavefunction is a linear combination of plane-waves, making manipulation easier, independent of the type of crystal and behaving the same across all space, unlike Gaussian and other localised functions, which are dependent on position.

2.4.4 Pseudopotentials

While using Bloch's Theorem to render the many-body wavefunction in a crystal as a series of plane waves helps to simplify the task of studying such a system, the large numbers of plane waves required to accurately represent the rapidly oscillating wavefunction of the electrons within the core would become prohibitively expensive in computational time. However since the core electrons are tightly-bound and behave largely independently of the chemical environment, they can be modelled as a fixed potential, leaving only the valence electrons to be explicitly treated in the calculations. The simulation of the core states as a potential is known as a pseudopotential and dramatically decreases the computational time needed for the calculation. The pseudopotential is used for the potential within a radius cut-off r_c, beyond which the valence wavefunction is used. For this reason it is important that the value of the pseudopotential is identical to that of the valence wavefunction at r_c. An example of a pseudopotential is shown in Figure 2.5.

One of the simpler pseudopotentials, as an example, is the Ashcroft empty-core pseudopotential. If the core electron orbitals of an atom are occupied, then due to the Pauli Exclusion Principle,

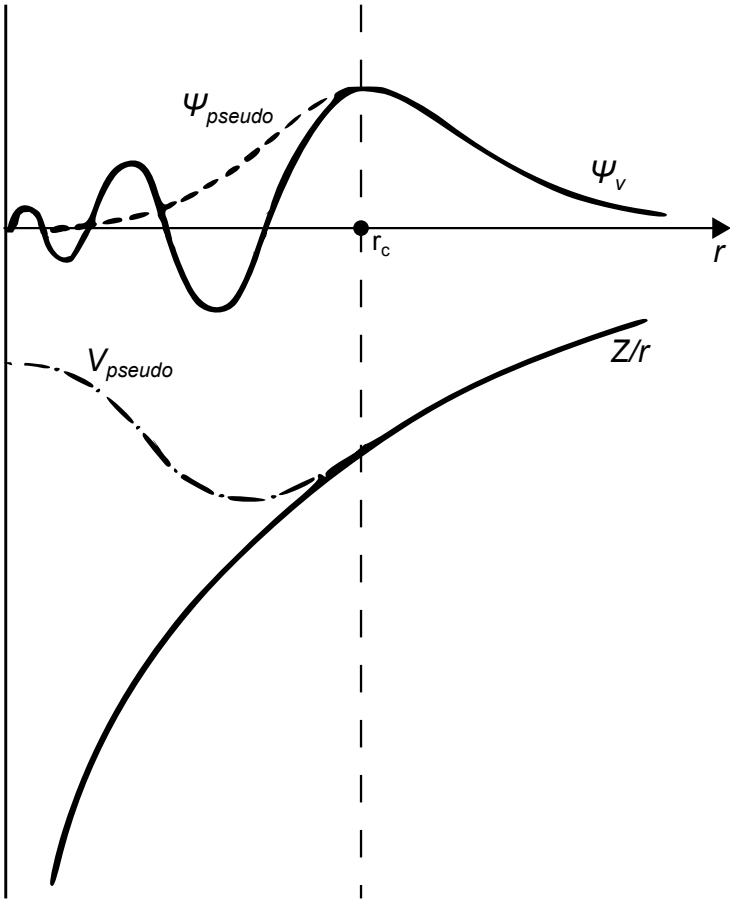

Figure 2.5: A comparison of the wavefunction due to the Coulombic potential of the nucleus to that found using a pseudopotential; the two wavefunctions are identical above a critical cut-off radius r_c. After[8].

the valence electrons cannot enter the core region. Due to the orthogonal relationship between the wavefunctions of the valence and core states, the valence electron experiences a repulsive potential within the core region that almost cancels the Coulomb attraction of the ion core, creating a reduction in the valence charge density close to the ionic core known as the orthogonality hole, as pictured in Figure 2.6.

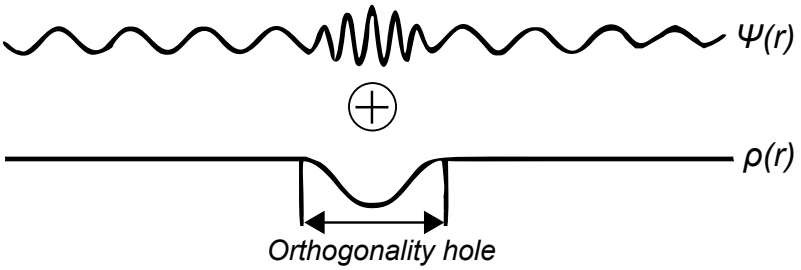

Figure 2.6: The charge density ρ and wavefunction ψ of a valence electron near an ionic core; the wavefunction shows a rapid oscillation in the core region so that ψ is orthogonal to the tightly bound core electrons, resulting in a lower charge density close to the ionic core. After [9].

The cancelling of the Coulombic attraction by the repulsive element allows a pseudopotential known as the Ashcroft empty-core pseudopotential. When $r < r_c$, the potential follows the Ashcroft pseudopotential, whereas at larger radii the potential follows the Coulombic attraction

$$\frac{-Ze}{(4\pi_0 r)} \tag{2.29}$$

This modifies the electron-ion interaction to

$$U_{ei} = \frac{-3Ze^2}{8\pi\epsilon_0 r_{ws}}[1 - (\frac{r_c}{r_{ws}})^2] \tag{2.30}$$

Where U_{ei} is the interaction energy between an electron and the ionic potential. r_{ws} is the radius of the Wigner-Seitz cell. The interaction energy U_{ws} of Z electrons in the Wigner Seitz cell and the point ionic charge $+Ze$ is $U_{ws} = U_{ei} + U_{ee}$, where the inter-electron repulsion U_{ee} is

$$U_{ee} = \frac{3Z^2e^2}{20\pi_0 r_{ws}} \tag{2.31}$$

In *ab initio* calculations used in this project, the pseudopotentials are generated before the main calculation takes place. Using an all-electron DFT approach, the psuedopotentials are generated by first calculating single atoms of each element required. The pseudopotential is constructed from all the electron eigenvalues of this atom.

2.4.5 Hartree-Fock Theory

Although the free-electron model is useful in showing the basic electronic structure of atoms and in grasping the concepts of band structure, it neglects the interactions between electrons. The simplest approximation of the electron-electron interaction is the Hartree approximation. [10] The Hartree approximation is also known as the self-consistent field (SCF) method as each time the calculation is made, the wavefunction is estimated and used for the subsequent iteration, so that

one cycle is consistent with the next estimate. Calculating the wavefunction of a many-electron system is complicated due to the electron-electron interactions, and as a result the Hamiltonian is dependent on the positions of all the electrons $H = H(r_1, r_2...)$, making calculation of the true wavefunction virtually impossible. The Hartree approximation simplifies this calculation by assuming that the interaction between an electron and all other electrons can be described by an averaged potential energy and each electron is then treated separately, so that the Hamiltonian depends only on the sum of single-electron terms:

$$H(r_1, r_2...) = H(r_1) + H(r_2) + ... \tag{2.32}$$

The assumption that electrons are independent is only a good approximation due to the screening of the electron-electron interaction by the remaining electrons. The many-body wavefunction becomes the product of the individual one-electron terms:

$$x_i(r_1, r_2...) = x_i(r_1) \times x_i(r_2) \times ... \tag{2.33}$$

Hartree's first formulation of the approximation was designed to create a solution to the time-independent many-body Schrödinger equation using *ab initio* fundamental methods. The initial Hartree Method did not contain all of the information required to describe the behaviour of fermions; it did not include the requirement for two electrons to have antisymmetric wavefunctions such that:

$$\psi(x_1, x_2...x_j, ...x_i...x_N) = -\psi(x_1, x_2, ...x_i, ...x_j...x_N) \tag{2.34}$$

Following work from Slater and Fock[11;12], the Hartree method was adjusted to use a determinant of single-particle orbitals to represent the wavefunction, as it allows an exact inclusion of electron exchange, which was not included in the original method. The Hartree-Fock method approximates the complicated true many-body wavefunction to a single Slater determinant of N spin-orbitals:

$$\Psi = \begin{vmatrix} \psi_1(x_1) & \psi_1(x_2) & ... & \psi_1(x_N) \\ \psi_2(x_1) & ... & & \\ . & & & \\ . & & & \\ \psi_N(x_1) & \psi_N(x_2) & ... & \psi_N(x_N \end{vmatrix} \tag{2.35}$$

This Slater determinant can be inserted into the Schrödinger equation to derive an expression for the total energy of the system. The wavefunction is normalised using a Lagrange multiplier e_i so that the the value of the determinant is left unchanged by non-singular linear transformations:

$$\frac{\delta}{\delta\psi}[< \widehat{H} > - \sum_j \epsilon_j] \int |\psi_j|^2 dr = 0 \tag{2.36}$$

This greatly simplifies the electron orbital wavefunctions to a set of one-electron wavefunctions, with the full Hartree-Fock equations for $E_i\psi_i(r)$ given by

$$E_i\psi_i(r) = \left(-\frac{1}{2}\nabla^2 + V_{ion}(r)\right)\psi_i(r) + \Sigma_j \int dr'(\frac{|\psi_j(r')|^2}{|r-r'|}\psi_i(r) - \Sigma_j \delta_{\sigma_i\sigma_j} \int \frac{\psi_j^*(r')\psi_i(r')}{|r-r'|}\psi_j(r)dr' \tag{2.37}$$

The first and second terms in the right hand side of the Hartree-Fock equation describe the kinetic energy and the potential energy of the interaction between the electron and the ion. The third term, known as the Hartree term, is the potential energy of the electron-electron interactions, in this case approximated by the electrostatic potential between an electron and the average charge distribution of N electrons in the system. The final term derives from the Pauli Exclusion Principle stating that two electrons cannot be in the same state and includes a delta-function for the behaviour when $j = i$, so that it cancels the effect of the third term having an unphysical self-interaction when $j = i$ but is zero when $j \neq i$.

The Hartree-Fock equation captures a lot of the physical detail required to solve the Hamiltonian accurately, with certain caveats. Hartree-Fock algorithms ignores relativistic effects, for example. The biggest weakness to the Hartree-Fock method is the lack of any consideration to electron correlation. The Hartree-Fock method considers all electron interactions as the interaction between a single electron and the average electric field produced by the remaining electrons in the system, whereas in a real system there are other types of electron-electron interactions such as Pauli repulsions that also contribute. Without consideration of the electron correlation, the total energy of the system calculated using Hartree-Fock is always higher than the actual energy of the system, with the difference between the two known as the correlation energy.

2.4.6 Density Functional Theory

Whilst Hartree-Fock is still in use for computational simulations, an alternative theory, density functional theory (DFT), has come to be just as important a tool for *ab initio* modelling. Significantly, density functional theory accounts for both exchange and correlation energies, where the Hartree-Fock algorithm only includes the former without additional modifications.[13]

Density Functional Theory was developed from a series of important papers from Hohenberg, Kohn and Sham[14;15] that proposed that the total density of electrons $n(r)$ would be used rather than the many-body Schrödinger equation used in the Hartree and Hartree-Fock methods. This simplifies calculations substantially as the many-body wavefunction does not need to be explicitly calculated. In density functional theory the electron charge density determines all the electronic behaviour of the system, so long as they are in the ground state. In their seminal 1964 paper Hohenberg and Kohn proposed that the ground-state energy of an interacting electron gas can be defined as a unique functional of the charge density $n(r)$. Calculations using density functional theory use a variational principle to find the ground-state energy, which is at its minimum when the charge density $n(r)$ is identical to the true ground-state charge density $\rho(r)$. The Kohn-Sham ground state energy functional is

$$E[\rho(r)] = T[\rho(r)] + \int [\rho(r)]\phi_N(r)dr + \frac{1}{2}\int \rho(r)\phi_H(r)dr + E_{xc}[\rho(r)] \tag{2.38}$$

As in the Hartree-Fock equation (shown in Equation 2.37), the first term in Equation 2.38 corresponds to the kinetic energy, whilst the second represents the energy due to the interaction

between the electronic charge q_i and the ionic potential, with

$$\phi_N(r) = \sum_i \frac{q_i}{4\pi\epsilon_0|r - R_i|} \tag{2.39}$$

Where R_i is the position of the ith nucleus. The third (or Hartree) term describes the energy of an electron moving through the electrostatic field of all other electrons in the system, with the Hartree potential $\phi_H(r)$ given by

$$\phi_H(r) = \int \frac{\rho(r')}{4\pi\epsilon_0|r - r'|} dr' \tag{2.40}$$

Similarly to the Hartree-Fock method, this Hartree term overestimates the Coulomb repulsion between electrons, and neglects the effect of exchange-correlation hole. Due to the Pauli exclusion principle, the chances of finding an electron close to an electron is much reduced, as electrons with parallel spins will repel, and this repulsion is not considered in the Hartree term. The fourth term in the ground-state energy functional compensates this overestimation of energy in the Hartree term. The exact exchange-correlation energy is defined by

$$E_{xc}[n] = \frac{1}{2} \int \int n(r) \frac{(n_{xc}(r, r')}{|r - r'|} dr dr' \tag{2.41}$$

In practice this exchange-correlation function is not known exactly and and so an approximation must be used. Density functional theory calculations often use forms of the local density approximation (LDA) or the generalised gradient approximation (GGA) to estimate the exchange-correlation energy. The various approximations for the exchange-correlation energy will be discussed in section 2.4.9.

The effect of the exchange-correlation hole allows the electrons to be treated as if they were independent, with no electron-electron Coulomb interactions. This leads to the Kohn-Sham equations transforming the N electron system into a N single-electron equations.

2.4.7 Kohn-Sham equations

As detailed in the previous section, the Kohn-Sham ground-state energy functional is given by Equation 2.38. The contribution of the exchange-correlation hole energy due to Pauli Exclusion effects means that the electrons can be treated as non-interacting independent particles that contribute the same charge density as a system of interacting particles. Subject to the number of electrons N being conserved, each ith electron can have its own Kohn-Sham time-independent Schrödinger equation such that

$$-\frac{h^2}{(8\pi^2 m_e)} \nabla^2 \Psi_i(r) + V_{\text{eff}}(r)\Psi_i(r) = E_i^{KS} \Psi_i(r) \tag{2.42}$$

where the effective Kohn-Sham potential $V_{\text{eff}}(r)$ is the combination of the Hartree potential $V_H(r)$, the potential due to the ion cores of the atoms in the system $V_N(r)$ and the potential due to the exchange-correlation hole $V_{XC}(r)$:

$$V_{\text{eff}}(r) = V_H(r) + V_N(r) + V_{XC}(r) \tag{2.43}$$

The key component of this approach is the electron density $\rho(r)$, since the Hartree term is dependent on $\rho(r)$ and the exchange-correlation potential is equal to the derivative of the exchange-correlation energy E_{XC} with density - $\frac{\delta E_{XC}[\rho(r)]}{\delta\rho(r)}$. In a density functional theory calculation for a periodic system (rather than a single molecule), the Kohn-Sham equations (Equation 2.42) are expanded in terms of a plane wave basis set using Bloch's Theorem and in terms of the reciprocal lattice vectors of the crystal. After the wavefunction $\Psi_i(r)$ has been estimated, the density $\rho(r)$ can be found by

$$\rho(r) = \sum_{i\ occupied} \Psi_i(r)\Psi_i^*(r) \tag{2.44}$$

Once the density has been found it can be used to recalculate the potentials in the Kohn-Sham equations, allowing a new wavefunction to be calculated and a new density, which leads to a new wavefunction and so on. This process is repeated until the energy is minimised and self-consistency is achieved. This 'self-consistency cycle' comprises the basic approach of density functional theory, which has been used to simulate the electronic and structural properties of many systems to good agreement with experimental results. Whilst the Kohn-Sham orbitals themselves lack true physical meaning, they can be a useful tool in observing the density and localisation of electrons within a crystal.

Once the self-consistent charge density has been calculated, geometry optimisation can be performed to reach a more accurate structural configuration of the atoms. The forces on each atom can be calculated from the total energy, as

$$F_a = -\nabla_a E. \tag{2.45}$$

The atoms are then moved in the direction of this force. The process then starts again, with the total energy and force on each atom is calculated, and the atom is moved again. The process repeats until the force on each atom falls below a certain tolerance level.

2.4.8 Convergence Criteria

It is easy to perform calculations using density functional theory methods that produce structural and electronic information about a system. However, because of the many variables in such a calculation, the result may not give physically realistic values unless these variables are properly calibrated first.

To ensure that the final calculations are providing realistic results, the various parameters are varied independently on a test case supercell. As the value of the parameter changes, the total energy of the simulated system should converge to a constant value, usually at the cost of additional computational time. For each variable, the computational cost versus accuracy is weighed up and a value chosen that gives the best compromise between the two. The most critical parameters for convergence are typically the cut-off energy and the density of k-points used in a Monkhorst-Pack grid to sample the Brillouin Zone.

2.4.9 Exchange-Correlation Functionals

The accuracy of a DFT calculation depends on the approximation for the exchange-correlation energy, as it is the one feature that cannot be calculated exactly. There are a number of different approximations that can be used, which each have their advantages and disadvantages and may be more or less suitable depending on the nature of the system being studied.

The local density approximation (known as the local spin-density approximation for the case of systems with non-zero total spin) is one of the more simple ways to approximate the exchange-correlation energy, as it depends only on a single variable, the electron density.

$$E_{xc}^{LDA}[N(r)] = \int n(r)\epsilon_{xc}^{hom}[n(r)]dr \tag{2.46}$$

Generally the LDA falls short of being able to model the complexity of many systems due to its singular variable, but it can be an effective tool for modelling simple covalent and metallic systems. For more complicated materials such as molecules and systems with widely varying electron densities, the more advanced generalised gradient approximate (GGA) is used instead.

The generalised gradient approximation takes the local density approximation and adds a second variable to improve the accuracy of the approximation. In addition to the density, the GGA also depends on the gradient of the density.

$$E_{xc}^{GGA}[n(r)] = \int n(r)\epsilon_{xc}^{GGA}\left[n(r), \nabla n(r)\right] dr \tag{2.47}$$

Because of the additional variable in the GGA compared to the LDA, the GGA can produce a more accurate wavefunction with a faster convergence than the LDA. Some examples of GGA functionals include the Perdew and Wang PW91 functional,[16] the original and revised PBE functionals[17;18] and the WC functional.[19] PW91 was the first reliable GGA and has been used to characterise a large number of materials, whilst the PBE, RPBE and WC functionals contain a mix of the features of the LDA and the PW91 functionals.

2.4.10 Bluecrystal Computing cluster

Bluecrystal is a High Performance Computing (HPC) machine located in the roof of the University of Bristol Physics department. It has achieved a performance of 28.4 TFlops/s and reached 86th place in the Top 500 supercomputer list in November 2008 when it opened. Top 500 ranks the fastest 500 supercomputers in the world as judged by their performance on the LINPACK benchmark, a performance rating for solving a dense series of complicated linear equations. Bluecrystal runs two separate login nodes - Phase 1 for serial jobs and small parallel jobs and Phase 2 for larger parallel jobs.

The computational calculations in this thesis required large parallel processing and so all work was carried out on Bluecrystal Phase 2. Login is done through a UNIX terminal and utilities such as CASTEP, Check2xsf and PDOS have been installed on the user area of the Bluecrystal node itself. Visualisation tools such as XCrysden and the python scripts used to create LDOS charts and to calculate workfunctions are located on the Linux machine used to access Bluecrystal, a virtual machine running 64 bit Ubuntu 10.10 Linux with 1024 of base memory and 12 MB of video memory. This system was run virtually using the tool VirtualBox as a partition on a Windows

7 machine with 3 GB of memory, an Intel Pro Core Duo processor clocked at 2.56 GHz and a Radeon HD4200 graphics card with 768 MB dedicated memory.

2.4.11 CASTEP

CASTEP[20] is a density functional theory software package developed by the Universities of Cambridge, York, Durham and St. Andrews as well as Rutherford Labs. Originally written in Fortran77, the code was substantially redesigned and rewritten in Fortran99 beginning in 1999, and continues to be maintained and improved. CASTEP uses the plane-wave approximation of Bloch's Theorem and the Born-Oppenheimer approximation to represent the nuclear and electronic coordinates, with a choice of pseudopotentials and XC-functionals available to reduce computational time.

Typically a user of the academic version of CASTEP (rather than the graphics-based commercial equivalent Materials Studio) will provide two text files, known as the .cell and .param files. The cell file contains all the information about the positions of the atoms in the supercell, as well as the density of the Monkhorst-Pack grid for Brillouin zone sampling. The parameter file contains the user's choice of settings for the calculation, such as the choice of XC-functional, cut-off energy and tolerances for geometrical and force convergence.

The geometry optimisation step of CASTEP has a choice of methods, including damped molecular dynamics (MD) and the similar FIRE scheme, but the default choice (and the one used in this project) is the Broyden-Fletcher-Goldfarb-Shanno (BGFS) method.[21–24] Approximating Newton's method, the BGFS method takes first order information about the gradient and uses it to approximate a Hessian matrix, saving considerable computational time compared to calculating an exact solution of the Hessian, which requires 2nd order gradient information.

2.4.12 Characterisation of Electronic States

Mulliken Bond Population Analysis

Mulliken bond population analysis is a technique to identify the electrons associated with a particular atom in a DFT calculation, in terms of a partial atomic charge. Whilst this approach does not give a complete description of the system, its simplicity helps to identify the bonding and electronic behaviour of a calculated structure. A basis function ϕ_i can be used to calculate the Mulliken bond population $p_\lambda(i)$ for each electronic state λ provided that the basis set consists only of basis functions B_{ki} associated with atomic sites.

$$p_\lambda(i) = \frac{1}{N_L}\Sigma(j,k)c_{k,\lambda,i}S^k_{i,j}c^*_{k,\lambda,j'} \tag{2.48}$$

where C_k are coefficients and N_L is the total number of electrons to normalise the total population so that $\Sigma_i p_\lambda(i) = 1$. S^k_{ij} are the overlap matrix elements which have the definition

$$S^k_{ij} = \int B^*_{ki}e^{-ik.r}B_{kj}dr \tag{2.49}$$

If an electronic state λ is dominated by an orbital centred on a particular atom, $p_\lambda(i)$ will be large, so that atom can be defined as the one most responsible for that electronic state. The population density can be split into *s*-, *p*-, *d*- and *f*-like components so that hybridisation and

bond type can be determined. The program used in this project, CASTEP, produces Mulliken population analysis for all atoms by default in a typical calculation.

Analysis of Kohn-Sham orbital wavefunctions

In addition to the numerical analysis of Mulliken populations, the output of modern DFT programs such as CASTEP can be displayed as a three-dimensional plot of the Kohn-Sham orbitals around the atomic structure using visualisation software such as XCrysden. The orbitals shown in this manner are not true one-electron functions, but the visualisation of such solutions to the Kohn-Sham equation can be useful in identifying the relationship between certain orbital energy levels with particular atoms in the structure. It can be especially useful in distinguishing between localised bonding, lone pairs and states delocalised within the lattice.

For a particular electronic state λ_i, the isosurfaces of the wavefunctions (or the square of the wavefunction for charge density) are drawn as three dimensional curves within a particular volume. States that are degenerate with the same characteristics can be plotted as superpositions of several wavefunctions.

Calculating the electron affinity and workfunction

The electron affinity is defined as the difference between the vacuum level and the lowest energy unoccupied state, $\chi = -(E_{LOC} - E_{VAC})$. In practice for computational calculations this is obtained by modelling a surface slab of diamond, thick enough that the atoms in the centre of the slab behave in the same way as atoms in bulk material. Figure 2.7 shows an example set of electrostatic potentials from a slab calculation of diamond, plotting the energy against the position along a line normal to the surface.

By averaging the bulk states, the average vacuum level and lowest unoccupied electron level can be calculated, which together with the bulk reference levels allow the calculation of the electron affinity and workfunction of the surface. DFT typically underestimates the band gap of semiconductors due to a poor representation of excited states, so typically a experimentally derived value for the band gap is used.

2.5 Chapter summary

This chapter has summarised the theoretical background of the density functional theory techniques used in this project to model the surface of diamond. DFT avoids the complexity of solving the many-body Schrödinger equation for all electrons by using the charge density as the basic variable for calculations. All aspects of this calculations can be calculated exactly except for the exchange-correlation functional of the electrons, which can be approximated by a number of methods, notably the local density approximation and generalised gradient approximation. Using a pseudopotential to approximate the behaviour of the core electrons removes the number of electrons in the system and speeds up calculations substantially.

DFT programs such as CASTEP use this theory to calculate the atomic structure and electronic properties of a material following a series of variational steps. The accuracy of DFT has been proven to be high for many materials, although some underestimation of semiconductor band gaps

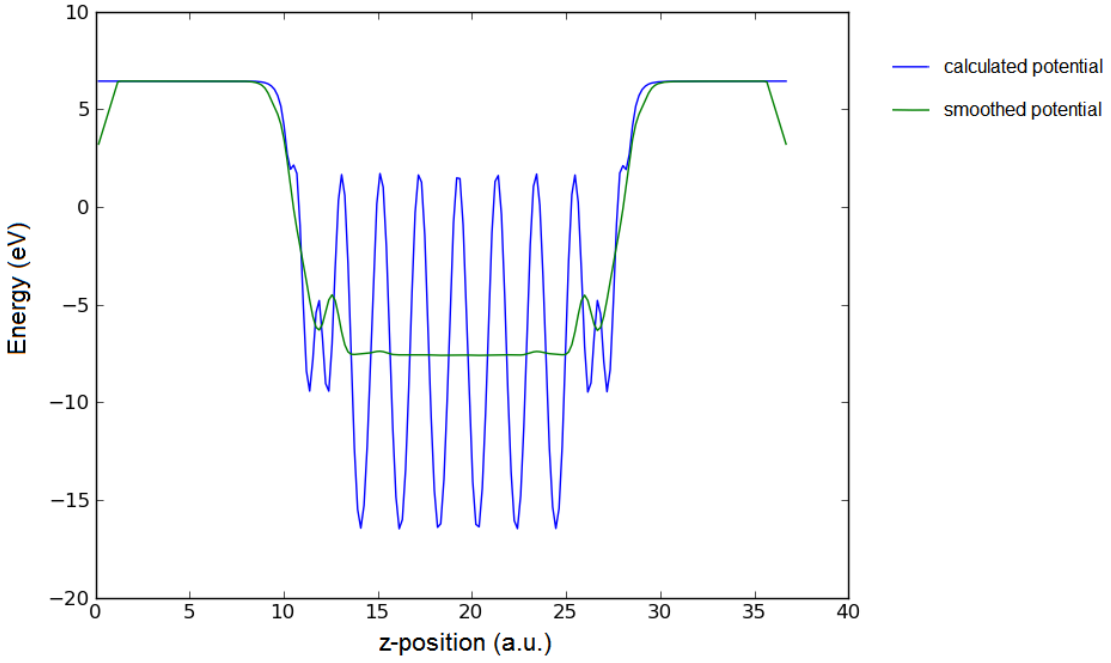

Figure 2.7: An example of the electrostatic potential in the x and y directions as a function of z for a slab of hydrogen-terminated diamond, showing a bulk-like region in the center tailing off to the vacuum level on either side of the slab. The green curve has been smoothed in the core region to allow easier calculation of the average energy levels.

is expected due to the poor representation of excited states. Despite this drawback, DFT is widely used to accurately model crystal systems with as many as several hundred atoms and can be an excellent tool to study the properties of bulk and surface materials.

REFERENCES

[1] Elliott, S. *The Physics and Chemistry of Solids.* Wiley, Chichester, UK, (1998).

[2] deBroglie, L. *Recherches sur la theorie des quanta.* PhD thesis, Paris, (1924).

[3] Thomson, J. *Philosophical Magazine* **24**, 209 (1897).

[4] Davisson, C. and Germer, L. *Physical Review* **30**, 705 (1927).

[5] Heisenberg, W. *Z. Phys.* **43**, 172 (1927).

[6] Naemen, D. *Semiconductor Physics and Devices 3rd edition.* McGraw-Hill, New York, NY, USA, (2002).

[7] Born, M. and Oppenheimer, R. *Annalen der Physik* **84**, 457 (1927).

[8] Payne, M., Teter, M., Allan, D., Arias, T., and Joannopoulos, J. *Rev. Mod. Phys.* **64**, 1045 (1992).

[9] Sutton, A. *Electronic Structure of Materials.* Oxford University Press, Oxford, UK, (1993).

[10] Hartree, D. *Proc. Cambridge Phil. Soc* **24**, 89 (1927).

[11] Slater, J. *Phys. Rev.* **34**, 1293 (1929).

[12] Fock, V. *Z. Physik* **61**, 126 (1930).

[13] Kaxiras, E. *Atomic and Electronic Structure of Solids.* Cambridge University Press, (2003).

[14] Hohenberg, P. and Kohn, W. *Phys. Rev.* **136**, B864 (1964).

[15] Kohn, W. and Sham, L. *Phys. Rev.* **140**, A1133 (1965).

[16] Perdew, J. and Wang, Y. *Phys. Rev. B* **45**, 13244 (1992).

[17] Perdew, J., Burke, K., and Ernzerhof, M. *Phys. Rev. Lett.* **77**, 3865 (1996).

[18] Hammer, B., Hansen, L., and Norskov, J. *Phys. Rev. B.* **59**, 7413 (1999).

[19] Wu, Z. and Cohen, R. *Phys. Rev. B.* **73**, 235116 (2006).

[20] Clark, S., Segall, M., Pickard, C., Hasnip, P., Probert, M., Refson, K., and Payne, M. *Zeitschrift fur Kristallographie* **220**(5-6), 567–570 (2005).

[21] Broyden, C. *J. Appl. Maths.* **6**(1), 76–90 (1970).

[22] Goldfarb, D. *Mathematics of Computation* **24**(109), 23–26 (1970).

[23] Fletcher, R. *The Computer Journal* **13**(3), 317–322 (1970).

[24] Shanno, D. *Mathematics of Computation* **24**(111), 647–656 (1970).

Bryan: I can tell you I don't have money. But what I do have are a very particular set of skills; skills I have acquired over a very long career. Skills that make me a nightmare for people like you.

Taken (2008)

3 Experimental Methods

In addition to the computational calculations explained in the previous chapter, this investigation used a large variety of material characterisation tools to investigate the structural and electronic properties of both diamond nanoparticles and single crystal diamond before and after its interaction with lithium.

In this chapter a brief outline to the techniques used in this thesis are presented. The first half will look primarily at the theory and practice of electron emission through thermal and field excitation, whereas the latter half of the chapter will discuss material characterisation tools such as electron microscopy and various forms of spectroscopy including electron energy loss spectroscopy, ultraviolet and X-ray photoemission spectroscopy.

3.1 Vacuum systems

Many of the techniques used in this investigation require vacuum conditions to be successful, for a number of reasons. Firstly, the contamination of adsorbate gases can cause damage and/or disruption to a sample, particular if it is being heated or subjected to an applied voltage. A 'rough' vacuum of $1 - 10^{-3}$ Torr will remove adsorbed gases from the sample and chamber, but a medium vacuum of $10^{-3} - 10^{-5}$ Torr is required to prevent further adsorption of contaminants like water molecules remaining in the system.

In addition to the need to prevent contamination, any experiment using a high voltage supply such as in field emission requires a high vacuum of $10^{-6} - 10^{-8}$ Torr to prevent arcing and breakdown. Most significantly, due to the low mean free path of electrons, investigations with free electrons or ions such as photoemission or thermionic emission require Ultra-high vacuum conditions of at least 10^{-9} Torr to reduce the risk of collisions with molecules in the gas phase which could alter the kinetic energy of the electrons. Surface science experiments require the vacuum to be sufficient that the mean free path of any electrons, ions or atoms in the vacuum is greater than the size of the apparatus itself, so that the majority of these particles will travel between sample and detector without interaction with gas molecules.

3.2 Thermionic Emission Theory

3.2.1 History of Thermionic Emission

The observation of electrical charge near to heated solids was first investigated by Becquerel in 1853[1], and was expanded by Elster and Geitel's 1882 studies into the emission of electricity from heated metal wires within a gas chamber of variable pressure.[2] Thomas Edison's discovery of the 'Edison effect' in 1883 was the inciting incident for a much more active study of the phenomenon.[3] Edison observed 'negative shadows' on the inner surface of a carbon filament incandescent bulb, a clean line parallel to the filament where black carbon deposit did not build up as on the rest of the bulb. Edison observed that the blackening of the wire occurred at the negative pole, with a blue glow at the positive pole, leading him to hypothesise that any particles being transported from the heated filament would be electrically charged.

In 1883 Edison added a second electrode to his lamp design.[4] When the additional electrode was negatively charged, no current flow was observed, but when this additional electrode was positively charged relative to the filament, a current flowed from the filament to the positive electrode. Edison patented what would become known as the thermionic diode, the first true electronic device. Although Edison had discovered the effect of thermionic emission and his work had been confirmed and expanded by Preece[5] and Elster and Geitel,[6] little was understood about the mechanism of the current flowing in a vacuum between the hot filament and the positively charged electrode until 1897, when Thomson discovered the electron.[7]

Thomson observed the deflection of cathode rays by electric fields in evacuated tubes, and this led to the measurement of the charge/mass ratio of the electron, and the inescapable conclusion that the charge in the ray was being carried by a sub-atomic particle. The realisation that charge was carried by 'corpuscles' had a huge impact on the understanding of electronic behaviour, including thermionic emission. In 1899 Thomson also confirmed that the charge transfer in photoemission and thermionic emission was also carried by electrons[8]. Owen Richardson first extrapolated a theoretical equation for thermionic emission in 1901,[9] based on the formulation of a theory for electron conduction in metals by Drude,[10] Riecke[11] and Thomson.[12] In 1905 Fleming patented the first electronic diode using thermionic emission, which is widely considered the birth of modern electronics.[13–15]

3.2.2 The Richardson-Dushman-Laue Equation

Once the electron's existence was known, it was possible to interpret the Edison effect as a current flow of electrons j from the hot wire to the positively charged foil. The original 1901 formulation of Richardson's equation[9] for thermionic emission assumed electron velocities followed a Maxwellian distribution, and those electrons with sufficient velocity could overcome the workfunction potential barrier at the surface ϕ, and escape. The theoretical considerations of thermionic emission were refined in 1913[16] to account for issues with the classical free electron theory as applied to the electrons in metals. Richardson proved that the current flow from a material was exponentially related to the workfunction of the material, and its temperature, T, such that:

$$J = AT^2 e^{\phi/kT}(1) \tag{3.1}$$

Where A is the Richardson constant in A/cm^2, and k is Boltzman's constant.

After Einstein and others proved that electrons at a barrier exhibit quantum rather than classical behaviour, Dushman later applied quantum theory to derive the universal constant $A_0 = \frac{4\pi mk^2e}{\hbar^3} = 1.20173 \times 10^6$ A m^{-2} K^2 for the Richardson constant and this discovery led to the equation being renamed the Richardson-Dushman equation in recognition of his efforts.[17] However in practice it was found that the value for A varied greatly from material to material. A number of different interpretations are used to account for this difference, typically with the effective Richardson Coefficient A_G comprising of the elementary Richardson constant A_0 multiplied by one or more other factors dependent on the material, such that $A_G = A_0\lambda_r$.

The simplest modification to the Richardson theory is the additional consideration of the wave-like nature of electrons, which results in the reflection of a certain percentage of the current flow at the emitter surface. In this case $\lambda_r = (1 - r)$, and the Richardson-Dushman equation becomes

$$J = (1 - r)A_0T^2e^{\frac{\phi}{kT}} \tag{3.2}$$

More recent interpretations also include a correction factor due to the band-structure of the material such that $A_G = \lambda_B(1-r)A_0$, where $(1-r)$ accounts for the reflection and λ_B is a second correction factor accounting for the band structure of the emitter.[18]

3.2.3 Complications to the RLD model

Although from the Richardson equation the emission current depends principally on the temperature and workfunction of the emitter, the performance of the device in reality is more complicated. The workfunction is not a fixed value with different temperatures and so the current and power density of a thermionic device depends on the relationship of workfunction with temperature.[19] In addition the power density of the device depends on the emission current multiplied by the voltage drop between the electrodes, which is defined by the difference in electrode workfunctions $\phi_E - \phi_C$. The maximum power output occurs when

$$P = IV = I_C(\phi_E - \phi_C) = AT_E^2e^{-\frac{\phi_E}{kT}}(\phi_E - \phi_C) \tag{3.3}$$

So that the maximum power depends on maximising the difference between collector and emitter workfunctions, which when coupled with the Richardson equations demands of a low workfunction for the emitter requires minimising the collector workfunction as much as possible. The maximum power output comes when $\frac{dP}{d\Phi_E} = 0$, such that:

$$\frac{\delta P}{\delta \phi_E} = AT^2\left(e^{-\frac{\phi_E}{kT}} - \frac{1}{kT}e^{-\frac{\phi_E}{kT}}(\phi_E - \phi_C)\right) = AT^2e^{-\frac{\phi_E}{kT}}\left(1 - \frac{1}{kT}(\phi_E - \phi_C)\right) \tag{3.4}$$

i.e. that the maximum power output occurs at $\phi_E = \phi_C + kT$.[19] The efficiency of the device in converting heat energy to electrical power conflicts with these high power demands, as it is defined by:

$$\eta = \frac{I_C(\phi_E - \phi_C) - P_{EL}}{I_C\phi_E + P_{TL}} \tag{3.5}$$

where I_C is the current, P_{EL} is the total power lost due to electrical losses, P_{TL} the total

power loss due to thermal losses. The electrical losses include the energy given to the electrons to overcome the emitter workfunction, losses in the interelectrode plasma and the energy used in producing the ions in a gas-filled system. Heat losses include the thermal kinetic energy transferred to the electrons from the emitter ($2kT$), dissipated heat in the electronic circuit and interelectrode plasma, as well as radiative losses from the hot electrodes. If the heat loss is dominated by the losses in producing the electron stream then $\eta = \frac{\Delta\phi}{\phi_E + 2kT}$.

This creates a problem, because if the work function difference is optimised for maximum power so that $\Delta\phi = kT$ then the corresponding efficiency must be low (around 7 %). The best efficiency is achieved when $\Delta\phi$ is around $0.5V = 30\%$ efficiency but this has trade-off in much lower power output. This is a key consideration when designing a thermionic device, namely that *it is not possible to have a device with both peak power output and peak efficiency.* Practical devices must be designed so their electrode workfunctions give a good compromise between power output and conversion efficiency. In addition, there is the potential problem of the space-charge limit to the current density, which can dramatically reduce power output.

3.2.4 Space Charge

A major complication to thermionic emission, and one that accounts for much of the difficulty in producing working thermionic energy converters, is the space charge. When electrons are emitted into a dielectric medium such as a vacuum, those electrons which are emitted but not absorbed by the collector remain within the interelectrode gap as a cloud of electric charge. This build-up of charge within the interelectrode gap acts to form a potential barrier to any subsequent electrons passing from the emitter to the collector. Thermionic emission suffers from this issue far more because thermally excited electrons leave with low KE compared to photoemission or field emission.

The space charge can dramatically decrease the current density of devices to the point where they are not commercially viable. The large potential barrier caused by space charge at sensible interelectrode gaps prevents all but the most energetic electrons reaching the collector.

The emission current of a space-charge limited thermionic emitter is governed by Child's Law (or the Child-Langmuir law).[20;21] The space-charge-limited emission current depends on the geometry of the emitter and collector, as well as the collector voltage V. The Child-Langmuir law for concentric cylinders gives

$$j = \frac{2}{9}\left(\frac{2e}{m}\right)^{\frac{1}{2}} \frac{V^{\frac{3}{2}}}{r} \tag{3.6}$$

so long as the radius of the cathode is less than a tenth of the collector radius r. In practice this means that any emission current is limited to the $\frac{3}{2}$ power of the collector voltage due to charge build-up within the interelectrode gap, so considerable engineering efforts are required to observe significant emission current without an applied voltage between the two electrodes.

There are three main proposed solutions to reduce space charge without a large applied voltage, which have been explored to varying success. The first method is to reduce the size of the interelectrode gap such that the space charge cloud lies close to the collector, allowing easy capture of the majority of electrons. In practice this requires interelectrode spacing of 3-5 μm or less,[19;22]

which shifts the problem from a physics challenge to one of engineering, as manufacturing such a small gap to survive at the high temperature operation of a thermionic converter is difficult. Attempts by Sandia National Lab researchers to create a microminiature thermionic converter [22] using barium oxide cathode emitters was beset by problems with keeping electrode surfaces smooth and parallel, and even small amounts of contamination caused the two electrodes to be in electrical contact.

The second method, which has been used in all successful thermionic converters to date, is to introduce a small quantity of charge-carrying gas into the interelectrode space. Traditionally caesium has been used for this purpose, as it is the most easily ionised element. With the lowest ionisation potential of any suitable element, caesium easily forms positive ions which can 'mop up' the space charge electrons and remove their current-limiting effect. Caesium is also adsorbed onto the electrode surfaces which can have a workfunction reducing effect due to the dipole formed on the surface. [19]

The metal based thermionic devices investigated by the Russian and American space agencies such as the TOPAZ I and II series of reactors used caesium vapour as a space-charge reducing agent. Instead of toxic caesium gas, a third alternative is an auxiliary discharge of positive ions such as argon, which can be used to mop up the space charge within the interelectrode gap. Recent work investigating nitrogen doped diamond thermionic emitters has used methane gas for an analogous purpose. [23]

Although both reducing the interelectrode gap and introducing a charge-carrying gas can reduce the space-charge cloud of low KE electrons within the interelectrode space and so increase the emission current, there are drawbacks to both methods. The most significant is that both practices make heat conduction between the electrodes easier, reducing the temperature difference and hence the workfunction difference between the emitter and collector. As the power output depends on the voltage caused by the difference in workfunction between the electrodes, both methods have a 'balancing act' effect on the power output, where the increase in emission current due to space-charge mitigation needs to outweigh voltage decreases due to a smaller temperature gradient.

3.3 Field Emission Theory

3.3.1 History of Field Emission

Early field emission was first investigated by Johann Heinrich Winkler in the 18th Century on needle-like metal tips, [24] using early vacuum pumps that likely did not reach low enough pressure for true field emission. His experiments were limited, but included the fluorescence of butter under excitation of the field emitting tip!

True observation of the field emission phenomena would not occur for another century, when it was first reported in 1897 by R.W. Wood, [25] during research on discharge tubes. W. Schottky was the first to put the observation into a theoretical context, [26] with the assumption that the applied electric field was lowering the potential barrier at the surface to electrons within the material.

The theory of field emission as a quantum-mechanical tunnelling effect was developed by R.H. Fowler and L. W. Nordheim in 1928, [27;28] linking the emission current to both the electric field and the material workfunction, complemented by the work by R. Millikan and C. Lauritsen [29]

confirming the exponential relationship between the electrical current density j and the reciprocal of the electric field strength $1/E$.

The advent of this understanding of the field emission process led to the invention of the field emission microscope in 1936 by E. W. Muller,[30] and the investigation of field emitters saw increasing current densities over the following decades, from 10^6 A/cm^2 by Haefer in 1940,[30] $10^7 - 10^8$ A/cm^2 by W.P. Dyke's group in the 1950s[31;32] and recently as high as 10^{11} A/cm^2 by Fursey *et al* in 1998,[30] close to the theoretical limit of electrons that can be supplied from a metal's conduction band. The work on field emitters in the 1950s led to the production of devices for pulsed X-ray sources for medicinal use,[33] as well as the possibility of using field emission sources to study surfaces at the atomic level in electron microscopes.[34] In recent years, the focus for new applications for field emission has been for microelectronic components, particularly for flat-panel displays. The work of Spindt in creating high surface-enhanced field emission metal tips has been a key development towards this aim,[35] but new materials such as diamond are also being studied as alternative sources for this application.

3.3.2 The Fowler-Nordheim equation

The field emission current density j is dependent on the flux of electrons n within the material incident on the surface barrier multiplied by the coefficient of transmission through the barrier D. D is dependent on the size of the electric field strength F at the surface.

$$J = e \int_0^\infty n(\delta) D(\delta, F) d\delta \tag{3.7}$$

Where e is the charge on the electron and the integral is from 0 to infinity as at zero the electron is trapped within the material. Alternatively the equation can be expressed in terms of the tunnelling probability $T(E_x)$ for an electron with energy E_x in the x direction:

$$J = e \int_0^\infty dv_x v_x N(v_x) T(E_x) \tag{3.8}$$

where $N(v_x)dv_x$ is the density of electrons with velocity between v_x and $v_x + dv_x$ in the x direction. The tunnel

$$\Psi(L) = \Psi(0) exp\left(- \int_0^L \sqrt{\frac{2m^*[V(x) - E]}{\hbar}} dx \right) \tag{3.9}$$

The WKB approximation assumes that the potential varies slowly enough that the wavefunction at L can be related to the initial wave function. For a triangular barrier with $V(x) - E = q\phi_B(1 - \frac{x}{L})$, The tunnelling probability $T(E_x)$ is

$$T(E_x) = \frac{\psi(L)\psi^*(L)}{\psi(0)\psi^*(0)} = exp\left(-2 \int_0^L \frac{\sqrt{2m^*}}{\hbar} \sqrt{q\phi_B(1 - \frac{x}{L})} dx \right) \tag{3.10}$$

Where ϕ_B is the barrier height and m^* the effective mass of the electron. After solving the integral the tunnelling probability with $E_x = \frac{\phi_B}{L}$ is

$$T(E_x) = exp\left((-\frac{4}{3}\frac{\sqrt{2qm^*}}{\hbar}\frac{\phi_B^{\frac{3}{2}}}{E_x}\right) \tag{3.11}$$

And as $j = qv_R nT(E_x)$, the tunneling current in field emission depends on the exponential of the barrier height to the $\frac{3}{2}$ power divided by the field.

In practice, the field emission of a sample can be observed by plotting IV characteristics in the 'Fowler-Nordheim' plot, where $ln(\frac{j}{E^2})$ is plotted on the y axis and $\frac{1}{E}$ is plotted on the x axis. A straight line indicates pure field emission behaviour.

3.3.3 The Surface Enhancement Factor

Although in theory the gradient of the Fowler-Nordheim plot of $ln(\frac{j}{E^2})$ versus $\frac{1}{E}$ should yield the workfunction, this relationship is complicated in practice. On a purely atomically flat surface, this relationship should hold, but on a surface with any roughness, geometric effects begin to influence this behaviour.

The one-dimensional approximation that makes up the Fowler-Nordheim equation typically holds for atomically smooth emitters with radii above 0.1 μm, as the curvature of the emitter is significantly larger than the width of the potential barrier.[36] When the radius of curvature of the emitter approaches the barrier width, the electric field can no longer be assumed to be uniform across the emitter surface, and the one-dimensional barrier assumption is also not valid. The sharper the tip of the emitter, the more charge is concentrated at its apex, and the easier it is for the electrons to tunnel across the barrier, essentially reducing the effective workfunction of the material.

To fully express this asymmetric potential, a complicated solution to the three-dimensional Schrödinger equation using polar coordinates is required, which is typically too complicated to perform and an approximation, the field enhancement factor, is included in the FN equation such that the workfunction ϕ is replaced by $\lambda\phi$ where λ is the field enhancement factor. The field enhancement factor should be unity for atomically smooth surfaces and increasingly large as the tip apex becomes sharper.

Another complication is that the Fowler Nordheim equation assumes Fermi-Dirac statistics for their electrons, following the Sommerfeld free electron model, essentially a one-electron theory. As the true behaviour of the electrons in an emitter material is a many-body problem, the Fowler-Nordheim equation omits a number of interactions not included in the one electron approximation. The energy dispersion laws often used to approximate the behaviour electrons in metals is also not included, which would imply that with increases in temperature the electron current should decrease, rather than increase as in the free electron model.

Attempts have been made to include the many-body behaviour of electrons through quantum mechanical statistics, but the problem rapidly increases in complexity and Fowler-Nordheim theory remains the most commonly used theory to explain and interpret field emission.

3.3.4 Thermal-Field Emission

It has been shown that the behaviour of electrons emitted from a material under the influence of large electric fields follows the Fowler Nordheim equation, and that electrons thermally excited

and emitted thermionically follow the Richardson-Dushman equation. What of systems in which both electric field and thermal excitation play a role in electron emission?

Fowler-Nordheim theory assumes a temperature of 0 K. Above this temperature, some electrons will have energy greater than the Fermi energy and will occupy energy levels above the Fermi level and these electrons will add to the emission current increasingly as temperatures rise.[36] Below 1000 K, the ratio of the thermal-field current $j(F,T)$ to the assumed FN emission current at 0 K $j(F,0)$ is

$$\frac{J(F,T)}{j(F,0)} = \frac{\pi\omega}{sin(\pi\omega)} \tag{3.12}$$

Where ω is the expression

$$\omega = 4\pi\sqrt{2mk\sqrt{\phi t(y)}he}\frac{T}{F} \tag{3.13}$$

Which can be approximated to $9.22 \times 10^3\sqrt{\phi}\frac{T}{F}$. This ratio is valid up to $\omega = 0.7$, above which Schottky emission is a more appropriate model. At higher temperatures, thermionic emission dominates and the current is best expressed by the Richardson-Dushman-Laue equation.

Even conventional thermionic emitters often contain a small electric field. Schottky demonstrated in 1914[37] that with no field applied, a large proportion of the workfunction consisted of mirror image forces between an emitted electron and its image in a conducting material. As a result, most thermionic devices apply an external electric field to counteract this image force, lowering the effective workfunction using the so-called Schottky effect. Typically the current measured at the anode will increase with higher anode voltage. The Schottky modified Richardson equation is described as:

$$J(F,T,\phi) = A_G T^2 e^{\frac{-(\phi-\Delta\phi)}{kT}} \tag{3.14}$$

where $\Delta\phi = \sqrt{\frac{e^3F}{4\pi\epsilon_0}}$ and ϵ_0 is the permittivity of free space. This Schottky-Richardson equation is applicable to fields below 10^8 V m^{-1}, above which the emission is field-dominated and follows the Fowler-Nordheim equation.

In practice to obtain the thermionic workfunction of a sample using the Richardson-Dushman-Laue equation, the Schottky effect is often used. Emission currents at specific constant temperatures are obtained for a number of different anode voltages, and the current at each anode voltage is plotted in a Schottky plot of the emission current j against the square root of the field F, and the intercept for zero field is extrapolated. It is this zero-field current that is then used for the Richardson plot of $ln(\frac{j}{kT})^2$ against $1/T^2$ from which the gradient is the workfunction ϕ and the intercept is the effective Richardson constant A_G.

3.4 Photoemission Spectroscopy

Photoemission or photoelectron spectroscopy uses the photoelectric effect to characterise the structure of a material. The photoelectric effect occurs when electrons in a material are excited by a photon of a high enough energy to eject it from the parent atom. By analysing the photoelectrons ejected from a material under the excitation of a high energy monochromatic beam of photons,

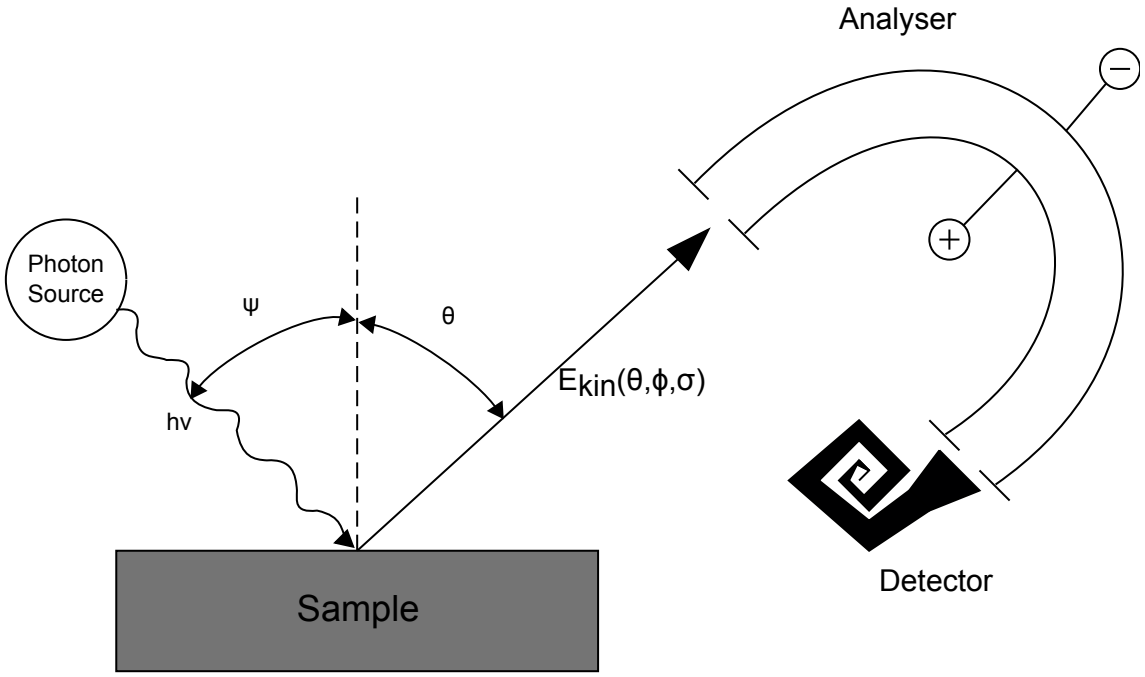

Figure 3.1: The general principle for a photoemission spectrometer. A photon source with energy $h\nu$ (either X-ray or UV) is shone onto a sample surface in an ultra high vacuum, with the kinetic energy of the resultant photoelectrons being analysed by an electrostatic analyser. After [38].

the composition of the surface and its electronic structure can be analysed, depending on the wavelength of light used.

Photoemission from a solid is a three step process. Firstly, an electron absorbs a photon of sufficient energy to remove it from its energy level, forming an electron-hole pair. The electron then transfers through the solid to the surface of the material, where, providing it still has sufficient energy, it is ejected into the vacuum.

A typical photoemission experiment is shown in Figure 3.1. When a photon of frequency ν is absorbed by an electron in an irradiated sample, the electron gains energy $E = h\nu$. If the energy is high enough to overcome the electron's binding energy E_b, it is ejected from the parent atom, with the remaining energy from the photon remaining as kinetic energy in the electron, which can be assessed by an analyser. By deducting the value of the electron's kinetic energy E_k from the energy $h\nu$ of the photon that excited it, the binding energy can be found such that:

$$E_b = h\nu - E_k \tag{3.15}$$

A photoemission experiment must be performed in a high vacuum to reduce the chances of ejected electrons interacting with gas molecules and losing energy. Any electron that suffers significant scattering on its way to the surface will no longer contain the information about the state from which it originated, so because of the low mean-free path of an electron in a solid photoemission spectroscopy is a very surface-sensitive technique, with only the first few atomic layers contributing to the spectra.

To perform a photoemission study the intensity of detected electrons with a certain energy is plotted against the energy, giving characteristic peaks at certain energies relative to structure within the sample. There are two main types of structure that can be observed using photoemission spectroscopy - excitation of the core level electrons using X-rays gives information about the chemical composition and bonding behaviour of the surface atoms, whilst excitation by ultraviolet light causes the ejection of valence band electrons, which gives information about the valence band electronic structure of the material. These are known respectively as X-ray photoemission spectroscopy (XPS) and ultraviolet photoemission spectroscopy (UPS).

3.4.1 X-ray Photoemission Spectroscopy

First developed in the 1960s by K. Siegbahn,[39] X-ray Photoemission Spectroscopy (XPS) is the analysis of ejected core electrons in a material excited by the illumination of the sample by a source of X-rays. It is sensitive to the first 5-10 nm of the surface and can detect all the core electron atoms i.e. every element bar hydrogen and helium. The sample is placed in an ultra-high vacuum chamber to ensure electrons can travel to the electron analyser around a metre above the sample. An X-ray source with either an aluminium or magnesium characteristic line irradiates the sample. X-ray photons liberate core electrons of the material surfaces, which are captured by the energy analyser and sorted according to energy. The spectrum produced gives characteristic peaks according to the binding energies of the elements in the material, with higher intensities corresponding to larger elemental concentration. The kinetic energy E_k recorded by the spectrometer corresponds to the binding energies of the core electrons E_b as follows:

$$E_k = h\nu - E_b - \phi \tag{3.16}$$

Where $h\mu$ is the X-ray photon energy (1486.6 eV for monochromatic X-rays from the Aluminium K_α line, or eV for magnesium K_α). The workfunction ϕ induced by the analyser, around 4-5 eV, is compensated artificially during the scan so isn't present in the resulting spectra. Wide scans from 0 eV binding energy up to $h\nu$ are used to scan the full range of the sample to identify the key peaks, which are then subject to higher resolution scans for more comprehensive analysis.

Peaks are designated according to the quantum level the photoelectron was ejected from - this can include spin orbit splitting at higher atomic number, with the relative intensities determined by the multiplicity of the corresponding energy levels. In addition to the X-ray photoemission peaks, Auger electrons can be detected, a two-step process where after an X-ray removes a core electron, an electron in a higher shell drops down to fill the hole, with the energy released by the transition transferred to another electron, which is ejected from the atom.

An example wide spectrum of palladium metal is shown in Figure 3.2, using a magnesium target to generate the X-rays. In this example the highest peak is at 335 eV, corresponding to the $3d$ level of Pd, with peaks at 534 eV and 561 eV due to the $3p$ levels and from the $3s$ level at 673 eV. The photoelectrons from the $4d$, $5s$, $4p$ and $4s$ levels are at low binding energies and only the latter two can be weakly detected at 54 and 88 eV respectively. Just below the main $3d$ is an Auger emission peak at 330 eV.

The removal of a core electron from an atom causes an increase in the nuclear charge experienced by the remaining electrons, and a relaxation of the valence electrons as a result can involve the

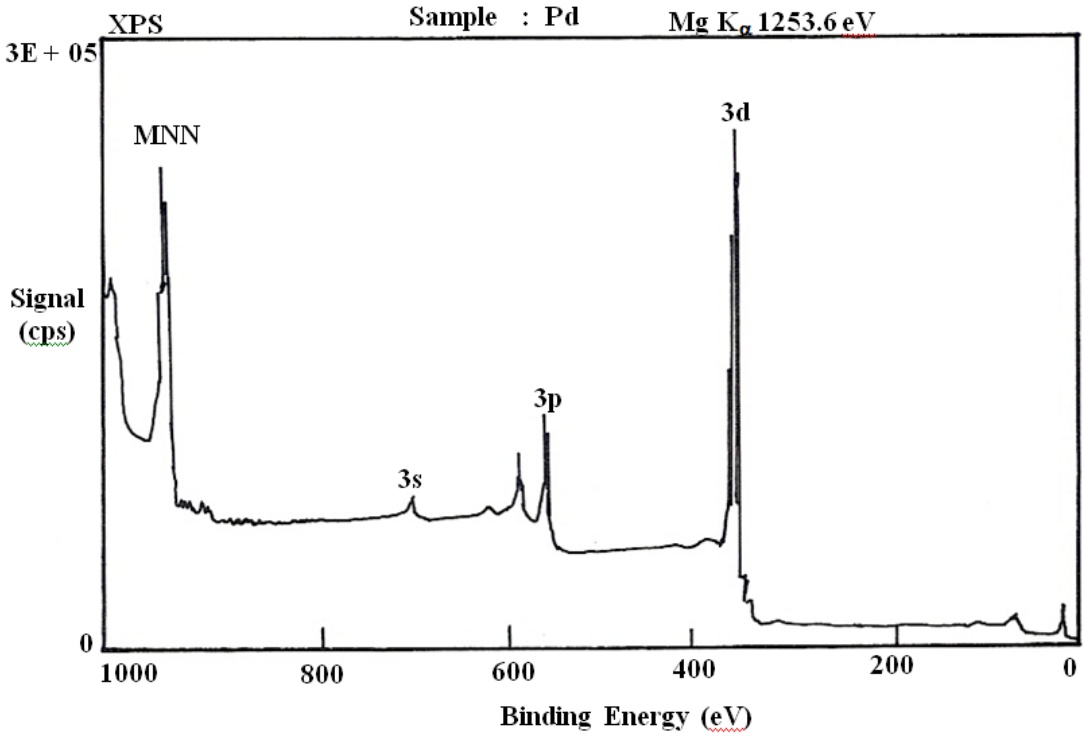

Figure 3.2: An example X-ray photoemission spectrum of palladium using the magnesium K_α line as the X-ray source. MNN refers to an Auger peak.[40]

excitation of an electron to a higher level, which can be observed as 'shake-up' electron satellite peaks at lower kinetic energy to the original core electron peak. Similarly a valence electron can be completely removed from the atom, known as a 'shake-off' satellite peak, detected at even lower kinetic energies than a shake-up satellite. Shake-off satellites are rarely detected in solid state samples as they are more likely to blend into the broad inelastic tail of the main spectra, but for transition metals and rare earth compounds strong shake-up peaks can often be seen.

Problems can arise from non-conductive samples in a photoemission system. As electrons leave the surface on excitation by X-rays, the insulating sample is unable to replace them, leaving a potential difference between the sample and the spectrometer, resulting in a retardant field that increases the amount of energy electrons need to reach the spectrometer, shifting their characteristic energy lines by as much as 150 eV. A number of methods are used to correct this, falling into two broad camps: returning more electrons to the surface via an electron flood gun or similar, or using a conductive element such as gold or silver as a reference. In the latter case, a small amount of a non-reactive metal is deposited in the centre of the sample, so that it is electrically isolated from the sample holder but in electrical contact with the sample. When the sample charges, the metal will be shifted from its natural binding energy by a similar voltage to the charging on the sample, so by measuring the difference in binding energy between a similar dot of metal on the sample holder and that on the sample, the sample's spectra can be adjusted to remove the charging effect.

Small changes in the chemical environment of the sample can change the sensitive binding energy of the core electron, causing chemical shifts of 0.1 eV to 10 eV, which can be used to study

the chemical structure of the element in the material. It is for this reason that another name is sometimes used for XPS, electron spectroscopy for chemical analysis (ESCA).

Although the reference binding energy of an electron energy level is specified at a certain binding energy for each element, the exact binding energy detected depends on the oxidation state of the atom from which the electron originated, as well as the local chemical and physical environment, with even small changes in these conditions leading to shifts in the peak positions of the XPS spectra. Providing the resolution of the instrument (i.e. the resolving power of the analyser and the line-width of the incoming X-ray) is high enough, these chemical shifts can be studied to investigate the bonding environment of the atoms on the surface of the material. Using a monochromator to generate the X-ray beam is the most significant way to improve resolution.

In general an increase in negative charge on an atom results in a shift to lower binding energy to the shift, whilst a higher positive oxidation state displays a higher binding energy, due to the additional coulombic attraction between the ejected electron and the less shielded nuclear core. For example, the carbon $1s$ peak for diamond or hydrocarbons is at approximately 285 eV, but when the carbon is bonded to an oxygen atom, the increase in charge transfer away from the carbon atom towards the C-O bond results in a higher energy of around 1-1.5 eV. In a C=O double bonded arrangement, the amount of charge moved away from the carbon atom is even higher, leaving it in a more positive oxidation state again, and resulting in a higher binding energy some 2-3 eV above the 285 eV peak. Correspondingly, the oxygen atom will be in a more negative oxidation state in a C=O bond and so will have a lower binding energy (around 531 eV for the double bonded case and 533 eV for the single bonded C-O case).

XPS is a very useful technique for characterising the atomic structure and chemical environment of the top surface of a material but to probe the electronic structure and density of states of a sample, another type of photoemission spectroscopy is used, with a different energy of photon, in the ultraviolet range of the electromagnetic spectrum.

3.4.2 Ultraviolet Photoemission Spectroscopy

Ultraviolet photoemission spectroscopy (UPS) uses ultraviolet photons in the region of 5-40 eV to excite the valence band electrons of a sample. Typically a helium-discharge lamp is used to generate ultraviolet light for UPS, using either the He I $1s^1 2p^1 \rightarrow 1s^2$ or He II transition in helium to generate photons with 21.22 eV and 40.8 eV respectively. Alternatively as with XPS a synchrotron source can be used as a photon source that can be tuned to the desired wavelength. Analysing a sample across several photon energies can help to analyse complicated spectra, as certain peaks will change in intensity as the photon energy changes.

The UV-excited electrons detected by a UPS spectrometer give information about the density of states of the valence band of the material, convoluted with a background of electrons inelastically scattered as they leave the sample.

The spectra of a sample changes depending on the solid angle seen by the electron spectrometer - i.e. the angle between the sample and the analyser. By analysing the UV-excited photoelectron spectrum through a number of angles, the two and three dimensional band structure of a material can be mapped, and this is known as angle-resolved ultraviolet photoemission spectroscopy or ARUPS. ARUPS is typically performed at synchrotron facilities and will not be a focus of this

investigation, but can be a comprehensive extension of the characterisation of a sample using traditional photoemission.

To understand the spectra produced using ultraviolet photoemission from the valence band it is helpful to understand the theory behind electron density of states.

3.4.3 Density of States

The number of distinguishable states in the first Brillouin zone is known as the density of states in k-space $D(E)$.[41] For the energy interval $[E, E + dE]$

$$D(E) = \frac{DF}{dk}.\frac{dk}{DE} = \frac{\frac{dF}{dk}}{|\frac{DE}{dk}|} \tag{3.17}$$

Where F is the number of states up to energy E. The density of states will be largest when $|\frac{dE}{dk}| \geq 0$ so that the energy level in the band is flat. However the above equation gives such close spacing of energy levels that they can be treated as continuous, allowing derivatives in energy. As the total density of states is discontinuous in both reciprocal space and energy, the expression for D(E) is written as

$$D(E) = \sum_{E_i} \delta(E - E_k) \tag{3.18}$$

Where $\delta(E - E_k)$ is the contribution to the density of states by the eigenstate lying at $E = E_k$.

The density of states can be viewed as distributed equally per atom only if all atoms are equivalent. Atoms that differ from the main structure such as grain boundaries, adatoms, dopants and other defects will have different local distribution of their density of states. When all these local density of states are summed, they add to the total density of states. This is known as the localised density of states (LDOS).

If the total density of states is a sum of delta functions:

$$D(E) = \sum_{all Ei} \delta(E - E_k) \tag{3.19}$$

Then the local density of states can be calculated for a particular atom n by projecting that atom's contribution to the total density of states onto that atom. For each individual contribution of energy E_i, we can add the weighting P_n^i, the probablility of finding an electron in an atomic state ϕ_n localised on atom n. The probability of finding an electron is given by the square of the wavefunction Ψ_i for that particular atomic state ϕ_i:

$$P_n^i = | < n|\Psi_i > |^2 \tag{3.20}$$

Where $\Psi_i = \Sigma c_a^i \phi_a$ and $c_a^i = \int \phi_i^* \psi_i dr =< \phi_a|\psi_i >$. Hence the local density of states on an atom n is given by

$$D_n(E) = \sum_{all\ E-iu} P_n^i \delta(E - E_i) \tag{3.21}$$

And the total density of states is recovered by summing these local density of states for all

electrons in the system.

3.4.4 Density of States in UPS

In XPS with $h\nu$ above 1000 eV the photoelectrons ejected by the X-rays are a good reflection of the density of states of the core electrons, but at lower photon energies of 50 eV or less such as in UPS, the electrons are scattered as they escape the sample, and the density of states information from the photoelectrons is convoluted with the inelastically scattered secondary electron background.

Figure 3.3 shows the photoemission process in terms of the sample band structure and the spectrum produced. An electron in the sample with E_B requires a photon of energy $h\nu > E_B + \phi_0$, where ϕ_0 is the workfunction, to be ejected from the sample. Once it has escaped into the vacuum, it can be detected by an electron analyser and the kinetic energy distribution of the photoelectrons excited by the UV beam gives a first order approximation of the occupied density of electronic states $N(E_B)$ within the sample.

Above 40 eV the excited valence band electrons generally converge to the same spectrum, but at $h\nu$ of 15-30 eV the UPS spectrum can vary in appearance quite substantially due to the changes in scattering. Photoelectron data can also vary from the total one-electron DOS due to hole lifetime broadening, and differences in cross-section, which vary widely according to the elemental species being studied, as well as multi-electron excitations which can produce peaks in the UPS spectra which are not in the density of states.

3.5 Secondary Ion Mass Spectroscopy

Secondary Ion Mass Spectroscopy (SIMS) is an alternative form of chemical composition analysis to XPS, but unlike XPS it is destructive to the sample. Rather than analysing electrons excited by the photoelectric effect, SIMS bombards the surface of the sample with an ion gun and analyses the mass of the species that are sputtered from the surface. This process is illustrated in Figure 3.4.

SIMS is performed in an ultra-high vacuum to ensure sputtered elements are able to reach the detector. Typically the sputtering ion gun uses high energy ions of an element not expected to be present in the sample, with argon and gallium being common choices for ion gun sources. These ions damage the surface, and any ions removed from the surface are detected using a mass spectrometer. As the surface is physically removed by the process, it is a non-reversible process, but it also allows depth profiling of a sample for the relative quantities of different elements, particularly useful when studying the effects of dopant elements into a substance like diamond. SIMS was only used briefly during this study, and a more in-depth discussion can be found elsewhere. [43]

3.6 Fourier-transformed Infra-Red spectroscopy

Fourier-transformed Infra-Red spectroscopy (FTIR) probes the allowed vibrational modes in a sample, which for covalently bonded materials can be excited by photons of energies between around 0.5 and 0.05 eV. Infra-Red spectroscopy irradiates the sample with an IR source, and measures the spectrum before and after transmission through the sample, any absorbed frequencies

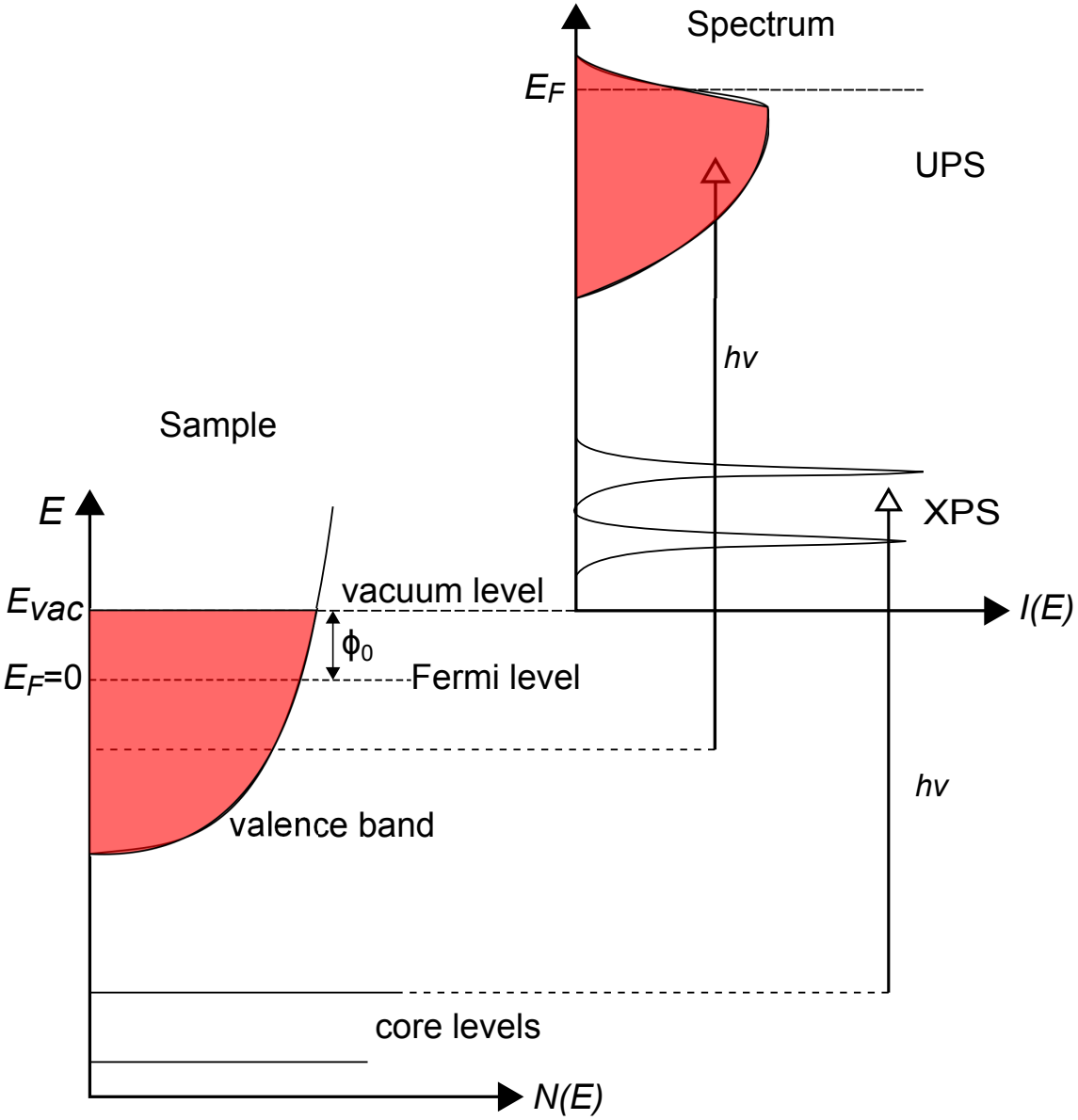

Figure 3.3: The photoemission process for a single particle, with the sample density of states on the left and the spectrum observed in analyser on the right. A photon with sufficient energy $h\nu > E_B + \phi_0$ can excite electrons with binding energy E_B above the vacuum level E_{vac}, with the remaining energy of the photon being observed as the kinetic energy of the ejected electron in the analyser. After[38].

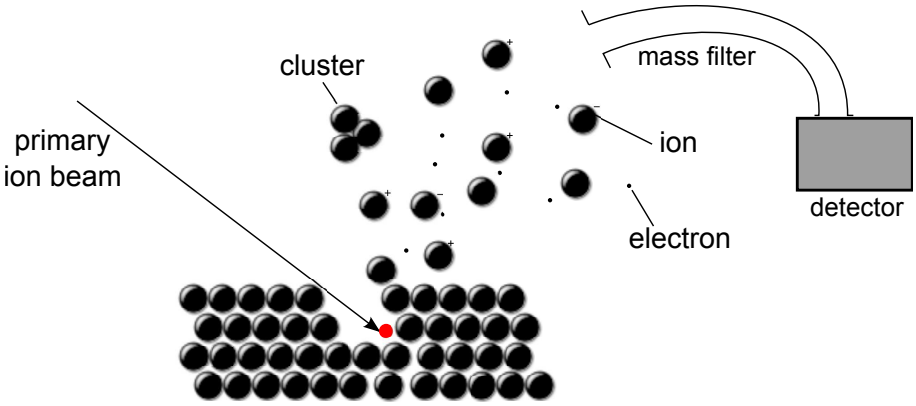

Figure 3.4: Illustration of the ion bombardment process and mass spectrometer detection used in SIMS. After[42].

giving information about the vibrational modes of the sample. These frequencies depend on the masses and inter-atomic potentials of the atoms involved, but also crucially on the bond lengths and orientations between the atoms. A number of different vibrational modes are possible - four bond bending modes (twisting, scissoring, wagging and rocking) and two bond stretching modes (symmetric and antisymmetric). Because a bond vibration requires an asymmetric dipole to absorb EM radiation, typically the absorption occurs on the bond between two atoms of different elements, so this technique is excellent for looking at defects in diamond, which without defects would show minimal absorption.

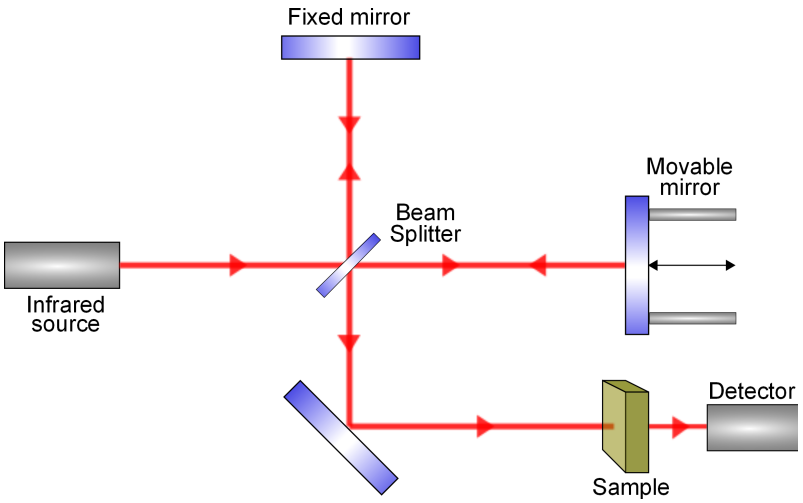

Figure 3.5: Schematic of a typical FTIR setup, where the spectrum of an IR source is measured before and after transmission through a sample, with the absorbed radiation giving information about the vibrational modes of the material. After[44].

Figure 3.5 shows a simplified diagram of a typical FTIR setup, which utilises a Michelson interferometer, which is a cheaper option than using a monochromator and sweeping through the range of frequencies required. Using the Michelson interferometer allows the IR source to use the

full range of frequencies, with Fourier transforms used to decompose the output. The IR beam is directed onto a beam splitter, which reflects the radiation half towards a movable mirror and the other half towards a fixed mirror. Both the fixed and movable mirror reflect the light back towards the beam splitter, where half the light is discarded and the remaining half is recombined and reflected towards the source, but with a difference in path length due to the two paths taken by the light after the first beam is split.

The path difference between the two recombined beams can be varied by moving the movable mirror, leading to deconstructive or constructive interference. By varying the mirror's position a complete beam profile can be determined using Fourier transforms of the recombined beam. When the beam is then passed through the sample, the recorded spectrum with the beam profile of the recombined beam deducted gives the absorption spectrum of the sample, which can be compared to known sample spectra to determine the origins of each absorption peak.

3.7 Low-energy electron diffraction

Low-energy electron diffraction (LEED) uses the diffraction of an electron beam at an angle close to the surface normal of the sample, with energies of 10-200 eV. Using these energies means that the electron energies correspond to De Broglie wavelengths of 1-4 Å and so only the very top atomic layers contribute to the electron diffraction. An example of a LEED experiment is pictured in Figure 3.6.

The electrons are reflected from the surface of the sample being studied onto a fluorescent screen, which is captured by a CCD or photographic plate. If it is assumed that the electron beam is kinematically reflected, then the vector difference $g = k' - k$ between the incoming electron wave-vector k and the reflected wave-vector k' is the crystal surface's reciprocal lattice vector, and from the full two-dimensional diffraction pattern the lattice type of the sample can be determined. The sharper the image, the more well ordered the surface, with blurring in the diffraction pattern spots indicating surface roughness or impurities and defects on the surface.

3.8 Electron Microscopy

Electron microscopes are a common tool in material science and nanoscience, as because they use electrons rather than visible light to image a sample, they can image at a higher magnification than a traditional optical microscope. There are two principle types of electron microscopy in wide use. Scanning electron microscopy (SEM) uses the reflection of electrons from a tightly focused electron beam and is suitable for imaging the surfaces of many conductive samples, whilst transmission electron microscopy (TEM) uses the transmission of electrons *through* a sample and so is only suitable for materials thin enough for electrons to pass through.

3.8.1 Scanning Electron Microscopy

A scanning electron microscope (SEM) follows a similar process to that used in the optical microscope, but with electrons rather than light reflecting off the surface. A standard SEM setup is pictured in Figure 3.7. To prevent arcing and contamination, an SEM sample chamber is pumped

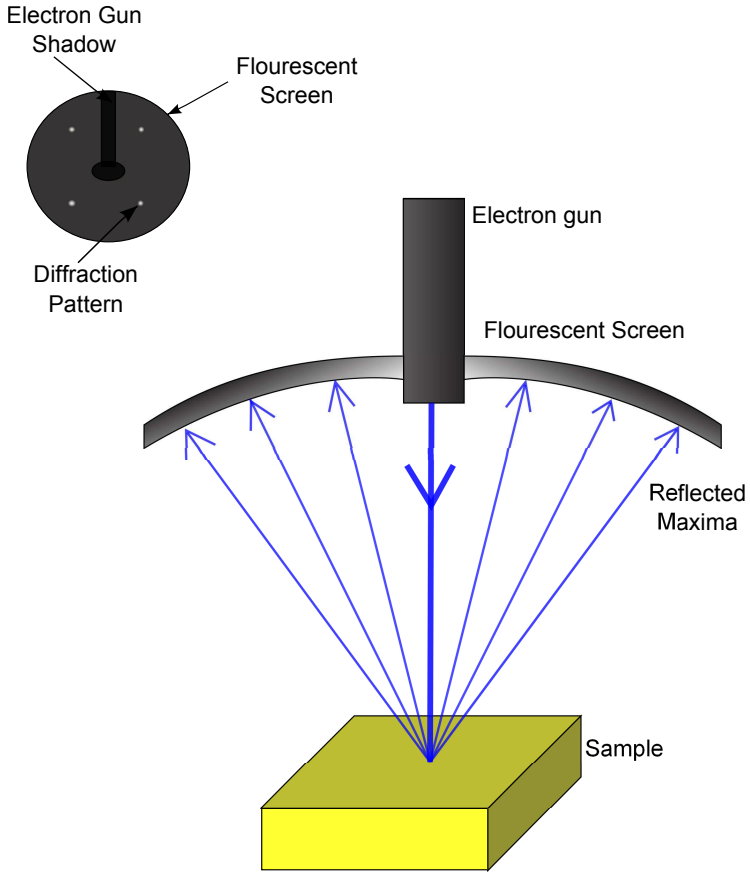

Figure 3.6: Schematic of a typical LEED setup, where the reflection of low energy electrons from an electron gun off a surface onto a fluorescent screen gives information about the crystal lattice structure of the sample. After[44].

to a high vacuum of at least 10^{-6} Torr. Electrons are excited in an electron gun, typically either by thermionic emission from a metal filament or from a field emission source, and accelerated by an electric field to energies of 10-25 k eV. The electron beam is focused onto the sample surface by a series of electrical and magnetic lenses. The electron beam is rastered across the surface, and secondary electrons emitted from ionised atoms in the top surface of the sample are collected and amplified by the detector, resulting in a micrograph showing the surface structure in two dimensions, similar to how a photograph does with light.

As with XPS and UPS, SEM requires a conductive sample, as insulating surfaces suffer from charging effects, where electrons knocked out of the sample by the incoming electron beam are not replaced, leaving a positive charge that distorts the image. Resistive samples can be studied by coating with a thin metal coating, around 10 nm, typically of gold or a platinum/palladium mix.

In addition to the morphological information given by a standard SEM scan, the chemical composition of a surface can be studied using Energy-Dispersive X-ray spectroscopy (EDX), which analyses the X-ray fluorescence given off when the sample is hit by the electron beam of the SEM. The incident beam excites a electron in a lower shell of an atom of the material, and when the hole is replaced by an electron from a higher shell, an X-ray is emitted of a wavelength characteristic of

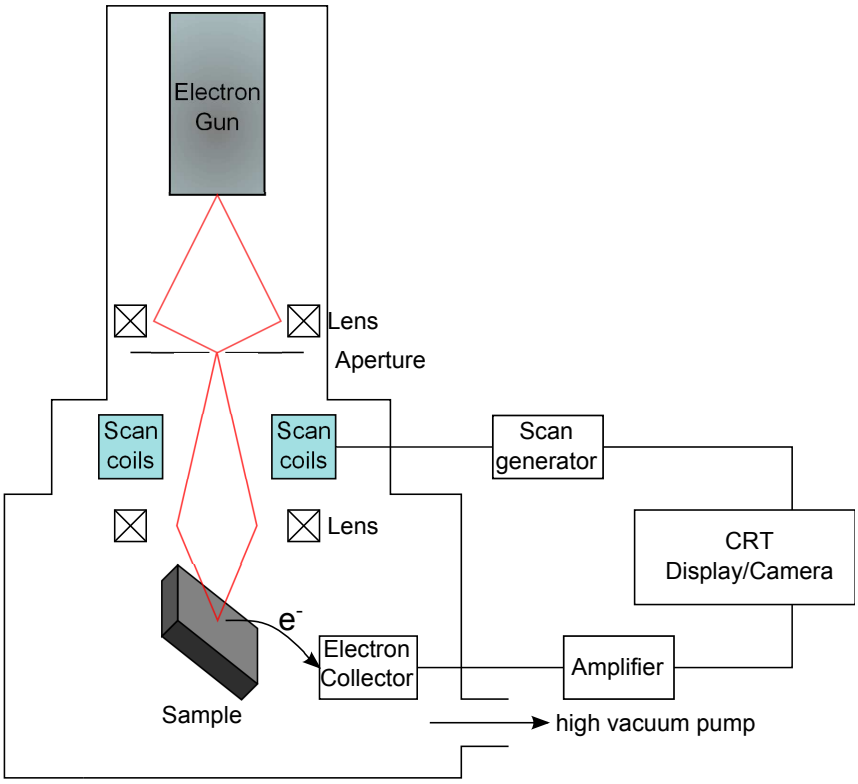

Figure 3.7: Schematic of a typical scanning electron microscope. After [42].

the element. Although this can be useful for atomic identification of the surface, it provides less information about the chemical bonding behaviour of the atoms than XPS, so is less useful for this project.

3.8.2 Transmission Electron Microscopy

Unlike SEM where the electrons reflected from a surface are used to create an image of the material, transmission electron microscopy (TEM) has its detector on the other side of the sample to the emission beam, and the image produced is of the electrons passing through the sample, which as a result is required to be very thin. TEMs are capable of magnification to incredibly high magnifications of as much as a million times or more, given appropriate sample stabilisers and beam optics.

Like the SEM, the TEM uses a tungsten filament or lanthanum hexaboride source to produce the beam of electrons, which is focused by a series of electromagnetic lenses. After passing through the sample, the beam is again focused onto a fluorescent screen and a detector system to record the image, which can be a photographic plate or a CCD detector. A typical layout of a TEM is shown in Figure 3.8.

TEMs have standard sample support 'grids', meshes of copper or other nonreactive metal, with the sample placed on top. For many applications a thin layer of graphite is deposited before the sample to ensure the sample has a support to lie on and is electrically connected to the grid.

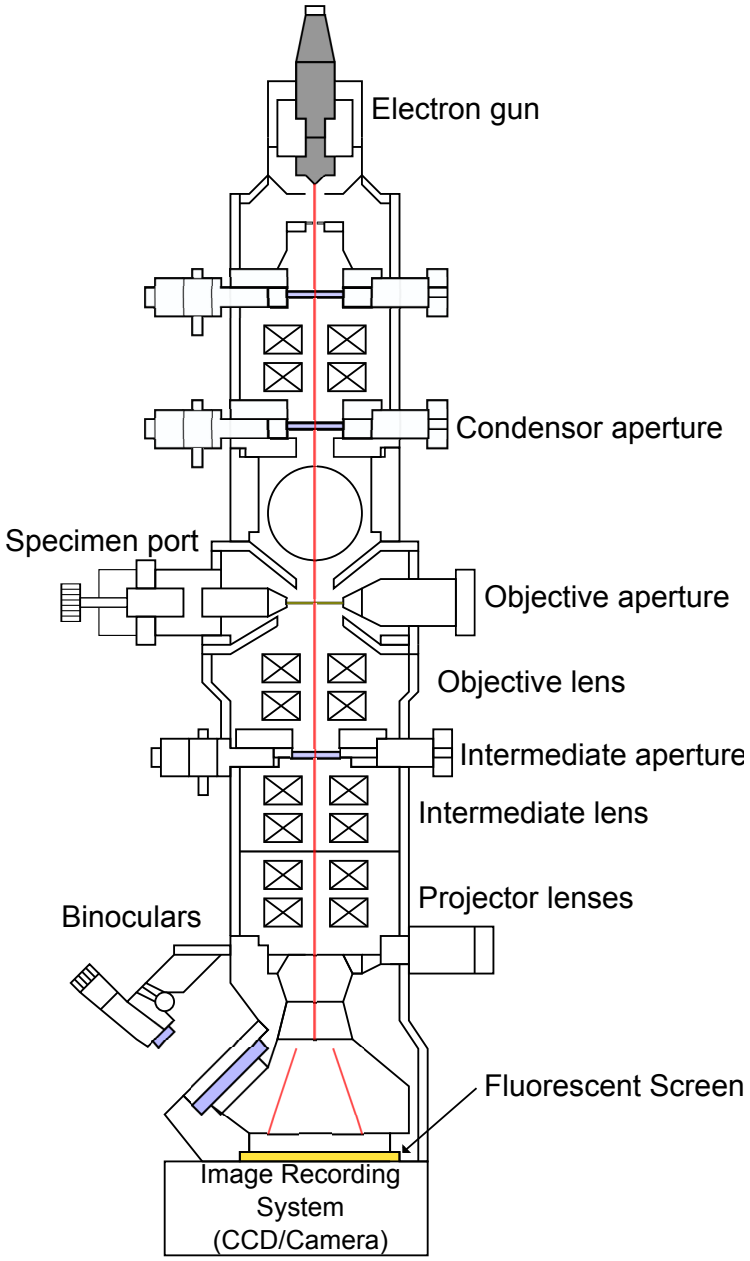

Figure 3.8: Schematic of a typical transmission electron microscope.

Typical sample thicknesses for good quality images are around 100 nm, but studying the edges of many materials of slightly larger dimensions can yield shards and thinner regions for imaging.

Typically images are performed in the 'bright field' imaging mode, where the contrast is adjusted so that the image is bright where there is no sample present and thicker regions of the sample appear dark. Changing the orientation of the sample in the beam can also be used to observe Bragg reflections from the sample, which can give information about the crystal lattice of the sample. When the main beam is not observed but the bright spots from Bragg scattering are, the image is known as a 'dark field' image.

3.8.3 Electron Energy Loss Spectroscopy

Another technique available on some TEM systems is that of electron energy loss spectroscopy (EELS). EELS uses a beam of electrons with a carefully calibrated range of kinetic energy. When the electrons pass through the sample, some will lose energy due to inelastic scattering events such as Cerenkov radiation, inner shell ionisations, plasmon excitations, phonon excitations and band transitions. By measuring the energy of the electron beam after passing through the sample with an electron spectrometer, the energy loss spectrum compared to the part of the beam which didn't lose any energy (the Zero-Loss peak) gives information about the sample.

EELS is seen as a complimentary technique to EDX, as EELS can characterise the chemical bonding and valence and conduction band properties that EDX cannot, as well as EELS being more sensitive to light elements than EDX. EELS is particularly sensitive to elements from carbon to zinc in the periodic table, making it ideal for studying $3d$ transition metals and carbon materials such as diamond. High resolution EELS systems can detect very small amounts of light elements that might otherwise be missed by an X-ray based detection system.

3.9 Chapter Summary

This chapter has given an overview of a variety of characterisation techniques that are useful for the study of diamond and that are mentioned or utilised in the work that follows. Chapter 4 explores the thermionic and field emission behaviour of diamond nanoparticles, and also uses TEM, EELS, XRD and FTIR to begin the characterisation of lithium's interaction with these diamond nanoparticles.

In Chapter 5, the computational techniques explored in the previous chapter are used to calculate the behaviour of lithium at the surface of C(100) and C(111) diamond, and the workfunction and electron affinity calculation methods previously explained are used to explore the electronic structure of the stable configurations.

X-ray photoemission and ultraviolet photoemission form the basis for the investigation in Chapter 6. XPS is used to study the effects on the atomic structure and chemical bonding environments when lithium is added to the hydrogen and oxygen-terminated surface of monocrystalline diamond C(100) substrates, as well as phosphorus-doped C(111) substrates. UPS is used to characterise the valence band structure of these surfaces and calculate the workfunction and electron affinity changes.

Finally, the work in Chapter 7 returns to field emission work, looking at the Li-O surface construction explored in the previous two chapters, as well as looking at the surface conductivity of this surface construction as a potential surface for transistor based devices.

REFERENCES

[1] Becquerel, E. *Ann. Chim. Phys.* **39**(355) (1853).

[2] Elster, J. and Geitel, F. *Ann. Phys. (Leipzig)* **16**(193) (1882).

[3] Jahl, F. *Menlo Park Reminiscences.* Edison Institute, Dearborn MI, (1937).

[4] Redhead, P. *J. Vac. Sci. Technol. A* **16**, 1394–1401 (1998).

[5] Preece, W. *Proc. R. Soc. London* **38**, 219 (1885).

[6] Elster, J. and Geitel, F. *Ann. Phys. (Leipzig)* **31**, 109 (1887).

[7] Thomson, J. *The Electrician* **34**(104) (1897).

[8] Thomson, J. *Philos. Mag.* **48**(547) (1899).

[9] Richardson, O. *Proc. Cambridge Philos. Soc.* **11**, 286 (1901).

[10] Drude, P. *Ann. Phys. (Leipzig)* **1**, 566 (1900).

[11] Riecke, E. *Ann. Phys (Leipzig* **66**, 353 (1898).

[12] Thomson, J. *Applications of Dynamics to Physics and Chemistry*, 296. Macmillan, London (1888).

[13] Fleming, J. *Proc. R. Soc. London* **38**, 219 (1890).

[14] Fleming, J. *U.K. Patent No. 24850, U.S. Patent No 803684* (1905).

[15] Dylla, H. and Corneliussen, S. *J. Vac. Sci. Technol. A* **23**(4), 1244–1251 (2005).

[16] Richardson, O. *Philos. Mag.* **26**, 345 (1913).

[17] Dushman, S. *Phys. Rev.* **5**, 212 (1915).

[18] Modinos, A. *Field, thermionic and secondary electron emission spectroscopy.* Plenum Press, New York, NY, USA, (1984).

[19] Tanner, P., Fraser, D., and Irving, A. *Sci., Meas. Tech., IEE Proc.* **152**(1), 1–6 (2005).

[20] Child, C. *Phys. Rev.* **32**(498) (1911).

[21] Langmuir, I. *Phys. Rev* **2**(450) (1913).

[22] Zavadil, K., King, D., and Ruffner, J. Technical Report SAND99-2982, Sandia National Labs, (1999).

[23] Koeck, F., Nemanich, R., Balasubramaniam, Y., Haenen, K., and Sharp, J. *Diamond Rel. Mater.* **In Press, Accepted Manuscript** (2011).

[24] Kleint, C. *Progress Surf. Sci.* **42**, 101 (1993).

[25] Wood, R. *Phys. Rev.* **5**(1) (1897).

[26] Schottky, W. *Z. Phys* **15**, 51 (1923).

[27] Fowler, R. and Nordheim, L. *Proc. Roy. Soc. series A* **119**(781), 173 (1928).

[28] Nordheim, L. *Phys. Zs.* (7), 177 (1929).

[29] Millikan, R. and Lauritsen, C. *Phys. Rev.* **33**(4) (1929).

[30] Fursey, G. In *Microdevices*, 205 (Kluwer Academic/Plenum Publishers, New York, 2005).

[31] Dolan, W., Dyke, W., and Trolan, J. *Phys. Rev* **91**(5), 1054 (1953).

[32] Dyke, W. and Trolan, J. *Phys. Rev.* **89**(4), 799 (1953).

[33] Charbonnier, F., Barbour, J., and Brewster, J. *Proceedings of the 2nd IEEE Particle Accelerator Conference* **NS-14**, 789 (1967).

[34] Crewe, A., Eggenberger, D., Wall, J., and Welter, L. *Rev. Sci. Instruments* **39**, 576 (1968).

[35] Spindt, C., Holland, C., and Brodie, I. *IEEE Transactions on Electron Devices* **36**(1), 225 (1989).

[36] Jensen, K. *J. Vac. Sci. Tech. B* **21**, 1528 (2003).

[37] Schottky, W. *Phys. Z.* **15**, 872 (1914).

[38] Reinert, F. and Hufner, S. *New J. Phys.* **7**, 97 (2005).

[39] Siegbahn, K., Nordling, C., Fahlman, A., Hamrin, H., Hedman, J., Johansson, G., Bergmark, T., Karlsson, S., Lindgren, J., and Lindberg, B. *Electron Spectroscopy for Chemical Analysis: atomic, Molecular and Solid State Structure Studeis by Means of Electron Spectroscopy.* almquist and Wiksells, Uppsala, (1967).

[40] Nix, R. *An Introduction to Surface Chemistry.* Queen Mary University, London, UK, (2003).

[41] Elliott, S. *The Physics and Chemistry of Solids.* Wiley, Chichester, UK, (1998).

[42] Leeds, S. *Characterisation of the gas-phase environment in a microwave plasma enhanced diamond chemical vapour deposition reactor using molecular beam mass spectrometry.* PhD thesis, University of Bristol, (1999).

[43] Flewitt, P. and Wild, R. *Physical Methods for Materials Characterisation*, chapter 6. IOP Publishing, Bristol (1994).

[44] Sque, S. *A first-principles study on bulk and transfer doping of diamond.* PhD thesis, University of Exeter, (2005).

Red Leader: It didn't go in, just impacted on the surface.

Star Wars: A New Hope(1977)

4

Electron Emission from diamond nanoparticles

4.1 Introduction

Thermionic and field emission devices require a low workfunction material for the collector and emitter surfaces, which can be achieved in diamond either by the use of an n-type donor or a negative electron affinity (or both). Lithium, as a theoretical shallow donor in diamond with predicted activation energy of 0.1 eV,[1] as well as as an alkali metal, could be a potential solution to both these workfunction lowering challenges.

High pressure, high temperature diamond (HPHT) nanopowders are made in large quantities for the industrial tools market and are often found on drill bits and saw blades, as well as for grinding powders and heat sinks. They are commercially available for a few pence a gram and, if they could be successfully processed to obtain a low workfunction, could be used in metal-diamond composites for low cost electron emitters.

In this chapter the processing of 50 nm and 500 nm HPHT diamond nanopowders at high temperatures with lithium salts will be discussed, with characterisation using electron microscopy, FTIR, SIMS and EELS, as well as attempts at measuring the electron emission through both thermal and field excitation.

4.2 HPHT nanoparticles

The Lithiated Diamond (LiD) used for this work is made from commercial High Temperature High Pressure (HTHP) monocrystalline diamond powder. These are relatively cheap to obtain, making them an attractive substrate for large scale electronic systems. The particles are created using a high temperature high pressure process and then graded using sieving techniques to obtain only particles of a certain dimension - in this project samples were used with 50 nm and 500 nm particle size obtained from Microdiamant AG. Both grades were produced by Microdiamant AG using a HPHT method.

The HPHT method is known to introduce nitrogen impurities into the diamond lattice. The particle size distribution in the 500nm grade was determined by a centrifugal particle sizing technique and found to exhibit a peak at 388 nm (half width 0.1324), with 85% of the particles having

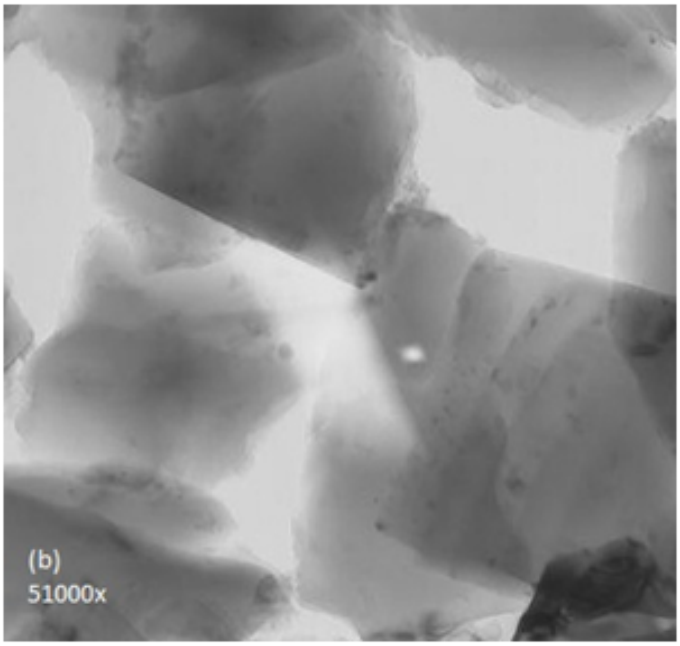

Figure 4.1: Transmission electron microscope image of a random selection of the 500 nm HPHT diamond nanopowders used in this work, showing a wide variety of shapes and edges.

diameters between 300 nm and 500 nm. When observed under transmission electron microscopy as in Figure 4.1, it is clear that this sizing only applies to a minimum of one dimension of the crystal, with a large variety of particle shapes observed, including many which appear to be chips from larger crystals. Due to the relative ease at which diamond fractures along the (111) plane, it is likely that many of the surfaces of these particles are (111) oriented.

Figure 4.2 shows the diamond powder in a scanning electron microscope, after it has been deposited onto a metal substrate. Note as with the TEM image the large variety of crystal sizes and orientation - although at least one dimension is approximately equal to the 500 nm particle sizing, in practice each crystal is very different to the next.

The particles in the powder do not exhibit any non-diamond carbon content as evidenced by UV Raman analysis performed prior to doping. Figure 4.3 shows FTIR spectra for the doped and undoped nanodiamond powders. FTIR spectra of the diamond prior to Li doping confirmed the manufacturer's specification that it has approximately 200 ppm of nitrogen from the HPHT synthesis process and may be expected to see a lower effective workfunction than undoped diamond. The ratio of the 1130 cm^{-1} single substitutional peak to the dip at 2120 cm^{-1} gives a ppm of nitrogen in diamond using the equation[2]:

$$N(ppm) = 137.5(1130\ cm^{-1})/(2120\ cm^{-1}) \tag{4.1}$$

The 1130 cm^{-1} line is related to the C centre, for electrically neutral single substitutional nitrogen atoms in the diamond lattice, compared to the 2120 cm^{-1} line which is used as a representative of the two-phonon region between 1400 and 2700 cm^{-1}, which is invariable for all forms of diamond.[3] Figure 4.3 shows the FTIR spectra for the undoped powder as well as after the reaction

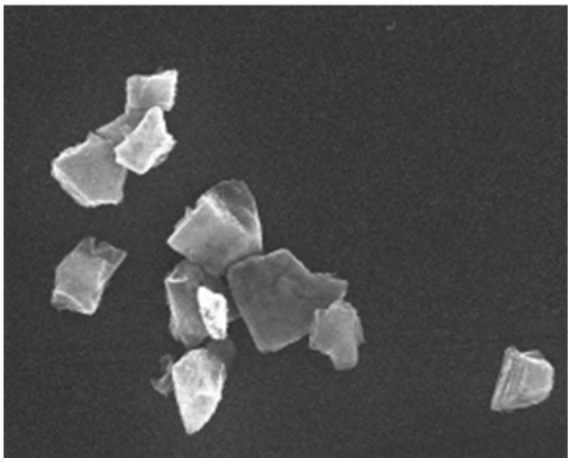

Figure 4.2: A SEM image of the 500 nm HPHT diamond crystals deposited on a metal substrate.

with a lithium salt as described later. Before doping, using equation 4.1 yields a nitrogen content for the as-received HPHT powder of between 160 and 200 ppm for all types of diamond studied according to Equation 4.1. There was no significant difference between the undoped and lithium doped material, and no significant aggregated nitrogen signal (1290 cm^{-1} line).

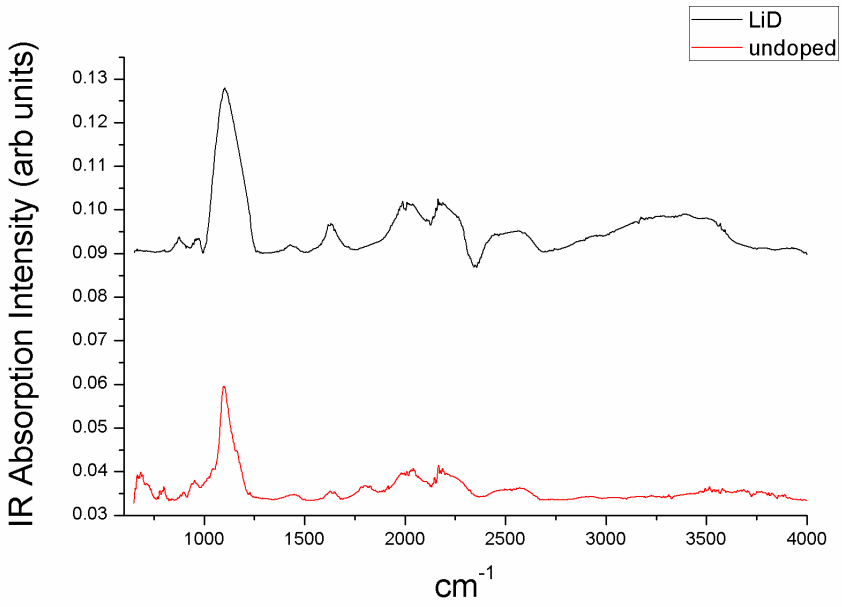

Figure 4.3: FTIR Spectra for undoped nanodiamond powders (red) and Lithiated nanodiamond powders (black)

In summary, the undoped samples are a varied selection of single diamond crystals, with a significant quantity of nitrogen present and a large variation in dimension and surface facet distribution. The next phase of the project was to use lithium salts as an attempt to introduce lithium

into the diamond crystals, but first the emission setup was testing using a commercial barium oxide cathode.

4.3 Thermionic emission testing of commercial BaO cathodes

The thermionic system is pictured in figure 4.4. It consists of a high vacuum chamber evacuated by a turbomolecular pump capable of pressures down to 1×10^{-9} Torr. The chamber is large, with a number of mounting structures allowing numerous different possible configurations. For the thermionic tests, a micrometer stage was installed in the top flange of the chamber, with a ceramic rod allowing any object affixed to the end of the rod to be in electrical isolation from the remainder of the setup. This rod was used to mount the collector. The emitter was mounted from a stand affixed to the bottom of the chamber, again with ceramic offsets to keep the emitter in electrical isolation. Several types of heater including filament and button heaters were able to be affixed to this stand depending on the size of the sample, with the electrical connection through the bottom of the chamber. The sample mounted to the top of the heater is the emitter, and the emitter-collector distance can be varied using the micrometer stage.

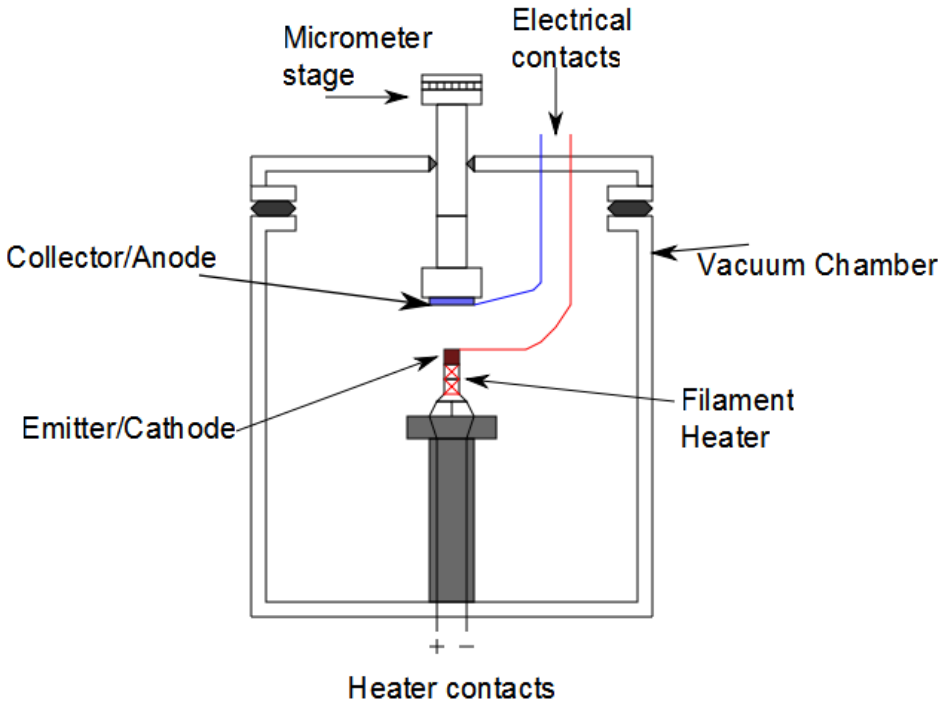

Figure 4.4: Diagram of the vacuum chamber setup used for the thermionic emission experiments.

To calibrate the thermionic emission testing system, a commercial barium oxide cathode made

by Blackburn Microtech was tested against a variety of collector anode materials. BaO cathodes aren't as prevalent as they once were due to the rise of flat panel displays, but until the late 1990s they were widely used in cathode ray tube displays and are still in production for high quality amplifiers. They consist of a small electrically isolated wire filament covered by a nickel cap, with a deposition of barium carbonate powder on top.

The cathode is placed under vacuum and activated using a series of heating steps, during which the $BaCO_3$ decomposes to BaO with carbon dioxide removed from the surface. The cathode can only be used once, as once vacuum is broken the BaO reacts with CO_2 and water vapour in the air and loses performance. When in operation at $800 - 1200$ °C, the cathode operates by the physical transport of charges through the BaO layer - a potential is placed between the nickel base of the cathode and the anode, and barium picks up an electron and takes on a more negative oxidation state at the base of the nickel cap, and this electron is emitted from the cathode. [4]

When the heated filament is run at the current and voltage suggested by the manufacturer with a distance of 250 μm to the anode, the current-voltage behaviour shown in Figure 4.5 follows the relationship predicted by thermionic theory, with the current limited by the space charge, following an exponential increase with increasing voltage up to a saturation after around 20 V of applied voltage. Two different sets of carbon nanotubes were used for the collector, one with rod length of 0.1 μm and the other a much thicker arrangement of 2mm long rods. Although in theory the longer nanotubes should provide a greater surface area for collection and so be a better collector, in practice the 2 mm rods were very tangled and non-aligned, with the top surface more like the surface of graphite than a true array of rods. The 0.1 μm rods were much more aligned and so seemed to give a better current collection enhancement.

Figure 4.6 shows the behaviour of the BaO cathode at a fixed temperature of approximately 1000 °C and an anode voltage of 10V, showing the strong dependence on interelectrode spacing. As before, the shorter 0.1 μm nanotube sample was a better collector likely due to the higher degree of symmetry between the rods, as the 2 mm nanotubes were not aligned and were very tangled. Even with the optimised collector, the current density was very low above spacings of 0.5 mm.

The emitter/collector material has a great effect on the output of the device, as does the collector morphology. Roughening a surface to inhibit electron reflection can increase the devices' current by an order of magnitude or more. Hence small multi-faceted diamonds, either in a CVD film or a metal composite should be lot more effective than a flat diamond sheet. Figure 4.7, shows the emission current at zero field using the same BaO emitter, but a variety of collector materials and morphologies. These included flat and roughened tungsten, zinc oxide nanorods, graphite and the two forms of carbon nanotubes of different lengths used in the previous figures, clearly showing the advantage of using a collector with high aspect ratio. Both sets of nanotubes were grown on silicon by other research groups.

The thermionic emission results from the commercial cathode show the importance of space charge in limiting the current output of an emitter - without either applying a significant voltage between the electrodes (which will be a significant power drain in an energy conversion device) or using a very small electrode gap (something which presents significant engineering challenges, especially as cathode area is increased), the current densities even on a mass-produced device are incredibly small, fractions of a $\mu A/cm^2$. In a device which simply requires high energy electrons for other purposes such as a cathode ray tube or X-ray tube can use input power to overcome the

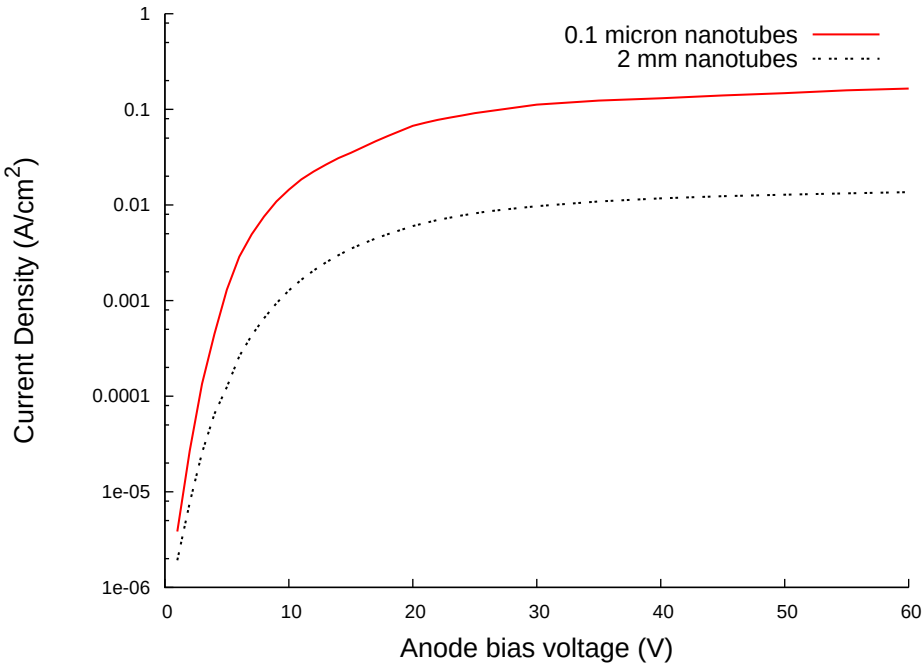

Figure 4.5: Typical Emission current against voltage for the BaO cathode for two different carbon nanotube collectors at an electrode-spacing of 250 μm. The current is plotted logarithmically showing the exponential thermionic saturation curve.

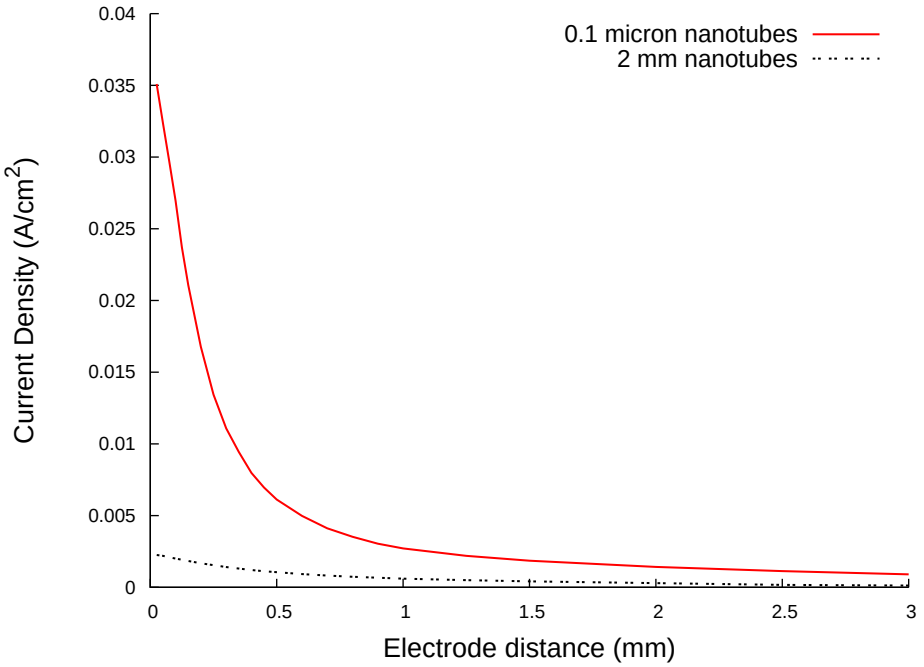

Figure 4.6: Typical emission current versus electrode spacing curve for the BaO cathode with a fixed anode voltage of 10 V.

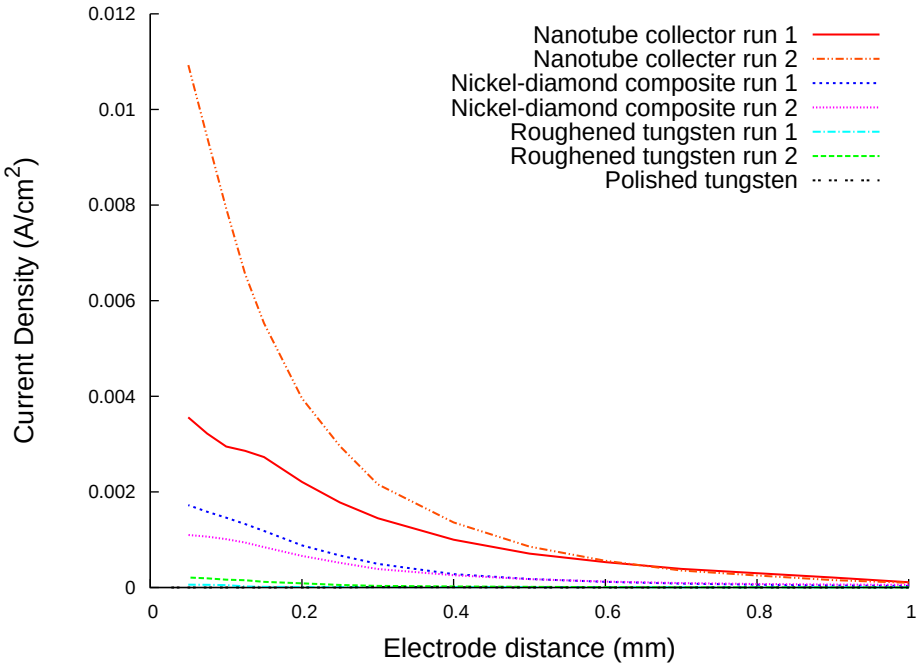

Figure 4.7: Graph of emission current against electrode spacing for varying collector materials and morphologies using the BaO cathode with no field applied to the anode.

space charge, but for an energy conversion device, even an excellent diamond electron emitter may struggle to overcome these engineering challenges.

4.4 Thermionic emission testing of lithiated 500 nm diamond nanopowders

Using lithium hydride or lithium nitride as a lithium precursor, 500 nm and 50 nm graded monocrystalline nanodiamonds were lithium doped at elevated temperatures in a low ambient of either argon or nitrogen gas.

Work initially concentrated on characterising existing batches of 500nm nanodiamond, doped by Dr. Neil Fox using a variety of lithium salts at high temperature, in a low pressure of ambient gas. Lithium hydride (LiH) and lithium nitride (Li_3N) were the principle candidates for the former, while both nitrogen gas and argon gas were used for the latter. The decomposition of lithium hydride and lithium nitride at high temperature in lithium and assorted by-products is exothermic and the hypothesis was the high energies might help the lithium diffuse into the diamond lattice giving a doping effect. Typically a 1:1 ratio between diamond and lithium compound powders were used, and the pressure was around 1 Torr. Temperatures varied between 800 and 1400°C.

Emission studies on the diamond initially focused on small pellets of the 500nm nanodiamond pressed into nickel tubes, which were heated by filament. There were two main types of powder-pressed devices - those in which the nickel cap of a Microtech cathode was removed and replaced with a diamond powder plug, and those where a pressed pellet was affixed using silver paste to

the top surface of a cathode with the BaO removed by acid-cleaning. The diamond emitter was separated from a graphite anode by a gap of $250 - 1000$ μm, with a voltage applied across the gap to assist emission.

Following lithiation the samples were milled to form a free-flowing powder and pressed into discs approximately 1 mm thick and 2 mm in diameter. Each disc was fitted into the end of a thin-walled nickel tube with an electrically isolated radiative heater. The disc was heated to in excess of 600 °C to de-gas the LiD sample and pumped to a base pressure of 5×10^{-7} Torr in an oil-free high vacuum chamber. Electron emission measurements were performed using a stainless steel plate as anode-collector, mounted on a micrometer stage to allow variable separation of the cathode and anode. The temperature of the LiD disc was monitored using a Minolta-LAND Cyclops 52 optical pyrometer. The emission current versus applied voltage (I-V) measurements were made using a Keithley 2400LV source meter with a range of 0-21 V and a maximum current of 105 μA. A 100 Ω load resistor was placed in series with the source meter to prevent arcing damage to the measurement equipment. A graphite block was used as a collector.

Numerous issues with the emission setup were found, including the discovery that the high voltage system used to characterise the emission was severely limited by the surge protection resistance. Later refinements of this method found workfunctions for the material in the range $0.8-2.2$ eV, although the Richardson-Dushman approach to finding the workfunction has a number of limitations and large uncertainties,[5] so these numbers should be approached with care. Due to the need for a small field across the electrodes to overcome space-charge, the interpretation of a Schottky plot ($\sqrt{E}$ vs $\ln j$) is used to find the zero field current.

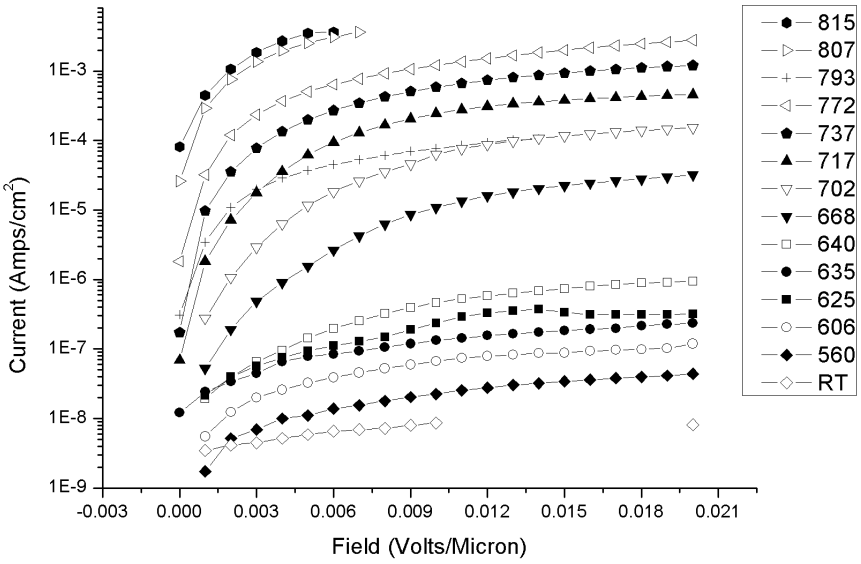

Figure 4.8: An example thermionic emission plot from the lithiated diamond using a graphite collector, showing turnon around 550 °C

Figure 4.8 represents thermionic emission curves for the lithiated material. Emission becomes significant at a cathode temperature of 530 °C. Towards zero field the emission current is limited by

the space-charge effect. By increasing the applied electric field to mitigate space-charge, emission increases until at around 0.005 V/μm the emission becomes saturated. A sustained progression of higher emission at lower field strengths is seen with increasing temperature. The exposed area of a single diamond pellet is approximately 0.029 cm^2, giving current densities up to 3.64 mA/cm^2.

To determine the workfunction of the material, the saturated part of the emission curves were extrapolated as straight-line Schottky plots to eliminate the field-dependent term and find the current intercepts for zero field.[6] These are plotted in figure 4.9, as a Richardson-Dushman graph. For comparison, a sample of undoped (and nominally hydrogen-terminated) diamond material was tested and yielded a workfunction of (2.40 $\pm$ 0.08) eV, and an emission current almost three orders of magnitude less than LiD samples.

In addition the log-log Richardson-Dushman plot (Figure 4.9) is very susceptible to small changes, especially in emitter temperature or surface composition, which can dramatically impact the calculations of both the workfunction ϕ and the effective Richardson constant A^*.

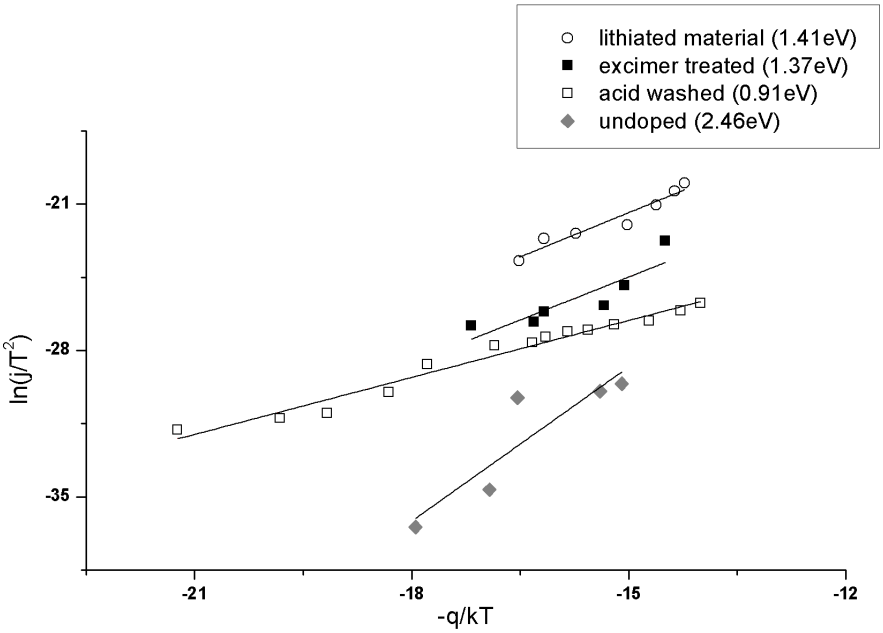

Figure 4.9: Richardson-Dushman plots for the lithiated nanodiamond powders. Note that the log-log plot gives any uncertainty in the measurements large weighting on the resultant gradient used to calculate workfunctions.

The lithiated material showed a workfunction of (1.41 $\pm$ 0.05) eV. The undoped material has a much less stable emission current and a workfunction of (2.46 $\pm$ 0.08) eV. In addition to the as-reacted material, a batch of the doped nanopowder was washed in a fuming nitric acid at a temperature of 200°C, followed by water washing in a Buchner funnel. The lithiated material which had been acid washed had a lower workfunction of (0.91 $\pm$ 0.09) eV, albeit with lower maximum current. The maximum observed current from the lithiated material was 100 μA at a collector voltage of 21 V and an electrode spacing of 300 μm. The macroscopic current density, calculated as the emission current divided by the exposed pellet area, amounts to 3.64 mA/cm^2. However, since our material has a high resistivity, it is likely that only a very small fraction of the

nanodiamonds actually emitted during testing, suggesting actual emission site current densities orders of magnitude higher. The emission current for the acid washed material was several orders of magnitude smaller than the unwashed material, suggesting a reduction in the number of emission sites.

In summary, the lithiation of nanocrystalline diamond particles has been shown to successfully generate a low workfunction material. Whether doping of the diamond or surface states (or a combination of both) dominate the emission behaviour is at present uncertain. The sensitive dependence on the surface treatment suggests that surface complexes play a role, and in particular the speculation that Li-O surface complexes might contribute to the very low workfunction seen in the acid-washed material, following the suggestion of Cs-O complexes causing an NEA effect on diamond.[7;8]

4.4.1 Field Emission from diamond nanoparticles

In addition to the thermionic emission measurements, tests were made for the field emission properties of the lithiated diamond powders. The field emission tests were performed in the same chamber as the thermionic emission, at 1×10^{-8} Torr. A voltage was applied using a Brandenburg high voltage supply, capable of producing 0-10 kV between a similarly doped grade of diamond and a YAG screen anode, coated in a conductive phosphor. The current was measured using a Keithley 2000 multimeter protected from arcing damage by a 200 MΩ resistor in series with the emission circuit.

Figure 4.10 shows a typical field emission IV curve for the lithiated material, with a low turn-on of 1 V/μm. Most interesting is the linear Fowler-Nordheim behaviour seen in the inset. Although linearity is expected in Fowler-Nordheim theory, non-metallic emitters such as carbon nanotubes often exhibit significant curvature.[9] Such curvature has been attributed to resistivity of the emitter[10] and the absence here may therefore indicate low resistivity between the electrical contact site and the emission site on the nanodiamond.

4.4.2 Summary of the electron emission studies on lithiated nanodiamond powders

In conclusion to the emission device testing of HPHT diamond nanopowders before and after reacting with lithium salts, it does appear that there is some form of enhancement effect occurring after the lithiation step, with increased current density, lowered turn-ons, and lower effective workfunctions for both thermionic and field emission.

Attempts were made to scale up the size of the emitter used, using a variety of CVD films and metal-diamond composites produced using electrodeposition of metal between the HPHT nanoparticles. These were more successful for field emission where the high field strength means large gaps can be used, and turn-ons of 2-10 V/μm were observed for samples up to an inch squared in size, although the distribution of charge on the surface when observed under the fluorescent YAG screen was very uneven with generally only a few isolated spots on the surface lighting up. It seems like further characterisation is needed to ensure an even effect of whatever is causing the enhancement.

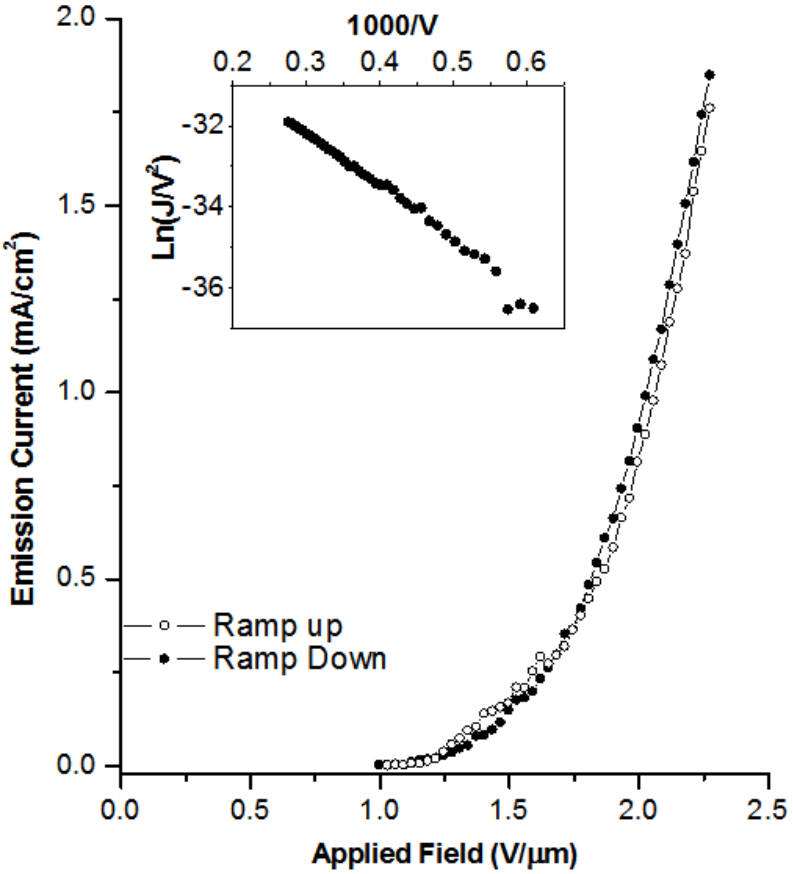

Figure 4.10: Field emission results for lithiated diamond, showing a low threshold for emission of 0.2 V/μm. A Fowler-Nordheim plot is shown inset displaying strong field emission behaviour.

Larger scale thermionic testing proved difficult to achieve, partially for the same need for further reliability and understanding of the lithiation process, but primarily due to the difficulty in achieving a small enough interelectrode space at high temperature to see significant emission current due to the space charge effect. The issue is that without an interelectrode gas (which causes heat distribution problems where the collector reaches equilibrium with the emitter and the voltage drops) or high fields (which uses substantial power and isn't suitable for an energy conversion device), it is difficult to achieve significant current densities without a very small gap of less than 10-20 μm. The engineering challenges of achieving such a spacing have proved very difficult - using a micrometer stage to set the anode above the emitter surface had issues due to the thermal expansion of the heater being larger than the interelectrode gap, whilst attempts to use quartz spacers had problems with the high temperatures on the emitter surface.

Perhaps the best way to get around this space charge problem in a working device is to use additional excitation to the electrons in the emitter and the interelectrode gap, most notably through photoemission. Recently it was reported that gallium nitride devices showed photon-enhanced thermionic emission by the combination of quantum and thermal processes,[11] and this has recently begun to be explored on nitrogen-doped diamond films.[12] By using an emitter that is heated by solar radiation but also allows photons to enhance or add to this emission, it may be possible to avoid this space-charge limit. Regardless of the possible engineering outcomes, the work in this section shows that although there are some promising signs that lithium causes an enhancement in electron emission from diamond, much more work is needed to characterise the cause of this change.

4.5 Characterisation of the lithiated diamond nanoparticles

The previous results in this chapter showed that reacting HPHT nanodiamond powders with lithium salts seemed to produce an improvement in the emission properties of the powders when studied in thermionic and field emission tests. Acid washing following the lithiation step improved the emission properties further, with higher current densities and a lower turn-on.

However the improvement in emission properties with lithiation and acid washing was not predictable or reliable, with some samples performing better than others but no real trend linking this performance difference discovered. Following these early emission results, more work was required to characterise the surface and bulk properties of the diamond nanopowders to determine exactly what effect (if any) the lithium was having to cause such changes in electron emission profile.

The nanodiamond powders were studied via transmission electron microscopy (TEM) before doping, after doping and after a number of different washing techniques. Before dopants were added, the diamond studied was monocrystalline. After lithiation the diamond is seen to be coated in a thick grey particulate, only some of which was removed by filtering with cold water. Figure 4.11 compares the diamond nanoparticles before and after doping, and after doping followed by an acid wash.

Figure 4.12 shows the diffraction pattern from the nanodiamond powder after lithium doping. Analysis of the LiD material by electron diffraction gave a ring pattern for the particulate with a lattice spacing of 4.02 Å, consistent with theoretical values for the lithium hydride precursor

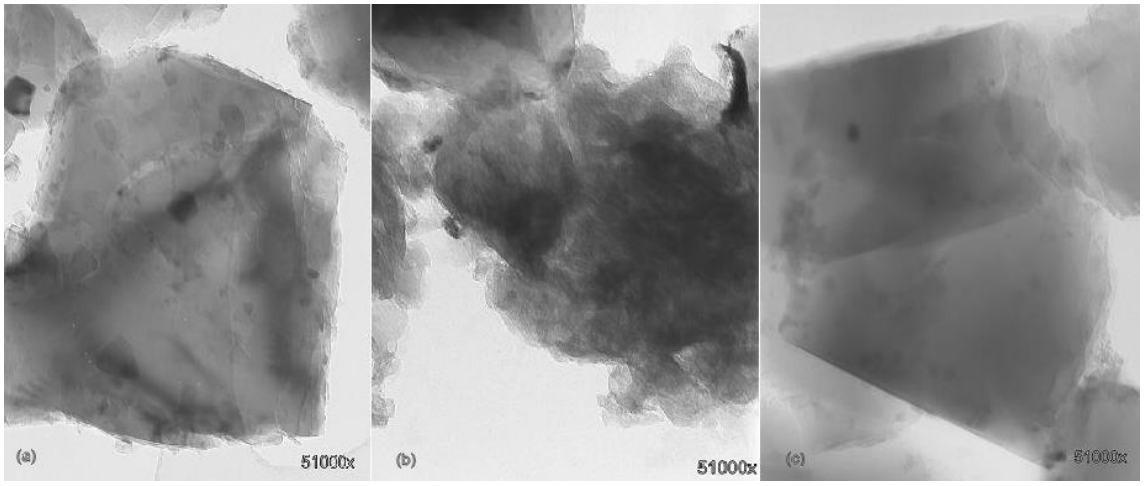

Figure 4.11: TEM images of (a) undoped diamond and (b) lithiated diamond after indiffusion technique and (c) after indiffusion followed by washing with fuming aqua regia. Precursor materials from the doping process were removed by the acid washing technique to reveal pure single crystal diamond particles.

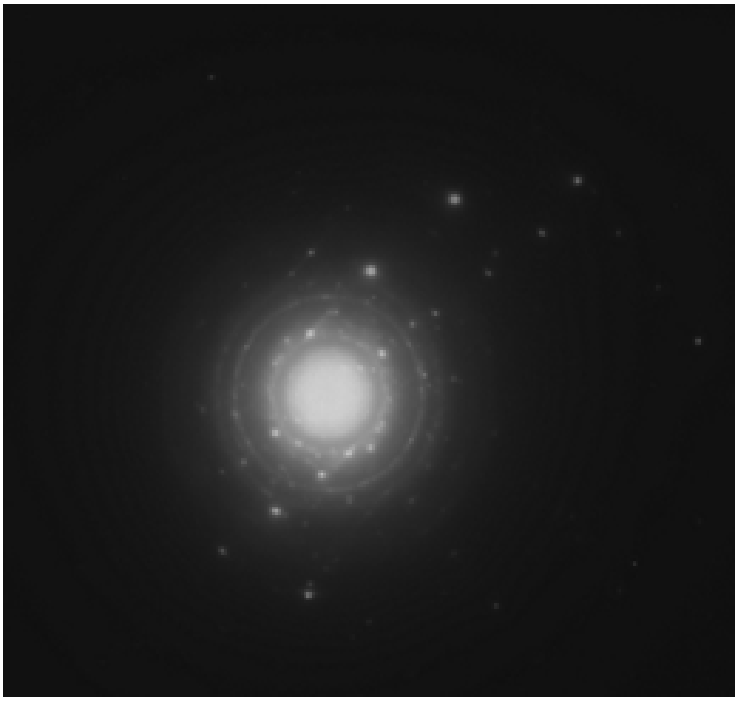

Figure 4.12: Electron diffraction pattern from the lithiated nanodiamond powder in TEM. The lattice spacing of the ring pattern is consistent with lithium hydride.

material.[13] After a 40 minute washing in fuming aqua regia (200°C), this surface coating of LiH was removed, leaving a surface resembling that of the original material.

Secondary ion mass spectroscopy (SIMS) profiling of shards of the 500 nm particles using a gallium source SIMS system showed a doping level of 6×10^{18} cm^{-3} Li in the single crystal diamond

particles. To clarify the doping behaviour on different facets, single crystal HPHT diamond squares made by Element Six were also doped using the same lithium hydride process to determine the effect of lithiation on large surfaces. The crystals were $(2.5 \times 2.5 \times 0.5)$ mm (100) oriented squares, polished to less than 10 nm roughness. Figure 4.13 shows the depth profiling of the lithium doped C(100) sample.

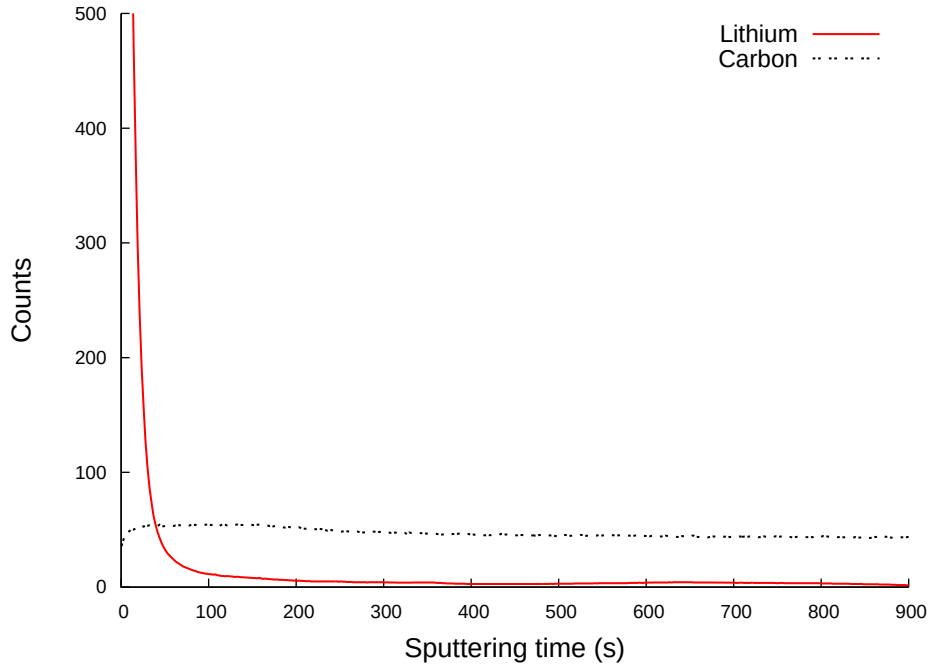

Figure 4.13: SIMS depth profiles for lithium and carbon signals on lithium doped single crystal squares with (100) faces. The vast majority of lithium is within the first 5 nm of diamond using this method.

The SIMS profiling of the single crystal C(100) squares show a large quantity of the lithium is found close to the surface, with a thermal diffusion tail. The large size of the crystal may be disadvantageous to lithium incorporation compared to the high surface area of the 50 nm and 500 nm diamond powders, which showed much more vigorous activity during doping. The lithium diffusion constant in diamond is high, at $D_{Li}(T)=2\times10^{-10}\exp(-0.9eV/kT)cm^2s^{-1}$.[14]. The experimental activation energy for diffusion has been found to be 0.9±0.3 eV, in agreement with the theoretical literature value of 0.85 eV.

Figure 4.14 shows a high resolution TEM image of the edge of a diamond nanoparticle, showing a polycrystalline layer of material on the very edge of the sample even after acid treatment. It is unclear from these images whether this is some remaining lithium salt as observed in the previous TEM images, or a change in the diamond surface as a result of the reaction with LiH at temperature. To try and establish the content, electron energy loss spectroscopy (EELS) was performed on one of these polycrystalline regions.

Figure 4.15 shows the Electron Energy Loss spectra from a shard of the nanodiamond powder after lithiation as viewed in the previous TEM image, comparing the bulk and edge spectra. It is difficult to interpret as the electron energy loss peak for lithium in the 20-40 eV region is very close

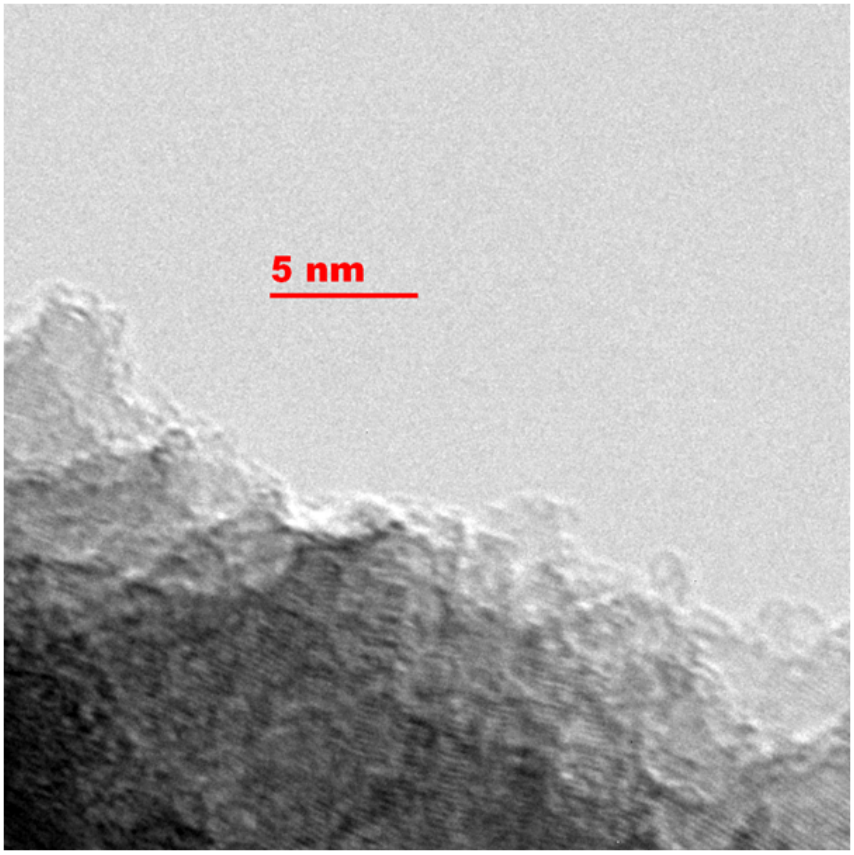

Figure 4.14: High resolution TEM image of the edge of a lithiated nanodiamond, showing a polycrystalline region on the surface which may be leftover salt or a reaction product between the diamond and lithium salt at temperature.

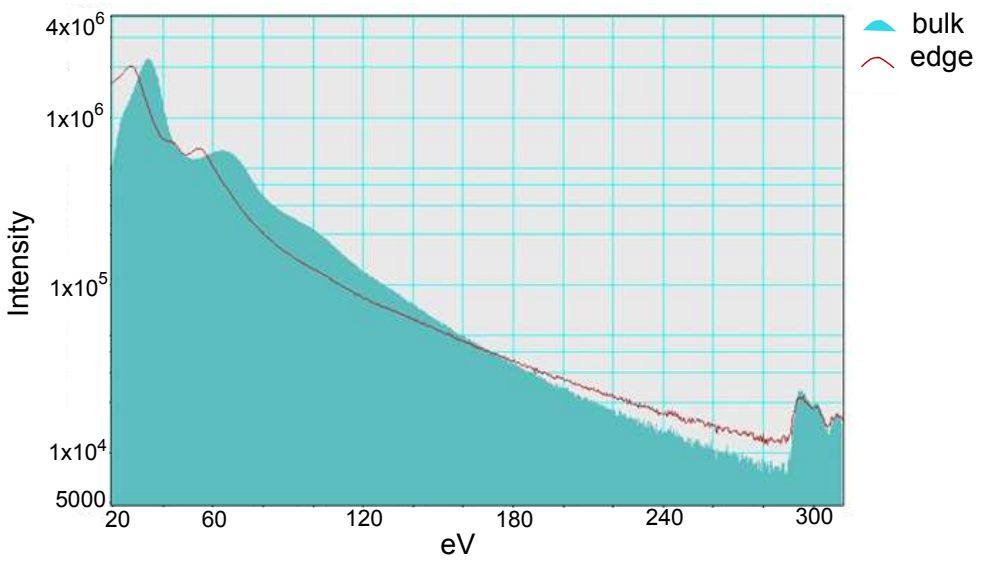

Figure 4.15: Electron Energy Loss Spectroscopy spectra for the edge of one of the 500nm nanodiamond powder crystals, showing in blue the bulk and in red the edge spectra. The additional bump near 50 eV maybe characteristic of lithium, but could be due to the second surface plasmon of diamond.

to the expected second bulk plasmon for diamond. It is probable there is lithium on the surface, but without studying the material on thinner diamond particles to minimise plasmon effects and with a higher resolution instrument, it is difficult to be sure exactly what the composition of this surface layer is.

In summary, characterisation of the HPHT diamond nanoparticles has been attempted using TEM, electron diffraction, FTIR, EELS and SIMS. Before doping, the as-received material is principally single crystal when observed in TEM, and has a nitrogen content of around 150-200 ppm according to FTIR. Samples were reacted at high temperatures with lithium hydride in a low ambient pressure of nitrogen and further study was performed.

TEM studies show that immediately after reaction with lithium salts, large amounts of the reactant remain, with electron diffraction patterns confirming that LiH is the principle constituent of the polycrystalline substance observed on the nanodiamond crystals. After water washing, some of this material is removed, and the surface returns to its single crystal appearance after acid washing in fuming nitric acid. On observation in a higher resolution TEM instrument, some very fine polycrystalline coatings are observable on some facets of the acid washed material, but it is unclear whether this is some reactant remaining on the surface or a reaction between the lithium salt and the diamond surface, perhaps a graphitisation or carbide forming layer.

Some lithium appears to be present using EELS in these regions, but the signal is close to the second plasmon for diamond and the result is uncertain. The difficulty in characterising the nanodiamond particles and the random nature of each crystal and facet make it difficult to conclude much about the surface structure after the lithium treatment and it is suggested that more careful study of the interaction between lithium and the principle facets of diamond are required, both through computational calculations and precise characterisation of controllable single crystal

substrates.

There are two principle unanswered questions - first, if lithium is interacting with the diamond surface, what is the chemical environment and bonding structure? Secondly, if it is changing the surface termination of the diamond, what effect does this have on the surface band bending and energy levels of the diamond? Both these questions can be answered computationally, and experimentally can be investigated primarily by probing of the surface atoms and their core and valence electrons using photoemission spectroscopy. This will form the subject of the work presented in the subsequent chapters of this thesis.

4.6 Conclusion

In conclusion, emission studies have been inconclusive about the success and lifetime of doping, particularly as insufficient understanding of where and how the lithium is active means any successful batches are difficult to optimise. More thorough characterisation of effects of lithium doping is vital to move forward. A probable lack of conduction within the diamond nanoparticles makes large thermionic or field emission currents unlikely. Current doping techniques do not appear to successfully n-type dope the material and even if a large NEA is created on the surface, few charges may be available for emission.

Reliability of thermionic testing stage has been improved substantially on initial designs but satisfactory consistent electrode spacing remains elusive. All electrode designs to date are too rough in surface profile to allow satisfactory small gap devices. Without clear signs of a negative electron affinity (NEA) small gap devices remain only reliable way to overcome space charge. In addition, Richardson-Dushman analysis of thermionic data is not sufficiently accurate for reliable workfunction claims. Large uncertainties in both ϕ and A^* can result from small variation in emission current and temperature. Likewise for field emission, the difficulty in determining the field enhancement factor for such widely varying surfaces makes determination of the workfunction difficult. Nevertheless, there does seem to be an enhancement of electron emission performance following the lithiation step and further assessment is warranted.

Characterisation of the diamond nanopowders ran into similar difficulties. The small size of the nanopowders and the random nature of the facets and orientation meant that it was difficult to assess the general effect of the lithiation process. SIMS data on single crystal diamond shows that the lithiation process is almost certainly not causing a significant bulk n-type doping effect, and that the vast majority of the lithium detected is confined to the first 5 nm of the surface, not much more than the RMS roughness of the single crystal.

This suggests that any improvement of the emission properties is predominantly a surface-enhancement effect, perhaps the formation of a negative electron affinity, as lithium is an alkali metal similar to caesium, which has been observed to have an NEA-inducing effect on diamond [8]. The subsequent improvement in effective workfunction after acid washing may suggest oxygen-termination on the surface is also important, or it may simply be removing more surface contaminants to allow higher emission site density.

After the difficulty in assessing the potential of lithiated diamond nanopowders precisely, it was decided that a more careful study of the interaction between lithium and isolated single-crystal diamond facets was required. This proceeded down two parallel routes, detailed in the following

two chapters - firstly, the computational modelling using density functional theory of the stability, electronic and atomic structure of single lithium atoms on the bare and oxygenated C(100) and C(111) diamond surfaces, and secondly the characterisation using photoemission spectroscopy of the surface of single crystal diamond substrates before and after the addition of atomic lithium.

REFERENCES

[1] Kajihara, S., Antonelli, A., Bernholc, J., and Car, R. *Physical Rev. Lett.* **66**(15), 20102013 (1991).

[2] Zhang, Y., Zang, C., Ma, H., Liang, Z., Zhou, L., Li, S., and Jia, X. *Diamond and Related Materials* **17**(2), 209 – 211 (2008).

[3] Kanda, H., Akaishi, M., and Yamoaka, S. *Diamond Rel. Mater* **8**, 1441 (1999).

[4] Zavadil, K., King, D., and Ruffner, J. Technical Report SAND99-2982, Sandia National Labs, (1999).

[5] Marshall, A. *Surface Science* **517**(1-3), 186–206 (2002).

[6] Herring, C. and Nichols, M. *Reviews of Modern Physics* (1949).

[7] Loh, K. P., Foord, J. S., Egdell, R. G., and Jackman, R. B. *Diamond and Related Materials* **6**(5-7), 874 – 878 (1997).

[8] Geis, M., Twichell, J., Macaulay, J., and Okano, K. *Applied Physics Letters* **67**(9), 1328 (1995).

[9] Jensen, K. *Theory of Field Emission*, 33–104. John Wiley and Sons, Inc. (2002).

[10] Minoux, E., Groening, O., Teo, K., Dalal, S. H., Gangloff, L., Schnell, J., Hudanski, L., Bu, I., Vincent, P., Legagneux, P., Amaratunga, G., and Milne, W. *Nano Letters* **5**(11), 2135–2138 (2005).

[11] Schwede, J., Bargatin, I., Riley, D., Hardin, B., Rosenthal, S., Sun, Y., Schmitt, F., Pianetta, P., Howe, R., Shen, Z.-X., and Melosh, N. *Nature Materials* **9**, 762 (2010).

[12] Sun, T., Koeck, F., and Nemanich, R. *Bulletin of the American Physical Society* **56**(1) (2011).

[13] Vidal, J. P. and Vidal-Valat, G. *Acta Crystallographica Section B* **42**(2), 131–137 Apr (1986).

[14] te Nijenhuis, J., Cao, G. Z., Smits, P., vanEnckevort, W., Giling, L., Alkemade, P., Nesladek, M., and Remes, Z. *Diamond Relat. Mater.* **6**, 1726 (1997).

David Lightman: [typing] What is the primary goal?
Computer: You should know, Professor. You programmed me.
David Lightman: Oh, come on.
David Lightman: [typing] What is the primary goal?
Computer: To win the game.

Wargames (1983)

5 Computational studies of Li on diamond

5.1 Diamond surfaces

5.1.1 Introduction - the main surfaces of diamond

Under normal growth conditions, the surface of a diamond crystal will become dominated by three principle planes - the (100) plane, the (111) plane and the (110) plane, with a small percentage of the (113) plane. Figure 5.1 shows the growth rate of the planes for homoepitaxial CVD diamond with different methane concentrations. The (100) and (111) planes are the slowest to grow [1] so are the most likely to remain, whilst other faster growth planes grow quickly out of a crystal. The (111) plane is the natural cleavage plane for a break in a diamond crystal, which is an additional reason for its predominance.

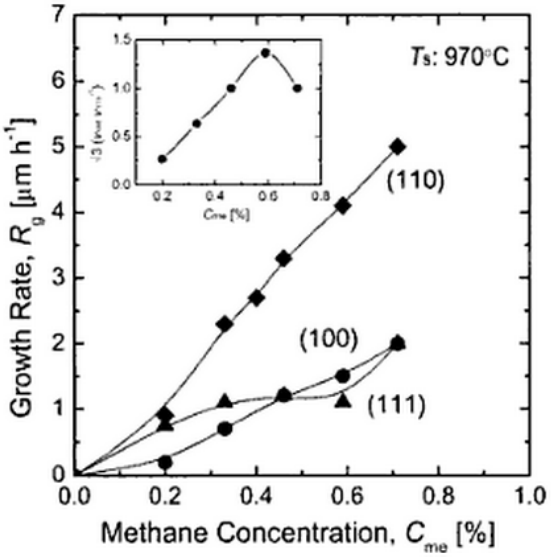

Figure 5.1: Graph showing the growth rate of homoepitaxial diamond films with methane concentration for different crystal orientations. [1]

The α-parameter is often used to determine the shape of CVD single crystals.[2] This parameter is defined as: $\alpha = \sqrt{3}\frac{v_{100}}{v_{111}}$ where v_{100} and v_{111} are the growth velocities in the (100) and (111) directions respectively. In single crystal diamond, alpha varies between 1 for cubes to 3 for octahedra, whereas in polycrystalline films, careful control of alpha through growth gases and temperatures can determine the predominate surfaces grown. By comparison, the beta-parameter relating the ratio of the (111) to the (110) and the gamma-parameter concerning the ratio of (110) to (100) are much smaller and the (110) surface is less common than the (100). In general, the beta and gamma parameters are much smaller than the alpha parameter and so the alpha parameter is the most important factor for determining the structure of the growth surface.

5.1.2 C(100) bare surface

The clean C(100) surface has two dangling bonds per unterminated surface carbon atom, compared to one dangling bond for the (110) and (111) surfaces. To minimise the surface free energy, in the absence of any suitable terminating species the clean surface experiences a reconstruction where the surface carbon atoms dimerise to form a π-bonded surface structure, which gives rise to a (2×1) symmetry in the clean LEED pattern. Homoepitaxial CVD growth on the C(100) surface of diamond can produce surface growth of near atomic flatness,[3] making it an attractive surface for surface experiment and simulation. C(100) diamond growth has showed a lower defect concentration using atomic force microscopy,[4] scanning tunnelling microscopy[5] and scanning electron microscopy.[6]

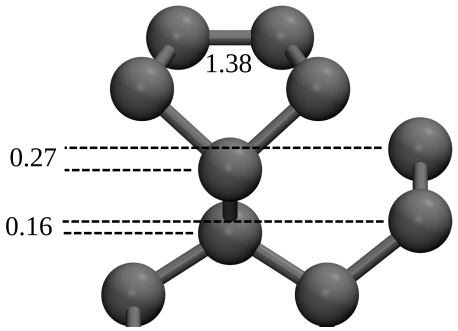

Figure 5.2: The optimized structure for the clean reconstructed C(100) surface.

Figure 5.2 shows the structure of the C(100) surface after reconstruction to the (2×1) structure. The C-C dimer for the clean surface has been calculated using *ab initio* methods to have a bond length of around 1.36 Å, slightly larger than the 1.34 Å C-C double bond length in molecules, but significantly shorter than the 1.54 Å bond length for a single-bonded C-C bond, indicating that the C-C dimer bond on the C(100) surface is intermediate between the two, but closer to a double-bond character.[7] The reconstruction of the surface dimer contracts the first interplanar spacing by 24% when compared to the bulk interplanar distance.

The monohydride C(100)-(2×1):H surface is more energetically favourable than the clean surface. The dimer C-C bond has been calculated to be longer at 1.62 Å than that of the bulk diamond bond length, and the C-H bond length is 1.18 Å with a tilt of around 24° from the neighbouring C-H bond on the next carbon in the dimer. The increase in the C-C dimer length

from 1.36 Å to 1.62 Å indicates a transfer of charge from the double-bond character C-C bond to the C-H bond, with more single-bonded C-C character resulting. The hydrogenated C(100) surface sees only a 5% contraction of the first interplanar spacing compared to the bulk.

5.1.3 C(111) bare surface

The unreconstructed C(111) surface has a (1×1) configuration, but due to the dangling orbitals of the surface carbons the (1×1) construction is not stable and the lowest energy clean surface is the Pandey chain $C(111) - (2 \times 1)$ reconstruction.[8] In the chain model the surface dimerises so that the dangling orbitals are closer to their nearest neighbours and so have a stronger interaction, leading to π-bonds in the first upper two layers of the surface. Reconstruction from the ideal (111)-(1×1) bulk terminated structure to the $(111) - (2 \times 1)$ Pandey chain reconstruction has been observed at annealing temperatures above 1000 °C.[9;10] The clean reconstructed C(111)-(2×1) Pandey chain surface is shown in figure 5.3.

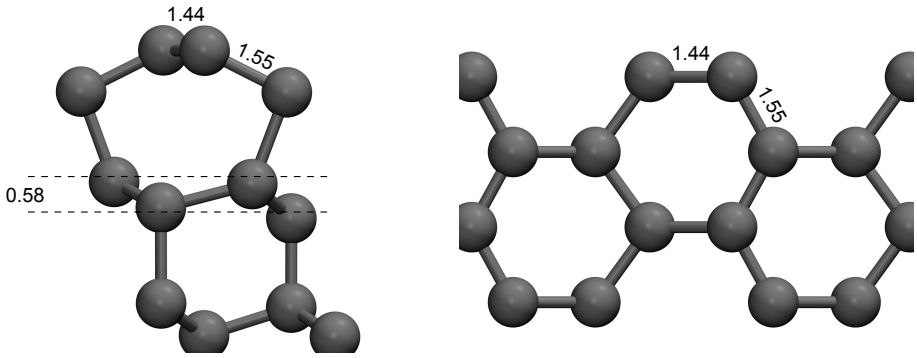

Figure 5.3: The optimized structure for the clean reconstructed C(111) surface.

The Pandey chain (111) reconstructed surface has zigzag chains on its first layer with an average bond length of 1.44 Å, comparable to the C-C bond length found in graphite[7], with the second carbon layer chain having a bond length of 1.55 Å compared to the bulk C-C length of 1.57 Å. No buckling of the dimerised surface π-bonded chain occurs.

The adsorption of oxygen[11] is preferred on the C(111)-(2×1) Pandey chain reconstruction, with an optimum oxygen coverage of $\frac{1}{3}$ ML. Hydrogen[12] on the other hand stabilises the (1×1) unreconstructed geometry by saturating the surface dangling bonds to form single C-H bonds above the top layer carbons. In the hydrogenated case the structure of the carbons at the surface resembles that of the bulk,[7] as hydrogen termination of the (1×1) surface is energetically favoured over the hydrogenation of the (2×1) Pandey chain.

5.1.4 C(110) bare surface

The (110) surface of diamond is less commonly found in CVD diamond, due to faster growth. The (110) surface is formed by layers of zigzag chains similar to the (2×1) reconstruction on diamond,

but the staggered stacking is present throughout the bulk. LEED of the C(110) surface shows a (1×1) pattern, and even after annealing to 1300 K no reconstruction is observed, unlike the C(100) and C(111) surfaces[13]. The C-C bond length of the surface carbon layer is about 1.44 Å, similar to that of graphite. The C(110) $-$ (1×1) surface is displayed in Figure 5.4.

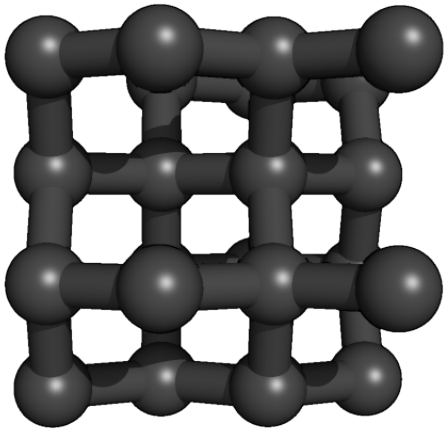

Figure 5.4: The optimized structure for the clean C(110) surface. Figure by James Richley.

Although the zigzag surface chains are similar in geometry to those of the Pandey chain on the C(111)-(2×1) surface, the zigzag chains on the (110) surface are buckled and tilted out of the surface plane, with about 0.14 Å between the high and low atoms in the chain. The second layer chain is not buckled with a C-C bond length of 1.51 Å, but distortions formed by the surface continue down to the seventh layer below the surface.[7] Hydrogen termination of the C(110) surface is again favoured over the bare surface and removes the buckling of the surface carbons, increasing the first layer C-C bond length to 1.54 Å, with a C-H bond length of 1.17 Å. Due to the relatively low prevalence of the (110) plane in most relevant diamond surfaces, this study concentrates on the (100) and (111) surfaces for the study of lithium adsorption.

5.2 Surface termination on diamond

5.2.1 Hydrogen terminated diamond

Hydrogen termination on diamond has been increasingly studied over recent decades, in part because of its interesting properties and also due to its ease of preparation and ubiquity in the advent of chemical vapour deposition (CVD) processes. The gas phase chemistry of a typical CVD reactor relies on a high proportion of hydrogen to other gases with a ratio of hydrogen to methane and other constituent gases being as high as 99% in some growth conditions. The presence of a hydrogen plasma removes graphitic sp^2 carbon, improving the quality of the diamond growth.[14] The free radicalisation of the surface sites of a diamond surface by the hydrogen within the plasma allows saturation of the resultant dangling bond with a hydrogen free radical. Exposure to even a few minutes of hydrogen plasma replaces any existing termination with hydrogen on the majority

of surface carbons and exposure to a hydrogen plasma has been shown to reproducibly induce a hydrogen termination on the C(100), C(111) and C(110) surfaces.[15] This hydrogen termination displays a 2×1 surface reconstruction in low energy electron diffraction on the C(100) surface,[16;17] indicating that single C-H bonds are formed on top of a reconstructed symmetric dimer row structure, as pictured in figure 5.5. On the C(100) surface the monohydride surface has two hydrogen atoms per surface unit cell, whereas on the C(111) surface the adsorption of hydrogen breaks the (2×1) structure.

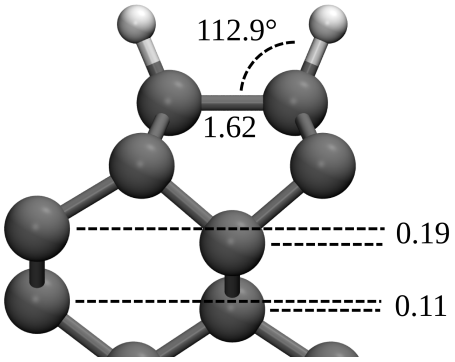

Figure 5.5: The optimized structure for hydrogen termination on the C(100) surface.

In temperature studies, hydrogen begins leaving the C(100) surface at approximately 740 °C, and after a suitable period of annealing is completely removed at temperatures between $900 - 1050$ °C in vacuum.[18]

The principle advantage to hydrogen terminating a diamond surface is that it induces a negative electron affinity, which puts it at the forefront of field emission and thermionic devices using diamond, as well as for tuning the interfaces between diamond and other materials for microelectronics. The calculated NEA of hydrogen terminated diamond on the C(100) surface is approximately -2 eV,[19;20] although experimental studies have consistently found a slightly lower value around -1.3 eV,[21] as well as measured lowered workfunction between 2.85 and 3.9 eV.[15;22]

In addition to the advantages to electron emission given by the negative electron affinity, under the presence of adsorbates on the surface, hydrogen terminated diamond displays a p-type conductivity layer from the surface to some 10 nm below the diamond surface.[23;24] This surface transfer doping behaviour is highly advantageous for devices such as field effect transistors.

5.2.2 Oxygen termination on diamond

The behaviour of hydrogen on diamond is perhaps best illuminated when compared with the oxygen-terminated surface, which takes one of two forms, the half monolayer ether bridge shown in Figure 5.6(a) in which the oxygen atom is shared between two of the surface carbon atoms, and the full monolayer on-top carbonyl configuration shown in Figure 5.6(b), where the oxygens lie vertically above each surface carbon atom in a double bond arrangement. Oxygen termination is found, amongst other mixed terminations such as carboxyl and hydroxyl groups, on natural and high pressure, high temperature diamond. It can also be created intentionally using a number of methods including washing in concentrated strong acids, exposure to an oxygen plasma and

exposure to ozone (O_3) under an ultraviolet light.

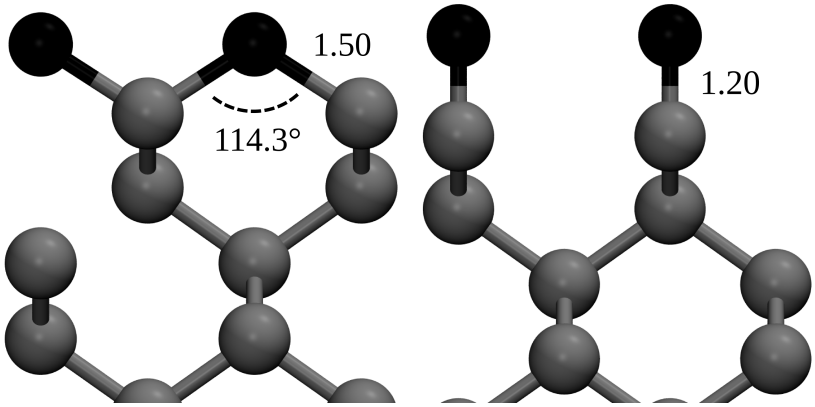

Figure 5.6: The optimized structure for oxygen termination on the C(100) surface with (a) ether-bridge bonding and (b) ketone-carbonyl bonding.

Unlike the hydrogenated surface, oxygen-terminated diamond does not display a negative electron affinity. Instead the opposite effect is observed, with a positive electron affinity of typically +2.45 eV,[25] giving the oxygen terminated surface a higher workfunction than the bare reconstructed C(100) or (C111) surfaces. This is due to the build-up in charge in the lone pair of the surface oxygen, which acts as a strong barrier to charge below the surface escaping.

5.3 Alkali metals on the diamond surface

As explained in the previous section, surface dipoles can have a large effect in changing the workfunction and electron affinity of the material. In the hydrogen-terminated case, the dipole is a fairly simple one, where the hydrogen atom becomes positively charged and donates its electron to the lattice below, forming a linear dipole between along the C-H bond. This causes a lowering of the workfunction and a negative electron affinity, but the effect is fairly small, with an NEA of around -1.3 eV. For many applications, a stronger effect would be desirable. To achieve a stronger effect, one would need to create a bigger dipole on the surface of the diamond. This requires a more strongly positive top layer, with a more negative region beneath it (the reverse would create a barrier to emission and have the opposite effect to that desired). There are a few approaches that can deliver such an increased dipole, centring around those atoms that form strongly ionic bonds - namely the alkali metals in Group I and II of the periodic table (highlighted in Figure 5.7). Monolayer coverage of alkali metals on transition metals has shown a workfunction lowering of several eV induced by electronic density rearrangement on the surface forming a dipole.

Although some very negative electron affinities have been observed from alkali metal layers on the surface of diamond, they are frequently weakly bound and only stable to low temperatures, as well as being reactive outside of vacuum. Using a sticking layer such as oxygen, or the deposition of an alkali metal ionic compound with a highly electronegative atom allows the formation of a surface layer that is potentially more strongly bound and with a stronger dipole effect. By comparison to the C(100) surface, the C(111) surface has received far less attention for studies of alkali metal

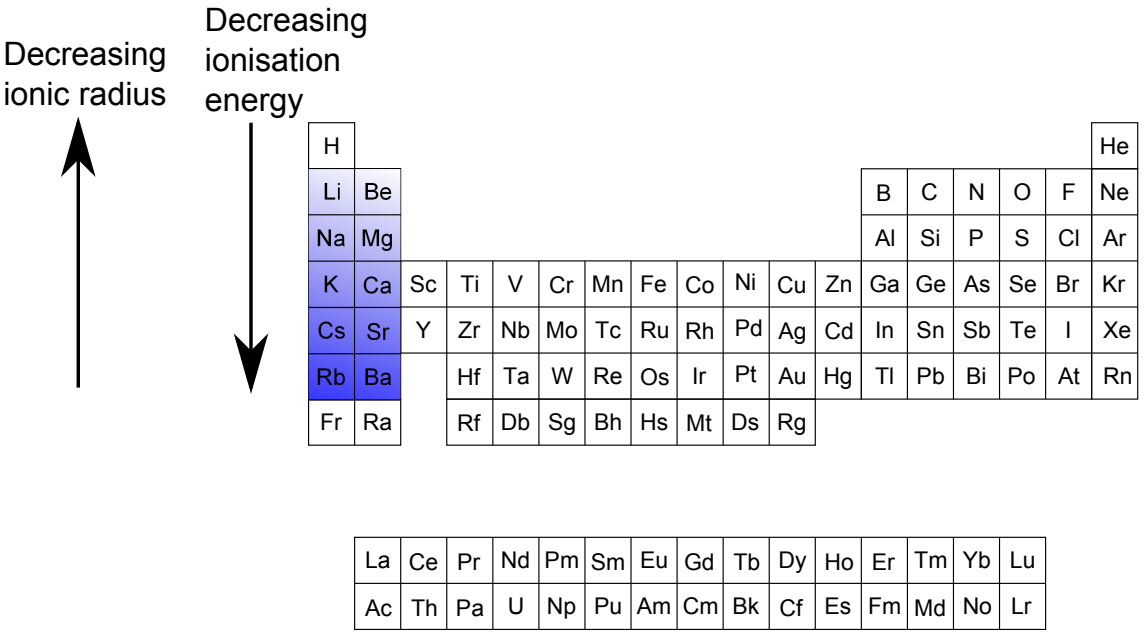

Figure 5.7: Periodic table showing the theoretical suitability of alkali metals.

adsorption, either experimentally or computationally, likely due to the relative ease of production of atomically smooth C(100) substrates.

The elements in groups I and II have incomplete outer shells with few valence electrons weakly bound to the central core, making them easy to remove. Group I has the lowest ionisation energy of all elements, with the energy needed to remove an electron falling as you move down the group from Li to Cs. In theory, the ease at which caesium loses its valence electron should make it ideal for forming an strongly ionic bond and therefore a good candidate for a large dipole on the diamond surface, although in practice the large size of the caesium ion compared to other alkali metals may mean other adsorbates can achieve better coverage.

Caesium has been widely studied for its electron affinity lowering effects on a variety of surfaces. Geis[26] first displayed the improved workfunction decreased and a large NEA was displayed after caesium deposition onto oxygenated-diamond that showed field emission turn-ons as low as $0.1V\mu$ m^{-1}. Later theoretical studies[25] predicted metallic surface with a 0.85 eV negative electron affinity, and a low workfunction of just 1.25 eV. Investigations by Diederich *et al*[27] on the hydrogen terminated and caesium coated boron-doped C(100) surface found a weak (1×1) reconstruction of Cs on the bare C(100)-(2×1) surface, with a clearer (2×1) LEED pattern for Cs on the hydrogen terminated C(100)-(2×1):H surface. XPS measurements showed a clear increase in the Cs $3d_{5/2}$, $4p$ and $4d$ peaks after Cs evaporation. An NEA was observed after 0.15 ML of caesium was adsorbed on the bare surface with a similar intensity of the hydrogenated surface. this peak decreased for Cs coverage above 0.5 ML. By comparison to the small degree of band bending on the hydrogenated surface, Diederich *et al* concluded that a charge transfer of donated electrons from the adsorbed Cs atoms to the boron-doped surface results in a shift of the Fermi level resulting in a downward band-bending of approximately 1.10 eV, an effect thought to increase if the surface is first oxidised before Cs evaporation.

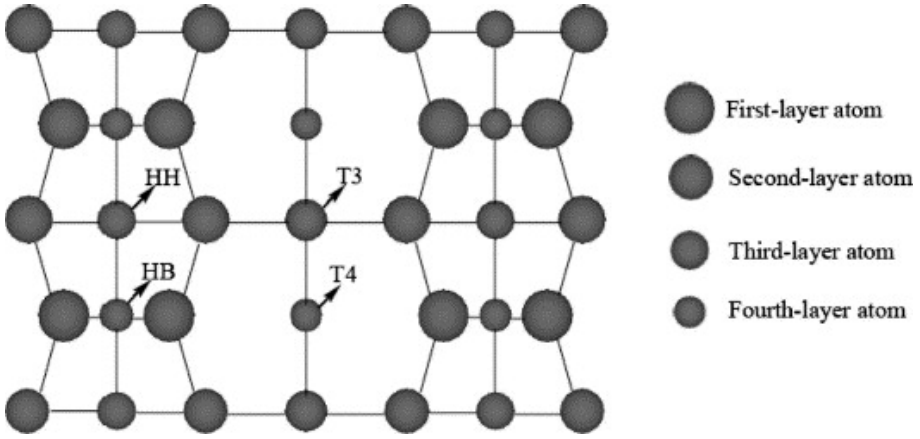

Figure 5.8: Sites considered by Nie on the bare C(100) surface for Na, K and Rb adsorption.[29;30]

DFT Calculations and spectroscopy by Loh *et al*[28] found that caesium on oxygenated homoepitaxially grown boron-doped C(111) diamond was stable to approximately 500 °C, with a reduction in UPS features linked to oxygen after 300 °C. Exposure of the caesium-oxide surface to further oxygen reduced the photo yield significantly, but didn't shift the high energy cut-off of the NEA surface. They found also that the same strength negative electron affinity was formed whether the caesium was introduced on the surface followed by oxygen, or the opposite order was used. Diederich, by comparison, found that exposure to 20 Langmuir of molecular oxygen removed the NEA induced by caesium evaporation.[27]

Other alkali metals studied for their effect on the electron affinity of diamond include rubidium and sodium. Nie *et al*[29;30] studied computationally the effect of sodium, rubidium and potassium adsorption on the C(100)-(2×1) surface. Their DFT calculations showed that the most stable adsorption on the bare surface occurred at 0.5 ML for all three alkali metals, with a similar maximum workfunction shift at 0.5 ML, with decreased stability and $\Delta\phi$ at 1 ML and above. The most stable site for 0.5 ML coverage in both cases was the T3 'Valley-bridge' site, with an adsorption energy per adsorbate of 1.35 eV for 0.5 ML Rb, 1.32 eV for 0.5 ML Na and 1.09 eV for 0.5 ML K. The T4 'Cave' site and HH 'Pedestal' site were of similar stabilities around two thirds that of the T3 site, with the HB 'Bridge' site the least stable of all. A summary of the adsorption site used by Nie *et al* is shown in Figure 5.8. The weaker interaction with the substrate for the potassium adsorbate compared to the sodium indicates a weakening of substrate to alkali metal interaction with increasing alkali metal radius.

For the half-monolayer adsorption, the bond between the adsorbate and the substrate was 2.629 Å for the Na-C bond, 2.833 Å for K-C and 2.96 Å for Rb-C when the alkali metal is located in the T3 position, and the C-C dimer bond lengthens by 0.135 Å for Na, 0.1 Å for K and 0.09 Å for Rb. This is characteristic of a reduction in electron density in the dimer and move to a more single-bonded character due to the presence of the positively charged adsorbate.

For the full monolayer of coverage, Nie *et al* found that the HH-T3 combination was most stable, with an adsorption energy per adsorbate of 0.90 eV for Rb, 1.0 eV for Na and just 0.276 eV for K, indicating a size effect explained by the larger potassium ion having an increased interaction with its neighbour, reducing the stability. On the Na-adsorbed surface the HB-T3 and HH-T4 combinations

were only marginally less stable than the HH-T3 combination, but on the Rb-adsorbed surface the HH-T3 surface had an adsorption energy at least 40% larger than the other possible combinations. Only the HH-T3 and HH-T4 combinations were found to be stable for potassium. The high stability of the HH-T3 site correlates with a number of investigations in the literature for alkali metals on silicon.[31–33]

All three elements had a significant reduction of the diamond workfunction with a minimum at 0.5 ML. A coverage of 0.5 ML gave a calculated workfunction change of -3.26 eV for Na, -2.776 eV for K and -2.80 eV for Rb, but in all case this effect was reduced at 1 ML, with a $\Delta\phi$ of -2.44 eV for Na, -1.92 eV for K and -2.4 eV for Rb, which was explained by Nie *et al* as a result of larger dipole-dipole repulsion with increased coverage, leading to a depolarisation effect and charge flowing back from the substrate to the alkali metals, as demonstrated by a reduction of dipole moment between 0.5 ML and 1 ML of 62.6% and 65.4% for Na and K (No dipole moment was reported for Rb).

Of the alkali metals simulated in Nie's paper, potassium has been the most explored experimentally. Petrick and Benndorf[34] found that potassium adsorption was negligible on the hydrogen terminated C(100) surface due to the need for the formation of a potassium ion that is hindered by the H-terminated surface. As in the caesium case, they found the adsorption of potassium was greatly improved on the C(100) surface after acid treatment due to the formation of oxygen-containing surface groups. After potassium absorption the oxygen coverage remained the same without a change in the XPS O 1*s* spectra to indicate salt formation. The K-covered acid-washed sample did not display a negative electron affinity. Hossain *et al*[35] studied the adsorption of potassium on the C(100)$-(2 \times 1)$ surface using electron energy loss spectroscopy (EELS), workfunction change measurement and thermal desorption spectroscopy (TDS). They found that two different chemisorbed states of K are detected at coverages above 0.5 ML, and that the bond between potassium and the substrate at 0.5 ML coverage is highly polarised causing the maximum in workfunction shift, which is decreased at increased coverage by charge regain by the K atoms.

Lithium fluoride[36] and rubidium fluoride[37] have also been shown to display an NEA on diamond. As both fluorides have high dipole moments of 6.326 D and 8.546 D respectively, they are expected to produce a large dipole on the diamond surface. Wong *et al* deposited ultrathin layers of the fluorides onto both oxygenated and hydrogenated boron-doped diamond, monitoring thickness using Auger spectroscopy. An NEA was observable using ultraviolet photoemission spectroscopy on both surfaces after a few Å of lithium fluoride coverage, the intensity of which decreased after a thicker layer of LiF was deposited. Kelvin probe measurement showed a decrease of workfunction on the hydrogenated surface of 0.77 eV to 2.87 eV, and a decrease from 4.36 eV to 3.15 eV was observed on the oxygenated surface on LiF adsorption. On initial LiF deposition the workfunction rapidly decreased by 0.5 eV, followed by a small decrease in ϕ with increasing coverage until reaching a constant of approximately 2.4 eV, the workfunction of pure LiF. Similarly for RbF, the deposition of approximately 1 ML of RbF (around 2.3 Å) produced a downward shift in the UPS spectra indicative of downward band bending and an NEA. Kelvin probe measurements found a rapid initial workfunction reduction followed by a small decrease with further coverage, stabilising at around ϕ =2.2 eV at higher coverages, an effective lowering of around 1.4 eV.

The adsorption of lithium metal and and lithium oxide on diamond had not been reported in the literature before the commencement of this project.

5.4 Simulating lithium on the C(100) diamond surface

5.4.1 CASTEP settings and convergence criteria

The C(100) surface modelling was performed using CASTEP[38] on the BlueCrystal Phase 2 high performance cluster at the University of Bristol by Kane O'Donnell.[39] The results are reported here as the predicted surface was the key step to the experimental observations reported in chapter 6, as well as for comparison with the C(111) theoretical predictions later in this chapter. A simulation cell of dimensions (5.05 Å × 2.52 Å × 42.84 Å) was used for the C(100) surface modelling, and these dimensions were fixed during calculations to the diamond lattice constant of 3.57 Å separately calculated from a conventional eight atom diamond unit cell. The C(100) surface was represented by a double-sided slab with 22 layers of carbon atoms with two carbon atoms per layer and 21 Å of vacuum between opposing faces to ensure the electric field decayed to zero between the two faces for accurate workfunction calculation. The cell was oriented to give a single (2×1) dimer unit of each face. For the exchange-correlation functional, The Perdew and Wang (PW91) generalised gradient approximation was used.[40] Ultrasoft Vanderbilt pesudopotentials[41] were generated for the elements C, Li, H and O used in the simulation. The bulk lattice constant for diamond using the C pseudopotential was calculated to be 3.57 Å compared to an experimental value of 3.560 Å.[42] Similarly, the bulk lattice constant of Li was calculated to be 3.46 Å compared to 3.511 Å in the experimental literature.[43] Both calculated values were within 1.5% of the experimental values. A Monkhorst-Pack[44] grid of $(6 \times 6 \times 1)$ k-points was used to converge the structural calculations using the Broyden, Fletcher, Goldfarb and Shannon method with a geometry convergence criterion of 0.02 eV/ Å, a fixed unit cell and no restrictions on atomic positions. A Monkhorst-Pack grid of $(12 \times 12 \times 1)$ k-points were used during the density of states calculations.

5.4.2 Calculating the workfunction and NEA

In each of the following simulations, the same method was used to calculate the adsorption energies, workfunction and NEA. The adsorption energies for the system, E_{ads} were calculated using the formula:

$$E_{ads} = \left(E_{substrate} + NE_{atom} - E_{tot}\right)/NE_{atom}. \tag{5.1}$$

where $E_{substrate}$ is the total energy of the surface before adding the adsorbate, NE_{atom} is the number of adatoms in the cell used in the simulation, and E_{tot} is the total energy calculated for the adsorbed surface. In this configuration, a stable adsorbate atom has a positive adsorption energy. The macroscopic averaging method of Fall, Binggeli and Balderschi[45] was used to calculate the work function ϕ using:

$$\phi = E_{vac} - E_{f,s} = E_{vac} - \tilde{V}_{es,s} + \Delta E. \tag{5.2}$$

where E_{vac} is the mean vacuum level in the vacuum gap, $\tilde{V}_{es,s}$ the plane-averaged mean electrostatic potential at the surface (i.e. the mean electrostatic potential parallel to the surface), $E_{f,s}$ is the Fermi level for the slab and ΔE is the difference between the bulk Fermi level $E_{f,b}$ and the plane-averaged mean electrostatic potential in the bulk $\tilde{V}_{es,b}$,

$$\Delta E = E_{f,b} - \tilde{V}_{es,b} = 10.52eV. \tag{5.3}$$

The bulk Fermi level was calculated using a (3×3) conventional unit cell involving 216 carbon atoms in the diamond structure. The electron affinity χ was calculated by subtracting the vacuum level from the conduction-band minimum. The conduction band minimum was taken as the slab Fermi level plus the experimental band gap of 5.47 eV.minimum was taken as the slab Fermi level plus the experimental band gap of 5.47 eV.

The analysis of the calculations presented here concentrate primarily on the effect of the adsorbates on the intrinsic diamond surface, and do not include the effects of band bending that would result on diamond with dopants and surface defects. For this reason the analysis focuses on the workfunction shift induced by the surface adsorbates, rather than the absolute workfunction, as for practical emission devices the combination of a doped substrate and an NEA inducing surface configuration would likely be needed.

5.4.3 Bare C(100) structure and dimer chain reconstruction

There are two dangling electrons per surface carbon atom on the clean, unreconstructed C(100) surface. Generally these dangling bonds are saturated by a terminating species, most commonly hydrogen and oxygen. The clean reconstructed C(100) $-$ (2×1) has a work function of 6.1 eV, exhibiting a positive electron affinity of +0.6 eV. This small positive electron affinity originates from the increased density of electrons on the top layer of the surface from the strong dimer bond, and is consistent with values for χ of +0.75 eV and +0.50 eV found experimentally by Baumann [46] and Maier, [21] as well as computational calculations. [19;20]

5.4.4 Oxygen termination on the C(100) surface

The various oxygen terminations on the C(100) surface typically show a (1×1) LEED pattern, [23;47;48] and are typically found in two configurations. The carbonyl or ketone structure, as pictured in Figure 5.6(b) consists of oxygen atoms lying directly above the top surface carbon atoms, with a double bond between them. It is slightly more stable than the ether bridge configuration shown in Figure 5.6(a), where the oxygen lies between two surface carbon sites, and is singly bonded to both. Most oxygen-terminated surfaces are believed to have a mix of the two configurations. Auger electron spectroscopy shows that oxygen remains on the diamond surface until around $1050 - 1100$ °C and it is hypothesised that its proposed method of abstraction is in the form of carbon monoxide. [46]

In this study both carbonyl and ether bridge bonded oxygen terminations were found to be stable, with absorption energies of 8.2 eV for the ether case and 7.88 eV for the carbonyl case, agreeing with other theoretical studies using density function theory [19;49] although other modelling techniques showed some deviation from this trend. The C-C dimer bond on the surface is broken in both configurations, and the bond length of the single bonded carbon oxygen bonds in the ether configuration is longer at 1.50 Å than the double bonded carbon oxygen bond in the carbonyl case. These bond lengths agree with past studies. The comparison of this study to previous theoretical studies for the clean, hydrogenated and oxygenated diamond surfaces are shown in table 5.1.

Structure	Source	E_{abs} (eV)	χ (eV)	$d_{11(C-C)}$ (Å)	d_{CO} (Å)	d_{CH} (Å)
C(100)-(2 × 1)	Present work	1.46[1]	0.62	1.38	-	-
	Prev. DFT	1.512[50]	0.51-0.69[19]	1.37[51]	-	-
			0.8[20]			
C(100)-(2 × 1):2H	Present work	5.32	-1.95	1.62	-	1.10
	Prev. DFT	4.54[51]	-2.0[19]	1.61[51]	-	1.11[52]
			-2.2[20]			1.1[51]
C(100)-(1 × 1):O (ether)	Present work	8.2	2.63	No dimer	1.50	-
	Prev. DFT	8.43[48]	2.61-2.70[19]	No dimer	1.48[47]	-
					1.49[48]	
C(100)-(1 × 1):O (carbonyl)	Present work	7.88	3.75	No dimer	1.20	-
	Prev. DFT	8.57[48]	3.64[19]	No dimer	1.25[48]	-
					1.16[47]	

Table 5.1: Key structural and electronic properties for the clean, hydrogenated and oxygenated diamond (100) surfaces, compared to other theoretical findings.

A full monolayer coverage of oxygen gives the C(100) surface a very large positive electron affinity due to the presence of the oxygen's lone electron pair above the surface creating a strong barrier to electrons in the diamond bulk. This study found an electron affinity of +2.63 eV for the ether configuration and +3.75 eV for the carbonyl structure, agreeing with the theoretical calculations of Rutter and Robertson[19] but falling substantially higher than the reported experimental values of 1.7 and 1.45 eV,[21;46] although the exact composition of the surfaces in the experimental reports is not clear and it has also been suggested that the difference between theoretical and experimental values is due to a less than unity surface coverage of oxygen termination. The difference in stability of the ether-bridge and ketone/carbonyl oxygen-terminations on the C(100) surface is small and so for the later work on lithium adsorption onto oxygenated diamond both surfaces were considered.

5.4.5 Hydrogen termination on the C(100) surface

The surface with 100% hydrogen termination has a (2 × 1) LEED pattern.[17;50;51;53] The monohydride surface consists of a reconstructed dimer row with single bonded C-H bonds. Hydrogen has been observed leaving the diamond surface at temperatures above 740°C and is completely removed after prolonged annealing at temperatures of $900 - 1050$ °C.[18] In this study, placing atomic hydrogen above the clean reconstructed dimerised surface has the same effect as placing the hydrogen above the unreconstructed bare surface - in both cases the surface optimises to the same (2 × 1) monohydride structure. The length of the surface C-C dimer bond increases when hydrogen is adsorbed, as would be expected from a transfer of electron charge from the C=C double bond to the C-H bonds.

The hydrogen terminated surface has an adsorption energy of 5.32 eV, higher than the 1.512 eV predicted by Furthmuller *et al.*[50] However, in practice it is somewhat easier to remove a hydrogen molecule as two neighbouring hydrogen terminating atoms than it would be to remove an isolated hydrogen atom, so in reality the adsorption of hydrogen has a lower energy than the theoretically calculated value, due to the increased kinetics of the hydrogen molecule abstraction reaction.[54;55]

Adding a hydrogen termination to the diamond C(100) surface reduces the workfunction to 3.5 eV, comparing favourably to the experimental value of 3.9 eV,[22] and the electron affinity of -1.95

eV also broadly agrees with experimental observations[21] of around -1.3 eV. In general the NEA in CASTEP simulations seems to be more negative than observed in experiment.

5.4.6 Lithium adsorption on the bare C(100) surface

Although the workfunction reducing effect of alkali metals on diamond is known, this project was the first to report theoretical predictions of the adsorption of lithium on the clean $C(100) - (2 \times 1)$ surface.[39] The Levine sites traditionally used for adsorption on silicon are also though to be likely absorption sites for alkali-metals on diamond,[29;30;32;35] although the exact sites for both Si and Ge are still somewhat uncertain. Figure 5.9 shows the four high symmetry adsorption sites used during this study based on those used for Si in previous studies.[56;57] They are known as the pedestal (HH), bridge(HB), valley-bridge(T3) and cave(T4) sites.

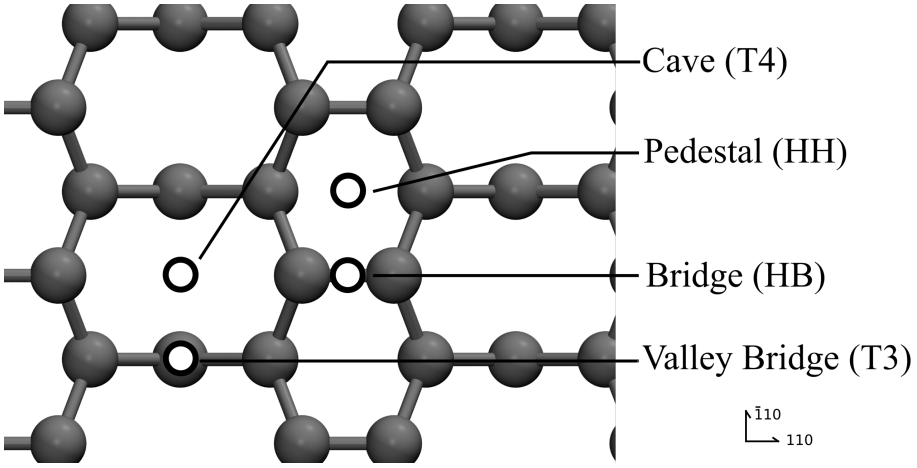

Figure 5.9: High symmetry adsorption sites considered for Li adsorption in the present study.

Both 0.5 monolayer and full monolayer coverage of lithium were considered, which translates to one and two lithium atoms per unit cell respectively. The results for lithium adsorbed on the bare C(100) surface are displayed in Table 5.2. The adsorption of lithium lengthens the C-C dimer bond from 1.38 Å on the clean reconstructed surface to between 1.46 Å and 1.53 Å after 0.5 monolayer of lithium adsorption, and to between 1.64 Å and 1.74 Å after a full monolayer of lithium is adsorbed. This bond lengthening is consistent with the clean double-bond becoming more single-bonded in character. The lowest energy structure for the 0.5 monolayer case is the T3 valley-bridge site with an adsorption energy of 3.10 eV. The HH pedestal and T4 cave sites are less stable but similar to each other with adsorption energies of 2.63 eV and 2.57 eV respectively, with the HB bridge site between the top layer carbons being the least stable at an adsorption energy of 2.12 eV, some 1 eV less than the most stable T3 site. The preference for the T3 valley-bridge site is consistent with Nie's findings for sodium, potassium and rubidium on diamond[29;30]. Figure 5.10 shows the lowest energy sites for the 0.5 ML and 1 ML Li coverages of the bare surface.

The lithium in the T3 adsorption site becomes positively charged, with a charge of approximately +0.8 e, with the first and second layers of carbon atoms in the diamond gaining a similar amount of negative charge. Projecting the Kohn-Sham orbitals of lithium suggests a hybridisation

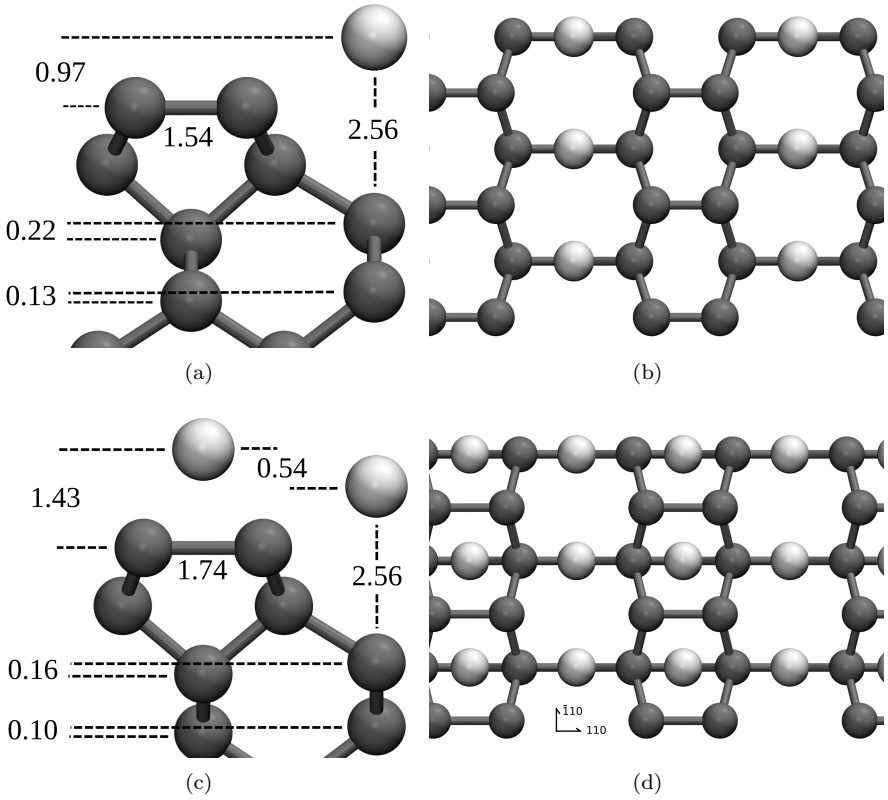

Figure 5.10: Lowest energy structures in section and plan views for (a, b) 0.5 ML and (c, d) 1 ML Li adsorption on C(100)-(2×1).

of the $2s$ and $2p$ lithium orbitals.

Coverage	Site	E_{abs} (eV/ads)	$d_{11(C-C)}$ (Å)	d_{C-Li} (Å)	$\Delta\phi$ (eV)	χ (eV)
0.5 ML	T3	3.10	1.52	2.22	-2.07	-1.45
	HH	2.63	1.53	2.13	-3.21	-2.59
	T4	2.57	1.51	2.10	-2.54	-1.92
	HB	2.12	1.46	2.21	-1.77	-1.15
1 ML	HH + T3	3.26	1.74	2.10	-3.32	-2.70
	HH + T4	3.04	1.68	2.10	-3.15	-2.53
	HB + T3	3.02	1.72	2.01	-3.29	-2.67
	HB + T4	2.74	1.64	2.04	-2.99	-2.37

Table 5.2: Calculated structural and electronic properties of the Li-adsorbed C(100) $-$ (2×1) surface.

All of the stable configurations of lithium on the C(100) $-$ (2×1) clean surface studied predicted a negative electron affinity ranging from -1.07 eV to -2.7 eV, with the most stable configuration in the 0.5 ML case having an NEA of -1.45 eV and the most stable full ML case having an NEA of -2.7 eV. These are comparable to the NEA strength observed for hydrogen adsorption, although the lithium adsorbates are less strongly bound than the hydrogen terminated case. In light of this, and the success of terminations such as Cs-O on diamond in inducing an NEA, a 'sticking layer'

of oxygen between the diamond surface and the lithium adsorbates was also considered.

5.4.7 Lithium adsorption on the oxygenated C(100) surface

After the demonstration that lithium has the expected workfunction lowering effect on the C(100) bare reconstructed surface, the next objective of this theoretical study was to simulate the behaviour of lithium on the oxygenated C(100) surface to determine whether an enhancement of both chemical stability and workfunction lowering effect would occur similar to that seen in the caesium-oxygen complex on diamond. As the computational absorption energies for the carbonyl-ketone and ether-bridge cases of oxygen termination are similar, both surfaces were considered for lithium adsorption, although in practice most oxygen-terminated diamond is likely to have a mix of the two terminations.

Because of the symmetry introduced onto the surface by oxygen termination, the C(100)-(1×1):O surface has only two high symmetry sites for a half monolayer of Li coverage, rather than the four observed on the clean surface. On the oxygenated surface, the HB bridge site and the T4 cave site are equivalent and are designated oxygen bridge (OB). Similarly, there is an equivalence between the HH pedestal site and the T3 valley-bridge site and for the oxygenated surface this site is designated the oxygen pedestal (OP) position. A lithium atom in the OB oxygen bridge position has two nearest oxygen atom neighbours, whereas a lithium atom adsorbed in the OP oxygen pedestal position has four nearest neighbours. Lithium atoms were placed in all four positions (HH, HB, T3 and T4) above the oxygen termination for the full monolayer case as for the full monolayer coverage carbon dimer rows are formed. Table 5.3 summarises the stability and electronic structure of the half and full monolayer adsorption of lithium onto the C(100)-(1×1):O surface.

Coverage	Structure	E_{abs} (eV/ads)	d_{CO} (Å)	$d_{11(C-C)}$ (Å)	d_{Li-O} (Å)	$\Delta\phi$ (eV)	χ (eV)
0.5 ML	OP	4.71 (K), 4.07 (E)	1.27	No dimer	1.87	-2.70	-2.08
	OB	3.54 (K)	1.25	No dimer	1.74	-1.87	-1.25
1 ML	HH + T3	4.70 (K), 4.38 (E)	1.40	1.65	1.81, 1.86	-4.52	-3.89
	HB + T3	3.90 (K), 3.76 (E)	1.36	1.66	1.67, 1.86	-3.00	-2.38
	HB + T4	3.36 (K)	1.35	1.62	1.67, 1.75	-2.30	-1.67

Table 5.3: Structural and electronic properties for lithium adsorption on the C(100) $-$ (1×1):O surface.

The lowest energy structure occurs on the ketone surface in which the oxygens lie directly above the surface carbon atoms. The lowest energy position for the lithium adsorbate occurs when the lithium atom sits in the pedestal site above the oxygen monolayer, with an adsorption energy of 4.71 eV per lithium atom in the OP position on the ketone bonded surface. Lithium atoms adsorbed at either the OP and OB positions on the ketone-bonded surface change the carbon-oxygen bond only slightly, and the OP-adsorbed position has a larger Li-O bond, with an increased negative workfunction shift and more negative electron affinity than the lithium adsorbed at the OB site. Figure 5.11 shows the most stable calculated configurations for the 0.5 ML and 1 ML coverages of Li on the ketone-carbonyl bonded oxygenated C(100) surface.

Lithium adsorption onto the ether-bridge oxygen terminated surface is more complicated. The

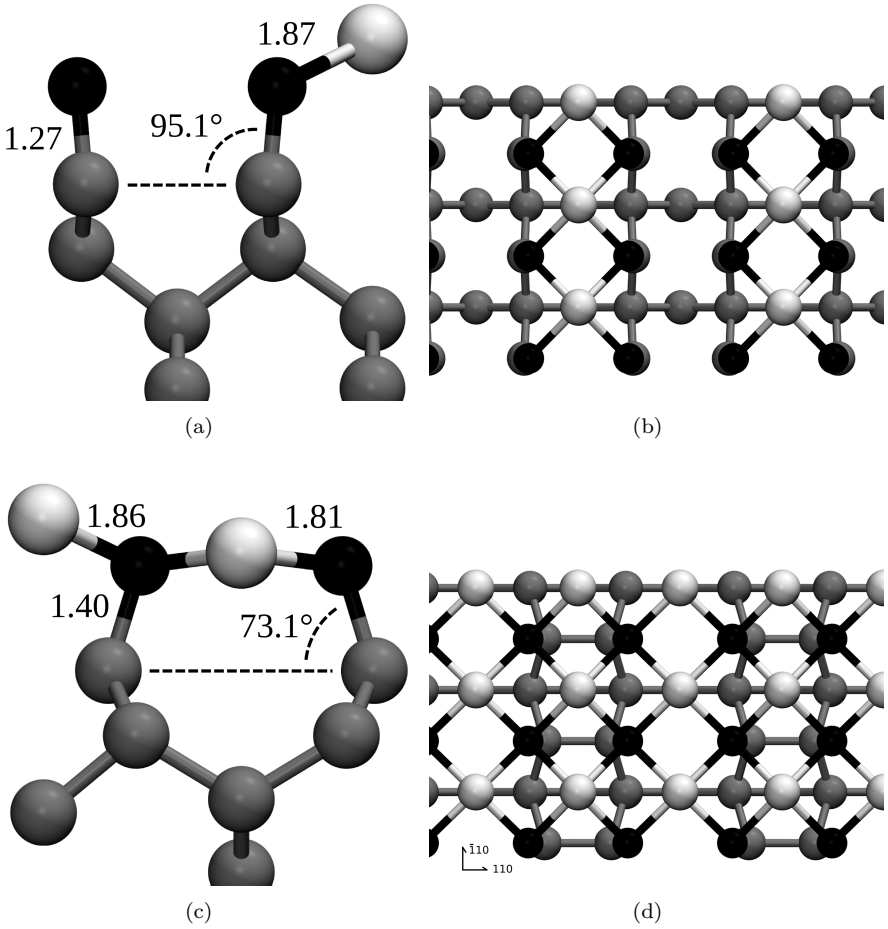

Figure 5.11: Lowest energy structures in section and plan views for (a, b) 0.5 ML and (c, d) 1 ML Li adsorption on C(100) − (1 × 1):O.

OP-adsorbed lithium on the ether-bridge surface breaks the C-O-C bridge structure of the oxygen termination, forcing the oxygens to sit above the carbon atoms in the same final configuration as for the OP-adsorbate on the ketone-bonded surface. When the lithium sits at the OB bridge position, the structure is asymmetrical and a local minimum was not found, with both carbon oxygen bonds skewed in the same direction. Figure 5.12 shows this configuration, which did not fully converge. The oxygen bridge ether has had its second bond broken and the move of the two oxygen atoms towards the upright position above the surface carbon dimer indicates that with further computational time, the OB-adsorbed lithium configuration would likely also result in a final state identical to that of the OB-adsorbate on the ketone-bonded surface. Assuming this to be true, the inference is that the presence of lithium on the oxygenated surface will break any ether bonds, and shift to the more ketone-like configuration. The C-O bond in the half monolayer case increases in length from 1.20 Å for the ketone C-O bond to around 1.27 Å, indicating a small change from the double bonded character of the ketone surface to a more single-bond character.

The full monolayer on the oxygenated surface has three unique pairs of sites for lithium adsorption. Using the nomenclature from the bare surface, these are the pedestal-valley-bridge (HH-T3),

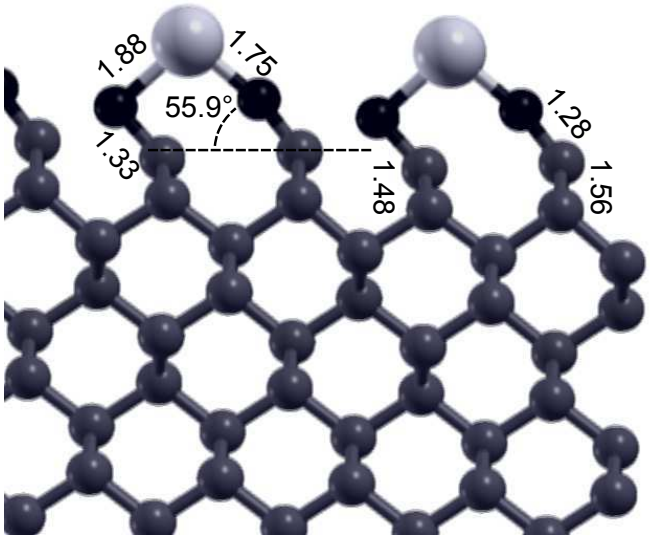

Figure 5.12: The unconverged final state of the OB position lithium on the ether bridge oxygenated C(100) surface, showing a movement of the oxygens towards that observed for the ketone-carbonyl surface.

the bridge-valley-bridge (HB-T3) and the bridge-cave (HB-T4) combinations. All three of these site pairs lead to unique stable configurations on the ketone-bonded surface, but on the ether-bridge surface stable monolayer coverage only occurs after the C-O-C bridge is broken in a similar way to OP-adsorbed lithium on the ether-bridge surface for 0.5 ML coverage. This didn't occur for the HB-T4 combination, for which all attempts to converge the adsorption on the ether structure resulted in the lithium atoms moving away from the surface. On the ether-bridge surface, both the HH-T3 and HB-T3 configurations of full monolayer Li coverage resulted in the breaking of the C-O-C ether bridge and the formation of final state configurations identical to those found for the HH-T3 and HB-T3 configurations on the ketone-bonded surface.

The lowest energy structure for the full monolayer coverage is the pedestal-valley-bridge (HH-T3) combination, with a binding energy of 4.7 eV per Li atom, a value much higher than the calculated value for the caesium atom on oxygenated diamond (1.34 eV per Cs atom)[25] and similar to that for hydrogen adsorption on the C(100) surface (5.3 eV per H atom). The HH-T3 full monolayer configuration has a near identical binding energy per Li atom when compared to the OP half monolayer case, indicating that the lithium atoms do not significantly interact with each other on the surface.

The oxygen monolayer and first layer carbons reconstruct slightly after the full monolayer of lithium is adsorbed, unlike the half monolayer case. The length of the carbon-oxygen bond increases much more substantially to around 1.40 Å, indicating a much larger increase in single-bonded character for the full monolayer compared to the small shift observed for the 0.5 ML case. The first layer of carbon atoms dimerise, but this dimer at 1.65 Å is much longer than the 1.38 Å C-C dimer bond length found for the bare surface, implying again a single-bonded nature for the

C-C bond after the full monolayer of lithium is adsorbed. The surface unit cell for the stablest case of the full Li monolayer on the oxygenated C(100) surface is close to a (1×1) structure with an Li-O basis, where each oxygen atom is surrounded by four lithium atoms. This is similar to the structure for oxygen adsorption on Li-coated Ag(111).[58]

Looking at the electronic behaviour of lithium on the oxygenated surface, the most stable half-monolayer coverage of lithium occurs when the lithium is in the oxygen-pedestal (OP) position on the ketone-bonded surface, with a binding energy of -4.71 eV per Li atom. This configuration has a workfunction shift of -2.70 eV and an electron affinity of -2.08 eV, higher than the values for the most stable T3 configuration for 0.5 ML of Li on the bare surface, which had $\Delta\phi$ of -2.07 eV and χ of -1.45 eV. The other configuration, with the lithium in the oxygen-bridge position, has a workfunction shift approximately a third less of -1.87 eV and an electron affinity of close to that of the hydrogenated surface, -1.25 eV.

The most stable full monolayer of lithium on the oxygenated surface is the HH-T3 combination, with a binding energy that is also 4.7 eV per lithium atom. The workfunction shift for this full monolayer coverage is almost double that seen for the 0.5 ML coverage at -4.52 eV, with a very large negative electron affinity of -3.89 eV, again nearly twice that observed for the most stable 0.5 ML case, and around a third greater in magnitude than the workfunction shift and NEA observed for the most stable full ML on the bare surface, indicating the oxygen layer is having more than just a structurally stabilising effect. This is very promising as although the caesium-oxygen complex has a slightly larger workfunction shift, the simulated stability of the Li-O system is much greater than that of the Cs-O system.

Subsequent simulation of increased lithium adsorption above a single monolayer showed a reduction in stability. Coverages were increased by 0.25 ML at a time, but above a full monolayer coverage only the 1.25 ML configuration shown in Figure 5.13 was found to be stable. The (2×1) reconstruction of the carbon dime remains after additional Li adsorption, and the C-O bond still displays single-bonded character. The additional lithium in the T3 position distorts the overlayer but does not significantly change the underlying diamond lattice.[59]

Although the structural deformation between 1 ML and 1.25 ML is small, there is a noticeable repositioning of the T3 lithium ion in the first monolayer, and this appears to cause a change in electron density on the surface resulting in a smaller workfunction shift. Above 1.25 ML coverages no stable configurations were found, suggesting that for the size of the surface unit cell studied, layer-by-layer growth is not energetically favourable above 1 ML, and below this level the workfunction shift is linear with coverage. These conclusions are promising for potential future technological implementation of this surface coverage.

Figure 5.14 shows the trend in workfunction shift as the lithium coverage is increased on the oxygenated C(100) surface in steps of 0.25 ML. Between 0 and 1 ML, increasing lithium coverage results in a monotonically increasing downward shift in the workfunction, to a maximum shift of -4.52 eV in workfunction for the full monolayer. However, when coverages above a single monolayer begin to form, the shift in workfunction becomes greatly reduced, similar to the observations of Nie *et al*[29;30] for Na, K and Rb on the C(100) surface albeit with a critical coverage of 1 ML for highest workfunction shift rather than 0.5 ML for the larger alkali metals they studied. The Li-Li bond length of the one-atom BCC lattice of lithium metal is substantially larger at 3.04 Å than the C-C bond length of 1.54 Å in diamond, so the interface between the C(100)-(2×1)-Li-O surface and

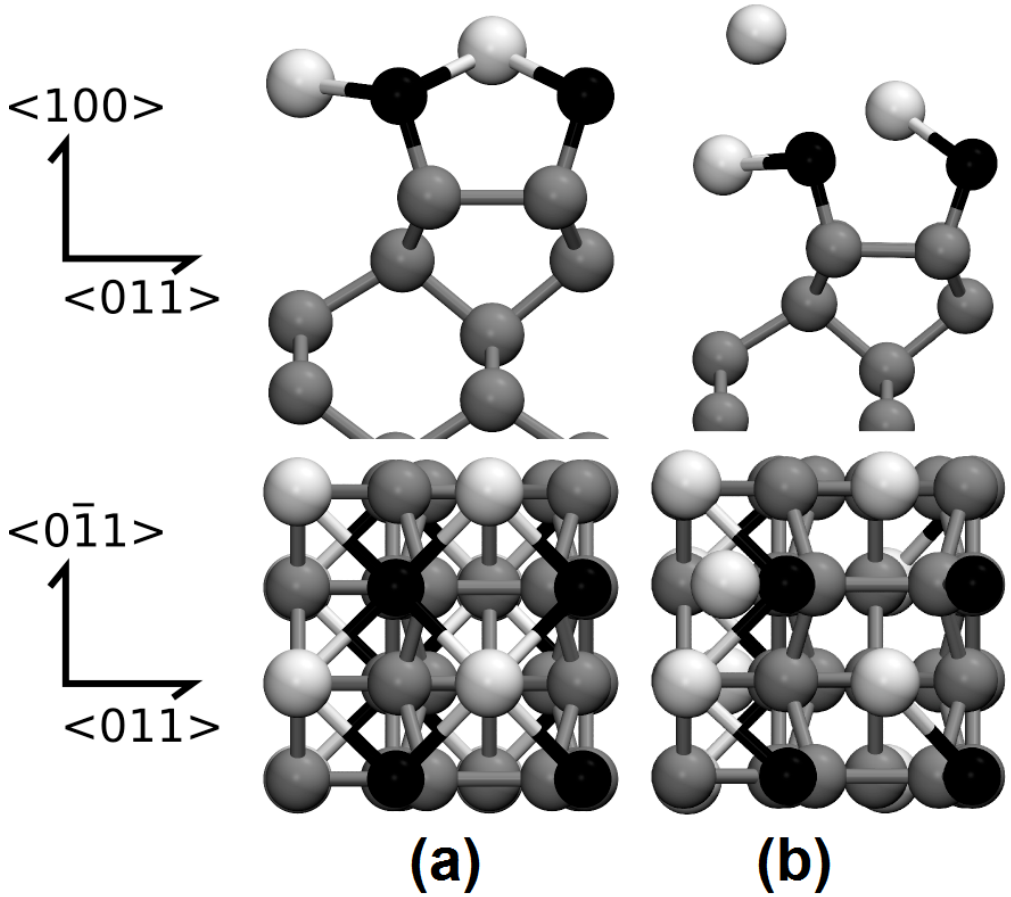

Figure 5.13: (a) the most stable full monolayer coverage of lithium on the oxygenated C(100) surface, and (b) the stable 1.25 ML coverage where an additional lithium atom is placed in the T4 position on top of the full monolayer configuration displayed in (a). [59]

further layers of lithium metal would likely have several disordered layers before the formation of BCC lithium. As the first monolayer of lithium is so much more strongly bound to the oxygenated diamond surface compared to later layers, it would be sensible to model the growth of lithium on diamond to have an independent scheme for the first monolayer compared to the formation of subsequent overlayers, which might follow the Stranski-Krastanov growth model observed for Na on Si(100)-(2×1).

The energy calculated per additional adsorbate lithium decreases substantially above 1 ML coverage to just 1.01 eV per additional Li, as shown in Table 5.4. Studying the Mulliken populations for the 1 ML coverage shows charge transfer between the Li atom and the four O atoms around it, consistent with an ionic bonding complex, with a net positive charge of between 0.7 and 0.9 electrons on each Li atom in the first monolayer, sitting in a net of negative charge sited on the oxygen atoms. When the 1.25 ML coverage adds an additional Li adsorbate, this lithium atom gains only a positive charge of 0.05 e, leading to a much weaker bond and a corresponding lower binding energy.

The trend shown in Table 5.4 is of particular interest when looking at the solvation of Li ions

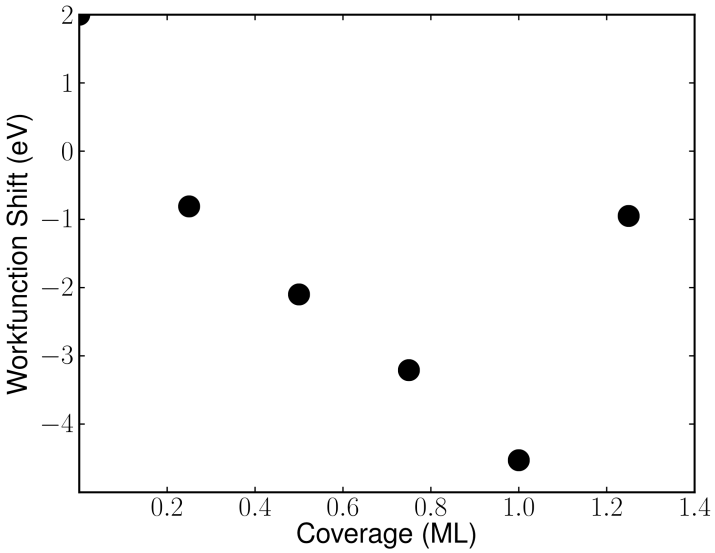

Figure 5.14: Graph showing the trend for workfunction shift with increasing lithium coverage on the oxygenated C(100) surface, showing a minimum ϕ at 1ML.

Coverage (ML)	E_B per adsorbed Li E_B(eV)	E_B per additional Li E_B (eV)
0.25	5.32	5.32
0.5	4.25	3.17
0.75	4.73	5.69
1.0	4.69	4.59
1.25	3.96	1.01

Table 5.4: Average energy per adsorbed lithium for additional coverage on the C(100) $-$ (2×1):O surface, showing that above 1 ML, the binding energy for adding additional lithium is significantly lower.

in water, which have a coordination number of between 4 and 6, so that the full monolayer of lithium on the oxygenated C(100) surface should intuitively have a similar binding energy to the energy of solvation of a single Li ion in water. However, the binding energy of adding additional lithium atoms to this first monolayer is significantly lower, indicating that the full monolayer of Li on oxygenated diamond may be stable in water (and hence air), whereas due to the solubility of lithium compounds any excess material above this first monolayer may be able to be washed away. This behaviour could prove very useful in device fabrication and is explored substantially in Chapter 6.

5.4.8 Projected Density of States of the C(100) Li-O surface

Projected density of state (PDOS) diagrams can be produced by CASTEP to show the density of electron states for a particular atom in the calculated structure. In addition to projecting individual Kohn-Sham eigenstates onto the atomic structure of the crystal studied to give an indication of the density of electronic charge near to an atom, the total density of states for the atom or atoms can

be plotted against the energy of each state, giving an approximate description of the valance band structure of the material. In general, delocalised, lattice-based electronic states will be shown as broad, nonspecific features across several eV, whilst localised states will be taller, sharper peaks. The information to be gleaned from the PDOS is not a comprehensive description of the electronic behaviour of the atoms involved, but can help provide an indication of the electronic states present.

In diamond, the typical PDOS structure involves broad, indistinct features between 5 and 15 eV corresponding to sp^3 bonds, and features symptomatic of sp^2 visible as a slightly higher density broad set of peaks between -8 and 0 eV. As the electron density of the sp^3 bonds is distributed across the carbons in the lattice, these features are much broader and have less intensity than the sp^2 features which are more localised.

The analysis of the stable configurations of lithium on the oxygenated surface clearly show a large workfunction shift, but the position of the lithium adatoms close to the oxygen terminated layer makes the explanation for this effect more complicated than the simple dipole seen on the hydrogen-terminated surface. By examining the projected density of states structure of the C(100)-(1×1):O surface before and after lithium adsorption, the distribution of the electron density at the surface that accounts for the workfunction shift can be ascertained. Figure 5.15 shows the density of states projected onto the surface oxygen atoms, top layer carbon atoms and bulk carbon atoms, before and after lithium is added to the surface.

The oxygenated surface without lithium displayed in Figure 5.15 (a) shows midlayer carbons with broad sp^3 features from around 2 eV below the Fermi level (zero on x-axis) and around -22 eV. The oxygen surface atoms have sharp spikes at -6 eV and 24 eV that are matched in the surface layer carbons, indicative of sp^2 bonding character. In addition to these states the surface oxygens have three sharp nonbonding peaks within the band gap at around -0.5 eV, -2 eV and -3.5 eV corresponding to the lone pair electrons on the oxygens. This structure is similar to the projected density of states calculated by Zheng *et al*[60], although the lone pair levels in this study are less closely spaced than in their case.

Figure 5.15 (b) shows the PDOS for the C(100) $-$ (1×1):Li-O structure after lithium is added to the oxygenated surface. The three sharp lone pair levels have been substantially downshifted in energy and overlap with the bulk levels. There is a matching signature in the surface carbon PDOS at around -3 eV and -4 eV and a general broadening of the oxygen features, indicating a delocalisation of charge and a shift of electron density away from the surface. This lowering of electron energy in the oxygen atom is consistent with an ionic bonding character with the Li^+ ion, which has an electronic population of $0.27 - 0.31$ electrons within the $2p$ states, indicating partial hybridisation. The ionic bonds formed between the oxygen and lithium atom appears to lower the surface energy enough to remove any occupied band gap states observed prior to the lithium adsorption.

Further exploration of the shift in electron density on these surface atoms upon lithium adsorption can be explored by looking at the sum of the Kohn-Sham densities for the electron bands in the slab, in particular looking at the change in localisation between the two surfaces. The Kohn-Sham orbitals do not represent single-electron bonds, but have been suggested to be useful in visualisation of general bonding trends[61;62]. Figure 5.16 shows the four localised groups of bands for the C(100)$-(1 \times 1)$:O system.

There are four localised set of orbitals for the oxygenated surface. The first is a rounded, σ-like

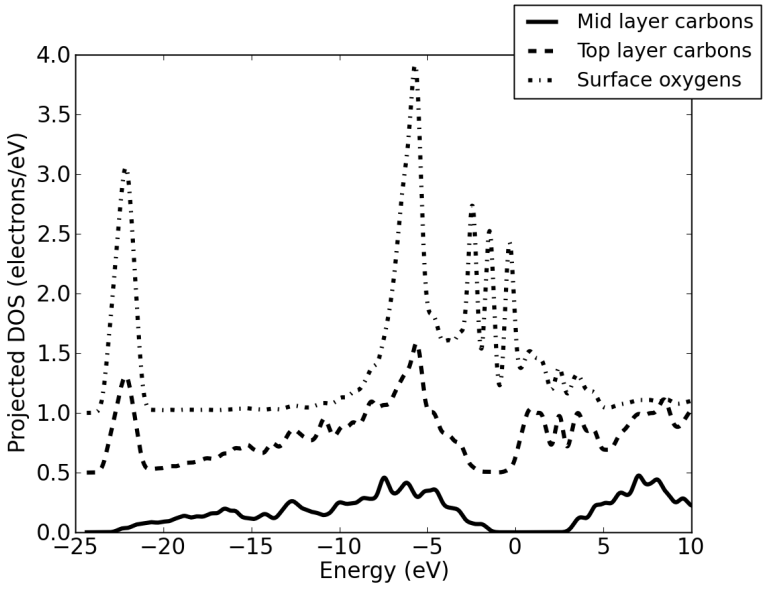

(a)

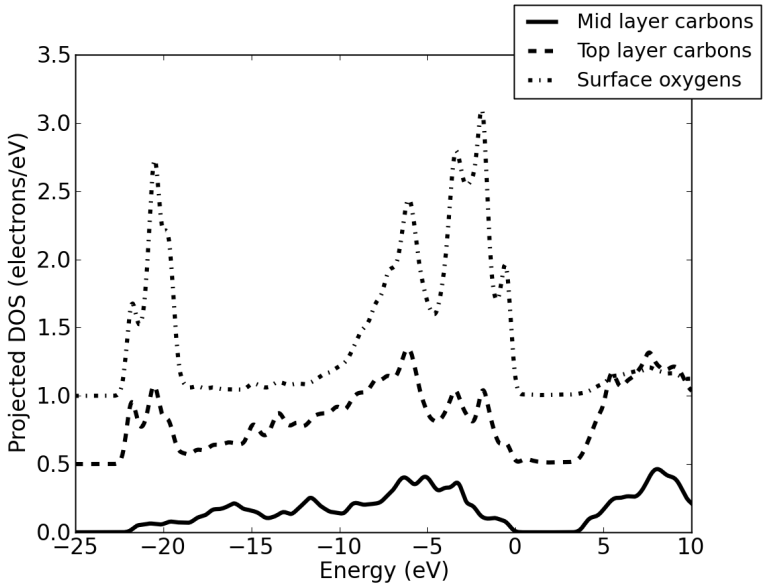

(b)

Figure 5.15: (a) Projected density of states (PDOS) for bulk C, surface C and surface O prior to Li adsorption on the C(100) − (1 × 1):O surface. (b) The PDOS for the same layers after 1 ML Li adsorption. All energies are relative to the Fermi level at 0 eV. Individual graphs have been shifted vertically for clarity.

bond distribution about the surface oxygens and carbons with band energies around 22 eV below the Fermi level. The second shows *sp*-like bonds, with band energies around -6 eV and the third π-like bonds with band energies between -5 eV and -2 eV. All three of these orbitals are characteristic of conventional C=O bonding. The fourth localised set of orbitals pictured in Figure 5.16 are the

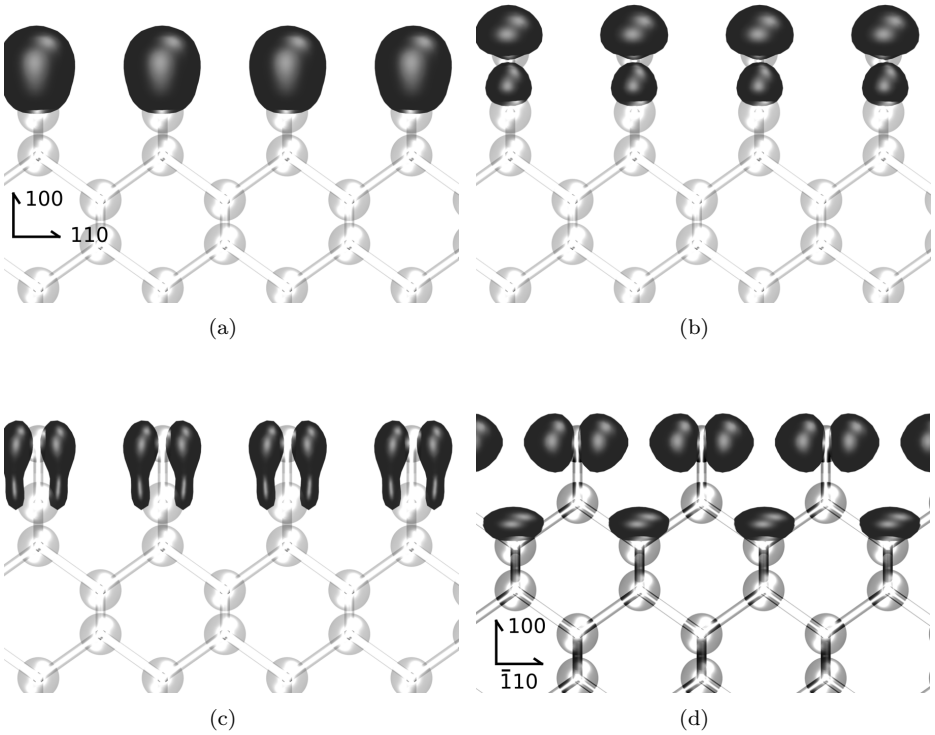

Figure 5.16: Sum of Kohn-Sham densities for the localized orbitals in the C(100) − (1×1):O system. (a) σ-like bonds with band energies around -22 eV relative to the Fermi level. (b) *sp*-like bonds with band energies near -6 eV. (c) π-like bonds with band energies in the range -5 to -2 eV. (d) *p*-shaped orbitals with energies near -2.44 eV, -1.47 eV and 0.34 eV. Note the orientation change in (d).

six highest Kohn-Sham occupied eigenstates and are p-shaped with energies near -2.44, -1.47 and 0.34 eV. These are similar to the positions of the sharply peaked lone pair states within the band gap of the PDOS for the surface oxygens and likely correspond to those states. By comparison to the four localised states in the C(100)-(1 × 1) :O system, figure 5.17 shows the sole remaining localised state after lithium adsorption, in addition to an example of the delocalised orbitals close to the Fermi level that are the result of the lithium addition.

On the two highest energy occupied bands in the C(100)-(1 × 1):Li-O surface shown in Figure 5.17(a) are localised, with the remaining bands being delocalised. The two localised bands are split between the two opposite faces of the model slab, so that each surface unit cell has only two surface-localised electrons near the Fermi level. Figure 5.17 (b) shows an example of the delocalised electron density found for the remainder of the occupied bands near the Fermi level, all of which show delocalisation at least across the first few atomic layers of the surface. Of particular interest are the high-energy occupied bands corresponding to the oxygen lone pairs on the C(100)-(1×1):O surface, which after the addition of lithium are no longer sharp distinctive bonding distributions between the surface atoms, but instead have charge distributed across the upper layers of the C(100)-(1 × 1):Li-O structure. This shift to a large delocalised electron charge in the atomic layers below the surface must contribute a strong dipole effect that by inference creates the large

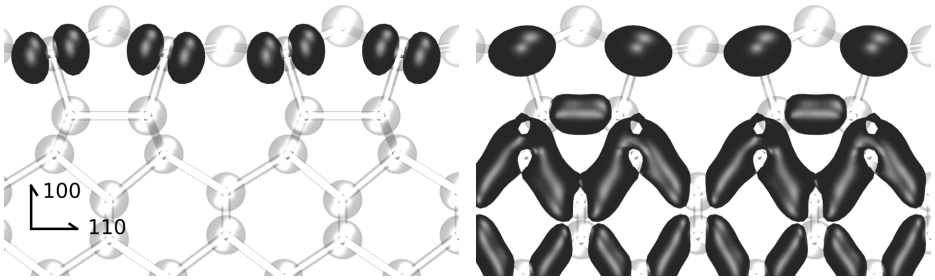

(a) (b)

Figure 5.17: (a) The sole localized orbitals (1 electron per surface oxygen) for the C(100)−(1×1):Li-O surface, with band energies in the range -0.4 to -2.0 eV. (b) The remaining orbitals near the Fermi level are delocalised.

workfunction shift of -4.52 eV after lithium addition, compared to a positive shift of around 2-3 eV for the oxygenated surface when compared to the standard diamond workfunction, depending on the type of oxygen termination.

The distributed charge dipole that is suggested as the cause of this shift is different to the more conventional atomic dipole model that has been applied for larger alkali metals such as caesium on both the C(100) and Si(100) surfaces.[63] The key reason for the difference appears to be a size effect, as the lithium atom is sufficiently small to accommodate within the oxygenated surface system without significantly distorting the overall structure, unlike the distortions observed by the adsorption of the larger alkali metals. The surface dipole on the Cs-O terminated surface has been shown to be partially due to repulsion between the Cs $5p$ semi core states and the C-O bonding states[25] but the $1s$ states in lithium sit much lower in energy than the Cs $5p$ states compared to the diamond lattice and are unlikely to be involved in the interaction on the C(100)-(1×1):Li-O surface.

5.5 Simulating lithium on the bare and oxygenated C(111) diamond surface

In light of these extremely promising calculations on the C(100) diamond surface, this report will look at the other principle surface commonly found in natural and CVD diamond, the C(111) surface, the natural cleaving plane of diamond.[12] C(100) was the subject of initial study as it is a better understood surface with more dangling bonds, but the C(111) surface is also important for both nanoparticle and CVD diamond.

Calculations were again made using CASTEP,[38] a density functional theory modelling program, on the Blue Crystal Phase 2 high-performance computing cluster at the University of Bristol. The wave functions of the atoms involved were expanded into plane waves using a cut-off energy of 700 eV. The Perdew Wang PW91 generalised gradient approximation[40] was used for all exchange-correlation functions, and ultrasoft Vanderbilt pseudopotentials[41] were generated for the atomic species used in the simulations - C, Li, H and O. A $(3 \times 6 \times 1)$ Monkhorst-Pack[44] point grid was

used for Brillouin-zone integration, using an energy convergence of 10^{-7} eV/atom.

For the C(111) orientation, the diamond surfaces were modelled as a finite slab of layers of carbon atoms, containing 8 carbon atoms per layer. Slab thicknesses of 8, 16, 20 and 26 atoms were considered, with energy convergence studies showing the 8 layer thick slab was sufficient to prevent interaction between the two surfaces. At the top and bottom of the slab, 21 Å of vacuum was present, with a variety of terminations studied for the surface carbon atoms, including single layers of hydrogen, oxygen, bare carbon both reconstructed and unreconstructed, in addition to later inclusion of metals such as lithium onto all of the above terminations. Geometries were optimised using the Broyden, Fletcher, Goldfarb and Shannon (BFGS) method[64–66] with a convergence criterion of 0.02 eV/Å, where the unit cell was fixed but all atoms were free to move.

The workfunction, binding energy of adsorbates and electron affinity calculations were performed in an identical fashion to the work reported for the C(100) surface.

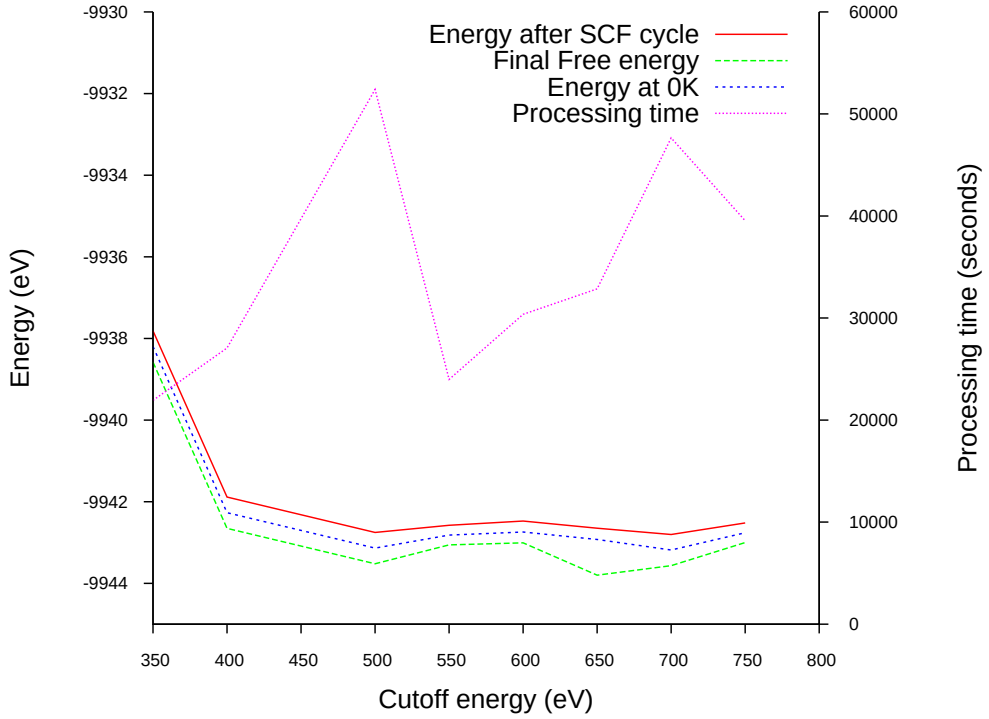

Figure 5.18: Graph comparing total energy of system(left axis) and processing time (right axis) versus cut-off energy for the 16 atom thick diamond slab.

Figure 5.18 shows the effect of increasing cut-off energy on the stability and processing time of the C(111) 16 atom thick slab. At low cut-off energies the system is not very physical, with the total energy converging at a cut-off energy above around 450 eV. A higher cut-off energy of 700 eV was chosen for the geometry optimisations however, due to the high mobility and ionicity of the lithium atom involved in later calculations.

5.5.1 Bare C(111) structure and dimer chain reconstruction

The unreconstructed C(111) surface has a (1×1) configuration, but due to the singly occupied dangling orbitals of the surface carbons the (1×1) construction is not stable. The lowest energy clean surface is the Pandey chain $C(111) - (2 \times 1)$ reconstruction.[8] In the chain model the surface reconstructs so that the dangling orbitals are closer to their nearest neighbours and so have a stronger interaction, leading to π bonds along the surface atoms. Low energy electron diffraction (LEED) patterns can not distinguish between disordered domains of (2×1) or a true (2×2) surface on diamond, but similarities between the angle-resolved ultraviolet photoemission spectra for C(111), Ge(111) and Si(111), and the latter two showing clear (2×1) LEED patterns led to the experimental conclusion that a (2×1) surface was present on diamond, which was confirmed by later calculations.[67;68]

The ideal Pandey chain has all carbon-carbon bonds with the same length as in bulk diamond, except the surface carbons, which have the same bond length as graphite. Vanderbilt's calculations also showed that the dimerisation of the Pandey chain model resulted in a higher energy, less stable system and in fact the fully relaxed structure was the most stable, where the bonds between the top surface and the bulk expands by 8.1 %, and the chain bonds are $2.1 - 4.4$ % shorter than the bulk diamond C-C bond of 1.54 Å, depending on the study.[67–69]

In this study, attempts to converge the $C(111) - (1 \times 1)$ surface resulted in surfaces approaching the (2×1) reconstruction as expected. As a result the study of oxygen and lithium adatoms concentrated on the C(111)-(2×1) reconstruction.

The bare C(111) cell without termination formed a (2×1) Pandey chain reconstruction with a upper Pandey chain length of 1.44 Å, a reduction of 6.94 %, slightly higher than that found by Vanderbilt and Sowa, with the lower Pandey chain having a length of 1.56 Å, a small expansion of 1.3 %, agreeing with the other studies. The bare surface has a positive electron affinity of +0.26 eV and a workfunction of 5.72 eV.

5.5.2 Hydrogen termination on the C(111) surface

Hydrogen termination as shown in figure 5.19 and the ether-bridge configuration of oxygen termination as shown in figure 5.20 (a) did not lift the (2×1) reconstruction. In the case of hydrogen termination, the bond length of the upper Pandey chain dimer increases by 0.12 Å, indicating a small transfer of charge from the double carbon-carbon bond to the bond between the hydrogen and nearest carbon atom.

The lower Pandey chain dimer decreases by a similar value, indicating a more electron rich bond between the two carbons. The hydrogen terminated layer shifts the work function of diamond to 3.49 eV and displays an electron affinity of -1.98 eV, which is consistent with experimental results[70] and previous *ab initio* calculations.[19] The value of 4.37 eV/adsorbate found for the adsorption energy of a hydrogen atom in this calculation compares well to the theoretical calculations of 4.94 eV found by Kanai *et al* for the monohydride surface,[71] as well as experimental observations using temperature-programmed desorption of 3.7 eV for the monohydride C(111) surface[72] and 3.5 eV for the monohydride C(100) surface.[73]retical calculations of 4.94 eV found by Kanai *et al* for the monohydride surface,[71] as well as experimental observations using temperature-programmed desorption of 3.7 eV for the monohydride C(111) surface[72] and 3.5 eV for the monohydride C(100)

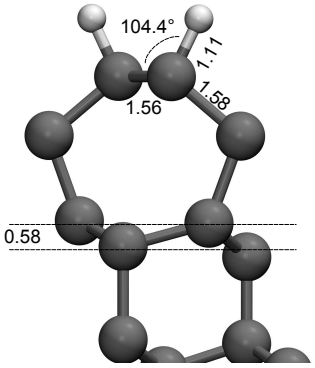

Figure 5.19: Side on image of the C(111)-(2 × 1) hydrogen-terminated surface

surface.[73]

However it has been shown that the dihydride terminated diamond surface is less stable than the monohydride surface as the energy required to remove two hydrogen atoms simultaneously as a H_2 molecule is lower than abstracting a single hydrogen atom. Theoretical studies in the literature have calculated an activation energy for desorption of 4.94 eV for the monohydride surface, compared to just 1.45 eV for the dihydride terminated C(100) surface. This is backed up by experimental values of 1.52 eV for desorption from the dihydride C(100) surface using electron-stimulated desorption[3] and 1.25 eV for the dihydride C(111) surface from analysis of the reaction kinetics.[74]

5.5.3 Oxygen termination on the C(111) surface

Both the C(111)(1 × 1) bare surface and its C(111) − (2 × 1) reconstruction were considered for oxygen configurations. The C(111)(1 × 1) configuration has been reported to prefer the on-top configuration with an optimum coverage of $\frac{1}{3}$ ML of oxygen, whilst the (2 × 1) reconstruction has been found to prefer a $\frac{1}{2}$ ML coverage of oxygen in the bridge configuration.[11] Beyond these coverages repulsion of adjacent oxygen adatoms reduces the stability of the structure. In addition, although the individual oxygen configurations on the (1 × 1) surface are slightly more stable in terms of the adsorption energy, the (2 × 1) reconstruction is still preferred and is more stable across the whole structure.

In the case of the two oxygen-termination configurations shown in Figure 5.20, the $\frac{1}{2}$ ML ether bridge surface is slightly more energetically favourable than the on-top carbonyl configuration, with an adsorption energy of -4.72 eV/adatom compared to -4.32 eV/adatom, agreeing with other DFT calculations.[11;28] The C=O bond length of 1.19 Å agrees with the 1.195 Å found by Derry for the full ML case of the on-top carbonyl configuration, and is shorter than the experimental value of 1.23 Å. The inclination of the C=O bonds in the full monolayer on-top carbonyl case buckles the uppermost carbon layer, resulting in a breaking of the (2 × 1) surface reconstruction to return to the (1 × 1) surface, with a C-C dimer length of 1.71 Å, which again agrees with other calculations. The carbonyl on-top surface has a strongly positive electron affinity of +3.65 eV,

shifting the workfunction from that of the bare surface by +3.39 eV.

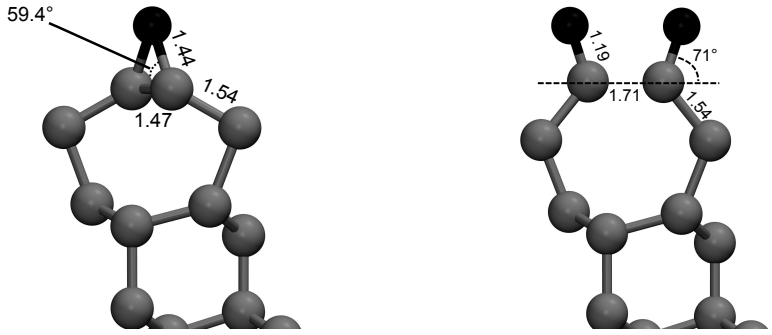

(a) (b)

Figure 5.20: Side-on images showing the structure for the C(111)-(2 × 1) surface with (a) 0.5 ML oxygen termination in the ether-bridge configuration and (b) 1 ML oxygen coverage in the carbonyl on-top configuration

By comparison, the $\frac{1}{2}$ ML ether bridge configuration is not sufficient to break the symmetry of the (2 × 1) reconstruction, with a C-O-C bonding length of 1.44 Å and upper and lower Pandey chain C-C bond lengths of 1.47 Å and 1.50 Å respectively. The ether bridge surface has one less oxygen atom per unit cell than the full monolayer of carbonyl termination, resulting in a workfunction shift of +1.83 eV and a positive electron affinity of +2.09 eV, just over half that of the carbonyl surface. Table 5.5 summarises the electronic and structural calculations for the bare, oxygen and hydrogen terminated C(111) surface, showing the bond lengths of the upper and lower Pandey chain carbon bonds and that of any adsorbates on the surface, in addition to the adsorption energies per adatom and the electron affinity and change in workfunction from the bare C(111)(2 × 1) reconstruction.

5.5.4 Lithium adsorption on the bare C(111) surface

The calculated structural and electronic properties of lithium adsorption on the clean and reconstructed C(111)-(2 × 1) surface are shown in Table 5.6 and illustrated in figure 5.21. Unlike the C(100) case,[39] where the four lithium sites provided different adsorption stabilities and electronic behaviour, all four of the initial sites for the $\frac{1}{2}$ ML coverage of lithium converged to the same site with only very small differences in energy. The upper Pandey dimer expands slightly compared to the bare reconstructed surface to 1.45 Å, and the lower Pandey contracts substantially, indicating an increase in charge across the bond. The length of the C-Li bond is substantially greater than that of the C-H bond in the hydrogenated case.

The 1 ML coverage of Li is marginally favoured over the 0.5 ML coverage, with a larger binding energy, lower workfunction and high NEA, although only by fractions of an eV. The upper Pandey dimer expands to 1.50 Å after a full monolayer coverage, indicating a further shift towards single

Structure	Source	E_{abs} (eV/ads)	χ (eV)	$\Delta\phi$ (eV)	d_{C-C_U} (Å)	$d_{11(C-C_L)}$ (Å)	d_{CO} (Å)	d_{CH} (Å)
$C(111)-(2\times1)$	This work	-	+0.26	0	1.44	1.56	-	-
	Vanderbilt[67]	-	-	1.48	1.56		-	-
	Cui*[75]	-	+0.38	0	-	-	-	-
	Sque[49]	-	+0.35	0	1.43	1.54	-	-
$C(111)-(2\times1)$-2H	This work	-4.37	-1.98	-2.24	1.50	1.52	-	1.107
	Sque[49]	-	-1.97	-2.32	1.52	1.52	-	1.12
	Cui*[74]	-	-1.27	-	-	-	-	-
$C(111)-(2\times1)$:O (ether)	This work	-4.72	+2.09	+1.83	1.47	1.56	1.44	-
	Derry[11]	-4.605	-	+1.9	1.463	1.559	1.417	-
	Loh[76]	5.23	-	-	1.457	-	1.433	-
$C(111)-(2\times1)$:2O (carbonyl)	This work	-4.32	+3.64	3.39	1.71	broken	1.20	-
	Derry[11]	-4.099	-	+2.9	1.697	broken	1.195	-
	Loh[76]	4.85	-	-	1.703	broken	1.195	-

Table 5.5: Structural and electronic properties for the basic structures of the C(111) surface, comparing results from this study to those in the literature. Results are computational unless specified with a *.

bond character. The C-Li bond is slightly shorter compared to the 0.5 ML case. Combined with the expansion of the dimer bond this indicates a larger shift of charge from the dimer to the C-Li bonds in the 1 ML case than that experienced by the 0.5 coverage. As Figure 5.21 shows, the position of Li atom in the 0.5 ML case is above the upper carbon atom chain. The full monolayer shares this position with an additional lithium sitting closer to the surface in the 'cave' position above the lower surface carbon chain.

Coverage	E_{abs} (eV/ads)	χ (eV)	$\Delta\phi$ (eV)	d_{C-C_U} (Å)	$d_{11(C-C_L)}$ (Å)	d_{C-Li} (Å)
0.5 ML Li	-1.21	-0.58	-0.84	1.45	1.50	2.12
1 ML Li	-1.50	-0.81	-1.06	1.50	1.50	2.05

Table 5.6: Key structural and electronic properties for full and half monolayer adsorption of lithium on the clean diamond C(111) surface.

When compared to the C(100) case, Li is less stable, with an adsorption energy of $1.2-1.4$ eV, compared to 3.10 eV for the stablest 0.5 ML coverage on the C(100) surface and 3.26 eV for the full ML case. The workfunction shift is also around half to a third the size in the C(111) case, and a similar decrease in the NEA strength is also observed. The very low adsorption energies for both 0.5 ML and 1 ML coverage indicate that Li on the bare C(111) surface is unlikely to remain at even moderate temperatures. One reason for this difference could be the reduced charge available on the C(111) surface compared to the C(100) surface, reducing the dipole effect causing the NEA effect of alkali metals on diamond.

Looking at the Mulliken population the lithium atoms in the 0.5 ML case pick up only a small positive charge of +0.43 to +0.53e, with the two chain carbon atoms gaining a negative charge equivalent to the charge lost by the lithium, but split between them so that the most negatively charged carbon atom gains only -0.31e. This is different to the situation on the (100) surface, where the lithium atom in the T3 site gains +0.8 e, creating at least double the electric dipole between the lithium adsorbate and the carbon surface. In addition, the C(100) case shows negative

charge on the second layer carbons, which is not observed in the HL C(111) case.

For the full ML on the clean surface, the Mulliken populations of the lithium are +0.29e and +0.72e. There is a larger transfer of charge to the upper chain carbon atoms (-0.34 e and -0.43 e respectively) and a more significant gain of charge on the lower chain carbons on the surface layer (-0.12 e compared to just -0.03 e for the 0.5 ML coverage). However, as with the 0.5 ML case there was no significant transfer of charge to the second layer of carbon atoms as observed for the C(100) surface. Interestingly the lithium atom with the stronger positive charge of +0.72 e in the full monolayer case is the one in the 'cave' position above the lower carbon surface chain, even though the majority of the negative charge is transferred to the upper carbon chain. This is in contrast to the 0.5 ML surface, where the lithium sits in a stable position above the upper carbon chain, albeit with a similar charge to the upper lithium in the full monolayer case. This would imply that the first lithium atom saturates the carbon dangling bond on the upper chain, with the second adsorbate inducing a more significant shift in charge.

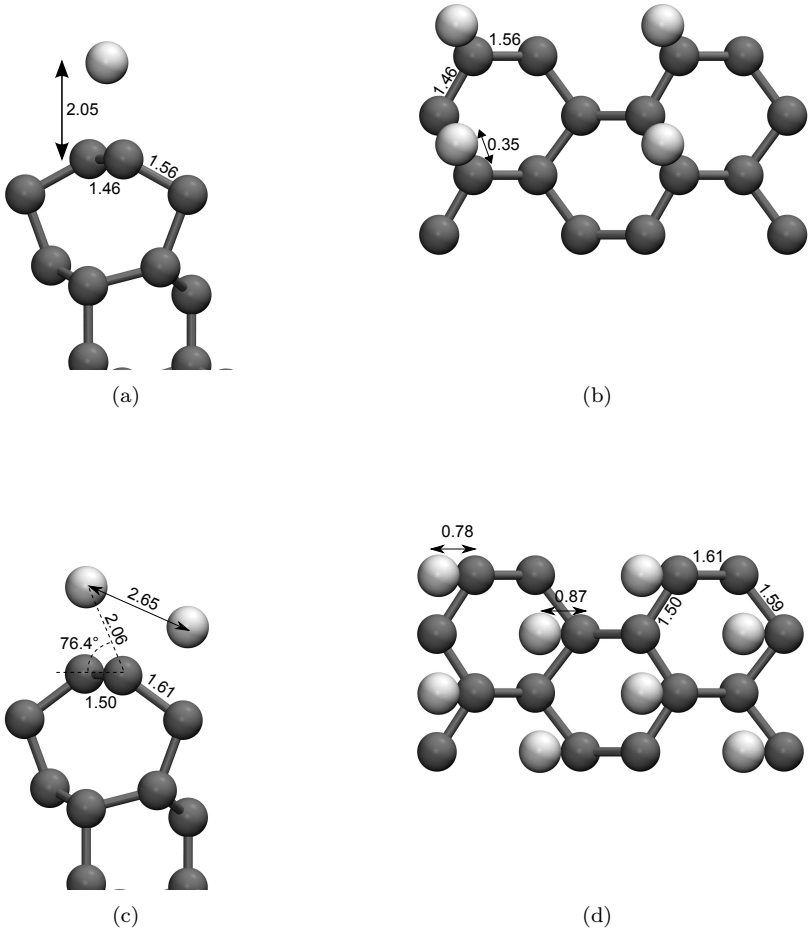

Figure 5.21: Side on and top down images of the 0.5 ML and 1 ML coverage of lithium on the C(111) bare surface

5.5.5 Lithium adsorption on the oxygenated C(111) surface

Although the adsorption of lithium on the bare C(111) surface is not as strongly bound or as strong a workfunction lowering layer as on the C(100) surface, when the effect of lithium on the oxygenated C(111) is modelled, it shows a similarly promising surface layer as on the oxygenated C(100) surface, albeit with a different surface construction and coordination. Both the carbonyl and ether configurations had stable systems, and both will be considered separately. Figure 5.22 shows the stable configurations of lithium adsorption on the on-top carbonyl termination, which had two oxygen atoms per unit cell. The calculated binding energies, bond lengths and electron affinities are shown in table 5.7.

Structure	E_{abs} (eV/ads)	χ (eV)	$\Delta\phi$ (eV)	d_{C-C_U} (Å)	$d_{11(C-C_L)}$ (Å)	d_{CO} (Å)	d_{OLi} (Å)
0.5 ML (Up)	4.10	-2.58	-2.84	1.50	1.53	1.26	1.82
0.5 ML (Down)	4.37	-3.97	-4.23	1.17	1.533	1.26	1.71
Full ML	3.54	-1.13	-1.39	1.50	1.53	1.33	1.81/1.73

Table 5.7: Key structural and electronic properties for full and half monolayer adsorption of lithium on the oxygen-terminated (carbonyl) diamond C(111) surface.

Unlike the C(100) system, where a full monolayer of lithium was favoured, the half monolayer of lithium coverage is preferred, with two different stable positions for the lithium atom in each unit cell. The 0.5 ML 'Up' position, where the lithium atom sits equidistant between three carbonyl oxygen atoms above the upper Pandey chain of carbons, has an adsorption energy of -4.10 eV, and a negative electron affinity of -2.58 eV, for a workfunction shift of -2.84 eV, a configuration slightly less strongly bound than the hydrogen termination, but with a more negative electron affinity. The Down position, in which the lithium atom sits above the lower Pandey chain and is again equidistant to three oxygen atoms, is slightly stronger bound with an adsorption energy of -4.37 eV, perhaps due to increased distance from the carbon atoms (the closest carbon atom is 2.86 Å away from the lithium atom in the Down configuration compared to 2.49 Å in the Up configuration). In addition, the Down configuration has a much more negative electron affinity and a larger workfunction shift, at -3.97 eV and -4.23 eV respectively.

The structures for the 0.5 ML coverages of lithium on the carbonyl bonded oxygenated C(111) surface are shown in Figure 5.22. In the 'Up' case the lithium atom sits in the pedestal between the two oxygen atoms, although it is closer to one oxygen atom than the other. In the 'Down' configuration there is a clear trigonal symmetry where the lithium sits centrally between three oxygen atoms, two belonging to one upper carbon chain and the third oxygen lying on the adjacent upper chain, with the lithium sitting above the lower surface carbon chain. The lithium in the 'Down' position sits closer to the oxygen atoms, albeit further away from the carbon atoms below. The oxygen-lithium bonds are 0.1 Å shorter on average in the 'Down' configuration than the 'Up' configuration indicating a stronger bond, as expected from the higher adsorption energy. The underlying oxygen-carbon bonds increase in length from 1.19 Å without lithium adsorption to 1.25 Å after the addition of lithium, indicating a reduction in charge between the two atoms.

After a full monolayer of lithium as shown in Figure 5.23 is adsorbed the system becomes less stable with an adsorption energy -3.54 eV but also a much less significant NEA effect is observed, with an electron affinity of -1.13 eV and a workfunction shift of just -1.39 eV, closer to that

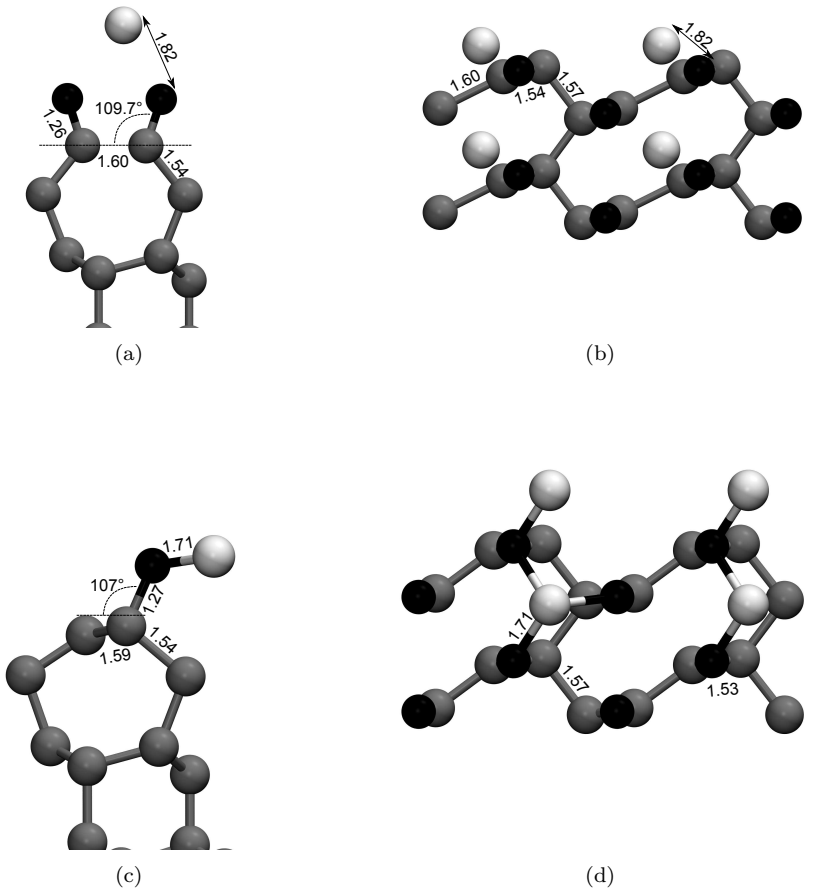

Figure 5.22: Side and top views of the two 0.5 ML coverages on the on-top carbonyl oxygen terminated C(111) surface with the (a) 'Up' (b) 'Down' 0.5 ML lithium coverages.

observed by lithium on the bare surface. The positions of the two lithium atoms are analogous to a combination of those in the 0.5 ML case with the Up lithium atom remaining further from its nearest carbon and oxygen neighbours than the Down lithium atom. The carbon-oxygen bond length does increase from 1.25 Å to 1.33 Å however, indicating a lessening of the charge in the bond when a full ML is present. The population of the C-O bonds change from 0.96 e to 0.80 e. The Mullikan population charge on the two oxygen atoms in the 0.5ML configurations are -0.52 e and -0.60 e for the 'Up' configuration and -0.56 e and -0.62 e for the 'Down' configuration, whereas both oxygen atoms in the full ML have a charge of -0.63 e. The lithium atoms have a charge of +0.74 e and +0.80 e in the 'Up' and 'Down' 0.5 ML configurations respectively, but this is reduced to +0.57 e and +0.45 e for each in the full monolayer case. This reduction in charge on the atoms in the surface dipole evidently contributes to the less negative electron affinity for the full ML case. In addition, there appears to be some mixing of the lithium $2s$ orbitals between the two lithium atoms in a metallic-like bond, rather than the purely ionic interaction between the oxygen and the

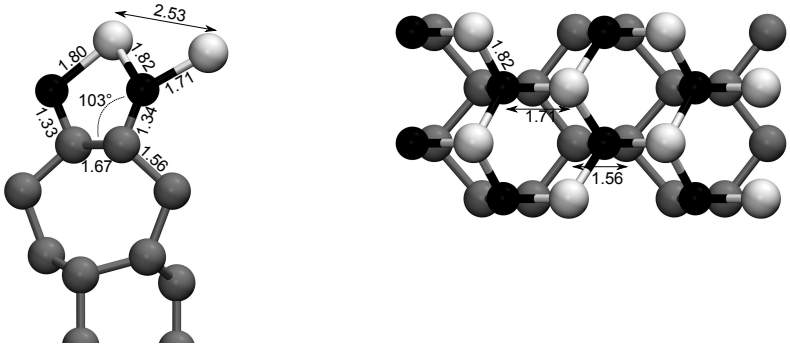

(a) (b)

Figure 5.23: Side and top views of the 1 ML coverage of lithium on the on-top carbonyl oxygen terminated C(111) surface.

single lithium in 0.5 ML case. This conflicting arrangement removes some of the charge used in the stronger bond on the 0.5 ML surface and accounts for the lower positive charge on the lithiums in the full monolayer.

The effect of lithium adsorption on the C(111):O ether bridge configuration is somewhat different to that of the on-top carbonyl termination. As shown in Table 5.8, the adsorption energies for both the 0.5 ML and the full ML coverages of lithium on the ether bridge surface are much lower. The 0.5ML coverages have adsorption energies around half that of the same coverage on the carbonyl surface, although again it is the lithium in the 'Down' configuration above the lower Pandey chain that is slightly more stable than the lithium position above the upper Pandey chain. Again in a reversal to the behaviour seen on the carbonyl surface but similar to the effect seen on the C(100) surface, the full monolayer is in this case stronger bound than the 0.5 ML case, with an adsorption energy of -2.69 eV/atom, although this is still around 1 eV/atom less than E_{ads} for the full monolayer of lithium on the carbonyl surface.

The electronic behaviour of the ether bridge case is also different. The full monolayer case and the 'Up' 0.5 ML configuration have similar electron affinity and workfunction shifts but around half as large an effect is observed for the other 0.5 ML 'Down' configuration. Unlike the carbonyl case, the 'Up' configuration has a more negative electron affinity than the 'Down' case, -2.91 eV compared to -1.61 eV respectively. The full monolayer has a marginally more negative electron affinity than the 'Up' configuration, with an NEA of -3.10 eV and a workfunction shift of -3.36 eV.

Structure Structure	E_{abs} (eV/ads)	χ (eV)	$\Delta\phi$ (eV)	d_{C-C_U} (Å)	$d_{11(C-C_L)}$ (Å)	d_{CO} (Å)	D_{O-Li} (Å)
0.5 ML (Up)	2.01	-2.91	-3.17	1.53	1.58	1.44	1.81
0.5 ML (Down)	2.26	-1.61	-1.87	1.54	1.59	1.41	1.83
1 ML	2.69	-3.10	-3.36	1.53	1.60	1.54	1.75

Table 5.8: Key structural and electronic properties for full and half monolayer adsorption of lithium on the oxygen-terminated (ether-bridge) diamond C(111) surface.

When the structure of the surface in the bridge configuration is studied after 0.5 ML of lithium coverage as shown in Figure 5.24 the breaking of the bridge structure after lithium adsorption seems to provide an explanation for this reversal in behaviour. Whereas in the carbonyl case each upper Pandey chain carbon atom remain bonded to the oxygen atom above even after lithium adsorption, in the ether configuration the bridge bonding the surface oxygen to the two upper Pandey chain carbon atoms below it is broken in the presence of lithium. In the carbonyl case, the double bond between the Pandey chain carbons and surface oxygens extends and reduces in charge, indicating a change closer to a single bond as the oxygen bonds with the adsorbed lithium. In the ether bridge case, however, the two bonds of the oxygen are split between two surface carbons, so one of these bonds needs to be broken in order to accommodate the adsorbed lithium.

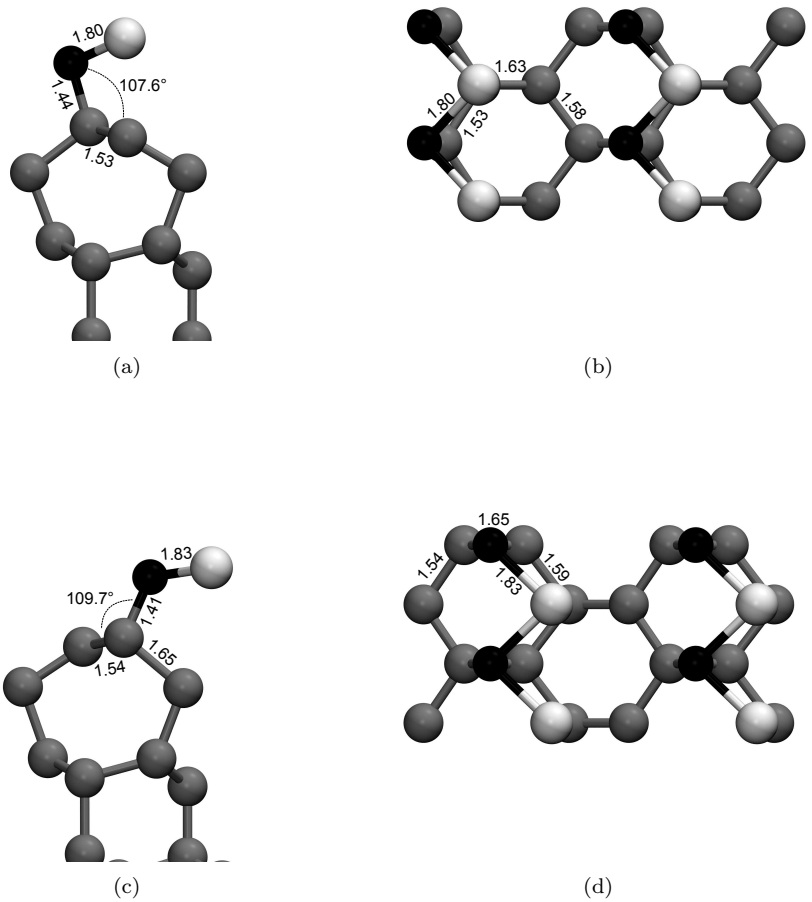

Figure 5.24: Side view of the 0.5 ML coverages of lithium on the ether bridge oxygen terminated C(111) surface configuration.(a) and (b) show the 'Up' configuration, whilst (c) and (d) show the 'Down' configuration.

The position of the lithium in the cell appears to define which carbon-oxygen bond is broken. In the 'Up' configuration, the lithium sits roughly above one of the upper chain carbon atoms, pushing

the remaining oxygen-carbon bond away from this point. The presence of the lithium above the now unsaturated surface carbon atom could help explain the less negative electron affinity of this case, as the dipole between the oxygen and lithium is lessened by the interaction between the surface carbon and the lithium. In the Down case, the position of the lithium pulls the oxygen away from the upper Pandey chain in the opposite direction, leaving the unsaturated surface carbon atom a considerably longer distance from the lithium. In both cases the carbon atom still bonded to the oxygen is raised compared to its unsaturated neighbour, with the distance between them increasing to from 1.47 Å without lithium coverage to 1.53 Å in the 'Up' case and 1.54Å for the 'Down' case, with an angle between the upper carbon and its two unsaturated neighbours reducing to 111.2° for the 'Up' surface and 110° for the 'Down' surface, from 116° for the surface before lithium adsorption.

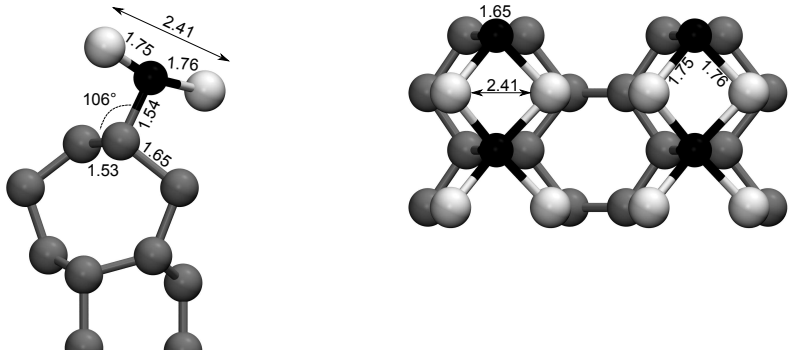

(a) (b)

Figure 5.25: Side and top views of the 1 ML coverage of lithium on the ether bridge oxygen terminated C(111) surface.

By comparison, the full monolayer coverage of lithium on the bridge-bonded oxygenated surface shown in Figure 5.25 resembles the surface structure of the Down configuration, where the unsaturated carbon is on the opposite side of the oxygen to the lithium lying above the lower Pandey chain in the pedestal position. In this case the second lithium lies above the unsaturated upper Pandey chain carbon in the bridge position. There is an increase in negative charge in the Mullikan populations of the surface layer of carbons, with a charge of -0.37 e on the unsaturated carbon beneath the lithium in the bridge position, and charges of -0.12 e on each of the two carbons in the lower Pandey chain beneath the pedestal lithium. The carbon bonded to the oxygen atom has no overall charge, whereas the oxygen atom has a charge of -0.75 e. The larger fraction of charge is lost from the pedestal lithium above the lower Pandey chain, which has a total charge of +0.81 e, whereas the bridge lithium above the upper Pandey chain has a charge of +0.56 e. The angle between the Upper chain carbon atoms is 111.7°, and the length of the bond on the Upper Pandey chain is 1.53 Å and that of the lower Pandey chain is 1.59 Å, similar values as for the 0.5 ML case where the lithium sits above that chain. The Li-O bond length decreases to 1.75 Å from 1.82 Å in the 0.5 ML case, and the C-O bond increases substantially, from 1.40 Å with 0.5 ML Li coverage

to 1.54 Å when a full monolayer of lithium is present. The angle between the two lithium atoms and the nearest oxygen is 86°.

5.5.6 Projected Density of States of the C(111) Li-O surface

Projected density of states for the carbonyl on-top configuration

Figure 5.26 shows the density of states (DOS) projected onto surface oxygen, first layer carbon and midlayer carbon atoms for the on-top carbonyl surface coverage, before and after Li adsorption. The mid-layer carbons without Li coverage in Figure 5.26 (a) shows broad sp^3 diamond features in the region -5 eV to -15 eV region as expected, with increased sp^2 bonding in the surface level carbons at states below the Fermi level. The pair of surface oxygens contribute sharp, non-bonded peaks below the Fermi level that correspond to the lone pairs on each Oxygen. As in the C(100) case[39], after the adsorption of 0.5ML lithium these lone pair peaks are broadened and shift, overlapping the bulk states, indicating a bonding of ionic character between the oxygens and the Li^+ ion and a delocalisation of the negative lone pairs. The change after lithium adsorption is less clear cut compared to C(100) case, where the initial lone pair levels are clearer and the broadening more distinctive, but for the two forms of 0.5 ML coverage, there does seem to be some trend towards delocalisation of the peaks in the 0 to -5.5 eV region.

After the full ML of lithium is adsorbed, a new feature appears within the band gap of both the surface oxygens and (weakly) the surface carbons, as well as a concentration of charge in the valence band closest to the Fermi level. There does seem to be more distinct, localised peaks in the full monolayer case than in either of the two 0.5 ML cases which are more broadened, as might be expected from the Mulliken populations showing a reduction in the positive charge on the full monolayer lithium atoms and a corresponding reduction in adsorption energy and workfunction shift.

Looking at the Kohm-Sham orbitals for the carbonyl surface, there are two localised orbitals in the system before lithium adsorption as shown in Figure 5.27. These appear to correspond with π-like bonds and p-shaped orbitals respectively, with no σ-like or sp-like bonds as seen on the C(100) surface, likely due to the lower number of dangling bonds available on the C(111) surface. The p-shaped orbitals on the right are the likely contributors to the sharp lone pair peaks observed in the PDOS figure above.

Figure 5.28 shows the localised Kohn-Sham orbitals for the carbonyl system after 0.5 ML of lithium coverage, in this case the 'Down' configuration. As before the oxygen π-like orbitals are observed, although there seems to be some disruption of the shape and some delocalisation across the four surface carbons. The p-shaped orbitals also remain, but again with slightly more delocalisation into the broader carbon surface. In addition to these two orbitals which remain similar to that on the bare surface there is a third semi-localised orbital, concentrated between the two oxygens below the lithium, and on the top two surface carbons. This is interpreted to be the delocalisation of the lithium $2s$ electron as observed in the shift in charge using Mulliken population analysis. The other 'Up' configuration of the 0.5 ML coverage shows a similar behaviour but with a larger electron density on the surface C-C bond, as might be expected when the lithium lies directly above it.

Figure 5.29 shows the Kohn-Sham orbitals for the full monolayer case. There are only two

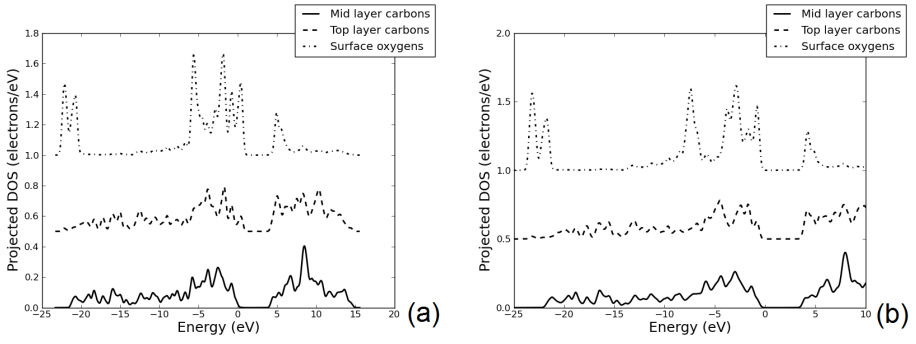

(a) (b) (c) (d)

Figure 5.26: Projected density of states of the bulk carbons, surface carbons and surface oxygens for the oxygen-on-top carbonyl termination with (a) no lithium coverage, (b) and (c) half ML lithium coverage in the 'Up' and 'Down' positions respectively and (d) full monolayer lithium coverage.

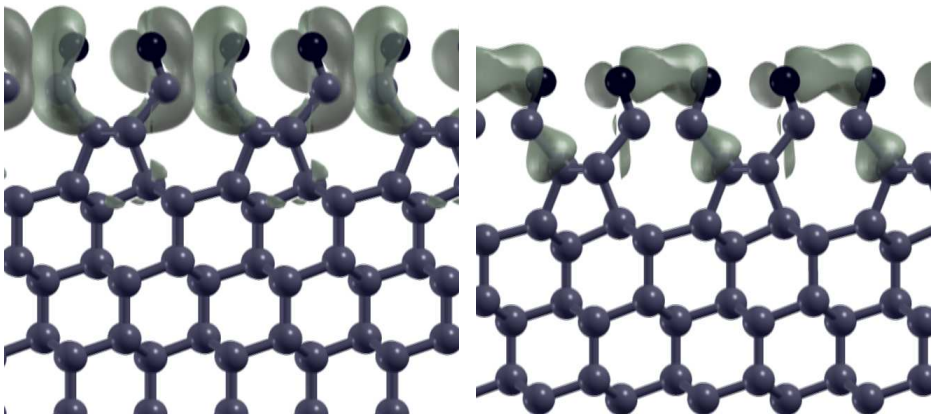

(a) (b)

Figure 5.27: The localised Kohn-Sham orbitals on the top surface of the carbonyl bonded oxygenated C(111) system.

localised bands on the top surface. The first again shows π-like bonding around the oxygen atoms, whilst the second is more complicated, showing a broad delocalisation through the top three layers of carbon atoms, as well as across the oxygen atoms and between the two lithium atoms. The bulk of the charge remains closer to the lithiums than in the 0.5 ML case, and the kind of surface dipole effect observed on the C(100) system does not appear to be present for the full monolayer of lithium on the carbonyl-bonded C(111) surface - the presence of the electronic charge between the lithium atoms and the oxygens below in particular would likely form a barrier to electron removal from the carbon bulk, potentially explaining the lower workfunction shift for the full monolayer adsorption, where the half monolayer case has less charge localised near the lithium atoms.

Projected density of states for the ether bridge configuration

The projected density of states of the surface oxygen, surface carbon and bulk carbon atoms in the oxygen-bridge configuration of the C(111) surface react in a slightly different manner to the carbonyl configuration, as shown in Figure 5.30. Because of the single lone pair on the sole oxygen in each unit cell, the feature below the Fermi level is simpler. After the adsorption of 0.5 ML of lithium, this feature becomes more pronounced and is separated more clearly from the lower energy features, indicating a localisation of charge. This effect is greatly reduced for the full ML coverage, where the oxygen lone pair features are shifted lower in energy and broadened, indicating a delocalisation of charge far larger than for 0.5 ML coverage of Li.

Unlike the carbonyl surface, the ether bridge oxygenated C(111) surface before lithium adsorption has four localised orbitals, each shared between the top and bottom surfaces of the slab. Three show *sp*-like or *p*-shaped orbital behaviour, whilst the fourth (Figure 5.31(a)) is a more amorphous distribution between the surface carbons and oxygen atom.

Figure 5.32 shows the localised bands for the ''Up' configuration of the 0.5 ML coverage on the ether-bridge surface. This configuration was slightly less strongly bound than the 'Down' configuration (an adsorption energy of 2.01 eV/adsorbate compared to 2.26 eV/adsorbate for the

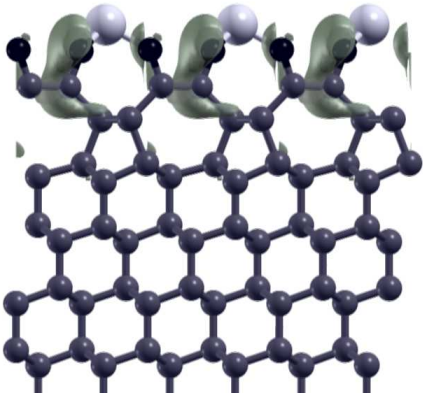

(a)

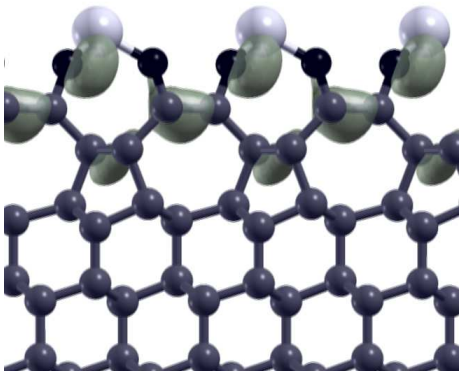

(b)

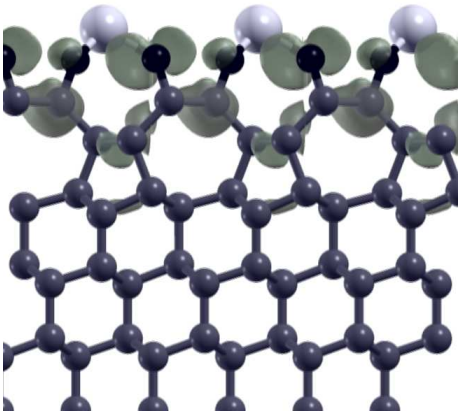

(c)

Figure 5.28: The localised Kohn-Sham orbitals on the top surface of the carbonyl bonded oxygenated C(111) system after a 0.5 ML coverage of lithium.

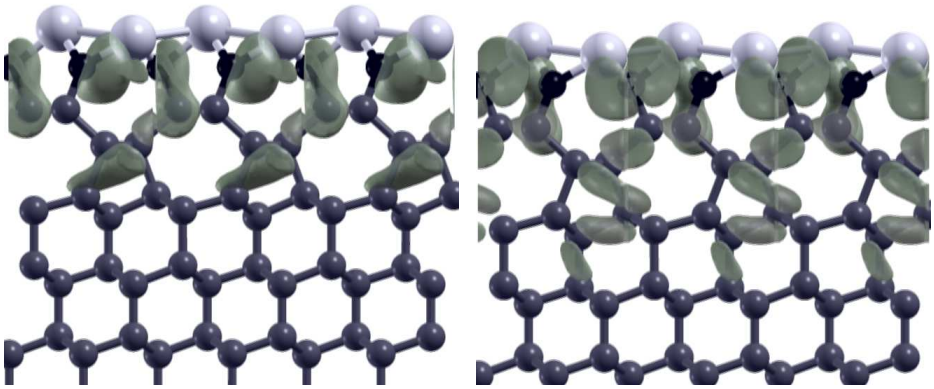

(a) (b)

Figure 5.29: The localised Kohn-Sham orbitals on the top surface of the carbonyl bonded oxygenated C(111) system after 1 ML coverage of lithium.

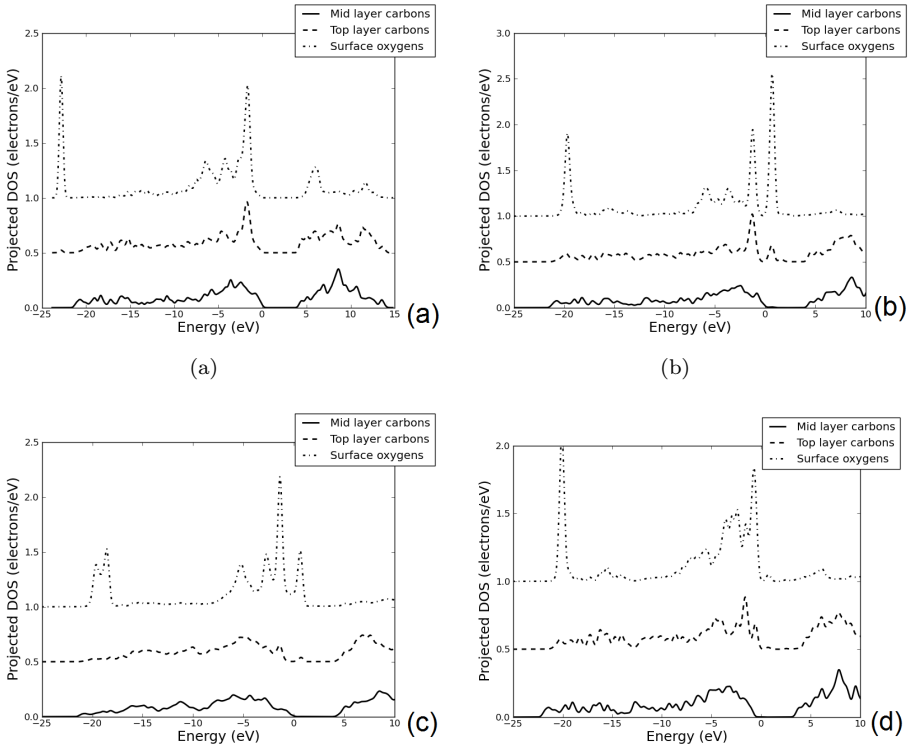

(a) (b)

(c) (d)

Figure 5.30: Projected density of states for the bulk C, surface C and surface O atoms for the ether-bridge surface termination, (a)prior to lithium termination (b) and (c) half ML lithium coverage in the 'Up' and 'Down' positions respectively and (d) full ML lithium coverage.

'Down' configuration), but the 'Up' configuration had a much higher workfunction shift of -3.17

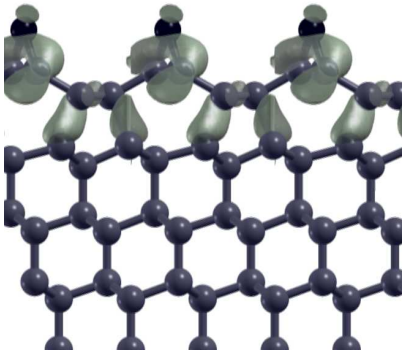

(a)

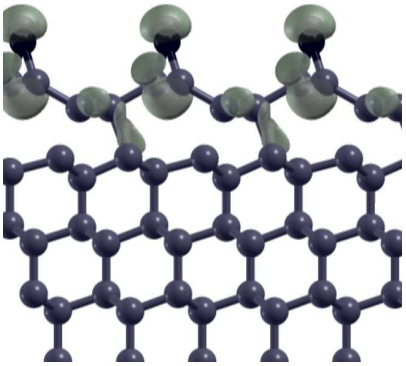

(b)

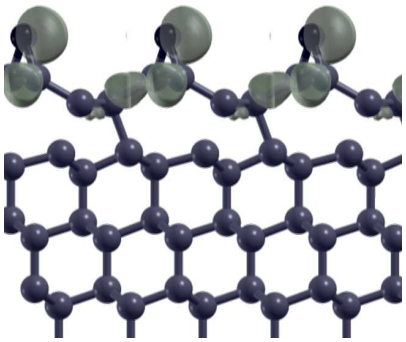

(c)

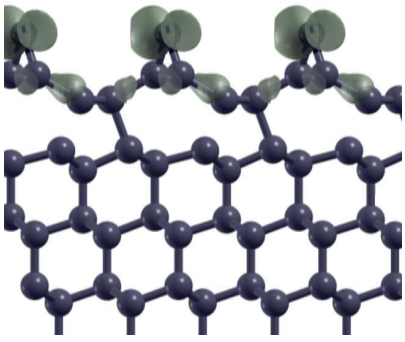

(d)

Figure 5.31: The localised Kohn-Sham orbitals on the top surface of the ether bridge bonded oxygenated C(111) system.

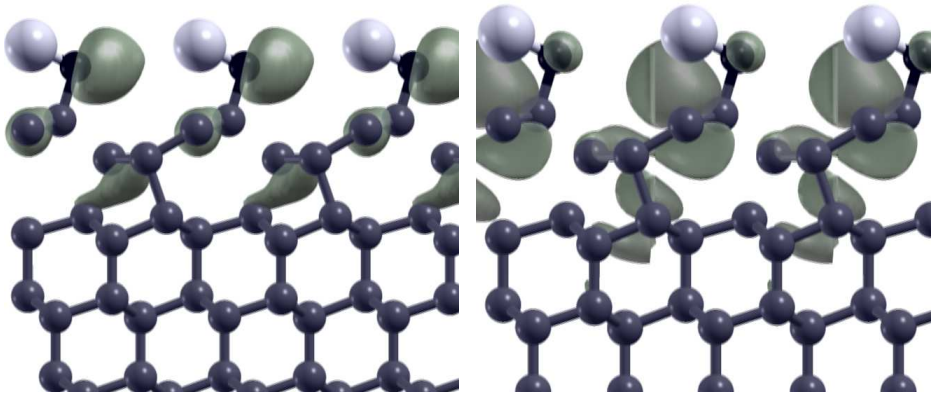

(a) (b)

Figure 5.32: The localised Kohn-Sham orbitals on the top surface of the ether bridge bonded oxygenated C(111) system after a half monolayer of lithium adsorption in the 'Up' configuration.

eV compared to just -1.87 eV for the 'Down' configuration. There are two localised orbitals per surface. The localised orbitals are no longer shared between the top and bottom surfaces but are localised only to one surface. This split where the site closer to the lower carbon chain is more stable but the site above the upper surface has a higher workfunction shift is similar to the effect for the 0.5 ML coverage on the bare C(100) surface, where the upper surface has less stability but the transfer of charge is larger from the upper carbon bond. The *p*-shaped orbitals appear to remain, with the bulk of the density shifted to the opposite side of the oxygen atom to the lithium's adsorbed position, and some charge distributed into the second layer carbons. The second localised orbital is more complicated, with a large amount of delocalisation into the first two carbon layers.

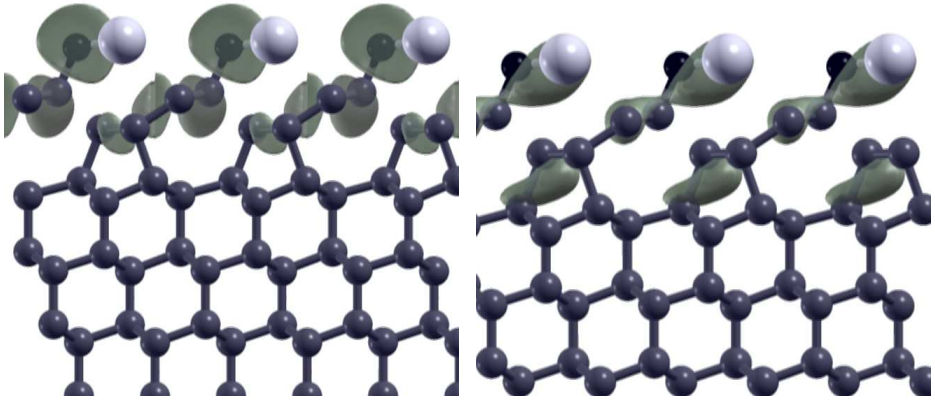

(a) (b)

Figure 5.33: The localised Kohn-Sham orbitals on the top surface of the ether bridge bonded oxygenated C(111) system after a half monolayer of lithium adsorption in the 'Down' configuration.

Figure 5.33 shows the localised bands for the 'Down' configuration of the 0.5 ML coverage on

the ether-bridge surface. Compared to the 'Up' configuration, the electron density of the Kohn-Sham orbitals is much more ordered, with far less delocalisation into the surface carbon layers and a larger percentage of the density surrounding the oxygen atom. It seems likely that the further distance between the lithium atom and the carbon lattice has a lower forcing effect on spreading the charge into the lattice, but the increased charge on the oxygen atom provides a stronger Li-O bond than on the 'Up' configuration, as evidenced by the marginally higher adsorption energy.

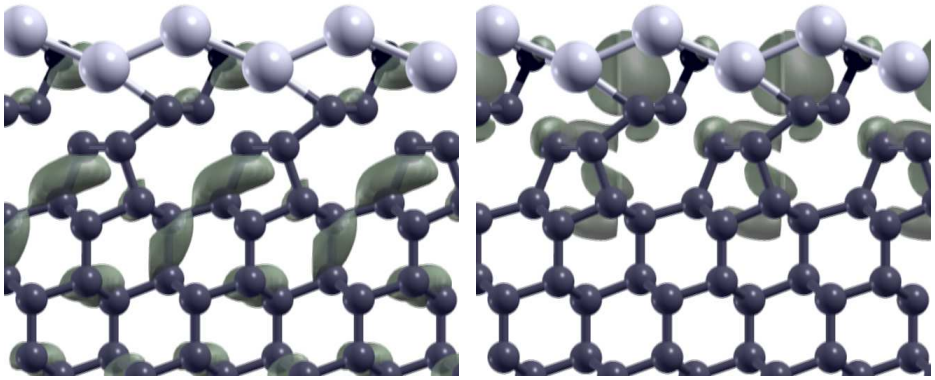

(a) (b)

Figure 5.34: The localised Kohn-Sham orbitals on the top surface of the ether bridge bonded oxygenated C(111) system after a full monolayer of lithium adsorption.

Figure 5.34 shows the localised bands for the full monolayer coverage of lithium on the ether-bridge surface, which had a adsorption energy of 2.69 eV/adsorbate and a workfunction shift of -3.36 eV, both larger than either of the constituent half monolayer coverages, unlike the reduction seen with the full monolayer on the ketone surface. Even the localised bonds on the top surface show large amounts of delocalisation into the carbon lattice, with charge reaching as far as the fifth carbon layer in one orbital. This delocalisation is dramatically more than in either 0.5 ML coverage, perhaps as with the lithium coverage occupying both available stable adsorption sites the electron density disturbed by the lithium atoms in their ionic state cannot be shifted around on the surface, so must be pushed further into the lattice.

5.6 Comparison of the C(100) and C(111) Li-O surface layers

Although both the C(111) and C(100) surfaces show negative electron affinities when lithium is present on both the bare and oxygenated diamond surface, the behaviour of the two is somewhat different. In general, the C(100) surface shows consistently higher binding energies, especially on the bare surface where the maximum adsorption energy per adsorbate is just 1.50 eV for the full monolayer of lithium on the clean C(111) surface, compared to 3.26 eV for the HH + T3 combination on the clean C(100) surface. There are also a number more stable positions the lithium atom can occupy on the bare C(100) surface, probably due to the C(111) surface possessing one less dangling bond per surface carbon, leading to a weaker interaction between the lithium and

surface carbon dimer. There were four stable positions (the Levine sites) for 0.5 ML Li adsorption on the bare C(100) surface, but only one on the C(111) surface. Table 5.9 compares the binding energy per Li atom, workfunction shift and electron affinity for all the stable Li adsorption sites on the bare and oxygenated surfaces. By comparison, Table 5.10 shows the same information for the C(111) surface.

Coverage	Structure	surface	E_{abs} (eV/ads)	$\Delta\phi$ (eV)	χ (eV)
0.5 ML	T3	bare	3.10	-2.07	-1.45
	HH	bare	2.63	-3.21	-2.59
	T4	bare	2.57	-2.54	-1.92
	HB	bare	2.12	-1.77	-1.15
1 ML	HH + T3	bare	3.26	-3.32	-2.70
	HH + T4	bare	3.04	-3.15	-2.53
	HB + T3	bare	3.02	-3.29	-2.67
	HB + T4	bare	2.74	-2.99	-2.37
0.5 ML	OP	oxygenated	4.71 (K), 4.07 (E)	-2.70	-2.08
	OB	oxygenated	3.54 (K)	-1.87	-1.25
1 ML	HH + T3	oxygenated	4.70 (K), 4.38 (E)	-4.52	-3.89
	HB + T3	oxygenated	3.90 (K), 3.76 (E)	-3.00	-2.38
	HB + T4	oxygenated	3.36 (K)	-2.30	-1.67

Table 5.9: Workfunction shift and negative electron affinity for lithium adsorption on the C(100) bare and oxygenated surface.

As well as being more stable on the C(100) clean surface, both the full and half monolayer of coverage of lithium show a much stronger negative electron affinity on the C(100) surface compared to the C(111) surface, as well as a correspondingly larger workfunction shift. The biggest workfunction shift for 0.5 ML coverage on the C(100) surface was -3.21 eV with an NEA of -2.59 eV, compared to just -0.84 eV and -0.58 eV respectively for the same level of coverage on the C(111) surface. Likewise, a full monolayer of lithium on the C(100) surface causes a workfunction shift of as much as -3.32 eV with an NEA of -2.70 eV, whereas the full monolayer on the C(111) surface exhibits a workfunction shift of just -1.06 eV and an NEA of -0.81 eV. This decrease on the C(111) surface is again likely due to the fewer dangling bonds on the surface carbon, which are likely to result in a smaller dipole effect between the ionic lithium atom and the electron-rich carbon lattice below. The low stability and relatively poor workfunction shift of lithium on the clean C(111) surface make it an unlikely candidate for a successful surface treatment for improving electron emission.

Comparing the behaviour of the two oxygenated surfaces is interesting. Stability-wise the C(111) carbonyl surface with lithium adsorbed compares fairly well with the same coverage on the C(100) surface, with adsorption energies of 4.10 eV and 4.37 eV/adsorbate for the two 0.5 ML coverages, compared to 4.71 eV/adsorbate and 3.54 eV/adsorbate for the two 0.5 ML configurations on the C(100) surface. Unlike the C(100) surface, the full monolayer of lithium on the carbonyl surface is less stable than the half monolayer by $0.56 - 0.83$ eV, indicating that a 0.5 ML coverage is favoured, whereas the most stable full ML configuration on the C(100) carbonyl surface had a similar adsorption energy to the most stable 0.5 ML coverage. This preferred 0.5 ML coverage for the C(111) surface may actually be useful experimentally, as the full monolayer has a much smaller

Coverage	surface	E_{abs} (eV/ads)	$\Delta\phi$ (eV)	χ (eV)
0.5 ML	bare	1.21	-0.84	-0.58
1 ML	bare	1.50	-1.06	-0.81
0.5 ML Up	Carbonyl	4.10	-2.84	-2.58
0.5 ML Down	Carbonyl	4.37	-4.23	-3.97
1 ML	Carbonyl	3.54	-1.39	-1.13
0.5 ML Up	Ether	2.01	-3.17	-2.91
0.5 ML Down	Ether	2.26	-1.87	-1.61
1 ML	Ether	2.69	-3.36	-3.10

Table 5.10: Workfunction shift and negative electron affinity for lithium adsorption on the C(111) bare and oxygenated surface.

effect on the workfunction than either 0.5 ML coverage.

The ether bonded oxygenated surface is less stable after lithium adsorption than the carbonyl surface on both the C(111) and C(100) surfaces. Interestingly on the C(111) surface the 1 ML coverage on the ether bonded surface is more stable and has a higher workfunction shift and NEA than the 0.5 ML coverage. The C(111) surface seems to be optimised when there are three adsorbate atoms per unit cell - either two oxygens and one lithium, or the reverse. This is one less than the preferred arrangement on the C(100) surface, but is logical considering there is one less dangling bond available on the C(111) surface.

By adsorbing lithium on the oxygenated diamond surface it has been predicted that a strongly bound surface system can be formed that shifts the workfunction dramatically downward and induces a strong negative electron affinity. The C(100) surface is the most stable and likely the easiest to control due to the simpler preferred structure of one monolayer of lithium on top of one monolayer of carbonyl-bonded oxygen. As a result attempts to produce such a surface on single crystal diamond would likely be more successful on the C(100) surface. However, the fact that some stable workfunction lowering structures are also formed on the C(111) surface is very useful for the possibility of producing such a surface on polycrystalline CVD diamond or multifaceted diamond crystals such as diamond grits, where the vast majority of faces will be a mix of the two. The fact that both surfaces should be able to display an NEA after oxygenation and lithium coverage is promising for potential device applications as these polycrystalline materials are cheaper and easier to produce.

REFERENCES

[1] Koizumi, S., Nebel, C., and Nesládek, M. *Physics and Applications of CVD Diamond*. Wiley-VCH, (2008).

[2] May, P. *PHil. Trans. R. Soc. Lond. A* **358**, 473–495 (2000).

[3] Hamza, A., Kubiak, G., and Stulen, R. *Surf.Sci.* **237**, 35–52 (1990).

[4] Sutcu, L., Chu, C., Thompson, M., Hauge, R., Margrave, J., and D'Evelyn, M. *J. Appl. Phys* **71**, 5930 (1992).

[5] Tsuno, T., Imai, T., Nishibayashi, Y., Hamada, K., and Fujimori, N. *Jpn.J.Appl.Phys.* **30**, 1063–1066 (1991).

[6] Ravi, K. *Mater. Sci. Eng. B* **19**, 203 (1993).

[7] Alfonso, D., Drabold, D., and Ulloa, S. *Phys. Rev. B.* **51**, 14669–14685 (1995).

[8] Pandey, K. *Phys. Rev. B* **25**(6), 4338–4341 (1982).

[9] Tong Lee, S. and Apai, G. *Phys. Rev. B.* **48**, 2684–2693 (1993).

[10] Hamza, A., Kubiak, G., and Stulen, R. *Surf. Sci. Lett.* **206**(35), L833–L844 (1988).

[11] Derry, T., Makau, N., and Stampfl, C. *J. Phys.: Condens Matter* **22**(26), 265007 (2010).

[12] Ristein, J. *Appl. Phys. A* **82**, 377–384 (2006).

[13] Lurie, P. and Wilson, J. *Surf. Sci.* **65**, 453–475 (1977).

[14] Mucha, J., Flamm, D., and Ibbotson, D. *Journal of Applied Physics* **65**, 3448–3452 (1989).

[15] Diederich, L., Aebi, P., Küttel, O., and Schlapback, L. *Surface Science* **424**(2-3), L314–L320 April (1999).

[16] Thoms, B., Owens, M., Butler, J., and Spiro, C. *Applied Physics Letters* **65**, 2957–2959 (1994).

[17] Ley, L., Graupner, R., Cui, J., and Ristein, J. *Carbon* **37**(5), 793799 (1999).

[18] Kataoka, M., Zhu, C., Koeck, F., and Nemanich, R. *Diamond Relat. Mater.* **19**, 110–113 (2010).

[19] Rutter, M. and Robertson, J. *Phys. Rev. B* **57**, 9241–9245 (1998).

[20] van Der Weide, J., Zhang, Z., Baumann, P., Wensell, M., Bernholc, J., and Nemanich, R. *Physical Review B* **50**(8) (1994).

[21] Maier, F., Ristein, J., and Ley, L. *Phys. Rev. B* **64**(16), 165411 Oct (2001).

[22] Diederich, L., Küttel, O., Aebi, P., and Schlapback, L. *Surface Science* **418**(1), 219–239 November (1998).

[23] Ristein, J. *Surf. Sci.* **600**, 3677–3689 (2006).

[24] Maier, F., Riedel, M., Mantel, B., Ristein, J., and Ley, L. *Physical Review Letters* , 14–17 (2000).

[25] Pickett, W. *Phys. Rev. Lett.* **73**(12), 1664–1667 (1994).

[26] Geis, M., Twichell, J., Macaulay, J., and Okano, K. *Appl. Phys. Lett.* **67**, 1328 (1995).

[27] Diederich, L., Küttel, O., Aebi, P., Maillard-Schaller, E., Fasel, R., and Schalpabach, L. *Diam. Relat. Mater.* **7**(2), 660–665 (1998).

[28] Loh, K., Xie, X., Yang, S., Pan, J., and Wu, P. *Diam. Relat. Mater.* **11**(7), 1379–1384 (2002).

[29] Nie, J., Xiao, H., Zu, X., and Gao, F. *Chemical Physics* **326**(2-3), 308 – 314 (2006).

[30] Nie, J., Xiao, H., Zu, X., and Gao, F. *Physica B: Condensed Matter* **383**(2), 219 – 225 (2006).

[31] Kobayashi, K., Morikawa, Y., Terakura, K., and Blügel, S. *Phys. Rev. B* **45**(7), 3469–3484 Feb (1992).

[32] Morikawa, Y., Kobayashi, K., Terakura, K., and Blügel, S. *Phys. Rev. B* **44**(7), 3459–3462 Aug (1991).

[33] Shi, H., Radny, M., and Smith, P. *Surface Science* **561**(2-3), 215 – 226 (2004).

[34] Petrick, S. and Benndorf, C. *Diam. Relat. Mater.* **10**, 519 (2001).

[35] Hossain, M., Kubo, T., Aruga, T., Takagi, N., Tsuno, T., Fujimori, N., and Nishijima, M. *Diamond and Related Materials* **9**(2), 162 – 169 (2000).

[36] Wong, K. W., Wang, Y., Lee, K., and Kwok, R. *Diam. Relat. Mater.* **8**, 1885–1890 (1999).

[37] Wong, K., Wang, Y., Lee, S., and Kwok, R. *Applied Surface Science* **140**(1-2), 144 – 149 (1999).

[38] Clark, S., Segall, M., Pickard, C., Hasnip, P., Probert, M., Refson, K., and Payne, M. *Zeitschrift fur Kristallographie* **220**(5-6), 567–570 (2005).

[39] K.M. O'Donnell, T.L. Martin, N. F. and Cherns, D. *Phys. Rev. B* **82**, 115303 (2010).

[40] Perdew, J. and Wang, Y. *Phys. Rev. B* **46**(20), 12947–12954 Jan (1992).

[41] Vanderbilt, D. *Phys. Rev. B* **41**(11), 7892–7895 Jan (1990).

[42] Rilby, D. *Nature* **153**, 587–588 (1944).

[43] Covington, E. and Montgomery, D. *J. Chem. Phys.* **27**, 1030 (1957).

[44] Monkhorst, H. and Pack, J. *Phys. Rev. B* **13**(12), 5188–5192 (1976).

[45] Fall, C., Binggeli, N., and Baldereschi, A. *J. Phys. Condens. Matter* **11**, 2689–2696 (1999).

[46] Baumann, P. and Nemanich, R. *Journal of Applied Physics* **83**(4) (1998).

[47] Tamura, H., Zhou, H., Sugisako, K., Yokoi, Y., Takami, S., Kubo, M., Teraishi, K., Miyamoto, A., Imamura, A., N.-Gamo, M., and Others. *Physical Review B* **61**(16), 1102511033 (2000).

[48] Zheng, X. and Smith, P. *Surface Science* **262**(1-2), 219 – 234 (1992).

[49] Sque, S., Jones, R., and Briddon, P. *Phys. Rev. B* **73**(8), 085313 Feb (2006).

[50] Furthmller, J., Hafner, J., and Kresse, G. *EPL (Europhysics Letters)* **28**(9), 659 (1994).

[51] Furthmüller, J., Hafner, J., and Kresse, G. *Phys. Rev. B* **53**(11), 7334–7351 March (1996).

[52] Yang, Y. and D'Evelyn, M. *J. Vac. sci. Technol. A* **10**(4), 978–984 (1992).

[53] Jing, Z. and Whitten, J. *Surface Science* **314**(2), 300 – 306 (1994).

[54] Koleske, D., Gates, S., Thoms, B., Russell, J., and Butler, J. *J. Chem. Phys* **102**, 992 (1995).

[55] Chang, X., Perry, M., Peploski, J., Thompson, D., and Raff, L. *J. Chem. Phys* **99**, 4748 (1993).

[56] Kobayashi, K., Morikawa, Y., Terakura, K., and Blügel, S. *Phys. Rev. B* **45**(7), 3469–3484 Feb (1992).

[57] Abukawa, T. and Kono, S. *Phys. Rev. B* **37**(15), 9097–9099 May (1988).

[58] Parker, S. and Rhead, G. *Surface Science* **167**(2-3), 271 – 284 (1986).

[59] O'Donnell, K., Martin, T., Fox, N., and Cherns, D. *MRS Proceedings* , 1282 (2011).

[60] Zheng, J., Xie, X., Wee, A. T., and Loh, K. *Diamond and Related Materials* **10**(3-7), 500 – 505 (2001).

[61] Baerends, E. and Gritsenko, O. *The Journal of Physical Chemistry A* **101**(30), 5383–5403 (1997).

[62] Stowasser, R. and Hoffmann, R. *Journal of the American Chemical Society* **121**(14), 3414–3420 (1999).

[63] Holtom, R. and Gundry, P. *Surface Science* **63**, 263 – 273 (1977).

[64] Broyden, C. *J. Appl. Maths.* **6**(1), 76–90 (1970).

[65] Fletcher, R. *The Computer Journal* **13**(3), 317–322 (1970).

[66] Goldfarb, D. *Mathematics of Computation* **24**(109), 23–26 (1970).

[67] Vanderbilt, D. and Louie, S. *Phys. Rev. B* **29**(12), 7099–7101 Jun (1984).

[68] Vanderbilt, D. and Louie, S. *Phys. Rev. B* **30**(10), 6118–6130 Nov (1984).

[69] Sowa, E., Kubiak, G., Stulen, R., and Van Hove, M. *J. Vac. Sci. Tech. A* **6**(3), 832–833 (1988).

[70] Takeuchi, D., Kato, H., Ri, G., Yamada, T., Vinod, P., Hwang, D., Nebel, C., Okushi, H., and Yamasaki, S. *Applied Physics Letters* **86**(15), 152103 (2005).

[71] Kanai, C., Watanabe, K., and Takakuwa, Y. *Jpn. J. Appl. Phys.* **38**(7A), 783–785 (1999).

[72] Su, C., Song, K.-J., Wang, Y. L., Lu, H.-L., Chuang, T. K., and Lin, J.-C. *J. Chem Phys.* **107**, 7543 (1997).

[73] Su, C. and Lin, J. C. *Surface Science* **406**(1-3), 149 – 166 (1998).

[74] Cui, J. B., Ristein, J., and Ley, L. *Phys. Rev. B.* **59**(8), 5847 (1999).

[75] Cui, J., Ristein, J., and Ley, L. *Phys. Rev. Lett.* **81**(2), 429–432 Jul (1998).

[76] Loh, K., Xie, X., Yang, S., and Zheng, J. *The Journal of Physical Chemistry B* **106**(20), 5230–5240 (2002).

Depth must be hidden. Where?
On the surface.

Hugo von Hofmannsthal
(1874-1929)

6

Experimental observation of the Li-O NEA surface

6.1 Introduction

In the previous chapter the computational predictions were presented for a lithium coating on the oxygenated C(100) and C(111) surfaces. A single monolayer of lithium (two lithium atoms per unit cell) on the oxygenated C(100) surface was calculated using CASTEP to have a negative electron affinity of -3.89 eV and a workfunction shift of -4.52 eV from the bare surface, comparable to the shift observed for caesium oxide on the diamond surface,[1;2] but with a much higher predicted stability of 4.7 eV/adatom.[3] A similarly strong construction on the C(111) surface was predicted for a 0.5 ML coverage of lithium on the carbonyl surface, with a negative electron affinity of -3.97 eV, a workfunction shift of -4.23 eV and a binding energy of 4.7 eV/adsorbate. The calculations suggest that if a thin lithium film can be carefully prepared onto oxygenated diamond, a stable, strongly negative electron affinity surface can be produced, with a number of promising applications.

Following these computational predictions of a stable NEA when lithium is adsorbed on the oxygenated C(100) and C(111) diamond surface, a series of photoemission experiments were designed to try and observe such a surface experimentally. Although such surface constructions could have been produced on the nanodiamond powders studied in Chapter 4 or on polycrystalline CVD films, to unambiguously study the effect, monocrystalline diamond crystals oriented in the (100) and (111) directions were obtained commercially. The experiments used CVD and HPHT grown single crystal diamond substrates in both the C(111) and C(100) orientations, in addition to conductive C(100) boron-doped overlayers. The effects of hydrogen and oxygen termination on the X-ray Photoemission Spectroscopy (XPS) and Ultraviolet Photoemission Spectroscopy (UPS) behaviour of the samples was studied, as well as the effect of lithium treatment on the oxygenated surface.

The experiments used the XPS system in the Interface Analysis Centre for early work, but the resolution and vacuum quality was deemed insufficient for the lithium analysis, as the sensitivity of the lithium 1s signal in XPS is very weak compared to other elements. For the later XPS measurements and UPS spectra, samples were taken to the Advanced Technology Institute at the University of Surrey, where time was acquired on the Omicron UHV Multiscan system in place there.

6.1.1 Previous photoemission studies of diamond surfaces

Previous XPS studies of diamond surfaces

X-ray photoemission studies are fairly well established for diamond, with a large numbers of studies of the hydrogen and oxygen-terminated surfaces in particular.

Bonding configuration	Binding Energy (eV)	Binding Energy relative to main peak (eV)
sp3 (diamond)	285	0
sp2 (graphitic)	284.5	-0.5
C-O	286.5	+1.5
C=O	288.5	+2.5
COO (carboxylic acid groups)	289	+3
C-H (hydrocarbons)	284.5	-0.5
CO_3 (carbonates)	292	+7

Table 6.1: Features of the carbon 1s XPS peak due to different atomic bonding.[4]

Table 6.1 shows the principle peaks observable from the carbon 1s XPS peaks. The carbon 1s peak of diamond is typically centred at 285 eV, after adjustment for any charging effects on non-conductive samples. Close to this peak centre is the characteristic peak of both graphite and hydrocarbons, which if present on diamond are usually observable as a shoulder 0.5 eV below the diamond line. In the case of charging, the conductivity of graphitic components means the 284.5 eV peak should stay where it is, whilst the diamond peak will be shifted. The presence of carbon-oxygen bonds can be observed as a series of shoulders at higher binding energy to the main diamond line, with increasing chemical shifts for more negative carbon-oxygen bonds - so a shift of around 1.5 eV implies a single C-O bond, a shift of $2-3$ eV is characteristic of a double bond between the two elements, and higher chemical shifts implies an even more negative environment as found in compounds such as carboxylic groups and carbonates.

In diamond the XPS line at 285 eV should be much more intense than any of the shoulders.

Bonding configuration	Binding Energy (eV)
single bonded O (for hydrocarbons)	533
double bonded O (for hydrocarbons)	531
Li_2O	531.3
CO_3 (Carbonate)	531.5
LiOH	531.8

Table 6.2: Features of the oxygen 1s XPS peak due to different atomic bonding.[4]

Table 6.2 shows the principle peaks observable from the oxygen 1s XPS peaks. The oxygen 1s spectra can be found between 529 eV and 535 eV, depending on the bonding state of the material studied - typically the higher the binding energy, the less negatively charged the oxygen atom and the more single-bonded in character the oxygen bond is.

Table 6.3 shows the principle peaks observable from the lithium 1s XPS peaks. The main lithium peak for lithium in its metallic form and for bonds such as those in lithium hydroxide is found at 55 eV, with more polarised ionic bonding configurations observable at higher chemical

Bonding configuration	Binding Energy (eV)
metallic Li	55
LiOH	55
ionic Li^{2+}	57

Table 6.3: Features of the lithium 1s XPS peak due to different atomic bonding.[4]

shifts of $+(1-3)$ eV.

Previous UPS studies of diamond surfaces

A negative electron affinity was first discovered by Himpsel *et al*[5] on diamond using UPS spectra from the (111) surface. Himpsel used synchrotron radiation between 13 and 35 eV to prove that the vacuum level lay below the conduction band minimum. Photon stimulated ion desorption (PSID) showed this surface to be hydrogen terminated,[6] with a (1×1) LEED pattern. Hydrogen termination was shown to be removed for temperatures between 825 and 1300 °C,[7–10] and after removal of hydrogen the characteristic NEA peak in the UPS spectra disappears and a positive electron affinity has been observed for both CVD diamond[11] and natural diamond.[12] The workfunction for the hydrogen terminated C(111) surface showed a workfunction of 3.4 eV, rising to 4.8 eV after hydrogen removal[13], with field emission turn-ons of 2-5 V/μm.

There is still some debate over the process involved with NEA surfaces. The model suggested by Cui *et al*[14] is that the NEA is due to surface dipole layers, in the hydrogenated case between the hydrogen adatoms and top surface carbon atoms, creating a negatively charged state in the carbon lattice with a positively charged top adatom layer, making the barrier to emission far less than when there is a large electron density at the top surface as in the bare or oxygenated surfaces. Bandis and Pate[15] suggest that electrons thermalised to the conduction band minimum interact with holes to form surface dipoles, that allow them to then photoemit, with the transport from bulk to surface of the electron-hole pairs occurring during the photo-excitation. Diederich *et al*[16] suggest that due to momentum conservation, an NEA peak should not be observed from the C(111) surface, yet UPS spectra from hydrogen termination or Zirconium and Cobalt metals on C(111) diamond[17] and hydrogen terminated or caesium-oxide terminated C(111) diamond[1] do show a characteristic peak indicative of an NEA surface on C(111) oriented diamond.

6.2 Single Crystal Diamond Surfaces

The substrates used in this study were sourced from Element 6[18], consisting of three principle types. CVD single crystal diamond squares of dimensions $(2.6 \times 2.6 \times 0.3)$ mm, oriented to within 3 ° of the (100) direction and polished to better than 10 nm roughness on one side, were used for the majority of the photoemission studies, due to their low percentage of other elements, with a guaranteed concentration of less than 1 ppm of nitrogen and less than 0.05 ppm of boron. The edges were laser cut to the (100) plane, with edge features of the order of less than 200 μm. An example plate is shown in figure 6.1 (a).

In addition to the CVD material, two types of single crystal high pressure, high temperature (HPHT) Type Ib plate were used in the initial characterisation work. The $(2.6 \times 2.6 \times 0.3)$ mm (100)

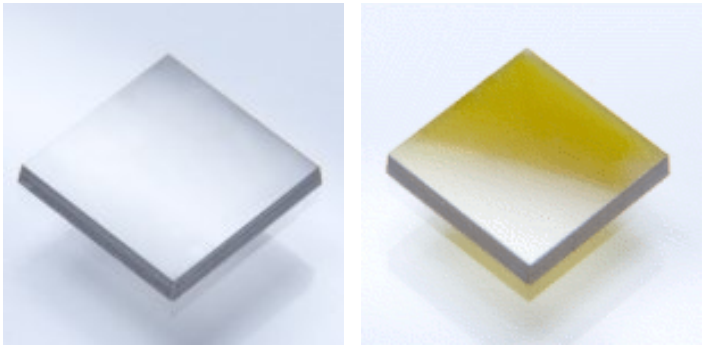

(a) (b)

Figure 6.1: Photograph of an example plate of the Element 6 C(100) oriented $2.6 \times 2.6 \times 0.3$ mm diamond samples used in this experiment. (a) shows the CVD and (b) the HPHT substrates. [18]

oriented HPHT plates as pictured in Figure 6.1(b) were very similar to the as-received CVD plates, with a polished top surface with a roughness below 10 nm and a $\pm 3°$ error in the crystallographic orientation. The principle different was in the nitrogen content, which was approximately 200 ppm, with a boron content below 0.1 ppm. Typically the plates were more than 80% single sector, with slightly higher probability of growth sector boundaries than in the CVD plate. In addition to the (100) oriented samples, some HPHT plates in the (111) orientation were also ordered. These had similar properties to the (100) HPHT plates but were of a smaller size, of the order of $(2 \times 2 \times 1)$ mm.

For later UPS and XPS measurements where a conductive surface was required to prevent charging, 2-4 μm boron-doped overlayers were grown onto these CVD (100) samples using microwave plasma-enhanced CVD growth. The exact preparations steps for this overlayer is presented later in this chapter.

6.3 Characterisation of surface termination on diamond

6.3.1 Contact Angle measurements of hydrogen and oxygen-terminated diamond

For initial study, the contact angle of water drops on the different terminations of the diamond was studied. The hydrogenated surface is strongly hydrophobic, resulting in large contact angles to a droplet of water on the hydrogenated diamond surface, whereas the oxygenated surface is hydrophilic and wets much more easily. As well as checking this behaviour to test the effectiveness of the hydrogen/oxygen termination steps, the lithium-oxygen surface was tested for its contact angle with water. For this process and the later XPS characterisation, fifteen samples were prepared - five HPHT C(100) squares, five CVD C(100) squares and five HPHT C(111) squares. All the samples were obtained from Element Six Ltd and were sonicated in isopropanol, acetone and isopropanol again before any studies were made, to remove any surface contaminants.

The samples were divided into five groups of three chips, with one of each chip in each group. One group was left unchanged as a control, with notional hydrogen termination from the growth

steps. The second group was acid washed in a fuming nitric acid solution (50 ml sulphuric acid at 200 °C with 5 g of potassium nitrate added once white fumes appeared) - this was done twice for an hour each time.

A third group was placed in a Jelight UVO Ozone cleaner under an oxygen gas flow, with a UV power source a few mm from the samples. Ozone treatment was performed in four five minute runs. After the various surface treatments, CVD squares from each group were tested for their contact angle with water.

Figure 6.2: 0.2ml of water dropped onto diamond squares with different surface treatments (a) as recieved diamond, (b) ozone treated diamond (c) acid washed diamond. All samples were CVD (100) single crystals, (c) is mounted on XPS tungsten stage.

Figure 6.2 shows three 0.2 ml water droplets on each of the samples. The first shows the as-received material, with a contact angle of 40° indicating some degree of oxygen termination. Figure 6.2(c) shows the same type of diamond crystal after acid washing, mounted on a tungsten XPS stage. It has a much steeper contact angle (60°) indicating a lower percentage of oxygen termination and a higher hydrogen termination (or potentially OH termination), indicating that the acid treatment has not had the desired effect of increasing oxygen coverage on the diamond surface.

Figure 6.2(b) shows a CVD square after ten minutes exposure to ozone. It has a much shallower contact angle (30°), compared to the acid washed material, indicating a much larger presence of hydrophilic oxygen terminations. Interestingly although the ozone treated sample had a lower contact angle than the as-received material, the acid washed surface was far higher than either, indicating that the oxygen termination predicted by multiple acid wash treatments is not occurring in any great degree here, as suggested by Ostrovskaya *et al*,[19] who suggest that 3-4 acid treatments are required for substantial oxygen coverage.

6.3.2 XPS of hydrogen and oxygen terminated diamond

The same group of fifteen samples from the previous section were also used as a base for studies using X-Ray Photoemission Spectroscopy (XPS). Samples were stuck to a tungsten sample holder using silver dag and a small spot of gold was evaporated onto their centres for charge compensation referencing. After these preparations the tungsten sample holder was mounted on a heating stage and inserted into the XPS system, where it was allowed to pump down to a vacuum of roughly $1\text{x}10^{-8}$ Mbar. Samples were resistively heated to 150 °C to degas any water vapour.

Samples were illuminated using an aluminium X-ray source (1486 eV) at room temperature and substrate temperatures of 200 °C and 400 °C, to study the effect of temperature on charging or charge conduction in the diamond samples. Scans were taken of the wide XPS spectrum as well as the regions corresponding to the carbon $1s$, oxygen $1s$, silver $4d$ and gold $4f$ excitations. The gold reference in the central region was calibrated against its expected 83.95 eV position and the other

spectra were shifted by the Au $4f$ peak shift to match this and accommodate for charging effects. Intensities were adjusted to account for the different sensitivities of each element to detection in XPS. The Atomic Sensitivity Factors of the relevant elements are detailed in Table 6.4 as well as the typical peak positions of the elements in their pure form. Note that the lithium $1s$ sensitivity is orders of magnitude less than any other element, making detection harder.

Element	orbital	elemental peak position (eV)	Atomic Sensitivity Factor
Li	$1s$	55	0.02
C	$1s$	285	0.25
O	$1s$	532	0.65
Ag	$3d5/2$	368.1	5.2
	$3p3/2$	573	1.52
Au	$4f$	83.95	4.95

Table 6.4: Sensitivity factors for detection in X-ray photoemission spectroscopy for the elements observed in this study.[4]

Spectra were deconvoluted using Fityk,[20] a peak fitting program designed for broad use in spectroscopy. Peaks were fitted by hand using Voigt profiles,[21] and allowed to find the least squares positions and shapes using the Levenberg-Marquardt method.[22] A Voigt profile is appropriate for spectra broadened by both Gaussian and Lorentzian profiles and is a convolution of both profiles according to the equation

$$V(x;\sigma,\gamma) = \int G(x';\sigma)L(x-x';\gamma)dx' \tag{6.1}$$

where x is the frequency from the line centre and $G(x;\sigma)$ and $L(x;\gamma)$ correspond to the centred Gaussian and Lorentzian profiles:

$$G(x;\sigma) \equiv e^{-x^2/(2\sigma^2)}/\sigma\sqrt{2\pi} \tag{6.2}$$

and

$$L(x;\gamma) \equiv \gamma/\pi(x^2+\gamma^2) \tag{6.3}$$

At $\gamma = 0$, the Voigt peak is entirely Gaussian, whereas at $\sigma = 0$, the Voigt peak is entirely Lorentzian. When fitting the XPS peaks, the fitting method chooses the most appropriate balance between the two extremes, but the ratio can also be set manually. Areas and heights were calibrated against the area and heights of the respective gold peak for each sample to maintain fair comparisons across the samples.

Sample	RT shift	200 shift	400 shift
CVD (100)	0.9706	0.763	1.1712
HPHT (100)	3.8424	1.7443	1.0527
HPHT (111)	4.9158	3.3117	0.8754

Table 6.5: Comparison of the position of the gold $4f\frac{7}{2}$ peak with increasing temperature on the acid washed diamond samples.

Table 6.5 shows the change in charging of the gold $4f\frac{7}{2}$ peak with increasing temperature, calculated as the center of the observed peak in the XPS scan to the literature value of the Au $4f\frac{7}{2}$ peak at 83.95 eV.[4] As can be clearly seen, the HPHT samples showed a clear decrease in charging with increased temperature from 4-5 eV at RT to around 1 eV at 400 °C. The (111) sample charged more at RT which could be expected by its larger thickness but by 400 °C it was charging less than the (100) HPHT sample. In comparison with the HPHT samples, the CVD (100) crystal did not have a clear trend with increasing temperature and the charging changed only by around 0.2 eV from around 1 eV. The lower absolute value for the shift of the CVD samples's Au peak may be due to the gold being in contact with the silver dag at the edge of the sample, which might explain why it charges slightly more at higher temperatures where the organics in the dag are volatile. The lack of change in charging of the CVD material as temperature rises when compared to the sharp drop in the HPHT materials indicates that at elevated temperatures the nitrogen impurities present in the HPHT samples may introduce some conductivity. The shifts in the Au $4f$ peak was used to adjust the other elemental peaks in an attempt to accommodate charging effects as the isolated gold spot in the sample's centre should charge by the same proportion as the sample itself.

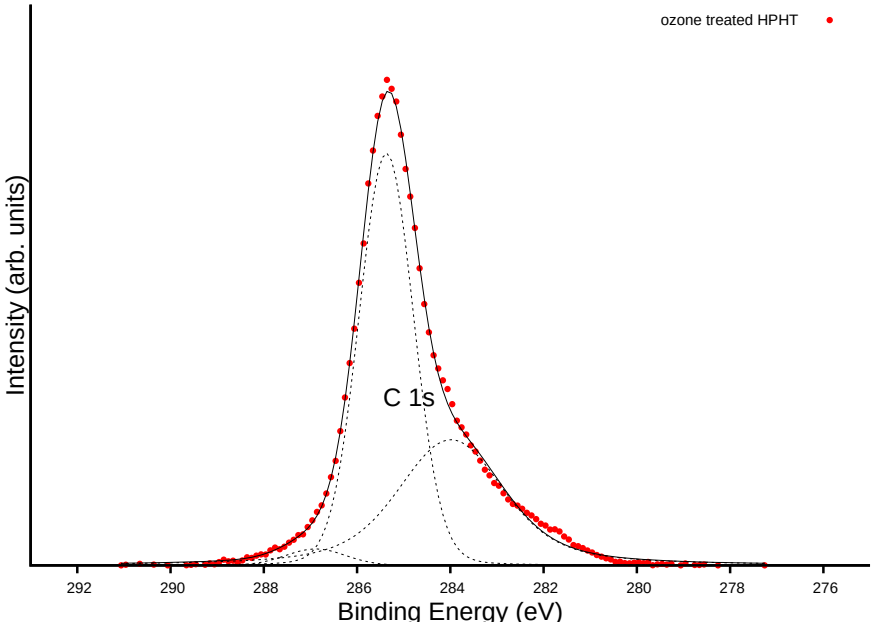

Figure 6.3: X-ray Photoemission spectra for the carbon 1s peak for the ozone treated HPHT(100) material.

Figure 6.3 shows the carbon $1s$ peak of the ozone treated HPHT (100) material, after centre correction using the Gold $4f\frac{7}{2}$ peak, at room temperature, with Voigt peaks modelled beneath each deconvoluted peak. It is dominated by the sp^3 diamond carbon peak at 286.35 eV, with the smaller signal from graphitic content or hydrocarbon contamination at 284.3 eV corresponding to the traditional sp^2 C-C/C-H carbon peak of 284.5 eV. Around 2 eV higher there is a small C-O signal, a low shoulder that is more noticeable than in the acid washed or as-recieved materials.

The oxygen $1s$ peak in XPS is centred at 533 eV for oxygen atoms with single bond to a carbon, such as those found in the ether configuration shown in Figure 6.4. Oxygens in the double-bond

carbonyl formation are shifted to a binding energy of around 2 eV lower than the single bonded case.[23]

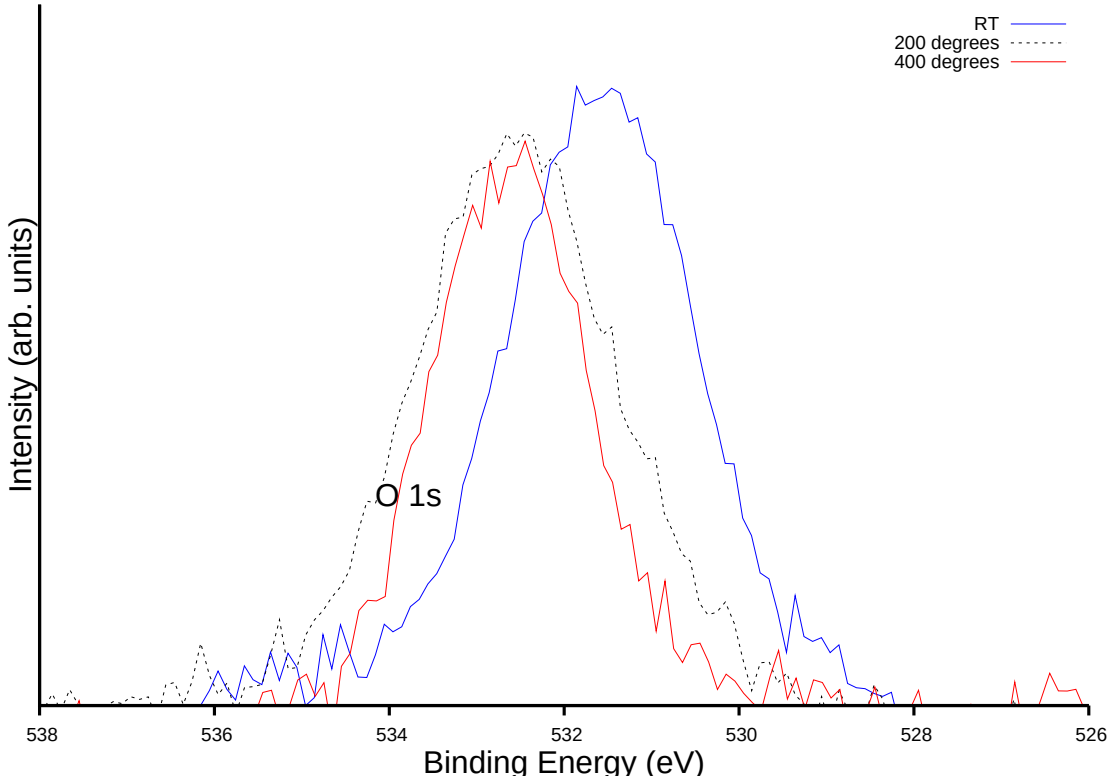

Figure 6.4: X-ray Photoemission spectra for the oxygen 1s peak of acid-treated HPHT(100) diamond, at room temperature(blue), 200°C (dotted) and 400°C (red), showing a clear shift from double bonded oxygens centred at 534 eV at lower temperatures to the single bonded case around 532 eV at higher temperatures.

Figure 6.4 shows the oxygen 1s peak of the acid-treated HPHT(100) sample at a series of temperatures, after calibration with the gold $4f\frac{7}{2}$ reference. It is notable that at room temperature the peak is clearly that of the 532.5 eV single bonded carbon-oxygen case, but at higher temperatures this shifts dramatically to include larger amounts of the the higher binding energy double bond case at around 534.5 eV. This is expected, as the oxygen termination on diamond has been observed to reconstruct to the double-bond at higher temperatures.

The literature peak for atomic lithium is at $54.6 - 55$ eV, with a number of shifts depending on bonding. Lithium oxide, Li_2O, is a lower shift of about 1 eV, wheras lithium peroxide, Li_2O_2 is shifted upwards in binding energy, to approximately 57 eV. Lithium nitride, Li_3N is found at 54 eV, and lithium hydride LiH is present at 55 eV.

Figure 6.5 shows the lithium 1s peak for a HPHT(111) sample lithiated using heating in lithium nitride powder under a nitrogen ambient. No ozone treatment was performed, only an acid washing step, so based on the relatively poor wetting of the acid-washed sample in the contact angle analysis, the actual oxygen coverage of this sample is likely to be low. Although the peak is very low, this

is to be expected, as the Li 1s peak at 54.6 eV has a very low sensitivity in XPS, 0.02 compared to 0.25 for carbon and 0.65 for oxygen. As a result even though this peak is small, when fitted and calibrated for the appropriate sensitivity, it is around three times the intensity of the oxygen peak. Here, after correcting for the charging shift using the gold reference, the lithium peak is centred at 56.6 eV, closest in BE to Li_2O_2. Assuming the oxygen is terminating the diamond surface, this arrangement would match the LiO dipole predicted by the surface modelling, with a monolayer of oxygen overlayed with a monolayer of lithium. The signal however, is very weak, likely due to low oxygen coverage and the C(111) orientation.

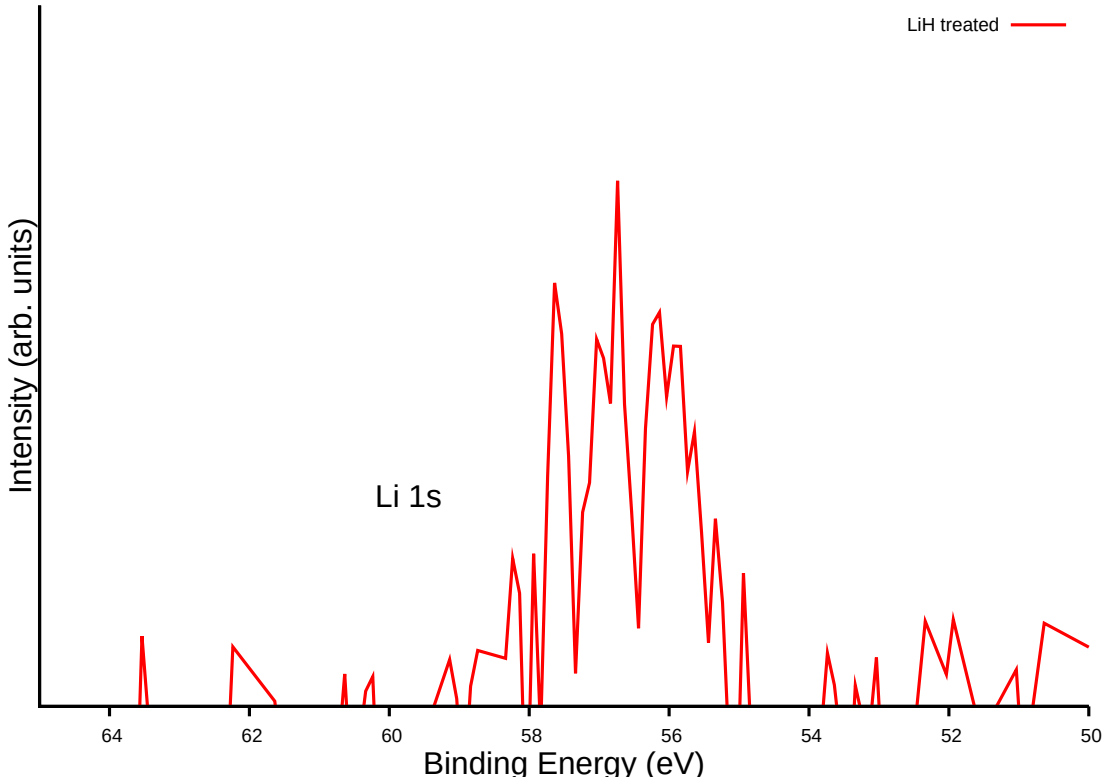

Figure 6.5: X-ray Photoemission spectra for the Lithium 1s peak of acid-washed HPHT(111) diamond, after heating in a nitrogen ambient with lithium nitride.

Next the effect of the lithium hydride and lithium nitride treatments used on the nanodiamond powders was attempted for the C(100) single crystal samples after ozone treatment. The HPHT (100) single crystals were placed within a tungsten boat together with around 1 g of 500 nm HPHT nanodiamond powder and an equivalent quantity of either lithium hydride or lithium nitride powder. The samples were placed in a Balzers 510 coating machine in a pressure of around 1 Torr of argon gas, and heated to approximately 1000 °C, above the decomposition temperature of the lithium compounds, and at a high enough temperature that lithium should be able to diffuse into the diamond lattice. After removal from the chamber, the samples were kept under oxygen-free argon for sample transferral to the XPS chamber. They had the excess diamond and LiH dust brushed off but were not washed before scanning.

Figure 6.6 shows the lithium peak for the acid-washed and ozone-treated C(100) surface observed after heating with lithium hydride. It has a much clearer lithium peak at around 58 eV when compared to the acid-treated C(100) sample. The carbon C 1s signal is shifted up by around 0.6 eV from the expected 285 eV centre due to charging effects on the non-conductive surface. This would make the lithium signal around 57 eV, symptomatic of ionically bonded Li. Whilst this could correspond to the expected Li_2O_2 structure on the surface, without cleaning down to a small number of monolayers this signal is likely due to LiH remaining on the surface.

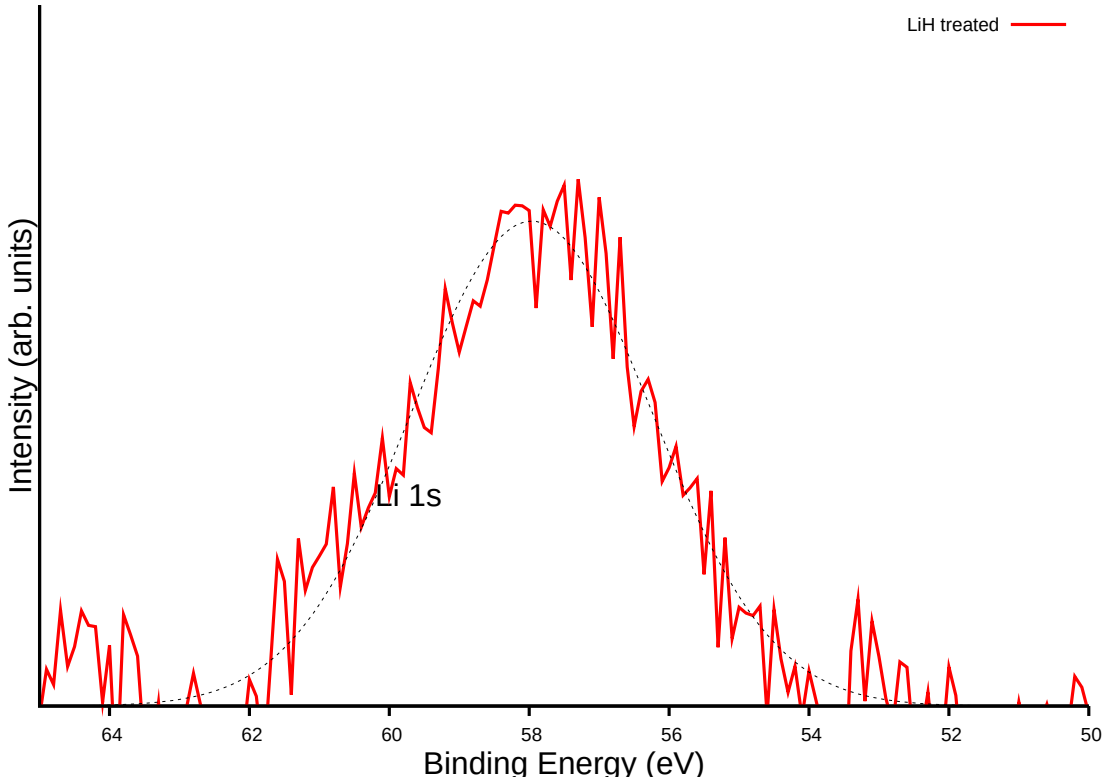

Figure 6.6: X-ray Photoemission spectra for the Lithium 1s peak of acid-treated and ozone treated HPHT(100) diamond, after heating in a nitrogen ambient with lithium hydride.

Figure 6.7 shows the lithium peak observed after heating with lithium nitride. It too shows a clear lithium peak with a centre just above 58 eV. The carbon peak is shifted upwards from 285 eV by approximately 1.5 eV, again showing significant charging. Similarly to the hydride case, without a more controlled method of depositing lithium onto the surface, it is difficult to conclude that the signal is not mostly contributed by the ionic lithium in the nitride.

To combat this problem, pure lithium was evaporated in vacuum onto the sample oxygenated by acid wash and thirty minutes of ozone treatment. Figure 6.8 shows an acid-treated HPHT(100) sample after thermal evaporation of around 50 nm of lithium metal in a Balzers 510 coater at a pressure of 6.6×10^{-4} mBar. The thickness was measured by the evaporation onto a quartz crystal microbalance. As with the hydride and nitride coated materials, a clear lithium is detected around 57 eV, but the carbon 1s peak had its centre at 287.2 eV rather than 285 eV, indicating again a

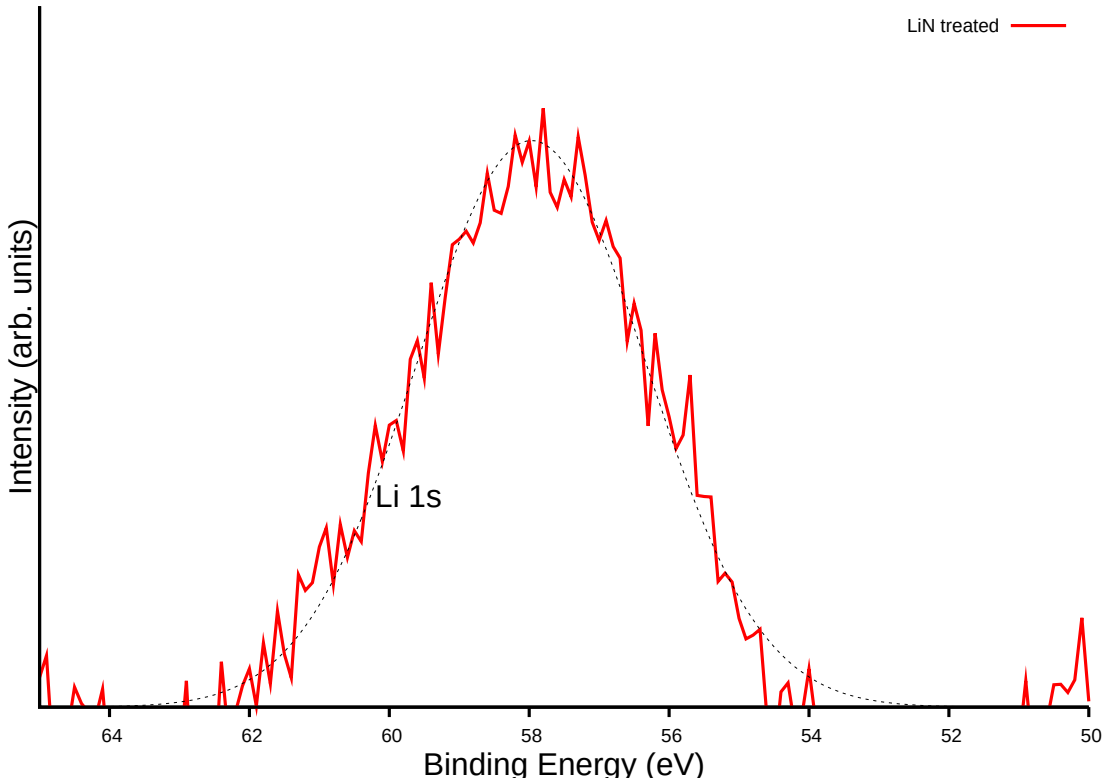

Figure 6.7: X-ray Photoemission spectra for the Lithium 1s peak of acid-treated and ozone-treated HPHT(100) diamond, after heating in a nitrogen ambient with lithium nitride.

clear charging effect.

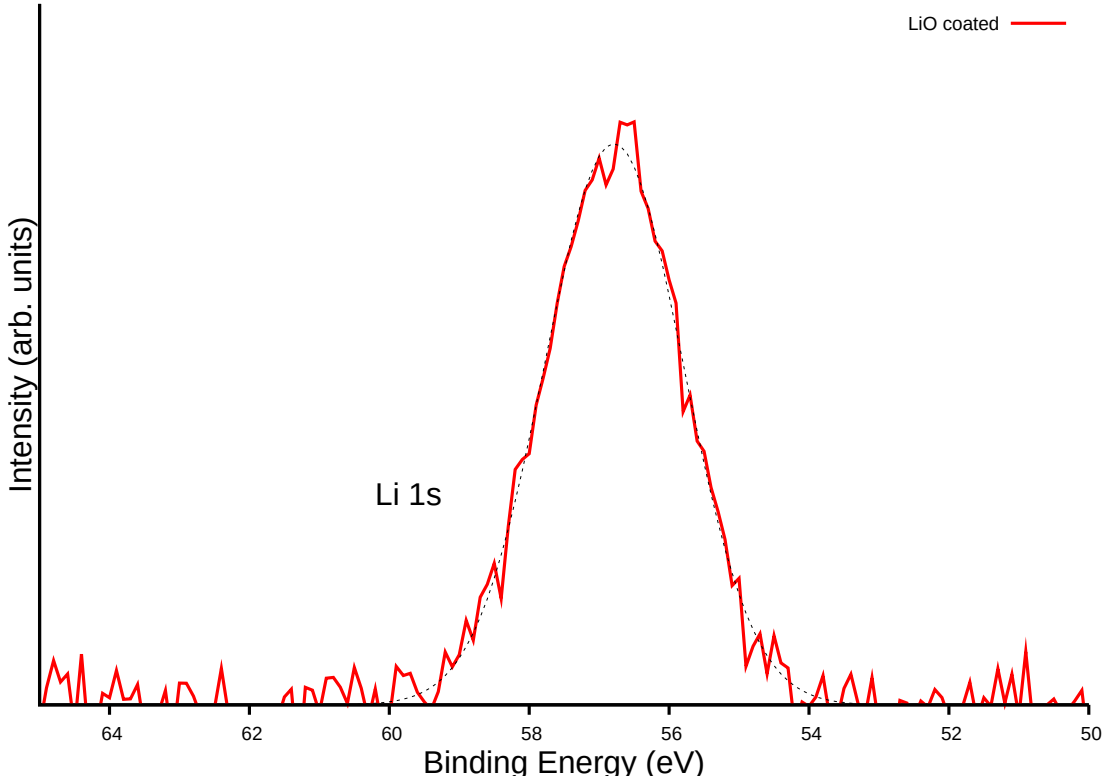

Figure 6.8: X-ray Photoemission spectra for the Lithium 1s peak of acid-treated HPHT(100) diamond, after the evaporation of around 50 nm of lithium metal onto the oxygenated surface.

These experimental results indicated the possibility that theoretically predicted structures are stable in reality, but the charging nature of the samples need solving before a true assessment could be made. Further XPS analysis of more carefully produced samples, with higher oxygen surface coverage was needed, but the low resolution and poor vacuum quality of the XPS system at the IAC in Bristol necessitated access to a better XPS system. Additionally, UPS measurements were not available at the University of Bristol and would be required to study the workfunction and electron affinity properties of this surface. For this reason, time was obtained on the Omicron UHV photoemission system at the University of Surrey, and boron-doped overlayers were grown in order to produce a conductive sample for more accurate spectra without charging effects. The remainder of the results were obtained on that system under the guidance of Hidetsugu Shiozawa and Cristina Giusca, together with Kane O'Donnell.

6.4 Characterisation of Li-O terminated diamond

6.4.1 Preparation of the Li-O surface

Following the XPS studies of oxygen termination on the C(100) surface, it was determined that 30 minutes of ozone exposure was sufficient to provide a good coverage. Boron-doped overlayers were grown to ensure a sufficiently conductive diamond surface for photoemission experiments.

6.4.2 Boron-doped conductive overlayers

In order to prevent charging during photoemission, a conductive substrate was required. To this purpose boron-doped diamond overlayers were grown epitaxially on free standing C(100) single crystal CVD squares, obtained commercially from Element 6, with dimensions ($2.6 \times 2.6 \times 0.5$) mm. The boron-doped overlayers were grown in a microwave plasma system at a pressure of 150 Torr, with 500 sccm of hydrogen, 25 sccm of methane, 40 sccm of argon and 0.5 sccm of boron precursor, which consisted of 5 % diborane in hydrogen. A growth plasma was ignited at a microwave power of 1.25 kW, with a substrate temperature of 720 °C and a growth time of two hours, resulting in an overlayer thickness of approximately 4 μm. After growth, the samples were left in a hydrogen plasma for two minutes at 60 Torr and 1 kW microwave power with only the hydrogen gas present, at a sample temperature of 600 ° C to ensure hydrogen termination. Figure 6.9 shows the microwave plasma within the reactor during boron-doped growth.

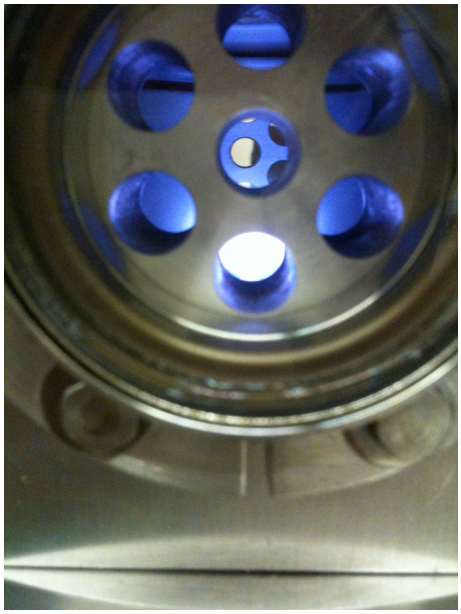

Figure 6.9: Photograph of the microwave plasma during CVD growth for the boron doped overlayers.

6.4.3 Achieving a lithium monolayer

Samples were oxygen terminated using an acid wash in fuming nitric acid for one hour followed by thirty minutes exposure to UV-excited ozone in a UVO ozone cleaner. After this oxygenation treatment, the contact angle on the diamond surface changed markedly from around 60 ° for the hydrogenated surface to 30 ° for the oxygenated surface, indicating the expected change from the hydrophobic hydrogen-terminated surface to the hydrophilic oxygenated surface. In addition, X-ray-photoemission spectroscopy of the as-grown and ozone treated surface showed a change in the C/O ratio of 47.7 to 17.7 when comparing the normalized height intensities of the C 1s and O 1s XPS spectra. In addition to the increase in intensity, the O1s peak position moved from 532.8 eV to 532.2 eV, indicating an increase in negative charge on the oxygen, from predominately single bonded oxygen or hydroxides to double bonded oxygen.[24] Similarly, a shoulder appeared on the C 1s peak at 287 eV after ozone treatment, indicating the presence of C-O-C or C=O bonds on the surface.[25]

For the purpose of the lithium coating, a number of different preparation techniques were considered, including the reaction with lithium salts already studied on the nanodiamond powders. However, this risks introducing a number of additional reaction products to the surface and it was judged that lithium evaporation in vacuum was least likely to introduce other contaminants. The sample had to be removed from the preparation chamber to move to the photoemission system and although this was done under pure argon gas, it is certain that there was some exposure to atmospheric oxygen, carbon dioxide and water moisture, which will result in lithium oxide, hydroxide and carbonate formation from the deposited lithium. Initially this was thought to be a potential problem, and so was the issue of getting to a single monolayer of lithium - whilst this is possible using very carefully calibrated lithium evaporators, in practice it was difficult to achieve.

For these reasons, a much larger coating of lithium was deposited, with the aim of protecting the lithium near the surface from atmospheric reactions. Lithium was evaporated onto the oxygen-terminated C(100) surface and an as-grown hydrogen terminated surface to a thickness of approximately 50 nm. Atomic lithium was deposited onto the diamond surface using thermal evaporation of lithium metal in a Balzer 510 coater at a pressure of 2×10^{-3} Torr. A quartz crystal monitor was used to estimate a lithium thickness of approximately 50 nm. The samples were removed from the chamber in an oxygen-free argon gas ambient in which they were stored until the samples were placed in the analysis system, although there was some atmospheric exposure during the sample transfer.

The next challenge was to find a suitable removal process for the excess lithium, most of which reacted with the atmosphere to form various compounds. Two methods were attempted with XPS monitoring of the lithium 1s peak - thermal evaporation and solvation in water. Although lithium metal has an evaporation temperature of around 200°C, a number of its compounds are stable to much higher temperatures - as detailed in table 6.6.

One possible way to remove the excess lithium proposed was to heat the samples so the non-bonded lithium evaporated. Three diamond samples had lithium evaporated to thicknesses of approximately 50, 100 and 150 nm using the Balzers coating machine. Following lithium deposition, a grey film was present on the diamond surface. Those samples stored under nitrogen turned a light brown colour, probably by formation of lithium nitride, but after exposure to air this returned

Compound	Melting Point $^{\circ}C$	Evaporation Point $^{\circ}C$
Li Metal	180.5	1342
Li_2O	1700	-
Li_2N_3	813	-
$LiNH_2$	390	430
LiOH	450	924 (decomposes)
Li_2CO_3	723	1310
Li_2O_2	195	decomposes to Li_2O
LiCl	614	1382

Table 6.6: Melting and evaporation temperatures for lithium metal and the various compounds that might be expected from lithium reacting in air. [26]

to a grey colour, possibly by reaction with oxygen and moisture.

These three samples were affixed to a molybdenum sample holder using silver dag and transferred into the Omicron SPM system in the NSQI at the University of Bristol at a base pressure of 1×10^{-9} Torr. The samples were resistively heated in vacuum to temperatures of 255 °C, 350 °C, 500 °C and 750 °C to observe the effect of the heat on the visual appearance of the grey lithium film and on the pressure of the chamber to indicate evaporation occurring.

Spikes in the pressure to around 2×10^{-5} Torr occurred at around 100 °C, 200 °C, 300 °C and then no noticeable changes in pressure were observed up to 750 °C. These spikes in pressure could potentially correspond to the loss of water moisture at around 100 °C, the evaporation of lithium metal at 200 °C and the decomposition of Li_2O_2 and $LiNH_2$ at 300 °C and 500 °C. Even to the naked eye however, the film on the surface of the diamond was only partially evaporated after 750 °C, and significant quantities still remained on the surface, making evaporation an unlikely route to near monolayer coverage.

Using lithium evaporated onto the oxygenated diamond surface, a number of different solutions were tested. Immersion in methanol removed a small amount of the surface layer over around a minute, but some of the layer was still present after removal from the solution. In triple distilled deionised water however, the grey layer was removed to the naked eye. It was hoped that observing this water washed sample in XPS would reveal some lithium still remaining on the surface, as the computational results predict a strong enough bond to remain.

6.4.4 XPS of Li-O terminated boron doped C(100) diamond

X-ray photoemission spectra (XPS) were taken in an Omicron Multiprobe UHV system with a base pressure of 5×10^{-10} Torr, using Al Kα radiation ($h\nu = 1486.6$ eV) from a VG XR3E2 twin anode source and an Omicron EA125 hemispherical analyser. Before XPS spectra were taken the samples were degassed at between $200 - 250$ °C to desorb contaminants. Scans were taken with pass energy of 50 eV, a dwell time of 0.5 seconds and a 0.1 eV step size. This pass energy is the energy filter on the detector and prevents the detector from being flooded with low energy electrons not relevant to the study. Spectra were normalized to the maximum intensity of the inelastically scattered electrons. Analysis was performed using the analysis package Fityk [20] using Voigt peaks and the Levenberg-Marquardt fitting algorithm. [22]

In addition to hydrogen and oxygen terminated surfaces for calibration, two lithium coated

samples were studied - one with lithium deposited on oxygenated diamond, the other on hydrogenated diamond for comparison. The oxygenated surface was scanned in the XPS system first as received after lithium deposition, and then again after washing in deionised (DI) water followed by isopropanol (IPA). Significant lithium signal remained after water washing on the oxygenated surface, indicating a thin strongly bound surface structure. By comparison there was no discernible lithium signal observed in XPS after water washing in the hydrogen terminated surface, indicating that the oxygen is playing a key role in retaining lithium on the surface. Figure 6.10 compares the Li 1s region of the XPS spectra for the unwashed and washed surfaces on oxygenated diamond and the washed hydrogenated surface.

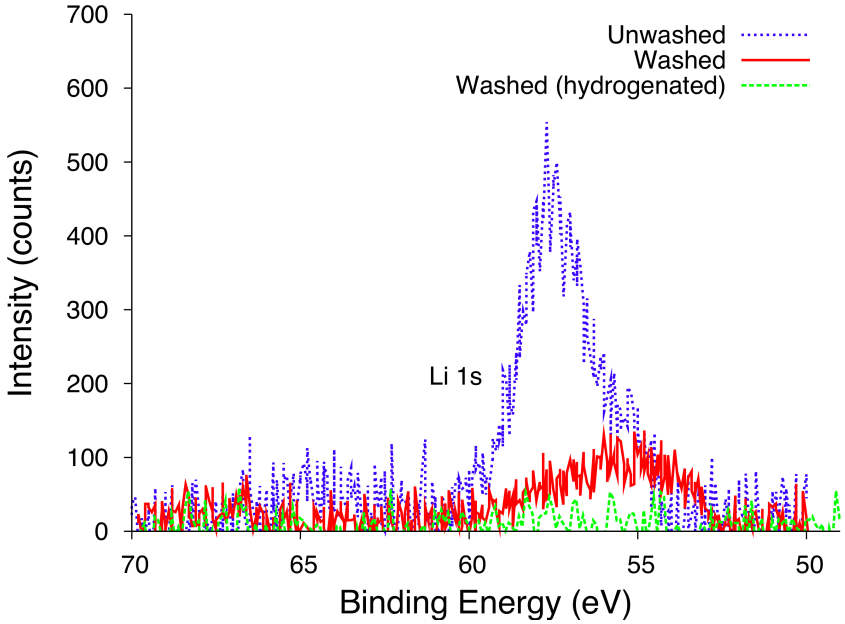

Figure 6.10: XPS spectra of the Li 1s region of the unwashed (blue) and washed (red) lithium-coated oxygenated diamond, as well as the lithium coated, washed hydrogenated surface (green).

After washing, there is approximately 4.4 times less lithium signal than before washing, indicating much of the coverage has been removed. Lithium compounds are typically highly soluble in water and the presence of lithium after washing only on the oxygen-terminated surface indicates that the bonding involved in the oxygen-lithium surface dipole is strong enough to prevent solvation. One possible explanation is that the lithium on the C(100) surface is four-fold coordinated to the oxygen atoms on the diamond surface, as it would be if dissolved in water.[27] The fact that no discernible lithium remains after washing the lithium-coated hydrogenated surface indicates that oxygen is playing an active role in the lithium remaining on the oxygenated surface. Figure 6.11 compares the XPS spectra for the carbon 1s and oxygen 1s regions across the two lithium-coated oxygenated surfaces, before and after washing in water.

The carbon 1s signal as shown in Figure 6.11(a) is significantly different before and after washing. Before washing the signal has roughly equal proportions of C-O bonded carbon at 286 eV and carbonate bonded carbon at 292.2 eV, with a smaller peak at 287.8 eV, a combination of peaks observed from exposure of lithium metal to air[28]. Lithium carbonate is formed by the

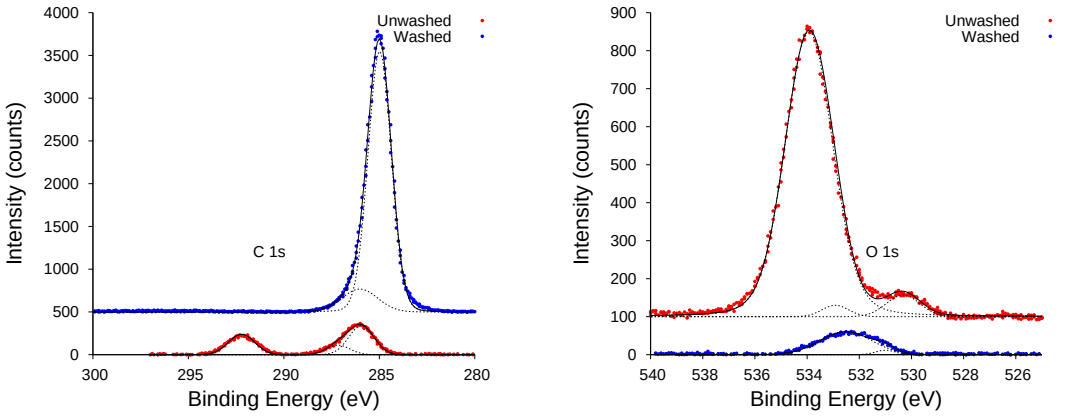

Figure 6.11: XPS spectra of the (a) carbon 1s, and (b) oxygen 1s for the unwashed lithium coated sample (red) and washed lithium coated sample (blue) on oxygenated diamond. Spectra have been offset on the y-axis for clarity. The dotted black lines show the deconvoluted spectra.

reaction of lithium oxide with carbon dioxide in the atmosphere. After washing the C 1s region is predominately characterized by the sp^3 diamond feature at 285 eV, with the C-O peak 1 eV above the diamond peak constituting approximately 18% of the signal. The size of the C 1s peak relative to both the O 1s and Li 1s peaks shows that only several monolayers of lithium at most remain on the surface.

The oxygen 1s region for the unwashed sample also shows several chemical states. The largest peak comprising 89% of the O 1s signal is at 533.9 eV, with smaller peaks at 530.2 eV and 532 eV. The peak at 533.9 eV has been associated with both oxygen-rich complexes and carbonates. In light of the presence of the carbonate signal in the C 1s peak, the 533.9 eV peak was assigned to be lithium carbonate. The 530.2 eV peak can be assigned to lithium oxide, which is a common product of the reaction of lithium metal with oxygen. This peak only accounts for around 7% of the O 1s signal. This is not surprising as Li_2O is known to react strongly with water to form lithium hydroxide,[28] a reaction that likely occurred during sample transfer to the XPS/UPS system. By this analysis, the majority of the surface layer of the unwashed sample is $LiCO_3$ and LiOH, formed by reaction of CO_2 and H_2O in the air with Li_2O or the initial Li deposited layer.

After washing, the oxygen 1s peak consists of two peaks - one larger peak at 532.2 eV and a second, much smaller peak at 531 eV. The larger peak corresponds to oxygen in the single bonded state, which together with the information from the carbon 1s peak suggests the scan is detecting the oxygenated diamond surface, with a small layer of lithium present on the surface. The latter is ascribed to again be lithium compounds left in place by the washing process.

Using the integrated peak areas of the Li 1s and O 1s peaks and their atomic sensitivity factors (O 1s = 0.65 and Li 1s = 0.02) we calculate a stoichemistry for Li/O of 2.1. This would suggest a Li_2O configuration, however the O 1s peak is dominated by the peak at 532.2 eV, suggesting a carbon-oxygen bond rather than the expected bond for Li_2O at 531.2 eV.[29] Based on this shift and

the high reactivity of lithium oxide with water it is suggested that the bulk of the oxygen content of the washed sample is involved in bonding with the diamond surface. Assuming approximately 1 ML of oxygen on the diamond surface, this implies around 2 ML of lithium remains in total, though the spatial distribution is as yet unknown.

Figure 6.12 shows the XPS C 1s spectra for the washed sample in more detail, using Voigt peaks constrained so all the deconvoluted peaks have an equal width. The carbon spectra is dominated by the diamond line at 285 eV as expected, with a fairly large shoulder at 286.5 eV characteristic of a C-O single bond, and only a small C=O double-bonded peak. This implies a single bonded oxygen-carbon configuration, as predicted by the computational results.

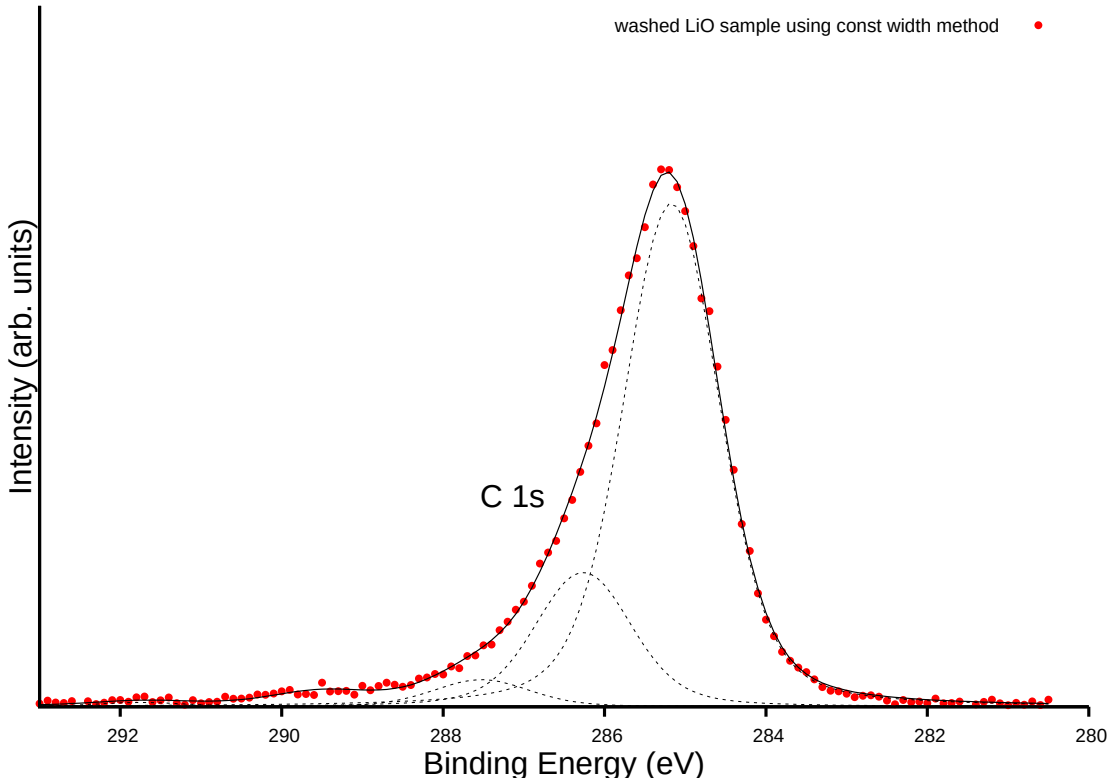

Figure 6.12: XPS spectra of the carbon 1s for the washed lithium coated sample, fitted with Voigt functions of equal widths. The dotted black lines show the deconvoluted spectra.

Figure 6.13 shows the oxygen 1s spectra for the washed LiO coated surface, showing three principle deconvoluted peaks - the largest at 531 eV characteristic again of a single bonded oxygen, with a smaller peak at 533 eV characteristic of double bonded oxygen and a relatively small peak at 535 eV which would imply a oxygen bonding environment more negative than a double bond - perhaps where the lithium ion is donating substantial electronic charge to the oxygen, as in the theoretical model where each oxygen gains around 0.8 e from the neighbouring lithium atoms in the full monolayer case on the oxygenated C(100) surface.

Figure 6.14 shows the lithium 1s spectra after fitting for constant width deconvoluting peaks. This is a more complicated system than the oxygen and carbon peaks, with a number of different

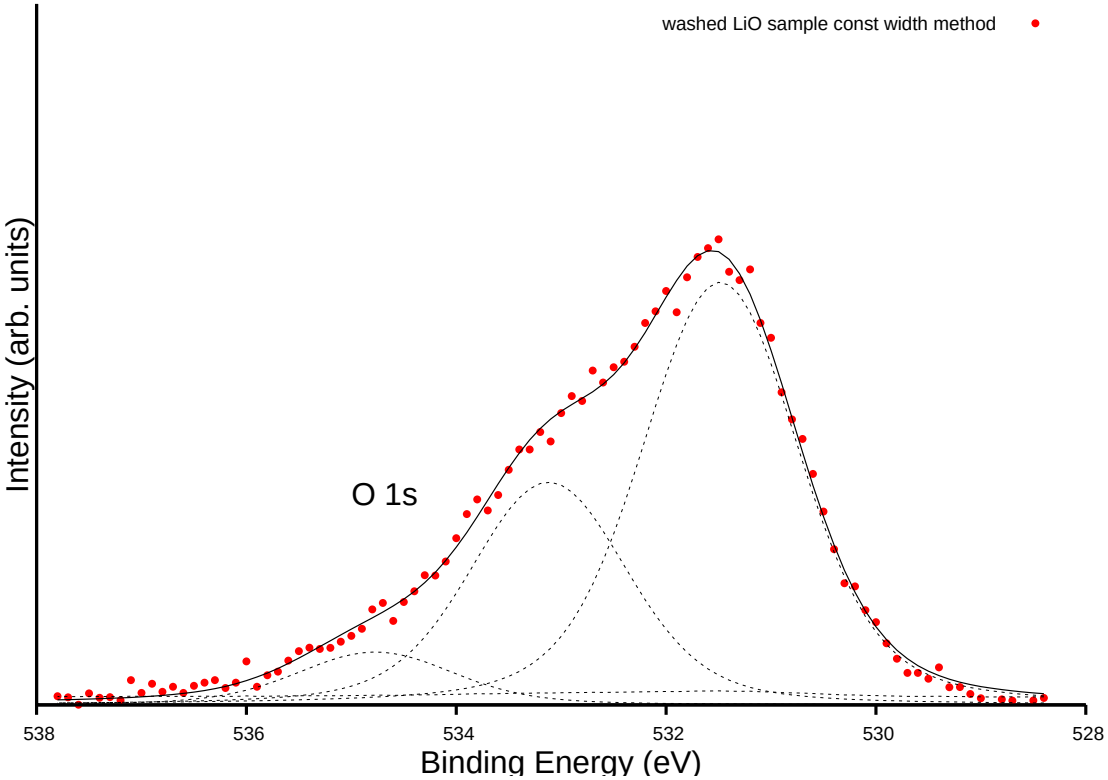

Figure 6.13: XPS spectra of the oxygen 1s for the washed lithium coated sample, fitted with Voigt functions of equal widths. The dotted black lines show the deconvoluted spectra.

bonding configurations between 54 eV and 61 eV (although the last peak may be an effect of the background subtraction method rather than a real peak). The broad nature of the lithium 1s spectra indicates that a number of different lithium bonding configurations are present on the washed surface, from lithium in the metallic/hydroxide state around 55 eV to more ionic compounds at 56 eV and above. This isn't unexpected as the surface is unlikely to be entirely smooth to the C(100) surface after the ozone treatment, and the washing of the surface with water will likely cause a number of bonding arrangements. The large numbers of ionic states is promising considering the lack of carbonate and oxide signals in the oxygen and carbon spectra as it implies the ionic lithium is bonding to the surface as predicted by the computational work rather than as deposits of compounds on the surface as in the unwashed spectra.

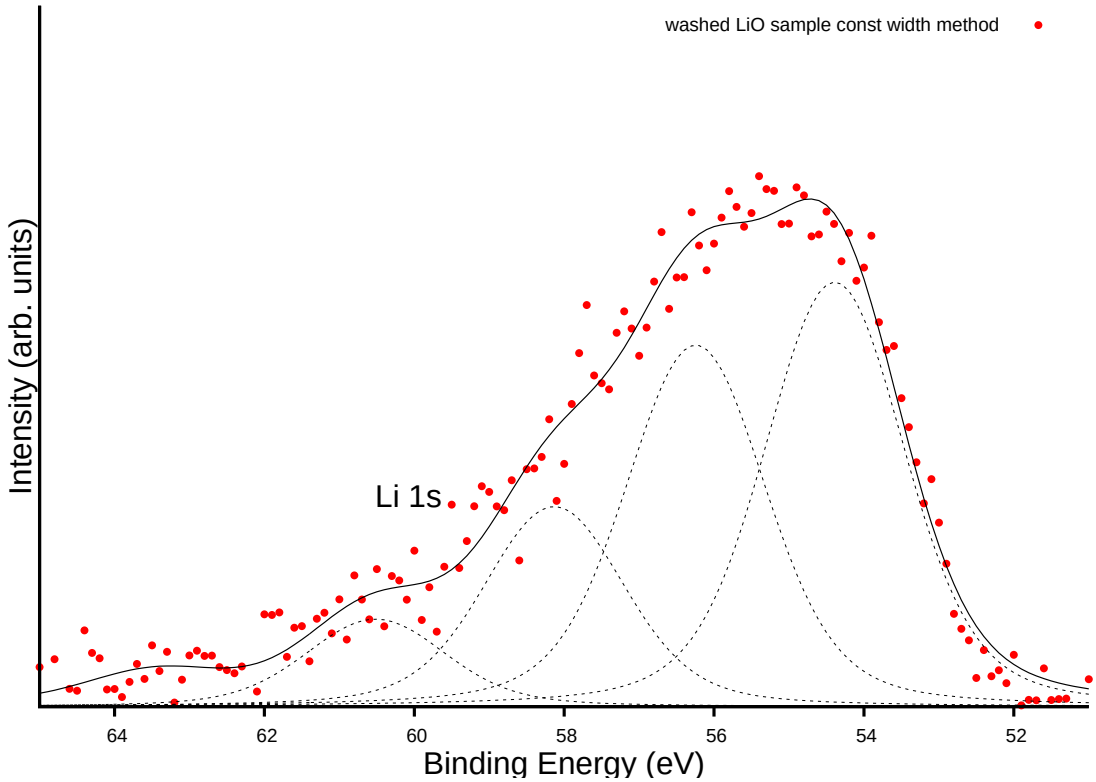

Figure 6.14: XPS spectra of the lithium 1s for the washed lithium coated sample, fitted with Voigt functions of equal widths. The dotted black lines show the deconvoluted spectra.

In addition to the XPS measurements of this surface, low energy electron diffraction (LEED) patterns were performed by Kane O'Donnell and Joshua Lay at the Rutherford Appleton Labs facility on the oxygenated and lithium coated boron-doped C(100) surfaces. Figure 6.15 shows the diffraction pattern using 100 eV electrons for the oxygenated surface, showing a clear 1×1 pattern as would be expected for oxygen-terminated diamond.[30]

By comparison, Figure 6.16 shows a diffraction pattern for 150eV electrons for the oxygenated surface after the lithium coating and washing treatment step. The 1×1 construction is still bright and evident, but there is a faint 2×1 pattern also discernible in-between the 1×1 spots, as we would

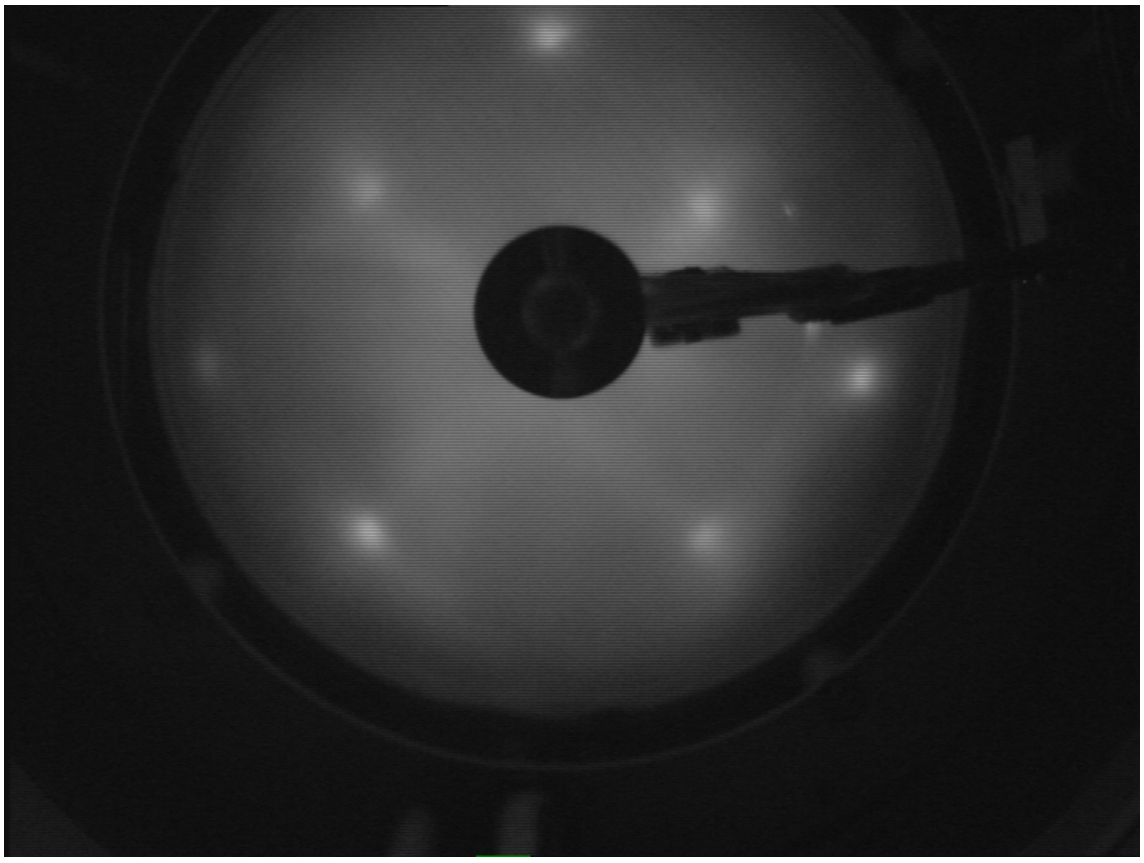

Figure 6.15: Low energy electron diffraction pattern using 100eV electrons on the oxygenated diamond surface showing a clear 1×1 pattern.

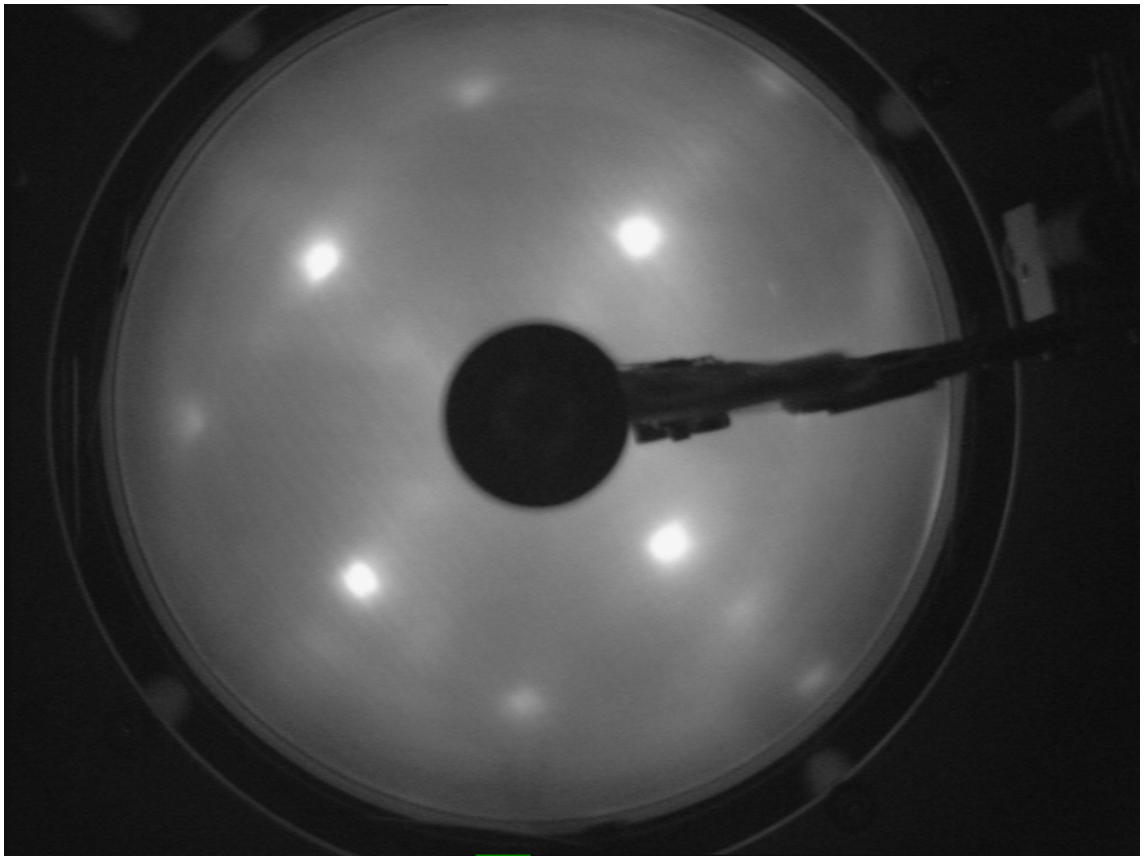

Figure 6.16: Low energy electron diffraction pattern using 150eV electrons on the lithium-oxygen terminated diamond surface showing the combination of the clear 1×1 pattern seen for the oxygen terminated surface with a fainter 2×1 construction.

expect from the LiO surface construction predicted in Chapter 5. This second layer construction is faint likely due to the small size of the lithium atom compared to the oxygen atoms but is nevertheless another good piece of evidence to the existence of an LiO complex on the diamond surface. It is also a strong indication that the lithiation process is not introducing a hydrogen termination rather than an LiO complex, as this would remove the 1×1 construction entirely and show a much stronger dominant 2×1 diffraction pattern.[31;32]

To summarise the XPS results, after washing with deionised water, significant lithium signal is still detected on oxygenated diamond in XPS, but not on hydrogenated diamond, indicating a strongly bound lithium-oxygen surface layer is formed, as predicted by the theoretical modelling in Chapter 5. This is confirmed by the change in LEED pattern between the oxygenated and lithium coated surfaces. The entire surface preparation process is illustrated in Figure 6.17.

Surface layers of close to monolayer thickness of lithium have been created on oxygenated diamond and observed using X-ray photoemission spectroscopy. Despite the high solubility of lithium and common lithium compounds with water, oxygenated diamond surfaces coated with 50 nm of lithium were still found to have detectable quantities of lithium on the surface after washing in deionised water. A similar lithium treatment on hydrogenated diamond had no discernible

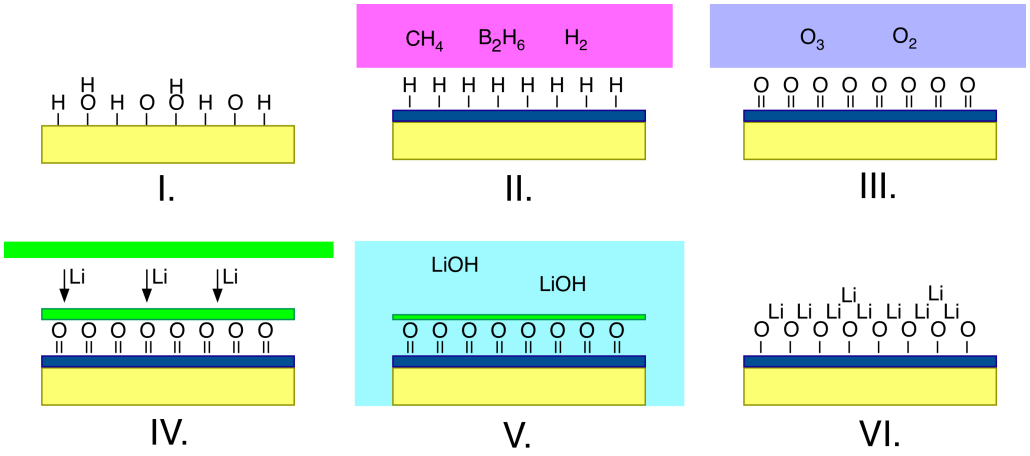

Figure 6.17: The lithium deposition process. (I) The as-received surface, (II) boron-doped overlayer growth via MW-PECVD, (III) ozone cleaning for oxygen termination, (IV) lithium deposition under vacuum, (V) deionised water and isopropanol washing to remove excess lithium and (VI) the final expected product.

lithium content after washing, indicating that thin layers of lithium are stable on the oxygenated diamond surface. The next step was to determine whether this stable surface would give the type of negative electron affinity predicted by the computational modelling.

6.4.5 SEM observation of electron emission from Li-O terminated diamond

One method for quick qualitative assessment of the NEA of a surface is to observe it under excitation from a low energy electron source such as a scanning electron microscope (SEM). If the incident electrons have an energy of $10 - 1000$ eV, their energy will be lost principally during collisions within the near surface of the material, and most of the energy of the incident electrons will be transferred to electrons near the surface. Some of these can overcome the barrier to emission and be ejected as secondary electron emission.[33] The lower workfunction of an NEA surface produces a much higher secondary electron yield in the scanning electron microscope due to the lower barrier to emission.

Figure 6.18 shows two C(100) CVD diamond crystals side by side in the JEOL 5600 SEM in the School of Chemistry. These samples have a boron-doped diamond overlayer as in the XPS studies to ensure no charging that could distort the image. The left square has a hydrogen termination from exposure to a hydrogen plasma in a microwave CVD reactor, whereas the right hand square has been exposed to 30 minutes of ozone in a Jelight UVO Ozone cleaner, giving a largely oxygen-terminated surface. The hydrogen terminated surface glows far more than the oxygen-terminated surface, indicating a much higher level of secondary electron emission due to the negative electron affinity surface given by the hydrogen termination.

The same assessment was also used for the Li-O coated C(100) surface, as pictured in Figure 6.19. Here the hydrogen and oxygen terminated samples are again shown, together with the LiO coated sample in the top right hand corner of the image. Qualitatively, the LiO shows a similar

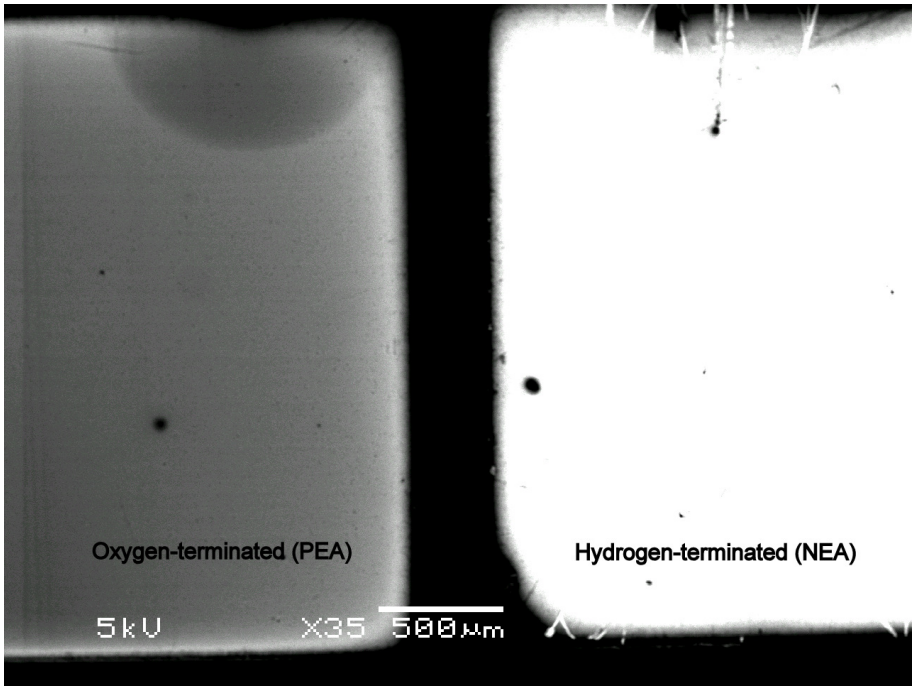

Figure 6.18: Scanning Electron Microscope image comparing two identical C(100) CVD single crystal diamond squares, one with hydrogen termination and the other oxygen termination after exposure to an ozone cleaner, showing a much larger intensity of secondary electron emission from the hydrogen terminated square.

intensity of secondary electron emission as the hydrogen terminated sample, albeit less consistently over the whole area of the surface, with some areas showing comparatively dark regions, possibly due to scratches or incomplete oxygen coverage.

The larger variation in emission across the LiO surface may be due to surface roughening caused by the ozone treatment, as the computational predicted NEA surface is only valid on smooth surfaces and AFM of the surface post-oxygen termination had a surface roughness of around 10 nm, likely due to roughening by the ozone treatment. In addition, there is likely to be a build up of surface charge around any step edges caused by this roughness, which will act as a barrier to emission.

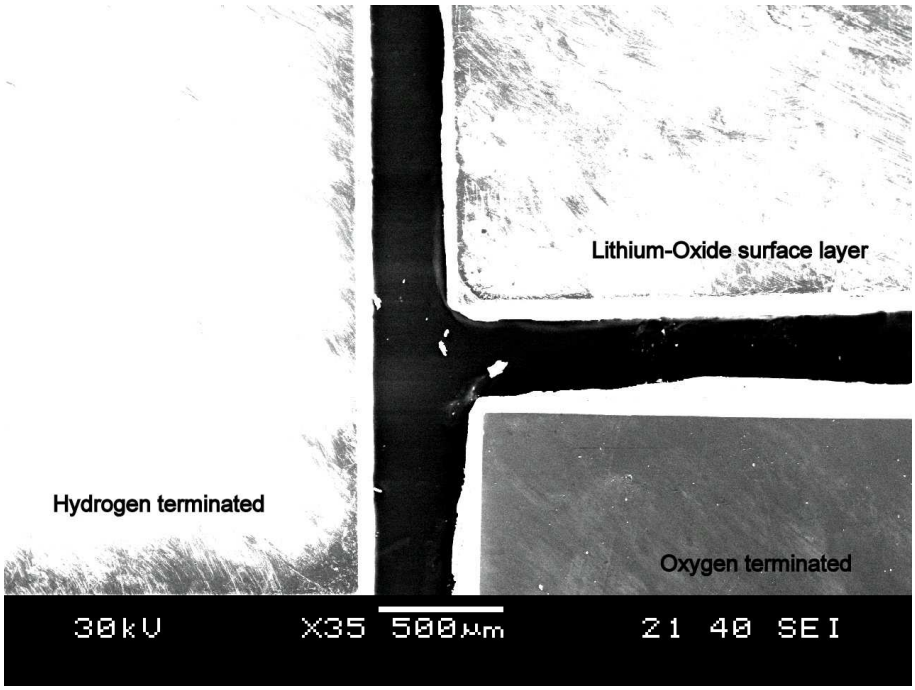

Figure 6.19: Scanning Electron Microscope image comparing three identical C(100) CVD single crystal diamond squares, one with hydrogen termination, one with oxygen termination and the third with an Li-O coating, showing a similar intensity of secondary electron emission from the LiO surface as for the hydrogen terminated square.

The high secondary electron emission from the LiO doped surface indicates that an NEA is present from the surface, and early XPS data for the Li 1s shows evidence of lithium, so it is likely due to the system predicted by the computational modelling. However, the results from the SEM analysis are only qualitative and UPS data is required to categorically say that there is an NEA responsible for the promising secondary electron emission.

Figure 6.20 shows similar oxygen terminated and lithium coated oxygen terminated surfaces to those in Figure 6.19 but on the surface of a single boron-doped C(100) sample. The sample was acid cleaned in fuming nitric acid for ten minutes before an ozone treatment in the UVO ozone cleaner for thirty minutes to ensure an even oxygen termination. Half of the sample was masked using a piece of 0.15 mm thick aluminium foil, placed diagonally across the centre of the sample. Lithium was then evaporated onto the unmasked region in the Balzers 510 coating machine, after heating

the sample above 100 °C to remove any water molecules on the surface that could interact with the lithium. After lithium deposition, the sample was washed in deionised water and isopropyl alcohol before mounting using silver dag and observation in a JEOL 5600 scanning electron microscope.

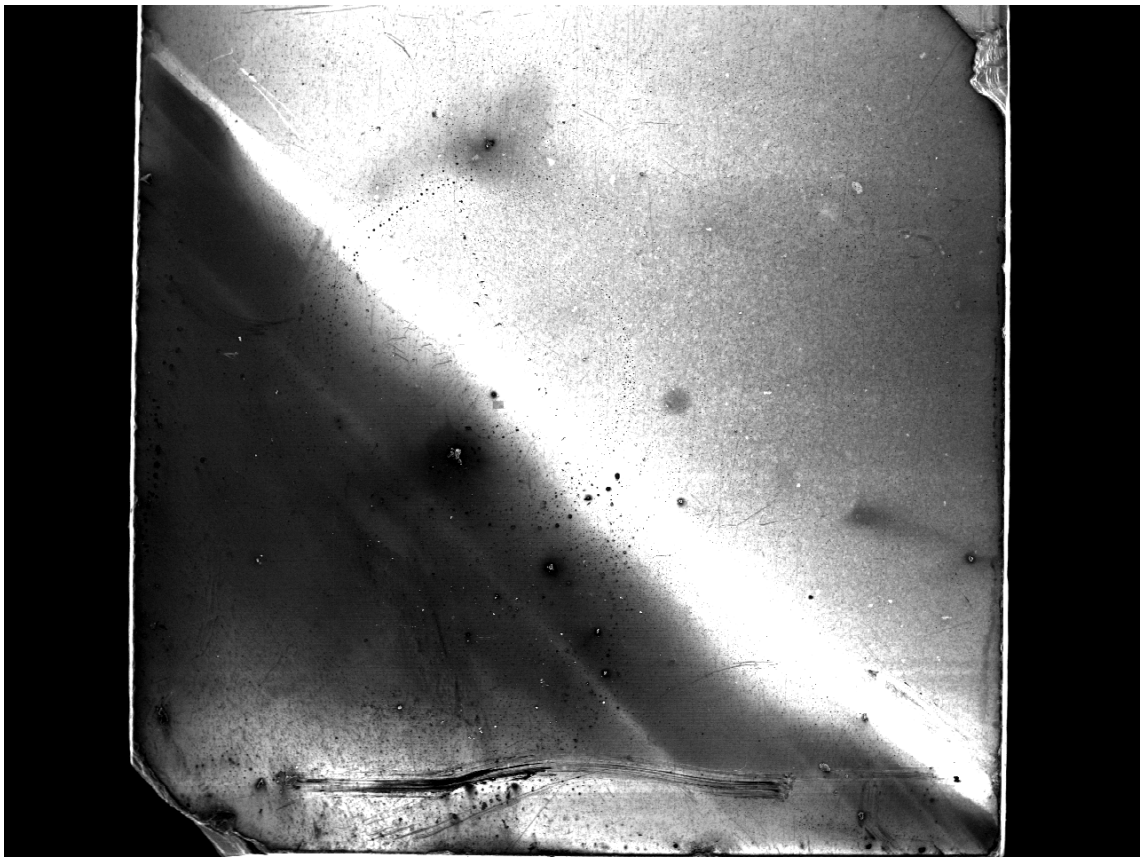

Figure 6.20: Scanning Electron Microscope image of a single oxygen terminated boron doped C(100) diamond sample, half of it having been masked and the other half coated in lithium. After washing, the lithium coated surface in the top right is much brighter in the SEM, behaviour indicative of an NEA. The diagonal region at the interface between the lithium coated and the purely oxygenated surfaces is the brightest.

Like the previous example, the oxygenated then lithium coated side of the sample is much brighter in the SEM than the purely oxygenated side, indicating a higher secondary electron emission from LiO surface, as expected from an NEA surface. Perhaps of most interest is the fact that the interface region of around 0.2 mm lying diagonally between the oxygenated and lithiated regions shows the highest brightness, suggesting stronger emission is coming from this region. This effect has been reported on electrochemically treated hydrogen terminated and oxygen terminated samples,[34] but an explanation for this effect was not fully given, with possible chemical changes due to the process steps posited. Figure 6.21 shows a closeup on this transition region. There were no noticeable charging effects and the sample was in good electrical contact with the stub, so charging should not be a contributing factor.

As the process steps for this LiO coated surface are so different and there are unlikely to be any geometrical steps, a electron emission 'lensing' effect similar to that described by Cui *et al*

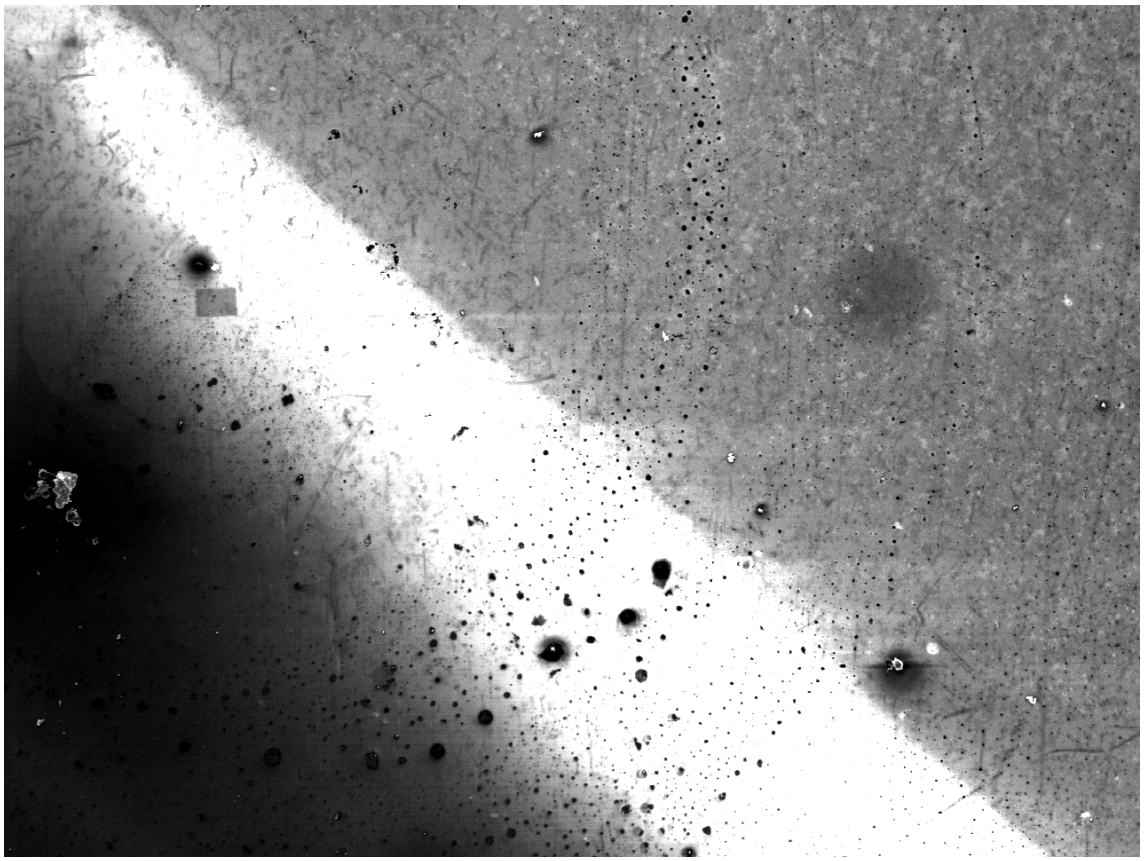

Figure 6.21: Scanning Electron Microscope image of a single oxygen terminated boron doped C(100) diamond sample, half of it having been masked and the other half coated in lithium. The figure is zoomed into the bright diagonal transition region at the interface between the lithium coated and the purely oxygenated surfaces.

is possibly the cause.[13] In that paper, which looked at the interfacial regions between graphite and hydrogenated diamond nanoparticles during field emission, it was suggested that electrons in graphite close to the lower workfunction diamond (around 3.4 eV for hydrogenated diamond compared to 5 eV for graphite) experienced a lower barrier to emission, and that electrons leaving the barrier within 20 Å of the interface effectively see the lower workfunction of the diamond. A similar behaviour could be occurring at the interface region in Figure 6.20, where electrons in the oxygenated diamond close to the interface experience a band bending effect due to the workfunction difference between the two surfaces and so there is an increased emission from this interface region containing electrons from both the oxygenated and lithium-oxygen terminated regions.

6.4.6 UPS of hydrogen and oxygen terminated boron doped C(100) diamond

A UPS spectrum shows a convolution of the density of states of the valence band material with the sensitivity of the detector. The difference between the photon energy of the UV light (21.22 eV) and the emission edge of the spectra gives the workfunction of the material. For a negative electron affinity material, there is an additional peak convoluted into the spectra - a sharp, angle-dependent peak from conduction band electrons, which is characterised by the distance (E_F - CBM). By deducting the position of the NEA peak on the UPS spectra from the diamond band gap of 5.5 eV, the difference between the VBM and E_F can be calculated.[16]

Before studying the UPS spectra for the lithium coated oxygen-terminated surface, the as-grown hydrogen terminated and ozone-treated oxygen terminated boron doped C(100) diamond surfaces were studied using UPS, in order to provide a good baseline comparison for the new surface under study. The UPS measurements were performed in the same Omicron system as the previous XPS measurements, typically within the same vacuum session to avoid changes in surface contamination between XPS and UPS measurements. Samples were heated to around 250 °C for 30 minutes to remove water and hydrocarbon contamination from the surface.

The UV He plasma source was ignited at around 100 mA and 1000 V. To overcome the workfunction of the analyser, a bias between the sample and the detector was applied of between 0 and 9 V. This bias and the value of the UV photon energy ($h\nu = 21.22$ eV)was later deducted from the spectra so that all UPS spectra shown in this report are relative to the Fermi level at zero eV. In addition, the Fermi energy of the system was calibrated to the Fermi edge of a clean molybdenum sample holder, as pictured in Figure 6.23. The Fermi edge of the substrate holder was found to be 0.195 eV above the zero used by deducting the photon energy from the spectra. All other UPS spectra in the study have had their zero calibrated to this Fermi edge value.

Using the workfunction cutoff ϕ from each spectra as illustrated in Figure 6.22, the electron affinity of the surface was calculated using the equation

$$\chi = \phi + \xi - E_g \tag{6.4}$$

where ξ is the difference between the Fermi level and the valence band maximum and $E_g = 5.45$ eV is the band gap of diamond, using the literature accepted value. ξ was calculated as the difference between the Fermi edge measured from the UPS spectrum of a clean molybdenum substrate as shown in Figure 6.23, and the valence band maximum of the sample from the extrapolation of

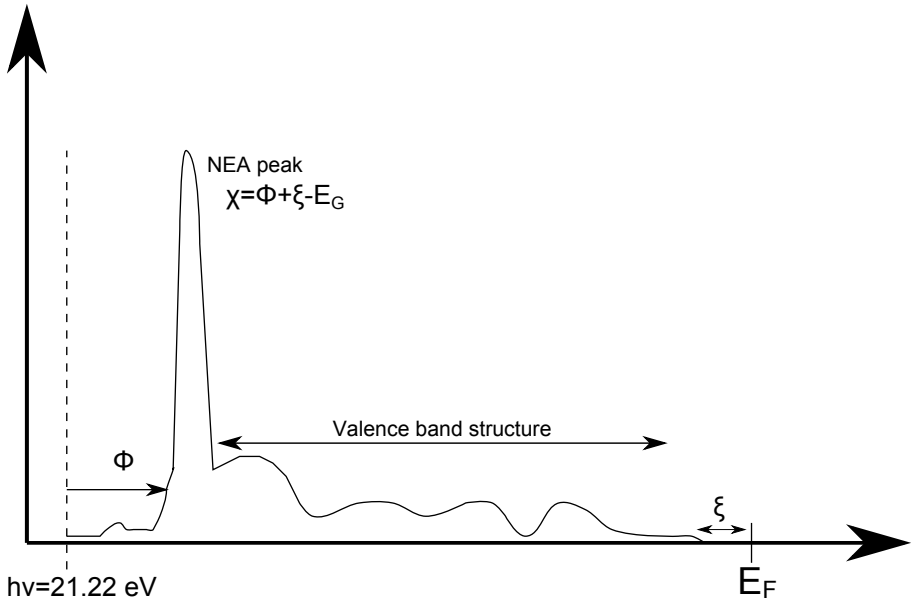

Figure 6.22: Example sketch of a UPS spectra showing how the workfunction ϕ, xi parameter ξ and electron affinity χ are calculated.

the high kinetic energy portion of the UPS spectrum to the background count level.

As expected, the hydrogen terminated sample displays a characteristic high intensity peak indicative of a negative electron affinity. Figure 6.24 shows the UPS spectra for the hydrogen terminated surface, with the spectra adjusted so that $E_F = 0$.

The hydrogenated sample has a workfunction cut-off of 3.62 eV, and a difference between the Fermi level and valence band minimum of $\xi = 0.3$ eV, giving an electron affinity of -1.5 eV.

Figure 6.25 shows the same hydrogen terminated sample, with an increasing angle away from the normal, so that the detector is no longer directly above the sample. As expected, the highly angle dependent NEA peak consisting mainly of electrons leaving normal to the surface decreases at increasing angles, with a large reduction in intensity at 20° rotation, and the complete disappearance of the peak at 40° rotation. This expected behaviour confirms the presence of a negative electron affinity peak on the surface.

By comparison, Figure 6.26 shows the oxygen terminated surface after acid cleaning and thirty minutes of ozone treatment. The NEA peak is no longer present, and the overall intensity of the spectrum is much reduced. The oxygen terminated sample has a workfunction cut-off of 5.3 eV and a ξ parameter of $\xi = 1.1$ eV, giving an electron affinity of +1 eV for this surface. The lowish positive electron affinity may indicate a mixture of terminations on the surface.

Figure 6.27 shows the spectrum for the hydrogen terminated surface in red, together with the oxygenated surface spectra in blue, at relative intensities. The main figure shows the valence band structure, whilst the inset shows the full spectrum, showing just how much more intense the emission from the NEA peak of the hydrogenated sample is, with the oxygen terminated sample's spectrum barely visible when displayed alongside the full height of the hydrogen terminated sample's NEA peak.

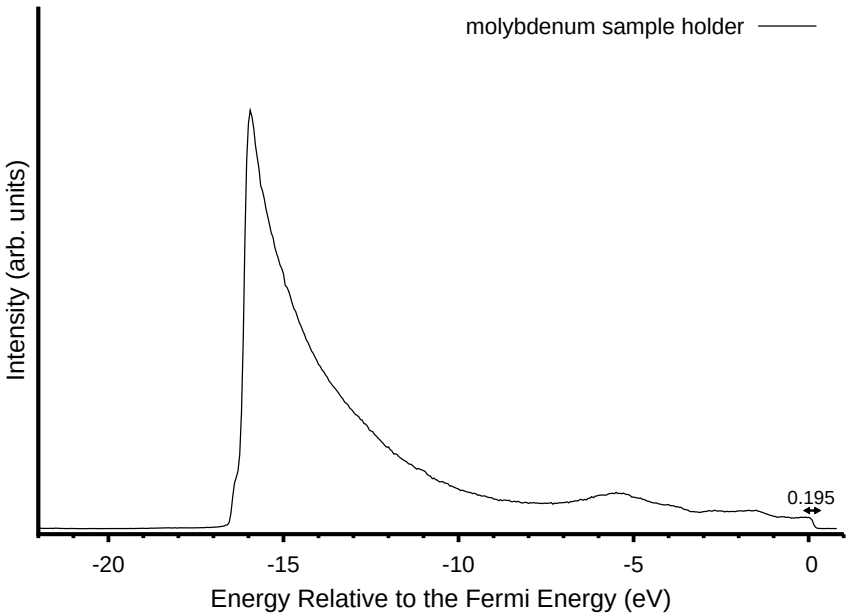

Figure 6.23: UPS spectrum of the valence band structure for a clean molybdenum sample holder, used to determine the Fermi energy of the overall system.

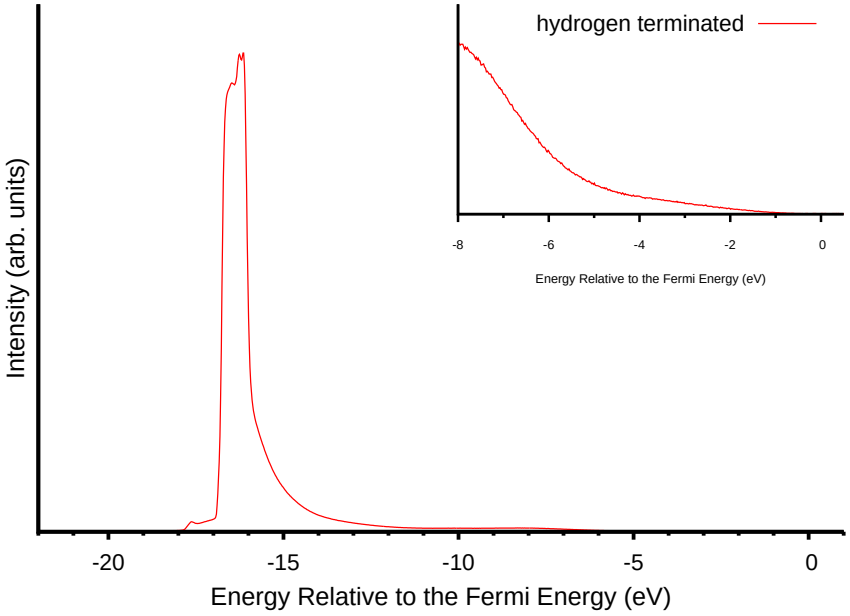

Figure 6.24: UPS spectra of the hydrogen terminated boron doped C(100) sample, with a close-up inset of the lower valence band structure close to the Fermi level. Note the very high intensity peak at around -16 eV (5.4 eV in Binding Energy) indicating a negative electron affinity is present.

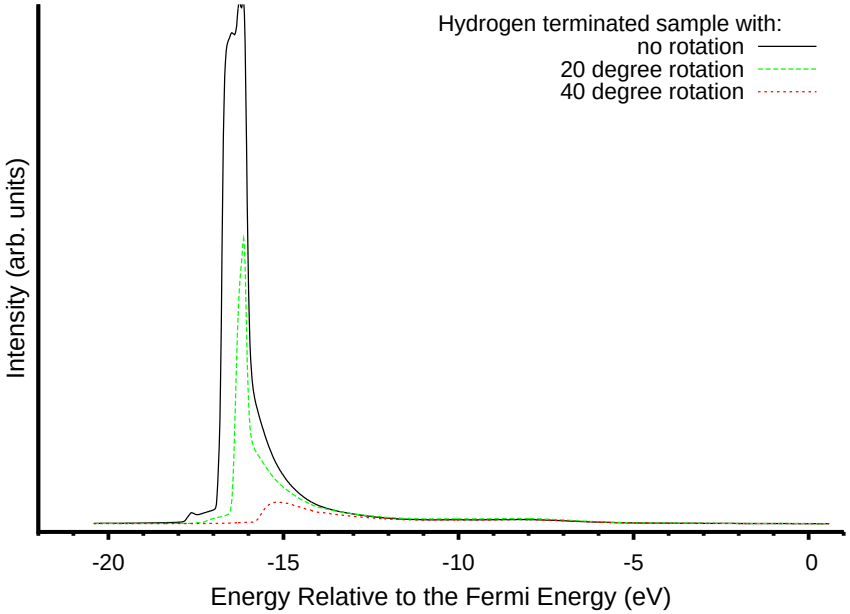

Figure 6.25: UPS spectra of the hydrogen terminated surface with the sample at increasing angle to the detector, showing a large decrease in the NEA peak with larger angles, as expected.

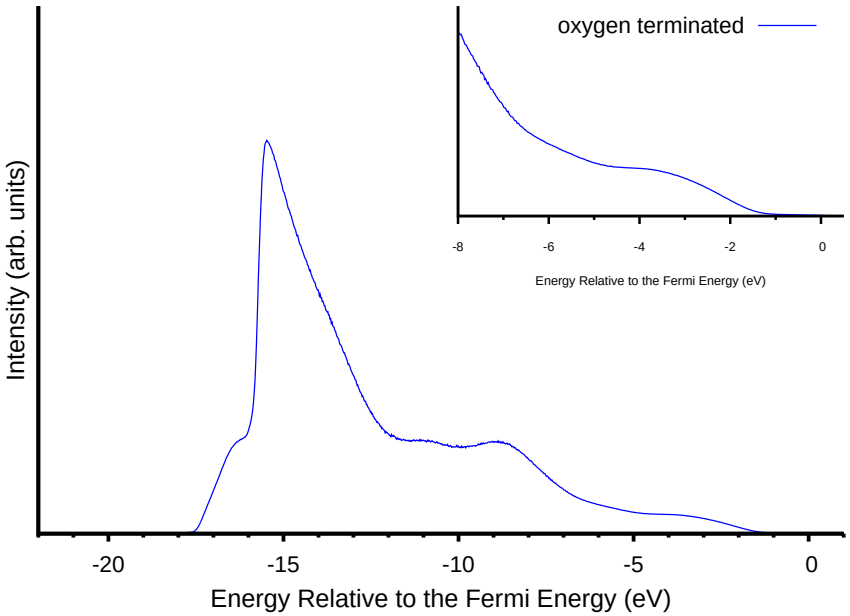

Figure 6.26: UPS spectra of the oxygen terminated boron doped C(100) sample, with an close-up inset of the lower valence band structure close to the Fermi level.

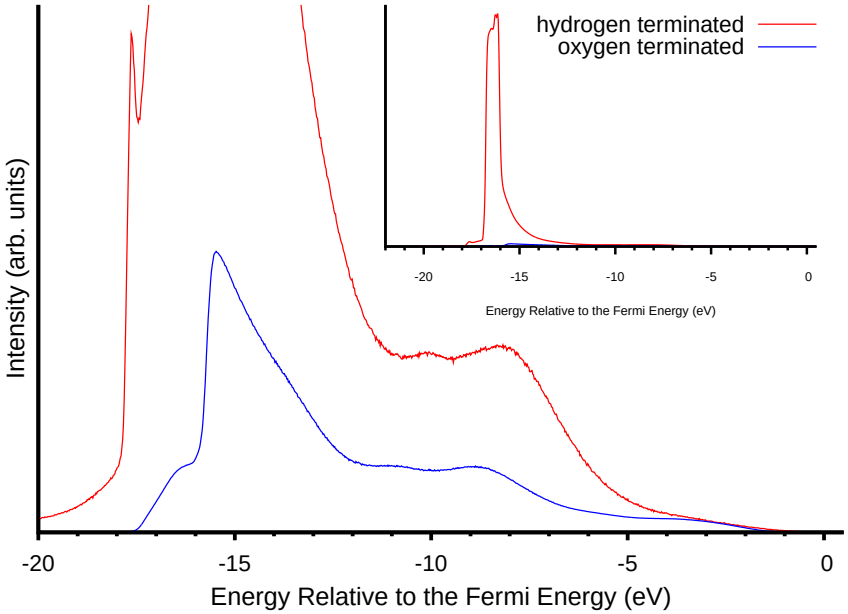

Figure 6.27: UPS spectra of the oxygen terminated and hydrogen terminated boron doped C(100) samples, focused on the NEA peak. The inset shows the full range. Compared to the hydrogen terminated surface, the intensity of the oxygenated surface spectrum is much lower.

6.4.7 UPS of Li-O terminated boron doped C(100)diamond

Again for the UPS measurements of the LiO surface, $(2.6 \times 2.6 \times 0.3)$ mm Element 6 CVD diamond squares were used, with a $2-4$ μm boron-doped homoepitaxial overlayer grown by microwave plasma-enhanced chemical vapour deposition, to ensure a conductive surface without charging. The samples were exposed to the UVO ozone cleaner for thirty minutes to give an oxygen termination, and an approximate thickness of 50 nm of lithium was deposited by thermal evaporation in the Balzers 510 coater at a pressure of 6.6×10^{-4} mBar. The samples were washed in deionised water and isopropyl alcohol before pumping down in the Omicron Multiscan Lab UHV chamber with base pressure 1×10^{-10} mBar.

Samples were sandwiched between a clean Si(100) chip and a thin tantalum foil, with a direct current through the Si(100) chip used for heating. The tantalum foil was used to provide an electrical connection with the system so that the sample surface was at the same ground state as the detector. An optical pyrometer focused on the Si(100) chip was used to estimate the sample temperature. The pyrometer was focused on the silicon rather than diamond as diamond does not emit in the infra-red, but no significant temperature difference was observed between the Si(100) chip below the diamond sample and the tantalum foil touching the diamond's top surface.

As before the UV source for UPS measurements used a discharge current of 100 mA at 1000 V, and a series of bias voltages were applied between the sample and the analyser to overcome the contact potential. As with the hydrogen terminated sample, a large negative electron affinity peak was observed, and initial spectra such as those in figure 6.28 were saturated above the peak intensity detectable by the analyser. To restrict the photoelectron count rate below the saturation

count rate a 1 mm aperture was used on the analyser with a 2 eV pass energy.

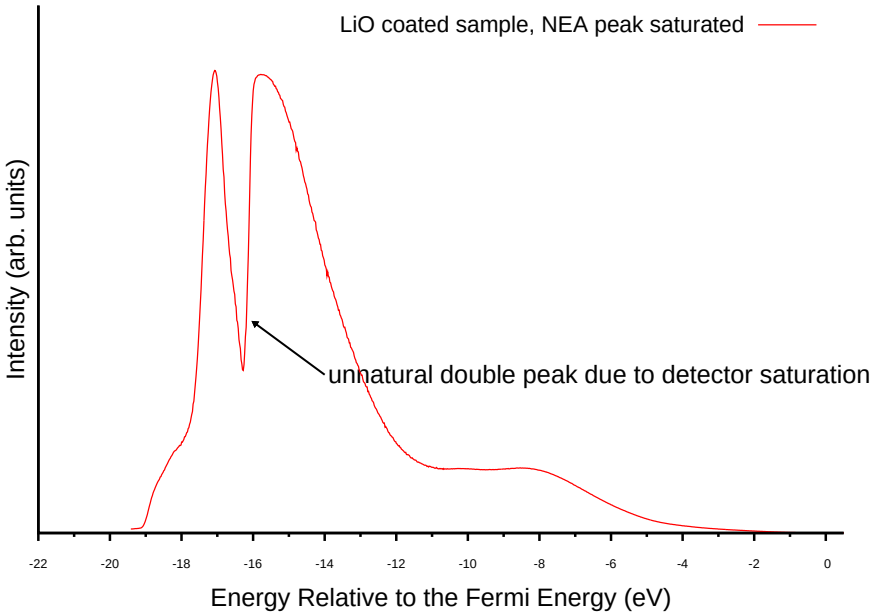

Figure 6.28: UPS spectrum showing the initial scan for the LiO coated diamond surface. The NEA peak is present but the peak intensity is above the saturation count rate, causing an unphysical double peak effect.

Figure 6.29 shows the UPS spectrum after adjustment so that the peak is not saturated. As with the hydrogen terminated surface, a clear peak associated with a negative electron affinity is observed at around 5.2 eV on the kinetic energy scale, or -16 eV in binding energy.

Figure 6.30 shows the LiO spectrum, with the spectrum for the oxygen-terminated surface also present for comparison, showing the clear difference between the positive affinity oxygen terminated surface without a high intensity NEA peak and the LiO, which displays such a phenomenon at 5.2 eV on the kinetic energy, or -16 eV in binding energy.

To estimate the sample workfunction, a closer and higher resolution scan of the cut-off was used, with a larger 2 mm diameter aperture and a pass energy of 10 eV. Figure 6.31 shows one of these spectra for the 250 °C annealed surface, indicating the workfunction cut-off.

This value of ($\xi = 0.6 \pm 0.1$) eV for the sample after the 250 °C anneal is higher than the expected bulk value of $0.1 - 0.3$ eV, indicating that a slight downward band bending is occurring at the surface. The workfunction for this sample was calculated from the low kinetic energy cut-off[16] to be (2.8 ± 0.1) eV, with a corresponding electron affinity of $\chi = (-2.1 \pm 0.1)$ eV.

6.4.8 Temperature dependence of the Li-O surface on boron doped C(100) diamond

In addition to studying the UPS spectra of the as-washed surface at low temperatures, the sample was heated in 30 minute annealing steps at temperatures of 250 °C, 550 °C, 925 °C, 1012 °C, 1140 °C and 1218 °C, as measured by the optical pyrometer focused on the silicon chip behind the

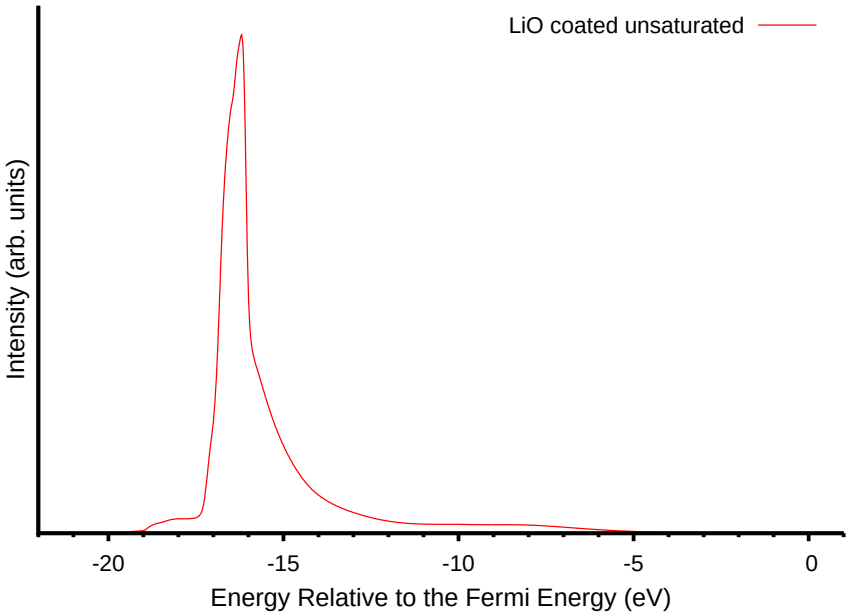

Figure 6.29: UPS spectrum for the LiO coated diamond surface after adjusting for the high number of counts by reducing the aperture size and pass energy. The NEA peak intensity is now below the saturation count rate, and a clear NEA peak is observable around 5.2 eV in kinetic energy (-16 eV in binding energy).

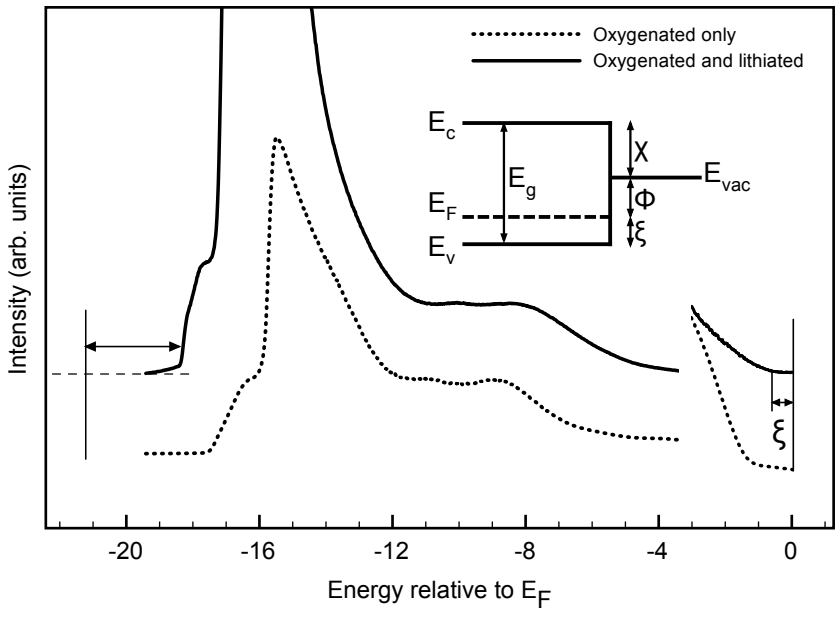

Figure 6.30: UPS spectrum taken from the Applied Physics Letters paper on this work showing the UPS spectra of the LiO surface compared to the spectrum of the oxygenated surface without lithium coverage, with the workfunction cut-off indicated (zero intensity is indicated by the dashed horizontal line).

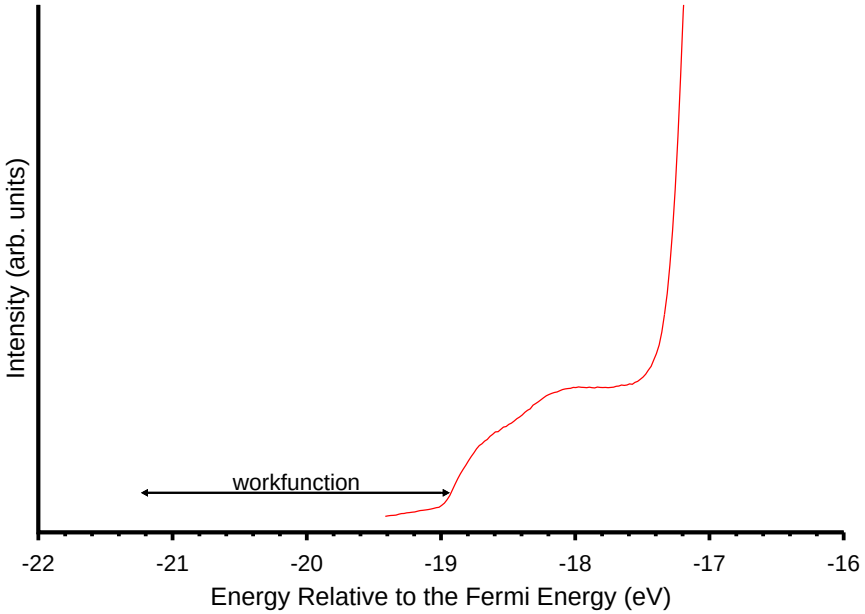

Figure 6.31: UPS spectrum closeup of the upper valence band structure with the workfunction cut-off indicated.

sample. In reality the temperature of the sample could be $100 - 200$ °C less due to temperature gradients between the diamond and silicon chip. After annealing for 30 minutes at temperature, the sample was allowed to cool before a UPS scan was taken.

The calculated workfunctions, electron affinities and the value for the parameter ξ for each annealing temperature are presented in table 6.7. In addition the intensity of the negative electron affinity peak relative to the highest intensity peak at 691 °C is shown.

Annealing Temperature (°C)	ξ (eV)	ϕ (eV)	χ (eV)	NEA peak intensity ($\times 10^6$ counts)	normalised peak intensity	total integrated emission yield ($\times 10^6$ counts)	normalised total yield
250	0.85	2.2	-2.4	1.45	0.66	1.62	0.85
550	0.58	2.8	-2.1	1.52	0.69	1.25	0.65
691	0.65	2.8	-2.0	2.20	1	1.91	1
925	0.73	3.3	-1.4	0.91	0.41	0.88	0.46
1012	0.60	3.5	-1.4	0.72	0.32	0.78	0.41
1140	0.59	3.3	-1.5	1.15	0.52	1.11	0.58
1218	0.30	3.6	-1.6	0.71	0.32	0.76	0.40

Table 6.7: Comparison of the calculated values for the parameters χ, ξ and ϕ for the Li-O terminated C(100) diamond sample after annealing for thirty minutes at different temperatures, as well as the normalised intensity of the NEA peak and total integrated area of the spectrum. Temperatures have an uncertainty of $\pm$ 50 °C and the energy parameters have an error of $\pm$ 0.1 eV.

The trends observed from table 6.7 are displayed graphically in figure 6.32. There can be observed a clear linear trend with increasing temperature for workfunction and electron affinity, with a less obvious correlation for the parameter ξ. The intensity of the negative electron affinity peak is higher for the first three temperatures than for the higher three anneals but it is not

a monotonically decreasing relationship. There does seem to be a significant decrease in NEA intensity at 925 °C and above but within these two groups there seems little trend in peak intensity with temperature.

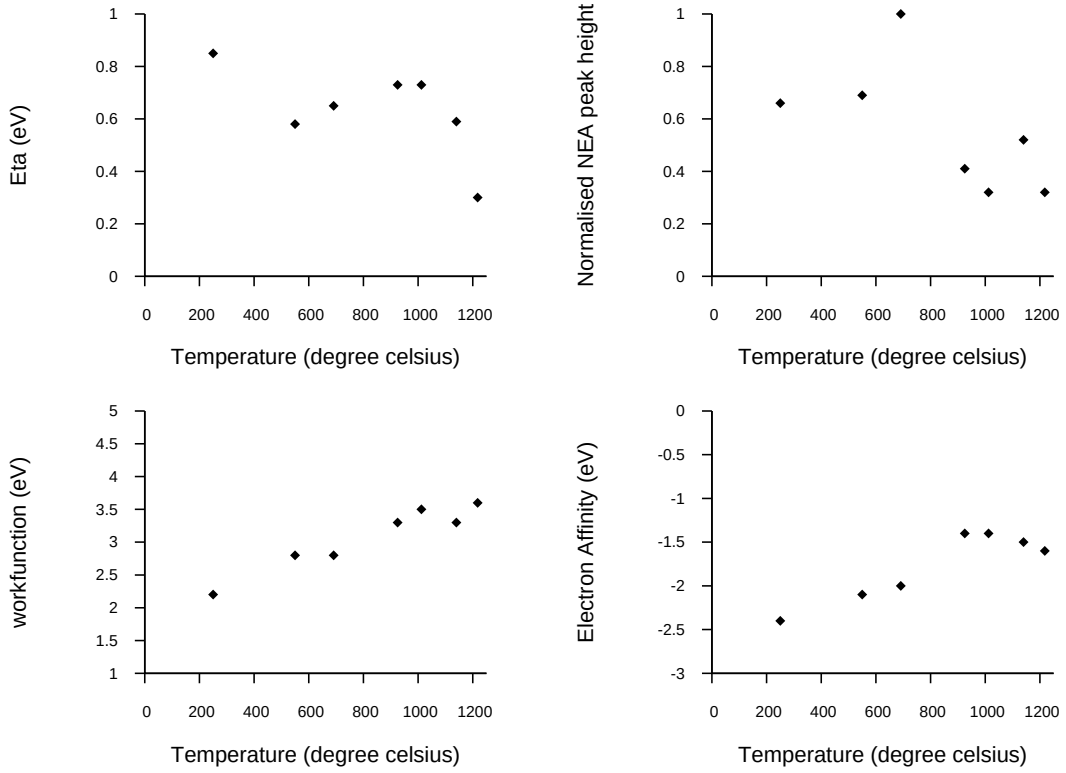

Figure 6.32: Graphs showing variation with increasing temperature for (a) the difference between E_F and the VBM (ξ), (b) NEA normalised peak height, (c) workfunction and (d) electron affinity.

From the graphs in Figure 6.32, there definitely seems to be a change between 691 °C and 925 °C, even on the electron affinity graph there seems to be a split between two different regimes. The lower workfunction between the 250 °C anneal and the 550 °C and 691 °C anneals can be mostly explained by the increased ξ parameter/shift in the Fermi level indicating a change in the Fermi level pinning, but up until the very highest temperature that doesn't then seem to change very much. The high NEA peak intensity at 691 °C is possibly due to more surface contamination being removed from the surface, but then there does seem to be a significant change after that point - perhaps around 800 °C. Oxygen termination has been observed to flip between the carbonyl and ether states at elevated temperatures, but molecular dynamics simulations by Kane O'Donnell predict that this shouldn't occur when lithium is present on the surface, so this is unlikely to be the cause. There is possibly a reconstruction of the surface between 691 °C and 925 °C that removes some of the lithium - the shift in ϕ and EA would correspond fairly well to the theoretical calculations of a shift from a full monolayer coverage to a 0.5 ML coverage of lithium, but without more detailed XPS information about this transition, it is difficult to conclude the nature of this transition.

Figure 6.33 shows the UPS spectra for the washed lithium-oxide C(100) diamond surface after each annealing step between 550 °C and 1218 °C with the spectra offset with the lowest temperature at the bottom and the highest 1218 °C anneal at the top of the figure. the initial 250 °C spectra is not shown here but can be seen in Figure 6.29. The NEA peak remains of high intensity even after annealing to a temperature of 1218 °C, although the rest of the spectra does begin to change at these high temperatures, as shown in the second part of the figure.

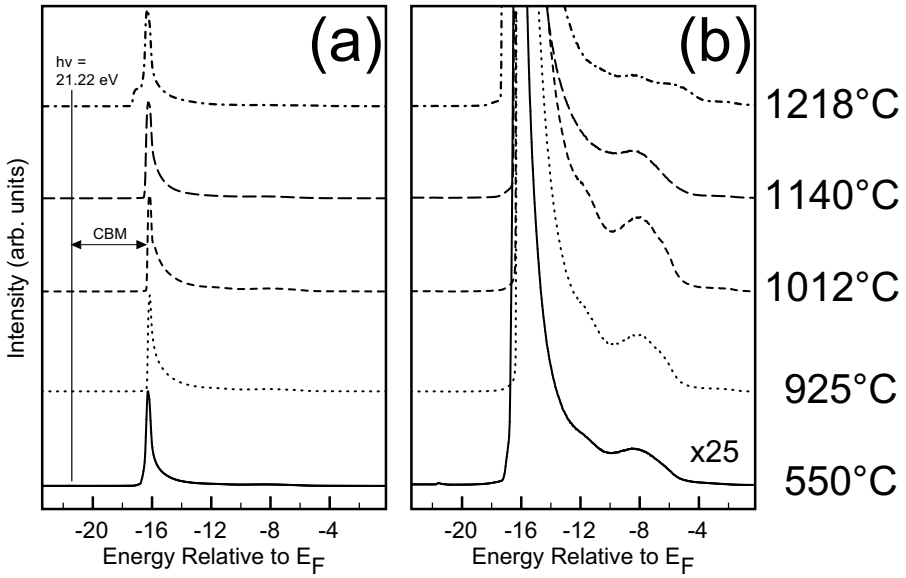

Figure 6.33: UPS spectra taken from the Applied Physics Letters paper on this work showing (a) UPS spectra for the C(100) diamond surface with LiO termination at a series of temperatures, normalized so all spectra have the same peak intensity. The cut-off of the NEA peak is indicated, being the conduction band minimum (CBM). (b) A close-up of the valence band spectra that is obscured by the large NEA peak in part (a).

Figure 6.33(a) shows the full spectra, whilst Figure 6.33(b) shows a close-up at $\times 25$ magnification of the valence band spectra detail that is obscured when the whole spectrum is shown, due to the NEA peak being of so much higher intensity than the rest of the spectrum. This figure shows little change in the upper valence band structure for annealing temperatures as high as 1012 °C aside from small horizontal shifts of around $0.1 - 0.5$ eV. These are likely due to changes in the Fermi level position after annealing.

The shoulder peak present in the valence band structure at -12 eV in the three lower temperature spectra disappears after annealing to 1140 °C. Oxygen has been reported to be completely removed from the C(100) diamond surface by 1050 °C,[17] and this may account for the removal of this -12 eV feature at temperatures above 1012 °C. In addition to this change at 1140 °C and above, a series of additional shoulders are present in the 1218 °C UPS spectrum not present at lower temperatures - a new shoulder below the NEA peak at around -17 eV, a new feature around -6 eV and a change in the shoulder near -8 eV. This indicates a different type of surface modification at this higher temperature, likely due to the onset of graphitisation or sp^2 dimerisation as non-carbon species are removed from the surface.[35]

Although it is not so clear in Figure 6.33, there is quite a substantial change in the NEA peak of the surface between the 550 °C anneal and the 1218 °C anneal, which is more clearly presented in Figure 6.34.

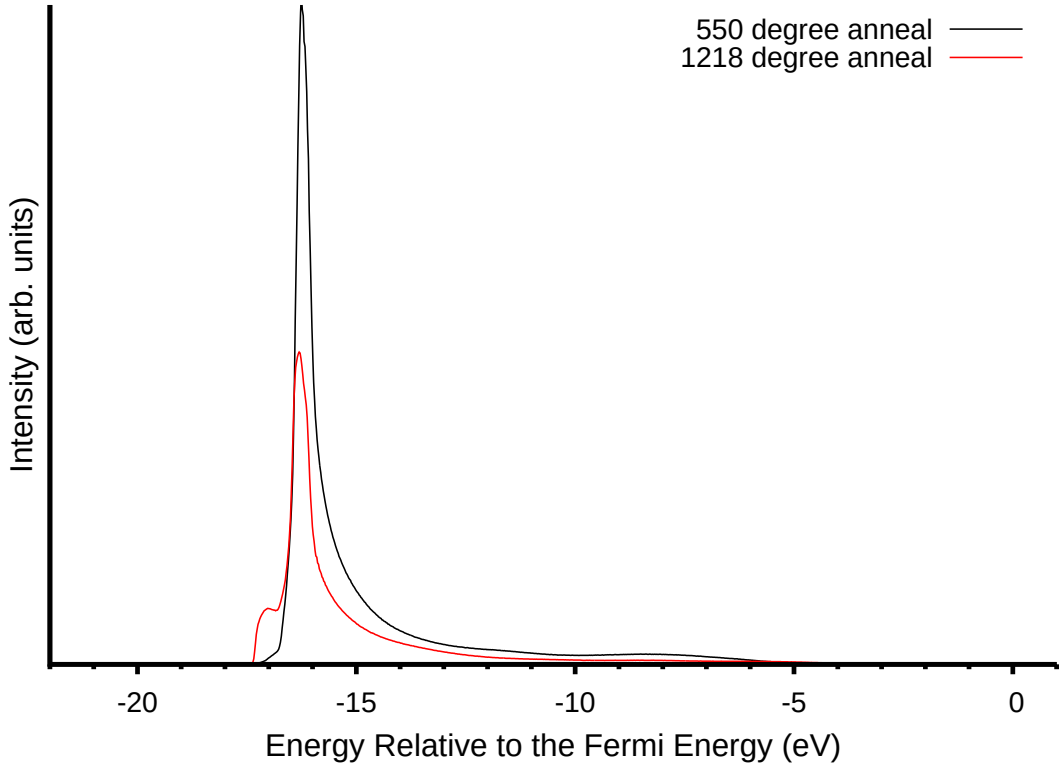

Figure 6.34: Ultraviolet photoemission spectra comparing the NEA peak of the Li-O sample after a degas to 550 °C (black), and after annealing at 1218 °C for 30 minutes (red). Intensities are relative to each other and should be comparable. After the higher temperature anneal, the NEA peak is under half as intense, with a much lower area, as well as a shift to higher binding energies.

There is a substantial change in the UPS spectra shown in Figure 6.34 between the 550 °C anneal (black) and 1218 °C anneal (green) which isn't very apparent in the previous figure comparing all five spectra. These spectra have the same capture settings, so the relative intensities should be correct. The NEA peak for the 1218 °C anneal is less than half the size, but also both the peak centre and peak edge are shifted up by around 1 eV, with a small shoulder that could be the remains of the original NEA peak present at 550 °C or a graphitic workfunction edge.

To further investigate the valence band structure changes, a series of XPS spectra were taken for the surface after annealing to 1218 °C, which are compared with the sample after annealing to 250 °C in Figure 6.35.

The XPS spectra for the oxygen 1s and carbon 1s in Figure 6.35 seem to back up the analysis of the valence band structure changes. After a 250°C anneal, there is a clear O 1s peak similar to that observed for the oxygenated surface in previous sections, made predominately by double bonded character, as would be expected on the oxygen-terminated C(100) surface. After annealing to

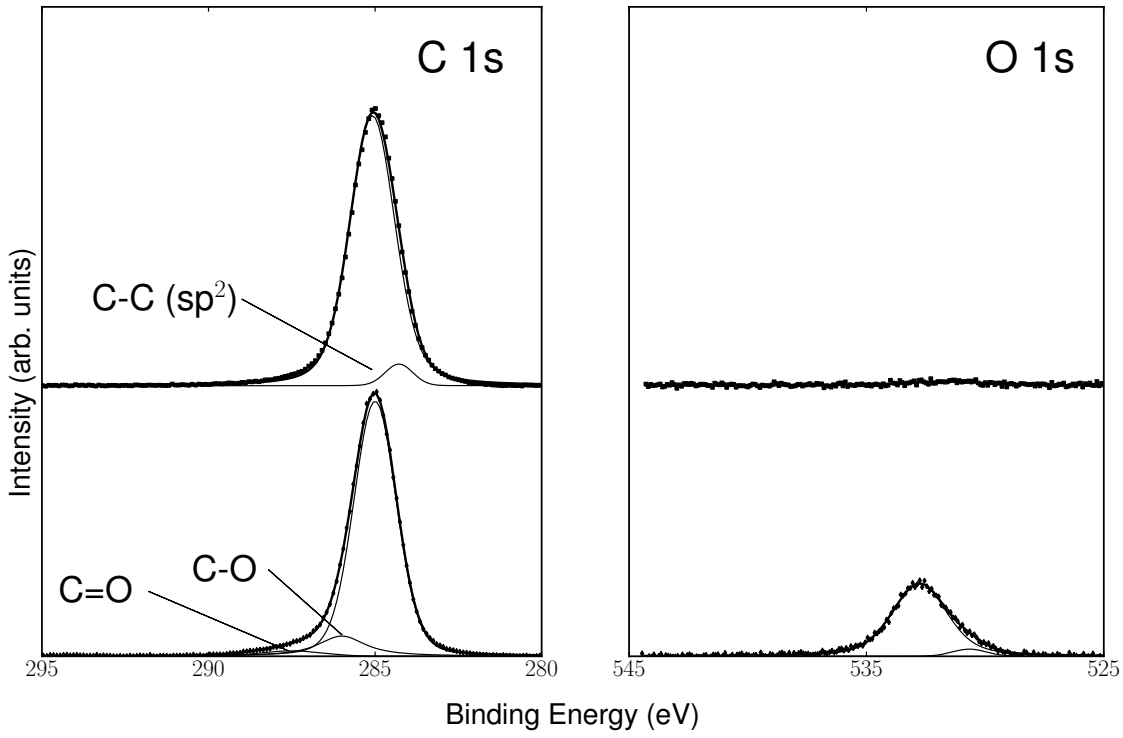

Figure 6.35: X-ray photoemission spectra taken from the Applied Physics Letters paper on this work showing the C 1s (left) and O 1s (right) for the Li-O coated C(100) boron-doped diamond surface. The lower spectrum was taken after a degas to 250°C, and the upper spectra had been annealed at 1218 °C for 30 minutes. There is a clear removal of oxygen at the higher temperatures and a change in the C 1s indicating an onset of graphitisation.

1218°C, there is little to no oxygen detected on the surface, indicating that the oxygen termination has been lifted, as would be expected from previous studies showing complete oxygen removal above 1050°C[17]. This seems to correlate with the removal of the feature at -8 eV in the UPS spectra that has been linked to oxygen termination[30].

The XPS of the carbon 1s peak also shows a clear change between 250°C and 1218°C. After the low temperature annealing there is a shoulder on the left hand side of the diamond peak at 285 eV (i.e. at higher binding energies) that fits to C=O and C-O carbon oxygen bonding, and little to no graphitic character on the lower binding energy side of the diamond peak. After annealing to 1218°C however, most of the carbon-oxygen bond character has been removed, and a significant sp^2 shoulder below the main diamond line is observable - signs that the oxygen-termination has been lifted and that there is graphitisation or surface reconstruction of the now mostly bare surface, which again correlates to the changes observed in the valence band structure.

6.4.9 UPS and XPS of Li-O terminated phosphorus doped C(111) diamond

In addition to the study of the LiO surface layer on C(100) boron doped diamond, ultraviolet photoemission (UPS) and X-ray photoemission (XPS) was also used to study Li-O surface layer on a phosphorus doped diamond overlayer on the C(111) surface supplied by Hasselt University.[36–38]

The same preparation treatment was used for the LiO coating on the C(111) samples. Samples were oxygen terminated using an acid wash in fuming nitric acid for one hour followed by thirty minutes exposure to UV-excited ozone in a UVO ozone cleaner. Atomic lithium was deposited onto the diamond surface using thermal evaporation of lithium metal in a Balzers 510 coater at a pressure of 2×10^{-3} Torr. A quartz crystal monitor was used to estimate a lithium thickness of approximately 50 nm. The samples were removed from the chamber in an oxygen-free argon gas ambient in which they were stored until the samples were placed in the analysis system.

X-ray photoemission spectra (XPS) were again taken in an Omicron Multiprobe UHV system with a base pressure of 5×10^{-10} Torr, using Al $K\alpha$ radiation ($h\nu = 1486.6$ eV) from a VG XR3E2 twin anode source and an Omicron EA125 hemispherical analyser. Before XPS spectra were taken the samples were degassed at between $200 - 250$ °C to desorb contaminants. XPS scans were taken with pass energy of 50 eV, a dwell time of 0.5 seconds and a 0.1 eV step size, whilst UPS scans were taken with a 5 eV pass energy and 0.05 eV step size. Spectra were normalized to the maximum intensity of the inelastically scattered electrons. Analysis was performed using the analysis package Fityk[20] using Voigt peaks and the Levenberg-Marqaurdt fitting algorithm.

Figure 6.36 shows the UPS spectra for the C(111) phosphorus doped sample after Li-O treatment and subsequent washing, showing what appears to be a sharp NEA peak around -17 eV (4.3 eV in Kinetic Energy). The sample has been biased to 5 V, and the spectra have been calibrated accordingly. This NEA peak centre is around 1 eV lower than might be expected from theoretical considerations. The NEA peak appears at the analyser workfunction plus the band gap of diamond of approximately 5.3 eV. The workfunction of the analyser is normalised to 0 eV in kinetic energy, or -21.22 eV in the spectra described in figure 6.36. If this is an NEA peak, it is likely that the sample is charging.

When we compare this spectra for the Li-O surface on the phosphorus doped sample with the

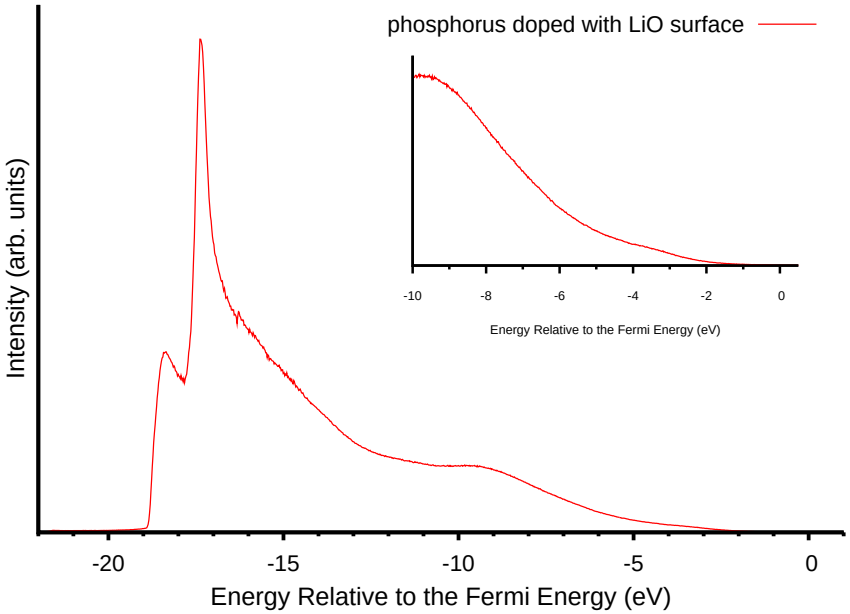

Figure 6.36: UPS spectra of the phosphorus-doped sample with Li-O surface layer, showing a probable NEA peak at approximately 4.3 eV. Inset shows the Fermi edge. Intensity has been normalised to the NEA peak intensity.

oxygen and hydrogen terminated boron doped samples from the previous section as in Figure 6.37, we can see that the intensity of the phosphorus doped sample is much higher than the oxygenated sample, with the peak at -21.22 eV comparable to the hydrogen NEA peak, albeit of lower intensity. The charging of the sample as explored below makes true determination of the sample workfunction and EA strength impossible but it does seem like there is evidence to suggest an NEA is also formed by LiO on the P-doped C(111) surface.

Figure 6.38 compares the UPS spectra for increasing bias voltages from 1 to 5 V, after calibration to these voltages. The spectra still show a differing peak position for both the NEA and low KE deep valence band features as the voltage changes, characteristic of sample charging.

Figure 6.39 compares the UPS spectra at 5 V for the sample at room temperature and after heating to approximately 200 °C in situ. The NEA peak shifts slightly lower to around 4.05 eV in kinetic energy, indicating that the enhanced conductivity at this temperature is still insufficient to remove charging effects.

Figures 6.40-6.42 show the XPS spectra for the phosphorus doped sample with Li-O surface treatment, taken at around 200 °C to try and alleviate charging. In Figure 6.40, there is some C-C and C-O behaviour near the expected values at 285 eV, but also a large peak at 292 eV. This could be remaining lithium carbonate (reference value 291.8 eV) but could also be the diamond peak charging significantly.

Similarly, the XPS spectrum for the oxygen 1s (figure 6.41) is shifted substantially from where we would expect it to be (530-535 eV), indicating charging of as much as 10 eV.

Figure 6.42 shows the lithium 1s spectra in XPS, showing a peak roughly in the region expected for lithium (around 55 eV for atomic Li and 56-57 eV for ionic Li), but due to the amount of charging

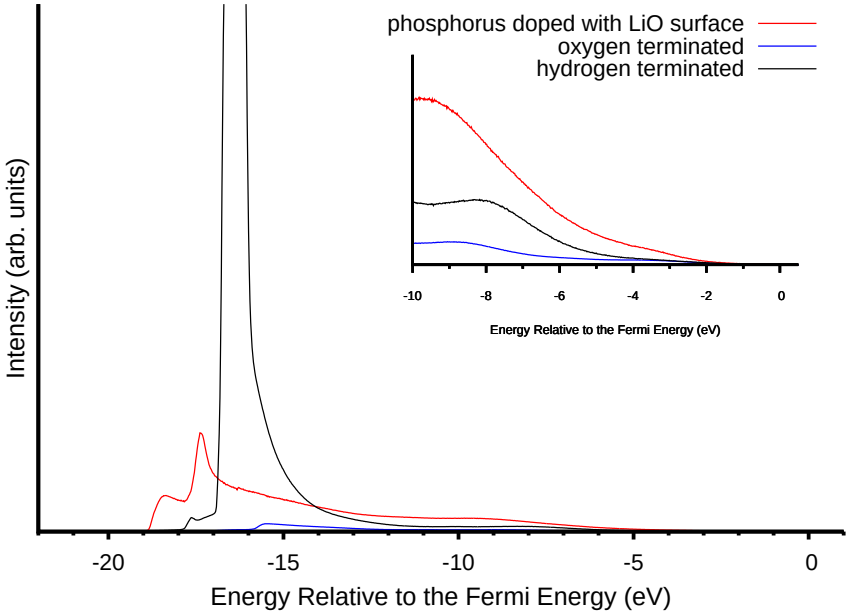

Figure 6.37: UPS He I spectra comparing the phosphorus doped sample (red) with the hydrogen terminated and oxygen terminated spectra on the boron-doped sample, showing the probably NEA peak for the P-doped sample. Inset shows the Fermi edge.

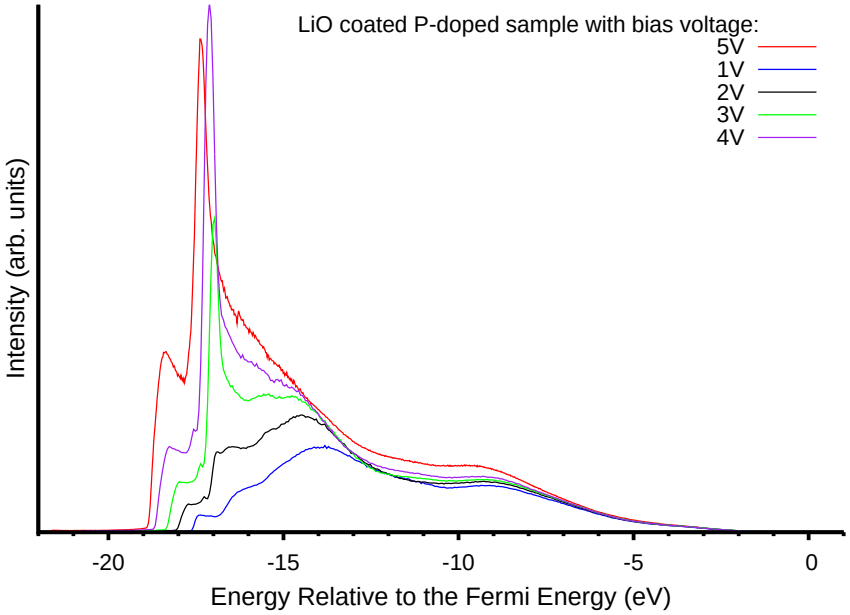

Figure 6.38: UPS spectra with increasing bias voltages for the phosphorus-doped Li-O treated sample, indicating charging is occurring.

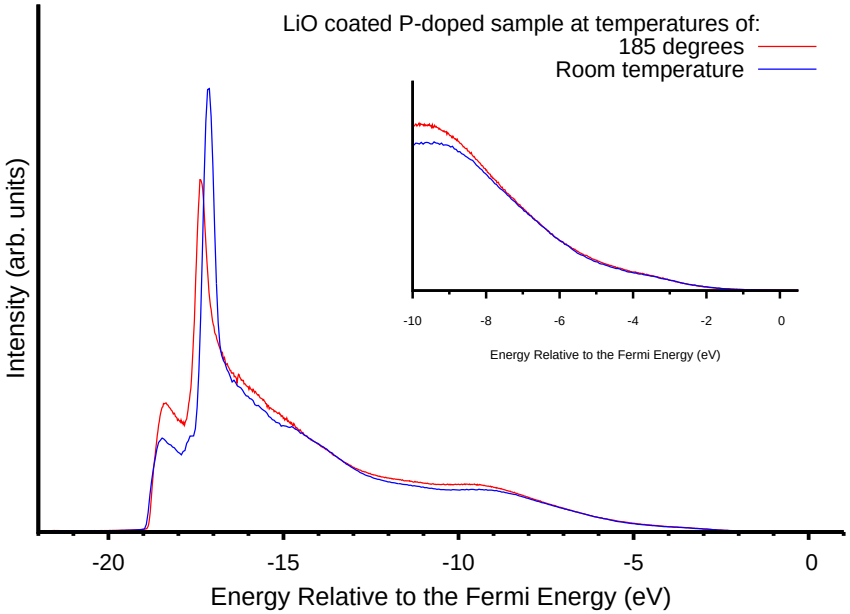

Figure 6.39: UPS He I spectra comparing the phosphorus doped sample at room temperature (blue) and at 200°C (red), indicating some charging effects are occurring. Inset shows the Fermi edge. Intensity has been normalised to the NEA peak intensity of each spectra.

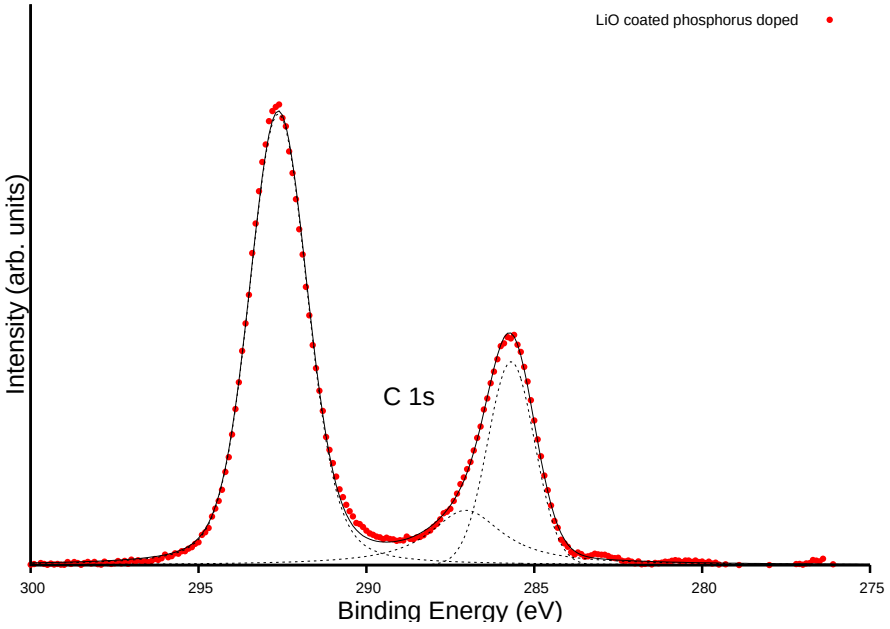

Figure 6.40: XPS spectra for the carbon 1s peak on the phosphorus-doped sample with Li-O coating showing large charging effects.

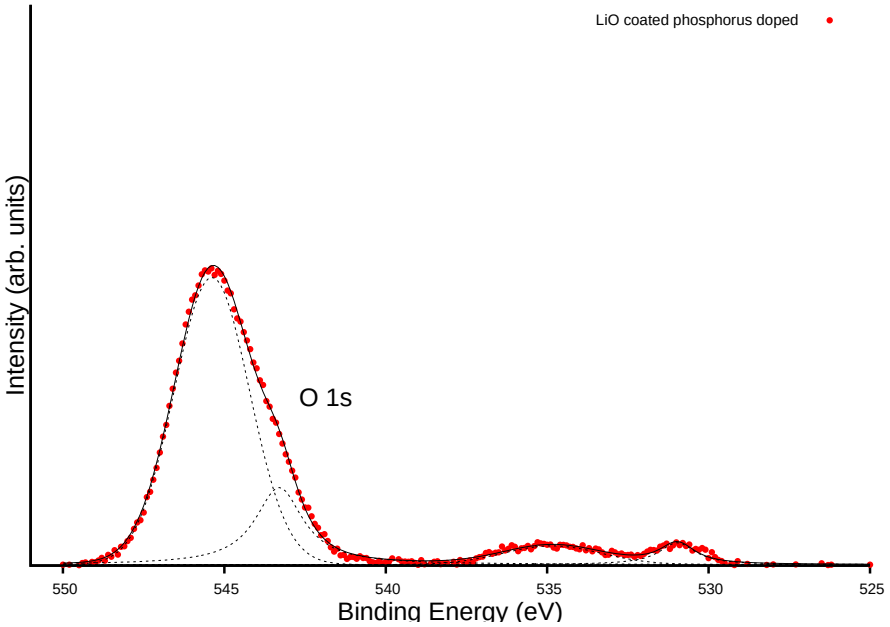

Figure 6.41: XPS spectra for oxygen 1s on the phosphorus-doped Li-O treated sample. This peak is shifted by approximately 10 eV from where it would be expected (between $530 - 535$ eV), indicating substantial charging.

on the previous spectra, this is difficult to confirm.

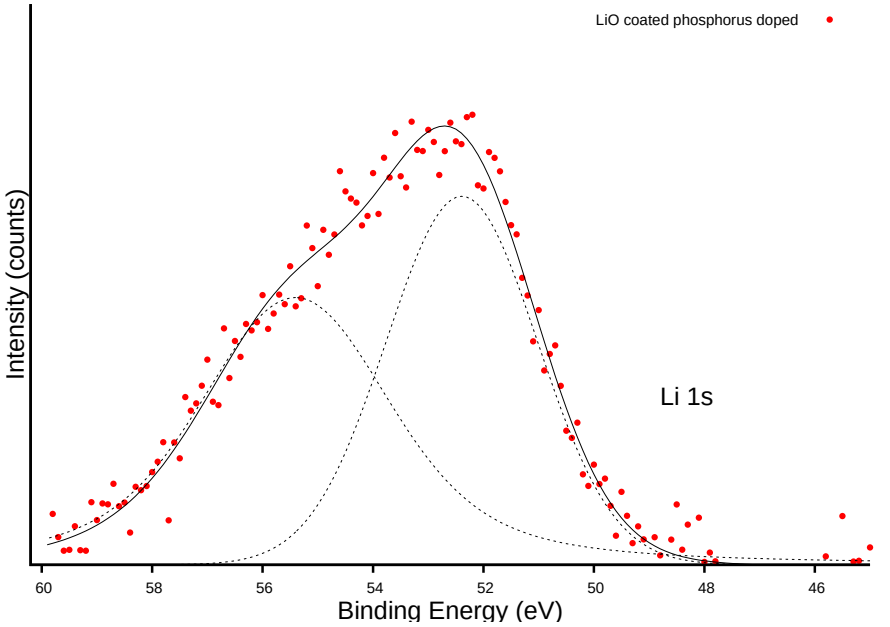

Figure 6.42: XPS spectra for Li 1s peak on the the phosphorus-doped sample with Li-O coating.

UPS spectra on phosphorus-doped diamond with a washed Li-O coating appear to show an NEA peak consistent with those observed on conductive C(100) boron-doped diamond, but with

substantial charging. XPS spectra also display large charging effects even at elevated temperatures. There is promise that an NEA is observed on C(111) phosphorus doped diamond using this Li-O surface as predicted from theoretical calculations, but further work on higher conductivity surfaces, samples at higher temperatures or (in the case of XPS) using a system with a flood gun is required to be certain. Nevertheless, the observation of an NEA on both the C(111) surface and on notionally n-type material is very promising.

6.5 Conclusion

After the prediction of a negative electron affinity surface with lithium adsorption onto the oxygenated C(100) and C(111) diamond surfaces, x-ray and ultraviolet photoemission studies were performed on single crystal diamond surfaces in an attempt to experimentally observe such a phenomenon. Four principle types of substrates were used - CVD C(100) monocrystalline and HPHT C(100) monocrystalline squares, each of dimensions $(2.6 \times 2.6 \times 0.3)$ mm, HPHT C(111) monocrystalline samples of dimensions $(2 \times 2 \times 1)$ mm, and boron-doped overlayers of thicknesses $2 - 5$ μm, homoepitaxially grown by microwave plasma-enhanced chemical vapour deposition onto some of the CVD C(100) chips. The principle difference between the HPHT and CVD samples was the nitrogen concentration, with less than 1 ppm in the CVD samples but around 200 ppm in the HPHT samples. The boron-doped overlayers were conductive and used to eliminate charging during photoemission experiments.

Initial X-ray photoemission spectroscopy studies of hydrogen and oxygen termination on the HPHT and CVD samples at the University of Bristol showed a much higher degree of charging for the HPHT samples, which decreased significantly with temperature, attributed to the activation of nitrogen centres at higher temperature. Contact angle measurements of water droplets on the diamond surfaces and XPS measurements of the oxygen $1s$ spectra showed that a single acid wash in fuming nitric acid at 200 °C was insufficient to form an oxygenated surface, with a contact angle of 60 ° indicating a more hydrophobic surface than the as-received hydrogenated surface. After thirty minutes of ozone treatment, the contact angle reduced to a much shallower angle indicating a much more hydrophilic surface indicative of oxygen termination, and the intensity of the XPS oxygen $1s$ peak increased.

XPS studies of lithium deposition showed a trend for increased lithium 1s signal when deposited on the ozone treated samples, raising the possibility of a lithium-oxygen complex as predicted by theoretical calculations. However, the signal intensity in the IAC XPS system was low due to poor vacuum conditions, and the samples displayed large levels of charging which would make any analysis of the valence band structure through UPS unreliable. To compensate for the charging issue, a series of 2-4 μm boron-doped diamond overlayers were homoepitaxially grown onto five CVD (100) squares using microwave plasma-enhanced chemical vapour deposition to provide a conductive substrate. In addition, time was secured on the Omicron multiscan UPS/XPS system at the University of Surrey to perform higher resolution XPS measurements, as well as UPS measurements.

The samples studied were oxygen terminated using ozone treatment for 30 minutes, followed by the thermal evaporation of 50 nm of lithium in a Balzers 510 coater. After the lithium treatment, XPS of the carbon and oxygen $1s$ peaks showed that the majority of the surface was made up

of carbonates and oxides, likely due to the reaction of lithium with atmospheric components such as oxygen, nitrogen and water. After the sample was washed in deionised water and isopropyl alcohol, XPS showed that lithium still remained on the surface on the oxygenated surface, but not on a similar coated and washed hydrogenated sample, indicating that oxygen-lithium bonding is occurring as predicted.

Ultraviolet photoemission spectroscopy showed a clear, high intensity peak around 5.4 eV in kinetic energy, characteristic of a negative electron affinity surface and similar to that observed from the hydrogen terminated sample used for comparison. This peak was not present on the positive electron affinity oxygenated surface, as expected. Analysis of the UPS spectra for the washed lithium-coated sample gave a workfunction of (2.8 ± 0.1) eV, with a negative electron affinity of (-2.1 ± 0.1) eV, stronger than that observed for the hydrogenated surface. In addition, scanning electron microscope images of the LiO coated surface showed a high intensity of secondary electron emission stimulated by the SEM beam, again indicative of a negative electron affinity.

When this LiO coated surface was annealed at increasing temperatures, the UPS spectra remained stable to around 925 °C, at which point the valence band structure began to change. Above this temperature the sample had a higher workfunction and lower NEA, and the intensity of the NEA peak fell by around half. In addition, above 1140 °C the shoulder peak at -12 eV in the valence band structure associated with oxygen termination disappeared, and new features appeared above 1218 °C indicating a breakdown of the surface. XPS scans of the sample after this annealing temperature showed little oxygen remained on the surface and a significant shoulder in the C 1s peak characteristic of surface graphitisation.

As well as the XPS and UPS data for the C(100) boron-doped samples, studies were performed on C(111) phosphorus doped samples provided by the University of Hasselt. The UPS spectra seemed to have a feature indicating an NEA was present after the lithium-oxygen surface treatment, but despite the doping the sample was not conductive enough and significant charging occurred, limiting interpretation of the UPS spectra on this sample.

The photoemission work presented in this chapter shows clearly that an effect similar to that predicted by the theoretical calculations in the previous chapter appears to be present, with lithium remaining on the surface after water washing only when the surface is oxygen terminated, and a clear NEA peak observable in the USP spectra. Further study of this surface is needed to quantify the effect and determine how easily a full coverage can be prepared, but these results are promising for the development of NEA based diamond devices using the LiO surface termination.

REFERENCES

[1] Loh, K., Xie, X., Yang, S., Pan, J., and Wu, P. *Diamond and Related Materials* **11**(7), 1379–1384 July (2002).

[2] Geis, M., Twichell, J., Macaulay, J., and Okano, K. *Applied Physics Letters* **67**(9), 1328 (1995).

[3] K.M. O'Donnell, T.L. Martin, N. F. and Cherns, D. *Phys. Rev. B* **82**, 115303 (2010).

[4] of Standards, N. I. and Technology. *NIST X-ray Photoelectron Spectroscopy Database, Version 3.5*. National Institute of Standards and Technology, Gaithersberg, MD, USA, (2003).

[5] Himpsel, F., Knapp, J., VanVechten, J., and Eastman, D. *Phys. Rev. B* **20**(2), 624–627 Jul (1979).

[6] Pate, B., Hecht, M., Binns, C., Lindau, I., and Spicer, W. *J. Vac. Sci. Technol.* **21**, 364–367 (1982).

[7] Koleske, D. D., Gates, S., Thoms, B., and Russell, J. *J. Chem. Phys.* **102**(2), 992 (1995).

[8] Thomas, R., Rudder, R., and Markunas, R. *J. Vac. Technol. A* **10**, 2451 (1992).

[9] Pate, B., Stefan, P., Binns, C., Jupiter, P., Shek, M., Lindau, I., and Spicer, W. *J. Vac. Sci. Technol.* **19**, 349–354 (1981).

[10] Schulberg, M., Fox, C., Kubiak, G., and Stulen, R. *J. Appl. Phys.* **77**, 3484–3490 (1995).

[11] Hamza, A., Kubiak, G., and Stulen, R. *Surf. Sci. Lett.* **206**(35), L833–L844 (1988).

[12] Pate, B., Oshima, M., Silberman, J., Rossi, G., Lindau, I., and Spicer, W. *J. Vac. Sci. Technol. A* **2**, 957–960 (1984).

[13] Cui, J., Stammler, M., Ristein, J., and Ley, L. *J. Appl. Physics.* **88**, 3667 (2000).

[14] Cui, J., Ristein, J., and Ley, L. *Phys. Rev. Lett.* **81**(2), 429–432 Jul (1998).

[15] Bandis, C. and Pate, B. *Phys. Rev. B* **52**, 12056 (1995).

[16] Diederich, L., Aebi, P., Küttel, O., and Schlapback, L. *Surface Science* **424**(2-3), L314–L320 April (1999).

[17] Baumann, P. and Nemanich, R. *Journal of Applied Physics* **83**(4) (1998).

[18] Element6. *Element 6 CVD catalogue.* (2010).

[19] Ostrovskaya, L., Perevertailo, V., Ralchenko, V., Dementjev, A., and Loginova, O. *Diamond Rel. Mater.* **11**, 845 (2002).

[20] Wojdyr, M. *J. Appl. Cryst.* **43**, 1126–1128 (2010).

[21] van de Hulst, H. and Reesinick, J. *Astrophysical Journal* **106**, 121 (1947).

[22] Moré, J. In *Numerical Analysis,* Watson, G. A., editor, volume 630 of *Lecture Notes in Mathematics*, chapter 10, 105–116. Springer Berlin Heidelberg (1978).

[23] Klauser, F., Ghodbane, S., Boukherroub, R., Szunerits, S., Steinmuller-Nethl, D., Bertel, E., and Memmel, N. *Diamond and Related Materials* **19**(5-6), 474 (2010).

[24] Petrick, S. and Benndorf, C. *Diam. Rel. Mat.* **10**(3-7), 519 (2001).

[25] Moulder, J., Stickle, W., Sobol, P., and Bomben, K. *Handbook of X-ray Photoelectron Spectroscopy.* Perkin-Elmer Corp., Physical Electronics Division, Eden Prairie MN, USA, (1992).

[26] Patnaik, P. *Handbook of Inorganic Chemical Compounds.* McGraw-Hill, Columbus, OH, USA, (2002).

[27] hrn, A. and Karlstrm, G. *The Journal of Physical Chemistry B* **108**(24), 8452–8459 (2004).

[28] Ensling, D., Thissen, A., and Jaegermann, W. *Applied Surface Science* **255**(5, Part 1), 2517 – 2523 (2008).

[29] Tanaka, S., Taniguchi, M., and Tanigawa, H. *Journal of Nuclear Materials* **283-287**(Part 2), 1405 – 1408 (2000). 9th Int. Conf. on Fusion Reactor Materials.

[30] Loh, K., Xie, X., Yang, S., and Zheng, J. *The Journal of Physical Chemistry B* **106**(20), 5230–5240 (2002).

[31] Thoms, B., Owens, M., Butler, J., and Spiro, C. *Applied Physics Letters* **65**, 2957–2959 (1994).

[32] Diederich, L., Küttel, O., Schaller, E., and Schlapbach, L. *Surface Science* **349**, 176 (1994).

[33] Baroody, E. *Phys. Rev.* **78**(6), 780–787 Jun (1950).

[34] Pehrsson, P., Long, J., Marchywka, J., and Butler, J. *Applied Physics Letters* **67**(23), 3414–3416 (1995).

[35] Francz, G. and Oelhafen, P. *Diam. Relat. Mater.* **4**, 539 (1995).

[36] Haenen, K., Meykens, K., Nesladek, M., Knuyt, G., Stals, L., Teraji, T., Koizumi, S., and Gheeraert, E. *Diamond Rel. Mater.* **9**, 952 (2000).

[37] Haenen, K., Meykens, K., Nesladek, M., Knuyt, G., Stals, L., Teraji, T., Koizumi, S., and Gheeraert, E. *Diamond Rel. Mater.* **10**, 439 (2001).

[38] Koeck, F., Nemanich, R., Lazea, A., and Haenen, K. *Diamond and Related Materials* **18**(5-8), 789 – 791 (2009). Proceedings of Diamond 2008, the 19th European Conference on Diamond, Diamond-Like Materials, Carbon Nanotubes, Nitrides and Silicon Carbide.

Enlow: If we could only say what benefit this thing has. No one's been able to do that...
Professor Milgate: That's because great achievement has no road map.

The West Wing, Season 4
Episode 15: 'Dead Irish Writers'(2002)

7

Device applications of the Li-O NEA surface

7.1 Introduction

With the confirmation in the previous chapter of the negative electron affinity from Li-O on diamond predicted by computational studies, for the final section of this work the behaviour of this surface layer for several device applications was tested.

Firstly a similar field emission experiment was briefly reported as in chapter 4, using boron-doped CVD diamond films with hydrogen termination, oxygen termination and using the Li-O coating reported on in Chapter 6.

Secondly, thermionic emission was studied again comparing the performance of the hydrogen terminated surface against the Li-O surface, using ultrananocrystalline CVD diamond films to aid conductivity to the surface.

Finally, the surface conductivity of the Li-O termination was studied using a transmission line model method and compared to the hydrogenated and oxygenated surfaces to see whether this surface would have any application for use in field-effect transistors.

7.2 Field Emission of Li-O terminated diamond

The effectiveness of the Li-O coating for enhancing field emission was tested using field emission from a boron-doped CVD diamond film grown using hot-filament CVD by Raquel Vaz.

The diamond film was first tested immediately after growth, with a nominal hydrogen-termination from the hydrogen plasma in the growth chamber. The sample was then ozone treated in a UVO ozone cleaner for 30 minutes to give an oxygen-terminated surface, and then field emission was again tested. Finally, a 50 nm coating of lithium was applied using thermal evaporation in the Balzers 510 coating machine and washed with deionised water and isopropanol before again testing in the field emission chamber.

The field emission setup was the same as that described in Chapter 4, where the sample was sandwiched between a YAG tin-coated phosphor screen with a spacer of glass. Voltages of $0-4000$ V was applied between the sample and the phosphor screen using a Brandenburg high voltage power supply, and the current readings measured using a Keithley 2750 multimeter, output onto

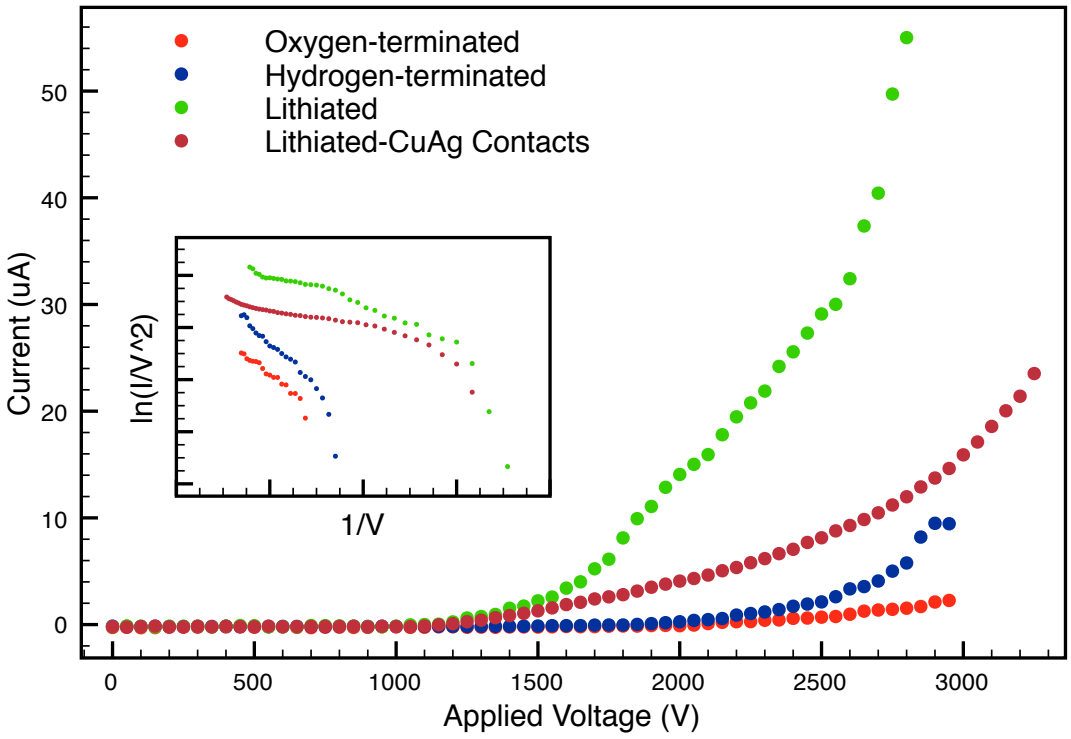

Figure 7.1: Field emission from the hydrogen terminated, oxygen terminated and Li-O coated boron doped CVD sample, showing a clear improvement between the hydrogen and Li-O films. The inset shows the Fowler-Nordheim plots for these samples.

a computer running data logging software programmed in LabView. Figure 7.1 compares the field emission of the sample after growth, with a hydrogen termination, after thirty minutes of ozone treatment, and then after lithium coating and water washing.

Figure 7.1 shows the clear degradation in field emission turn-on and Fowler-Nordheim plots when the hydrogenated surface was treated for 30 minutes in an ozone plasma, as would be expected. In actual fact, the performance of the hydrogen terminated surface was slightly poorer than expected from previous emission studies on hydrogenated boron-doped films, and may be due to a mixed termination on the surface.

Nevertheless, there is vast improvement in field emission performance after the ozone treated oxygenated surface is coated in lithium (and water washed), with the Fowler-Nordheim plot showing a straighter line and shallower gradient indicative of an improved workfunction, and a turn-on improving from around 1800 V for the hydrogen-terminated surface to around 1100 V. The second Li-O graph used copper contacts affixed with silver paste rather than bulldog clips to achieve a connection, seeing an identical turn-on but slightly lower currents.

7.3 Thermionic emission from Li-O terminated NCD CVD diamond

In addition to the field emission testing, the thermionic emission properties of the Li-O diamond termination were explored, compared to the hydrogen terminated surface of nanocrystalline diamond (NCD) films deposited using microwave plasma-enhanced chemical vapour deposition. NCD films were used rather than single crystal as work by other groups has shown that the grain boundaries in NCD films can aid emission due to increased conductivity.[1;2]

The NCD films were grown on top of 500 nm MSY HPHT diamond powder that was self-assembled onto a tungsten substrate using electrochemical self-assembly techniques (thiolated). A 5 mm diameter spot of nanocrystalline diamond was grown using microwave plasma-enhanced CVD techniques by Oliver Fox, using a higher nitrogen mix than usual to try and encourage higher nitrogen uptake in the film. The gas phase mix was approximately 0.5% N_2, 93% H_2 and 6.5% methane, with a pressure of 125 Torr. The film was grown for twenty minutes using a plasma excited by a microwave power of 1.2 kW.

After the CVD growth step the hydrogen terminated as-grown surface was thermionically tested in a vacuum system with pressure of $4{\times}10^{-5}$ Torr. The sample was heated radiatively using a tungsten strip heater at 1400 °C placed 1 mm below the sample, with the temperature on the sample measured using a Minolta optical pyrometer. A molybdenum collector of (1×3) cm was mounted 2 mm above the sample, with a small field applied between the two plates using a low voltage PSU. Figure 7.2 compares the IV characteristics of the hydrogen terminated and lithium-oxygen terminated surfaces (at two temperatures).

Figure 7.2 shows a huge jump in current density between the hydrogenated and Li-O terminated surfaces, with approximately a thirty-fold increase in current density. This is only a preliminary result and further exploration of the temperature dependence and turn-on of this surface treatment on NCD diamond would be an important next step, but as with the field emission data, this is a good indication that the Li-O surface coating has potential in improving thermionic and field electron emission, particularly when coupled with the conductivity inherent in NCD films.

7.4 Surface Conductivity and Field Effect Transistors using Li-O terminated diamond

7.4.1 Basic resistance measurements of the Li-O surface on diamond

To check for initial surface conductivity using the Li-O surface layer, four samples were prepared with evaporated titanium-gold contacts approximately 1.5 mm apart. The samples consisted of two C(100) HPHT crystals, one C(111) HPHT crystal and one C(100) CVD crystal, acquired commercially from Element six as in Chapter 6's UPS/XPS experiment.

The substrates were $(2.6 \times 2.6 \times 0.5)$ mm in dimension, with tolerances of $(+0.2/-0.0)$ mm in width and ± 0.05 mm in thickness. All samples had a surface smoothness according to the manufacturer of less than 10 nm. The CVD samples were typically 100 % monocrystalline, with less than 1 ppm of nitrogen and less than 0.05 ppm of boron impurities. The HPHT samples by

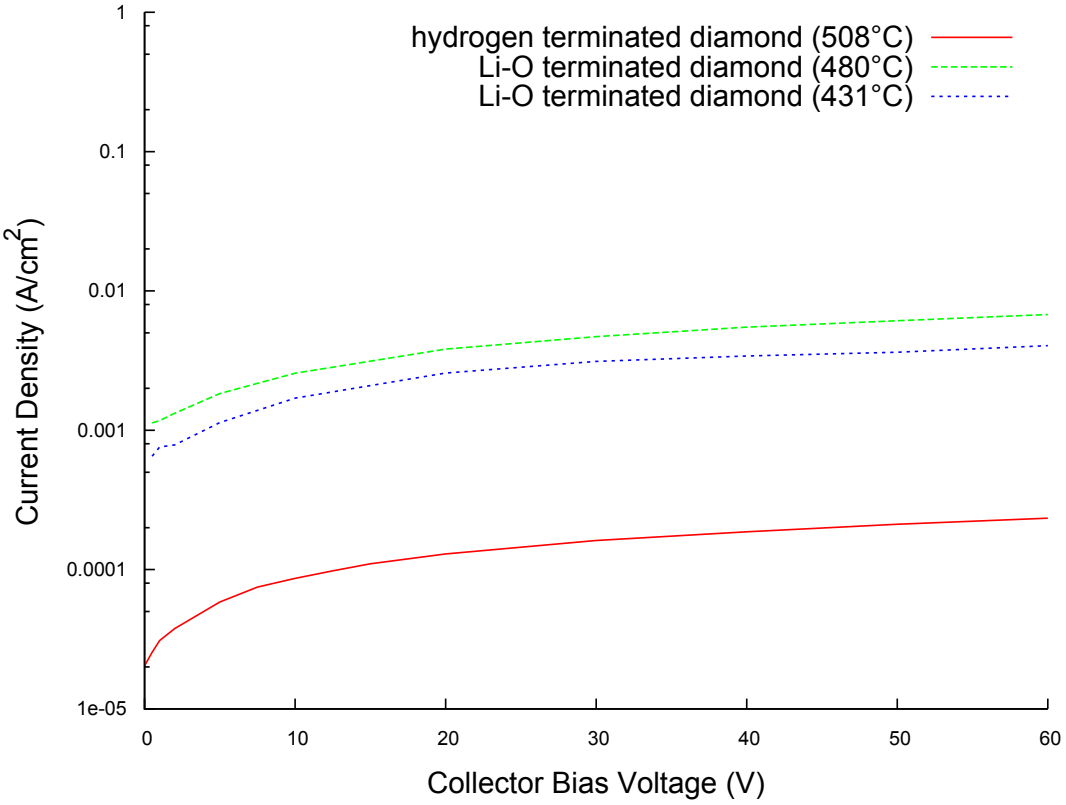

Figure 7.2: Graph showing the current density with increasing collector bias voltage observed for a hydrogen terminated NCD film at 508 °C and the same film with a Li-O termination at 480 °C and 431 °C

Sample	Resistance after oxygen termination ($k\Omega$)	Resistance after lithium termination ($k\Omega$)
CVD (100)	no conductivity	no conductivity
HPHT (100)	no conductivity	2-4
HPHT (111)	no conductivity	12

Table 7.1: Table showing basic two point resistance measurements of oxygen and Li-O termination on various diamond substrates

comparison had typically 80% single sector crystal and around 200 ppm nitrogen impurities.

After deposition of the Ti-Au contacts, the samples were ozone cleaned for thirty minutes in a UVO Ozone cleaner and had approximately 10 nm of lithium deposited by thermal evaporation, following similar preparation methods to the previous characterisation step. Surface resistance between the two contacts was measured using a Fluke Multimeter, before and after washing the samples in deionised water to remove excess lithium. The results of these measurements are shown in table 7.1.

The initial resistance measurements show an interesting divide in behaviour between the HPHT and CVD substrates. The CVD C(100) sample showed no noticeable conductivity after lithium deposition, and no change after water washing, the high resistance measured showing no conductivity on undoped diamond using an Li-O surface treatment.

On all three HPHT samples, however, low resistances were measured between the contacts.

The two C(100) samples showed similar resistances of 2-4 kΩ for a gap of around 1.5 mm, whereas the C(111) sample had a higher resistance of around 12 kΩ. After water washing, the surface resistance of the C(100) samples were little changed, indicating this conductivity is unlikely due to evaporated lithium bridges between the contacts, as this should be removed by water washing. The C(111) surface resistance was approximately doubled after water washing.

The fact that surface conductivity was observed for the HPHT samples but not for the CVD substrates is intriguing, as the only major difference between the substrates is a slightly lower single-crystal percentage and a much higher nitrogen content in the HPHT sample. This behaviour could be explained by the overlap between the surface electronic states induced by the Li-O surface treatment and the nitrogen donor levels in the bulk diamond. Further study was required to investigate the potential of this surface-substrate combination for devices such as field-effect transistors.

7.4.2 Sheet resistance calculations of the Li-O surface using TLM patterns

The Transmission Line Model (TLM) theory was first proposed by Reeves and Harrison [3] to allow the separation of sheet and contact resistances when measuring a sample's resistance. A TLM pattern consists of a series of contacts of the same contact width but different gap sizes on the desired surface. [4]

For each contact separation, a series of voltages was passed between them and the current measured using a Keithley 2400 source meter, and the resistance calculated from the gradient of the IV curves produced. The resistance is measured for each contact separation, and the contact spacing L is plotted against the total resistance R between the two pads, which can broken down into

$$R = 2R_c + R_s \tag{7.1}$$

Where R_c is the resistance due to an individual contact (hence why it is doubled in the above equation), and R_s is the resistance due to the semiconductor, which is defined as a function of the resistivity ρ and the sample width W and thickness t:

$$R_s = \frac{\rho L}{tW} = R_{sh}\frac{L}{W} \tag{7.2}$$

Where $R_{sh} = \frac{\rho}{t}$ is the sheet resistance of the material, in ohms/square. So the total resistance measured between the two contact pads can be written

$$R = 2R_c + R_{sh}(\frac{L}{W}) \tag{7.3}$$

So by plotting total resistance R against contact separation L the gradient of the graph is R_{sh}/W and the graph intercepts the x and y axis at L_x and twice the contact resistance $2R_c$ respectively. The contact resistance R_c is defined by

$$2R_c = \frac{2R_{sk}L_T}{W} \tag{7.4}$$

Where R_{sk} is the sheet resistance of the material underneath the contact pads (mostly oxygen-

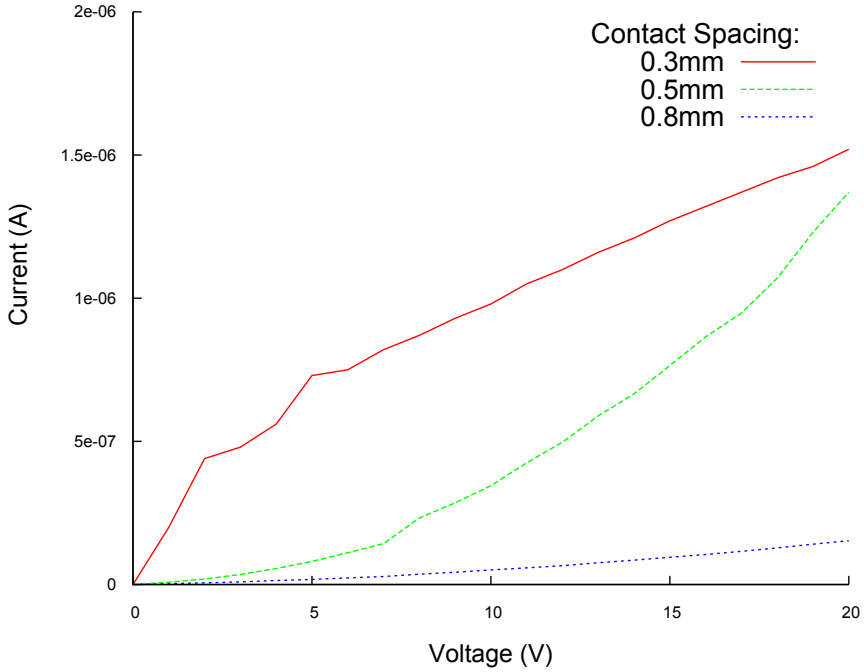

Figure 7.3: Graph showing the IV characteristics of a variety of hydrogen terminated HPHT CVD(100) diamond samples with various contact pad separations.

terminated diamond in this experiment) and L_T is the transfer length, defined as the distance needed if current is to flow into or out of the ohmic contact, which depends on the contact resistance R_c such that $L_T = \sqrt{\frac{R_c}{R_{sk}}}$.

Each sample in this experiment had two metal contact pads evaporated using a laser-cut tungsten mask, with contact pad dimensions of (0.8×1) mm and a variety of pad separations between 0.2 and 1 mm. The metal layers were deposited using a Balzers 510 coating machine at a pressure of around 10^{-3} Torr. Initially a titanium-gold evaporation was used, but this suffered from adhesion problems and so the samples were acid cleaned to remove this layer and aluminium contact pads were evaporated instead, with better results.

Three CVD single crystal C(100) oriented diamonds had contact gaps of 0.25, 0.5 and 0.75 mm deposited, whilst seven HPHT single crystal C(100) oriented diamonds were used with contact gaps of 0.2, 0.3, 0.4, 0.5, 0.6, 0.8 and 1.0 mm. All samples were acid washed in fuming nitric acid and ozone treated for thirty minutes in a UVO ozone cleaner before the contact pads were deposited to ensure an oxygen-termination was present.

Samples were hydrogen terminated in a microwave-plasma enhanced CVD reactor at 900 W and 80 Torr of hydrogen gas only, with a substrate temperature around 550 °C for five minutes, and tested again. Figure 7.3 shows example IV curves for three contact distances on the HPHT(100) surface, with the gradient of each graph being used to calculate the resistance.

Figure 7.4 (a) shows the resistance values calculated in Figure 7.3 plotted against the contact distance for that sample, for a sheet resistance of 2.09 $\times 10^8$ Ω and an intercept of 5.32×10^7 Ω, giving a contact resistance for each pad of 2.66 $\times 10^7$ Ω. Figure 7.4 (b) shows the resistance of three hydrogen terminated CVD(100) surface against contact pad separation distance. This gives

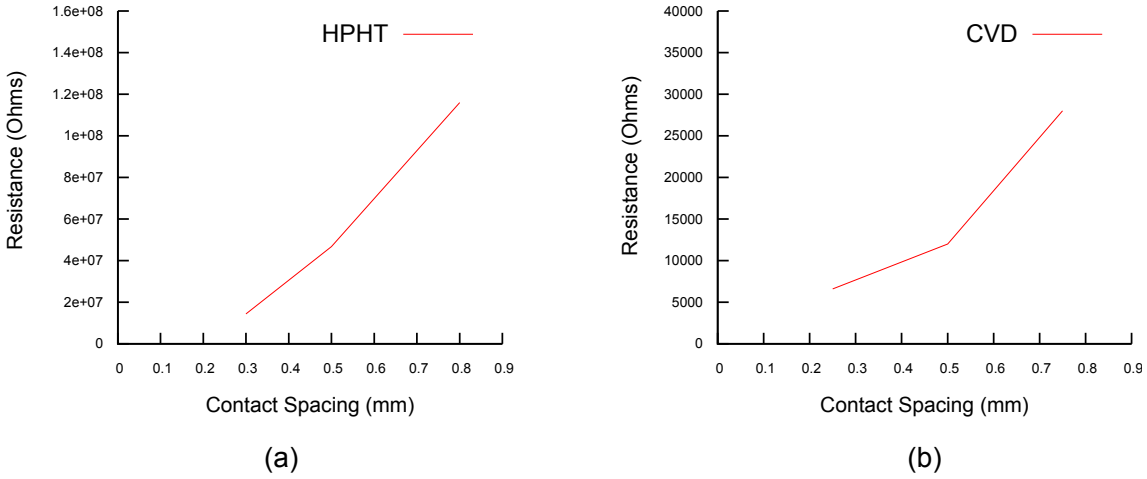

Figure 7.4: Figure showing the Resistance variation against contact pad separation for the (a) hydrogen terminated HPHT C(100) diamond and (b) hydrogen terminated CVD C(100) diamond samples.

a sheet resistance for the hydrogenated C(100) surface of 4.28×10^4 Ω and an intercept of 5.87×10^3 Ω, giving a contact resistance of 2.94×10^3 Ω.

After thirty minutes ozone treatment, there was no longer any discernable conductivity in any of the HPHT samples, and the CVD samples increased in resistance by around four orders of magnitude to around 1×10^8 Ω/mm, showing that the oxygen termination has replaced most of the hydrogen termination on the surface. After a further twenty minutes of ozone treatment, none of the CVD samples showed any surface conductivity either.

After the fifty minute ozone treatment, samples had approximately 50 nm of lithium deposited in vacuum using the evaporation of lithium metal in a Balzers 510 coating machine, the same process used as in the photoemission experiments in the previous chapter. Samples were again tested for conductivity, before washing in deionised water and isopropanol and conductivity tested once more.

Unfortunately, none of the lithiated samples showed significant conductivity either before or after water washing over a contact pad separation range of $0.2 - 1.3$ mm, using samples with both Ti-Au and Al contact pads. From this work it appears that either the Li-O surface preparation is not conductive or that the Li evaporation and washing technique gives insufficient coverages for conductivity on the mm scale. It is unclear why the initial results using the 1.5 mm separation contact pads showed such low resistances whereas the TLM study showed no conductivity - it may be that there was some kind of contamination or hydrogen termination on the surface of the HPHT samples in the initial study, or that there was a problem with the Li evaporation in the TLM study. Further exploration of this preparation together with XPS measurements would be desirable to gain a more definitive answer - using a combination of Kelvin probe microscopy for nanoscale conductivity measurements and XPS would be a good experiment that if performed on the same system would allow a clearer picture to be understood without exposure to atmosphere.

Table 7.2 shows the sheet resistance, transfer length and contact resistance for the samples studied. The measurements confirm the conductivity of the hydrogen-terminated surface and

Sample	termination	sheet resistance (Ω)	contact resistance (Ω)
HPHT	oxygen terminated	-	-
CVD	oxygen terminated	-	-
HPHT	hydrogen terminated	2.09×10^{8}	5.32×10^{7}
CVD	hydrogen terminated	4.28×10^{4}	5.87×10^{3}
HPHT	ozone treated (30 mins)	-	-
CVD	ozone treated (30 mins)	1×10^{8}	5×10^{7}
CVD	ozone treated (50 mins)	-	-
HPHT	lithium coated	-	-
CVD	lithium coated	-	-
HPHT	water washed Li-O	-	-
CVD	water washed Li-O	-	-

Table 7.2: Table comparing the resistance properties of the different terminations on the single crystal C(100) diamond surface

its removal by oxygen termination but no sample with the Li-O surface preparation showed any conductivity on the length scales used. It may be that there is no surface conductivity from this surface, or that there is insufficient coverage to observe such an effect on this scale. Using a Kelvin Probe microscope to study the surface conductivity of the Li-O surface on the nanoscale would be able to confirm or deny the existence of such surface conductivity to greater accuracy, but it can be concluded from this short study that if the Li-O surface is conductive, although the Li evaporation and water washing preparation technique is sufficient for creating an NEA surface, it does not provide sufficient coverage for a conductive surface. This may be important for optimisation of the NEA surface as well, and more careful surface preparation techniques could be explored in future work.

7.5 Conclusion

This chapter has reported some early attempts to characterise the suitability of the Li-O surface treatment explored in the previous chapters for several device applications. The stable negative electron affinity predicted by computational modelling for Li-O on the C(111) and C(100) diamond surfaces and detected using photoemission should have a number of important applications, and a few of them were explored in this chapter.

Firstly, the effect of the Li-O surface treatment on field emission was studied. A boron doped diamond film grown by hot filament chemical vapour deposition was placed in a high vacuum chamber with a spacing of 300 μm to conductive YAG phosphor screen. The electron current between the sample and the screen was measured for increasing voltage. It was found that the as-grown nominally hydrogen terminated film had a turn-on around 1800 V. After an oxygen treatment in an ozone cleaner, both the emission density and the turn-on deteriorated. When a coating of lithium was applied to the ozone-treated surface and the excess washed away with deionised water, the resultant Li-O surface increased the current significantly and saw the turn-on drop to around 1100 V. The relatively poor performance of the 'hydrogen terminated' film indicates that perhaps the as-grown material had a mixed termination, but the much improved performance of the Li-O coated film showed that this surface is a promising NEA treatment to improve diamond

field emission properties.

A similar approach was performed for thermionic electron emission. A nanocrystalline diamond film grown by microwave plasma-enhanced CVD was heated at a high vacuum using a tungsten resistive heater. A small field of $0 - 60$ V was applied on a molybdenum collector plate 2 mm from the diamond film, and the current recorded. It was found that the current density for the film after Li-O treatment was around thirty times higher than the same film with a hydrogen termination, again showing early promise in using this surface treatment to improve diamond emitters for thermionic emission.

The surface conductivity of hydrogenated, oxygenated and lithium-oxygen terminated HPHT and CVD C(100) diamond single crystals was studied using graphite contact probes and TLM patterned TiAu and Al contact pads with a range of separation widths. After exposure to a hydrogen plasma in a microwave plasma-enhanced CVD reactor for ten minutes, samples showed a clear conductivity, with the CVD samples having a sheet resistance of 4.28×10^4 Ω/mm and the HPHT samples having a significantly higher sheet resistance of 2.09×10^8 Ω/mm. After thirty minutes of exposure to an ozone cleaner, the HPHT samples showed no noticeable conductivity, and the CVD samples, whilst still noticeably conductive, had a much higher sheet resistance of 1×10^8 Ω/mm, but after a further twenty minutes of ozone treatment this conductivity was also removed. Samples then had around 10 nm of lithium evaporated onto them to test the surface conductivity of the Li-O surface layer, but no significant conductivity was observed for either the washed or unwashed Li-O surface, using TiAu or Al contact pads, on either the HPHT or CVD samples. Although it is possible there was insufficient coverage to provide a consistent surface for these measurements, the surface does not appear to be promising for use in field-effect transistors. A more careful study of the nanoscale conductivity of the Li-O surface using Kelvin Probe microscopy may yield better results.

REFERENCES

[1] Liu, Y., Tso, P., Pradhan, D., Lin, I., Clark, M., and Tzeng, Y. *Diamond Rel. Mater.* **14**, 2059 (2005).

[2] Koinkar, P., Patil, S., Kim, T.-G., Yonekura, D., More, M., Joag, D., and Murakami, R.-I. *Applied Surface Science* **257**, 1854 (2011).

[3] Reeves, G. and Harrison, B. *IEEE transactions on electron devices* **42**, 1536 (1995).

[4] Bashar, S. *Study of Indium Tin Oxide (ITO) for Novel Optoelectronic Devices.* PhD thesis, King's College London, (1998).

'Cause it's one thing to start it with a positive jam
And it's another thing to see it all through.
And we couldn't have even done this
If it wasn't for you.

"Stay Positive" by The Hold Steady (2008)

8 Conclusion

This thesis aimed to investigate the interaction of lithium with diamond as a potential bulk or surface dopant that would reduce the barrier to electron emission. Initially the work looked at diamond nanoparticles before and after reaction with lithium salts, noting an improvement in emission properties after the reaction, but with little control or understanding of the mechanism behind the change, although it seemed like the lithium was having an effect on the surface rather than the bulk of the nanodiamonds.

Later work used density functional theory to simulate the interaction of lithium on the bare and oxygenated C(100) and C(111) surfaces, predicting that on both surfaces lithium forms a strongly bound structure with a large negative electron affinity and a large workfunction shift. This surface treatment was then explored and characterised using X-ray and Ultraviolet photoemission studies, confirming the computational predictions. The surface treatment was also found to improve field and thermionic emission properties but no significant surface conductivity was found, possibly due to insufficient coverage.

8.1 Summary

8.1.1 Emission and characterisation of lithiated diamond nanopowders

Firstly the behaviour of nanodiamonds grown by the high pressure, high temperature (HPHT) process were investigated using a number of material characterisation and electron emission studies. These powders had a particle sizing of around 500 nm with a large variety of shapes and facets. Infra-red analysis showed 200 ppm of nitrogen was present in the material due to inclusion during the HPHT synthesis process.

The as-received material was treated at high temperature with a number of lithium salts in a low ambient pressure of inert gas. The electron emission of this lithiated powder was testing using thermal and field excitation and compared to the as-received material and to commercial Ba-O thermionic cathodes.

The behaviour of the commercial cathode at the recommended operating temperature of approximately 800 °C showed that there was a strong dependence on anode field strength, interelectrode spacing and on the material and morphology of the emitter, with carbon nanotubes achieving

a much higher emission current density when used as the collector when compared to tungsten or diamond. The large drop off in performance with even small increases in the interelectrode spacing makes design of larger devices difficult to achieve. Gaps of below 100 μm are desired unless large fields are used, a charge-carrying gas is present or electrons in the emitter are excited by additional energy sources to the heat, such as photon-enhanced thermionic emission.

Compared to the commercial emitter, the lithiated diamond showed a much lower current density but a lower temperature turn-on of around 500 °C, indicating a low workfunction but possibly poor conductivity between the nanodiamonds. This was substantially improved on the performance of the as-received material, which was a fairly poor emitter by comparison. Similarly, the lithiated material performed much better in pure field emission than the as-received powder, with turn-ons as low as 1 V/μm. The cause of the emission performance improvement was unknown at this stage, with both bulk and surface enhancement by the lithium treatment considered possible, but washing the powder in fuming nitric acid seemed to further improve the emission performance.

Attempts were made to characterise the lithiation treatment using a series of characterisation steps including electron microscopy, secondary ion mass spectroscopy (SIMS) and electron energy loss spectroscopy. Transmission electron microscopy and electron diffraction showed that after lithiation large quantities of the LiH precursor remained on the surface of the nanodiamonds, but after the acid washing step most of this was removed. SIMS analysis of a larger single crystal diamond showed that there was lithium present after lithiation but the vast majority was confined to the first 5 nm of the surface, indicating that bulk doping was unlikely. Due to the difficulty in characterising the nanodiamond powders, it was decided to concentrate on using these large single crystals for the remainder of the project, as well as looking at modelling the interaction of individual lithium atoms on the diamond surface using density functional theory.

8.1.2 Computational studies of the interaction of lithium on the C(100) and C(111) diamond surfaces

Computational modelling of the C(100) and C(111) surfaces was performed using CASTEP, a density functional theory modelling program running via a virtual machine using the University of Bristol's Bluecrystal supercomputing cluster. The C(100) and C(111) surfaces were studied as they are the most common facets seen on diamond and so the most likely to have displayed the behaviour shown in the previous chapter. The interaction with lithium was studied for both the clean surface and also the oxygenated surface, in light of the improved emission seen after acid washing, which can produce an oxygen termination on diamond.

The C(100) surface simulations were performed by Kane O'Donnell but are presented here as an important part of the story to understand the interaction of lithium with diamond. The C(100) surface was represented by a double-sided slab of 22 layers of carbon atoms with 21 Å on either side of the slab. After converging the bare, hydrogenated and oxygenated surfaces and confirming they agreed with the literature, the interaction of lithium with the bare and oxygenated surface was modelled.

The adsorption of lithium on the bare C(100) surface produced negative electron affinities for all the possible half and full monolayer configurations, but adsorption energies were fairly low, with most stable site being the T3 valley-bridge site for 0.5 ML coverage and the T3 and HH sites for the

full monolayer coverage, which was slightly more stable than the half monolayer. The adsorption energies for lithium on the oxygenated surface were substantially higher, with binding energies as high as 4.7 eV for both the full and half monolayer coverages on the ketone-bonded oxygenated surface. The Li-O surface also showed an even more negative electron affinity of -4.52 eV for the most stable full monolayer coverage, and a workfunction shift of -3.89 eV. This prediction is significantly better than the NEA of the hydrogen-terminated surface and much more stable than the similar Cs-O system. Above 1 ML of lithium coverage, the workfunction shift and stability were lower.

The C(111) surface showed somewhat similar behaviour but the lower number of dangling bonds on the surface changed the construction somewhat. Lithium was even less stable on the bare C(111) surface than the C(100) surface with absorption energies of just 1.50 eV, but the stability on the carbonyl bonded oxygenated surface was similar to the C(100) construction, with some key differences. Whereas the C(100) surface preferred four surface adsorbates per unit cell (two oxygen, two lithium), the most stable systems on the C(111) surface preferred a combination of three surface adsorbate atoms per unit cell - so on the ether-bridge surface with only one oxygen per unit cell, two lithium atoms could bond with high stability, whereas on the ketone-bonded oxygen surface with two oxygen atoms per unit cell, only one lithium atom was preferred. A similar trend was found for the NEA and workfunction shift, with the optimum configuration predicted to be the 0.5 ML coverage of lithium on the carbonyl surface, with an NEA of -3.97 eV and a workfunction shift of -4.23 eV.

The Mulliken electron population densities, Kohn-Sham wavefunctions and projected density of states (PDOS) for all the surfaces were studied to determine the reasons for the very large predicted workfunction shift. On the purely oxygenated surface there were clear sharp peaks in the PDOS and a predictable electron density at the top surface due to the presence of the oxygen lone pair. After lithium adsorption, it was found that this lone pair signature was disrupted and that the bulk of this electron density was delocalised deeper into the carbon lattice, with the sharp peaks in the PDOS becoming broadened and shifted as a result. It was theorised that this shifting of charge from the top surface into the first two layers of carbon atoms was causing a large distributed dipole effect that led to the large workfunction shift and NEA.

8.1.3 Photoemission studies of lithium on oxygenated diamond single crystal

Following the promising predictions using the DFT study, attempts were made to produce and characterise such a surface on C(100) oriented single crystal diamond. A series of X-ray and UV photoemission spectroscopy experiments were undertaken, firstly to characterise the hydrogen- and oxygen- terminated surfaces and then to observe the changes in both after lithium addition. Initial work using undoped crystals and the lithiation process used in chapter 4 were inconclusive due to the large amounts of charging in the XPS system, so conductive boron-doped overlayers were grown on single crystal diamond to ensure this wouldn't be a problem.

XPS of the boron-doped samples after ozone treatment showed an oxygen termination, and the sharp NEA peak from the as-grown hydrogen terminated surface was removed in UPS. After the evaporation of around 50 nm of lithium onto the oxygenated surface, the XPS data showed mostly

carbonates and oxides characteristic of lithium interacting with the air. When this surface was washed in deionised water however, the diamond signal returned but not all the lithium signal was removed, with a shift in peak position indicating a transfer of charge from the lithium atoms to the oxygen atoms. On the hydrogenated surface, no lithium remained in the XPS spectra after the water wash step, indicating that the oxygen termination was key to the lithium remaining bonded to the surface. Low energy electron diffraction patterns showed a shift in pattern from the strong (1×1) pattern for the oxygenated surface to a strong (1×1) pattern with an overlaid weak (2×1) pattern, further evidence of a lithium construction on top of the oxygen termination.

Secondary electron emission from the Li-O surface when observed in the SEM was high, comparable to the intensity observed on the hydrogenated surface, and both were much higher intensity than the oxygenated surface, as would be expected if the Li-O and hydrogenated surfaces displayed a negative electron affinity. To confirm this, the samples were also studied in UPS. The washed Li-O surface showed a very large characteristic NEA peak at approximately 5.3 eV, and an electron affinity of (-2.1 ± 0.1) eV was calculated from the spectra, with a workfunction of (2.8 ± 0.1) eV, a bigger shift than for the hydrogen surface ($\chi = -1.3$ eV).

When annealed to increasing temperature, the UPS spectra remained somewhat stable to around 925 °C, at which point the intensity of the NEA peak decreased and the workfunction increased. Above 1140 °C changes in the valence band structure began to be observed related to the loss of oxygen and the graphitisation of the surface, which was confirmed by XPS spectra after annealing to 1218 °C.

In addition to the C(100) study an attempt was made to characterise the phosphorus-doped C(111) surface but due to the high resistivity of this surface charging effects made interpreting the spectra difficult. There did appear to be an NEA peak present but little more was able to be said with any confidence and future studies of a conductive boron-doped C(111) surface would be more revealing. Nevertheless, the photoemission results from the C(100) surface indicate that a stable, strongly negative electron affinity surface is achievable using lithium on the oxygenated diamond surface and this presents a number of interesting opportunities for device applications.

8.1.4 Device application of the LiO surface treatment

Towards the end of this project, with the presence of the predicted NEA Li-O surface confirmed, some attempts to use this surface in some device applications were made. Boron-doped CVD diamond films were used to compare the field emission properties of hydrogen termination, oxygen termination and Li-O termination. The ozone treatment of the hydrogen terminated surface degraded emission current and turn-on threshold substantially, but after the addition of lithium on the surface the performance was greatly enhanced, with a substantially better performance than the hydrogen terminated surface.

Similarly, the Li-O surface termination showed a clear improvement in thermionic emission behaviour from the hydrogen terminated surface, with the thermionic emission at around 500 °C from a nanocrystalline diamond film showing a thirty-fold increase in current density from the Li-O surface treatment compared to the as-grown material.

The surface conductivity of the hydrogenated, oxygenated and lithium-oxygen terminated surfaces were studied using graphite contact probes and TLM pattern contact pads to assess the

suitability of this new surface for use in field-effect transistors. Resistance measurements of the hydrogenated surface showed a higher conductivity for the CVD C(100) surface compared to the HPHT C(100) surface, and this conductivity was removed after thirty minutes of ozone treatment for the HPHT surface and fifty minutes for the CVD surface. However, no significant conductivity was observed after the deposition of lithium onto the ozone-treated surface or after subsequent washing in deionised water on either substrate, using both TiAu and Al contact pads. It is possible that there was not sufficient coverage to provide a complete surface for such macroscopic resistance measurements and that nanoscale conductivity measurements using Kelvin Probe microscopy may yield better results, but this experiment suggests that even if the LiO surface is conductive, the simple surface preparation technique used to prepare NEA surfaces does not provide sufficiently continuous surfaces for use in FETs.

8.2 Future work

The work presented in this thesis has greatly improved the understanding of the interaction of lithium on diamond, with the photoemission and device characterisation of the Li-O surface confirming the computational predictions. The surface is an exciting alternative to hydrogen-termination for a number of applications requiring a stable NEA surface and there is a number of avenues for potential future research to explore.

Firstly, the electronic structure of this surface preparation can be studied further, through the use of angle-resolved ultraviolet photoemission spectroscopy (ARUPS) to characterise the band structure of the material, comparing it to theoretical calculations. This would require beamtime at a synchrotron facility, and the leadtime for such a study is long, which was the primary reason for it not being included in this study. Whilst doing a synchrotron study of the surface, near-edge X-ray absorption (NEXAFS) experiments could also be performed to gain further understanding of the atomic structure of the surface construction.

Secondly, the exploration of other alkali metals similar to lithium both computationally and experimentally would be useful to further understand the mechanism behind this NEA surface shift, and also potentially find even better surfaces. Caesium has already been used by a number of groups but lacks stability. Magnesium and sodium would be interesting alternatives to lithium, and work within the research department has begun to characterise magnesium on the bare and oxygenated diamond surface using the same methods described in this thesis.

Finally, much more exploration of the device application of this new surface is possible, with only the very surface scratched in this study. The method used to construct the Li-O surface is fairly crude and more controllable deposition of lithium and smoother diamond substrates could yield higher coverages and thus better performance. Combining the surface NEA with the most appropriate diamond substrate for donor/acceptor levels, conductivity and geometry will be important to optimise it for emission applications, and the engineering of test field and thermionic emission devices offers the possibility of much future work. As Richard Feynman famously said, “there’s plenty of room at the bottom!”

A

Publications and Presentations

A.1 Publications

T.L. Martin, K.M. O'Donnell, N.A. Fox and D. Cherns, *The Li-adsorbed C(111)-(1x1):O Diamond Surface*, (in preparation)

T.L. Martin, K.M. O'Donnell, N.A. Fox, D. Cherns, H. Shiozawa, C. Giusca and S.R.P. Silva, *High-temperature stable Negative Electron Affinity Lithiated Diamond*, Journal of Applied Physics (in submission)

Tomas L. Martin, Kane M. ODonnell, Hidetsugu Shiozawa, Cristina E. Giusca, Neil A. Fox, S. Ravi P. Silva and David Cherns, *Lithium monolayers on single crystal C(100) oxygen-terminated diamond*, Material Research Society Fall Meeting 2010 proceedings, 1282: mrsf10-1282-a06-03 (2011)

Kane M. ODonnell, Tomas L. Martin, Neil A. Fox and David Cherns, *The Li-adsorbed C(100)-(1x1):O Diamond Surface*, Material Research Society Fall Meeting 2010 proceedings 1282: mrsf10-1282-a05-04 (2011)

K.M. O'Donnell, T.L. Martin, N.A. Fox and D. Cherns, *Ab initio investigation of lithium on the diamond C(100) surface* Physical Review B, vol. 82, Issue 11, id. 115303

S. Furkert, T.L. Martin, *A diamond based thermionic solar energy converter*, Proceedings of Renewable Energy 2010

A.2 Oral Presentations

T.L. Martin, K.M. O'Donnell, N.A. Fox and D. Cherns, *Negative electron affinity diamond using lithium adsorption on the oxygenated C(111) and C(100) diamond surfaces* Hasselt Diamond Workshop 2011, SPDD XVI, Hasselt (Belgium), February 2011

T.L. Martin, K.M. O'Donnell, N.A. Fox and D. Cherns, *Low workfunction negative electron affinity diamond using temperature stable lithium-oxygen surface treatments* Material Research Society Fall Meeting 2010, Boston (USA), December 2010

T.L. Martin, K.M. O'Donnell, G. Fuge, S. Furkert, N.A. Fox, D. Cherns and M.N.R Ashfold, *Lithiated nanodiamond as a low threshold thermionic and field emitter*, Material Research Society

Fall Meeting 2009, Boston (USA), December 2009

A.3 Poster Presentations

Tomas Martin, Joshua Lay, Kane O'Donnell and Neil Fox, *Lithiated nanodiamond as a low threshold electron emitter*, Bristol Nanoscience Symposium, Bristol (UK), November 2009

T.L. Martin, S. Furkert, G. Fuge, N.A. Fox and D. Cherns, *Lithiated Nanodiamond as a low threshold electron emitter*, First Great Western Research Symposium, Bristol (UK), January 2010

T.L. Martin, S. Furkert, G. Fuge, N.A. Fox and D. Cherns, *Lithiated Nanodiamond as a low threshold electron emitter*, First Great Western Research Symposium, Bristol (UK), November 2008